Autonomous Systems Laboratory

Final Report: Phase I

Development of a Semi-Autonomous Underwater Vehicle for Intervention Missions (SAUVIM)

Submitted to the Office of Naval Research

October 30, 2000 ©2000

Form SF298 Citation Data

Report Date ("DD MON YYYY") 30102000	Report Type Final	Dates Covered (from... to) ("DD MON YYYY") 01081997 30102000

Title and Subtitle Development of a Semi-Autnomous Underwater Vehicle for Intervention Missions	**Contract or Grant Number**
	Program Element Number

Authors Yuh, J.; Choi, S.; Coutsourakis, G.; Easterday, O.; Kim, T. W.; Marani, G.; McMurtry, G.; Ghasemi-Nejhad, M.; Sugihara, K.; West, M.	**Project Number**
	Task Number
	Work Unit Number

Performing Organization Name(s) and Address(es) University of Hawaii at Manoa Dept. of Mechanical Engineering 2540 Dole St., Holmes Hall 302 Honolulu, HI 96822	**Performing Organization Number(s)**

Sponsoring/Monitoring Agency Name(s) and Address(es) Program Officer Chris F. Hillenbrand Office of Naval Research, Code 82 Program Office 1176 Howell St. B990/4 Newport, RI 02841-2650	**Monitoring Agency Acronym**
	Monitoring Agency Report Number(s)

Distribution/Availability Statement
Approved for public release, distribution unlimited

Supplementary Notes

Abstract

Subject Terms

Document Classification unclassified	**Classification of SF298** unclassified
Classification of Abstract unclassified	**Limitation of Abstract** unlimited
Number of Pages 272	

Copyright:

Summary

Technical Development Report: August 1, 1997 – October 30, 2000

The SAUVIM proposal was submitted under the ONR Annual Announcement of the July 11, 1996 Commerce Business Daily, and the project officially began on August 1, 1997 with an 18-month, $2.237 million research fund from the Office of Naval Research's Undersea Weapons Technology Program directed by Mr. James Fein. The project was later extended at no cost till October 30, 2000.

The first progress report was submitted to ONR during Mr. Fein's site visit of October 28, 1997. The second progress report was submitted to ONR during the Advisory Committee's (AdCom) site visit of February 24, 1998. The First Annual Progress Report was submitted to ONR in August 1998 and presented during the site visit of September 15-16, 1998. With the departure of Mr. James from ONR, Mr. Chris Hillenbrand became the new ONR Program Director for the SAUVIM project. The fourth progress report was submitted during Mr. Hillenbrand's site visit of April 8, 1999. The Second Annual Progress Report was submitted to ONR in August 1999 and presented during the site visit of May 10-11, 2000. During all site visits, each SAUVIM research group gave a presentation of their current progress. This is the Final Report for Phase I and describes the overall technical development of the project during the 3-year period of 1997-2000.

Objective

The primary research objective is to develop a Semi-Autonomous Underwater Vehicle for Intervention Missions (SAUVIM). Unlike the fly-by autonomous underwater vehicles (AUV), SAUVIM will have a manipulator work package. It will require an advanced control system and a precise sensory system to maintain high accuracy in station keeping and navigation.

Background

Most intervention missions - including underwater plug/unplug, construction & repair, cable streaming, mine hunting, and munitions retrieval - require physical contact with the surroundings in the unstructured, underwater environment. Such operations always increase the level of risk and present more difficult engineering problems than fly-by and non-contact type operations. For these intervention operations, the vehicle requires a dexterous robotic manipulator; thus the overall system becomes a high degree-of-freedom (dof), multi-bodied system from the coupling effects of the vehicle and the manipulator motions. These operations require precise force/torque feedback with high degree of accuracy even in the presence of unknown, external disturbances, i.e. undersea currents. All these issues present very complex engineering problems that have hindered the development of AUVs for intervention missions. Currently, the state-of-the-art in machine

intelligence is insufficient to create a vehicle of full autonomy and reliability, especially for intervention missions.

The development of '*undersea robots that can intelligently work with arms than just swim*' will have a great impact on worldwide underwater robotic vehicle technology and provide a cost-effective engineering solution to many new underwater tasks and applications that fly-by type submersibles have not been able to handle. The proposed vehicle – SAUVIM - is in response to the current local and national needs for the development of this technology and will ultimately be useful in many intervention missions. One such application field is the Pacific Missile Ranging Facility (PMRF) in Hawaii.

Development

The SAUVIM project was proposed as a two-phase research and development program. Phase I has three parts: (1) to study the major research components, (2) to develop and integrate the basic software and hardware of SAUVIM, and (3) to test the vehicle in a shallow water environment. Phase II is a continuation and completion of the research and development of Phase I with deep water environment testing.

As stated in the original proposal, the project consists of five major components:

- Adaptive, Intelligent Motion Planning;
- Automatic Object Ranging and Dimensioning;
- Intelligent Coordinated Motion/Force Control;
- Predictive Virtual Environment; and
- SAUVIM Design.

During the Phase I period, there have been approximately sixty people supported by this ONR project. Currently, there are thirty-one people working on the project - 6 faculty members, 7 full-time staff members, 10 graduate students and 8 undergraduate students. The Advisory Committee was formed to provide technical advice and direction by reviewing research directions and progress, and to provide advice and assistance in exploring potential applications and users. The four-member Advisory Committee consisted of Mr. Fred Cancilliere of the Naval Undersea Warfare Center, Dr. Alexander Malahoff of the University of Hawaii, Dr. Homayoun Seraji of the Jet Propulsion Laboratory, and Mr. Dick Turlington of the Pacific Missile Range Facility. Two additional members - Dr. Paul Yuen of the University of Hawaii and Mr. James Fein, the former ONR Program Director - have been included in the Advisory Committee. The SAUVIM organizational chart is shown in Figure A, and the updated research schedule is shown as an overall Gantt Chart in Figure B and as a sub-task Gantt Chart in Figure C.

- Adaptive, Intelligent Motion Planning (AIMP) – The AIMP aims at developing SAUVIM's motion planning, which is intelligent and adaptive in that the system is capable of decision-making at a task or mission level and can deal with unknown or time-varying environment. Motion planning for an AUV can be decomposed into path planning and trajectory generation, although they are not completely independent of each other. Path planning is a computation and optimization of a collision-free path in an environment with obstacles. Trajectory generation is the scheduling of movements for an AUV along the planned path over time. To simultaneously compensate for these objectives, a genetic algorithm (GA) based 3D-motion planner is implemented for both an off-line and on-line cases. An off-line case is when an environment is a

known and static, while an on-line case must be capable of modifications in response to dynamic, environmental changes. The utilization of GA-based approach has two advantages: 1) it is adaptive and 2) the dimension of space has less effect on performance than other methods.

The AIMP software has gone through three version upgrades. The first was *Version 1.alpha*, which integrates the off-line and on-line algorithms in C with a graphic user interface using OpenGL. This software version was tested on the Autonomous Systems Laboratory's autonomous underwater vehicle - ODIN. The second was *Version 1.0*, which integrates the path planning and trajectory generation algorithms. The third was *Version 1.1*, which optimizes the original software organization and data structures, and includes a database of mapping data on the main memory. Also, a Software Development Process (SDP) has been developed and implemented to oversee the various developments in software version changes. Several papers have been published in these subjects.

- Automatic Object Ranging and Dimensioning (AORD) – The main objective of the AORD is to develop a multiple sensor configuration to be utilized during SAUVIM's intervention missions. This three-sensor system consists of (1) a laser ranging sensor (LRS), (2) a passive arm sensor (PA) and (3) a manipulator homing sensor (MHS). The laser ranger, the homing sensor, and the passive arm have all been designed and prototyped. According to initial feasibility and prototype tests, all three sensors showed good performance.

  The underwater version of the PA has been fabricated and has been assembled. The PA is made of 6061-Aluminum, and it has two three-axis gimbaled joints and a single-axis hinge joint. The entire PA structure is compensated with mineral oil. It utilizes the original software developed for the prototype.

  The underwater versions of the LRS and the MHS are in the process of fabrication and assembly. The camera housings for both systems have been manufactured using 6061 aluminum with vacuum-sealed lens and underwater connectors have been ordered. The software for both systems has been developed using the prototypes.

- Intelligent Coordinated Motion/Force Control (ICM/FC) – The major objective of the ICM/FC is simple yet complex. The control of an AUV and its manipulator is a multi-bodied, dynamic problem of vast unknowns; therefore, this task was subdivided into four sub-tasks, which were Theoretical Modeling (TM), Low-Level Control (LLC), High-Level Control (HLC), and Dry Test Design and Set-up (DTDS). However, with the arrival of the 7-dof, underwater manipulator, the TM and DTDS were combined to form a common group – Manipulator Control and Test Platform (MCTP).

  The MCTP was recently developed to accelerate the progress in the TM and DTDS sub-tasks. With the acquirement of the Ansaldo 7-dof manipulator and constraints in time, the focus has been changed to the development of the Ansaldo software in conjunction with the manipulator kinematics, dynamics, force-control and coordinated motion control modules. Currently the Ansaldo manipulator runs off the VME bus system using VxWorks and Matlab with Simulink. Development in the "rapid prototyping, graphic software" has been the central point in enhancing the complex, underwater dynamic actions and reactions. The manipulator development will be mostly self-contained until its connection to the vehicle prior to wet testing.

The LLC has two objectives: 1) to design and develop an advanced vehicle control system for navigation and hovering, and 2) to design and develop an advanced coordinate motion/force control system of the vehicle and manipulator during the intervention mode. During this portion of Phase I, the focus has been on continuing efforts in obtaining high performance in navigation and hovering, and the development of a localization technique. The navigation and hovering uses the on-board sonar, inertial navigation, and pressure sensors. The localization technique being developed is an evidence grid approach. The grid method accumulates occupancy evidence from an array of spatial locations and slowly resolves the ambiguities as the AUV travels. Both the navigation and hovering, and localization techniques are being tested on ODIN.

HLC's objective is to develop a supervisory control module that will minimize human involvement in the control of the underwater vehicle and its manipulation tasks. This module involves the development of high-level task planning where a mission is always composed of two parts: the goal and the method of accomplishment. In other words, "what do I need to do" and "how do I do it." Following this strategy, a new high-level architecture of vehicle control, named the Intelligent Task-Oriented Control Architecture (ITOCA), is being developed for SAUVIM. ITOCA is an effective and efficient operation running on the VxWorks real-time operating system (RTOS) environment. ITOCA is four layers: a planning layer, a control layer, an execution layer and an evaluation layer. Every mission is broken into many smaller missions and the simplest mission is considered a task. The combination of different tasks in different sequences accomplishes various missions. Presently, a preliminary, pilot algorithm is being considered and developed. The HLC is one of the major research tasks for Phase II.

- Predictive Virtual Environment (PVE) – The PVE is aimed at developing a supervisory monitoring system for SAUVIM to smoothly and realistically integrate mapping data with on-line sensory information even in the midst of delayed and limited information. This virtual reality (VR) based system must also be able to accurately predict the current status and location of the vehicle under these conditions. The development for the PVE has been modular. The various modules are: the SAUVIM Simulation Software (SSS); the SAUVIM Video Overlay Software (SVOS); the Communication Software (CS); and the artificial neural network (ANN) Video Prediction Software (VPS). The SSS has been upgraded from its *Version 1* to *Version 1.1*, which includes the incorporation of a Magellan spaceball mouse, an accurate 3D graphical model of SAUVIM and the Ansaldo manipulator, scene-smoothing methods using interpolation techniques, and an easy-to-use user interface. The SVOS was developed to overlay video images of the seafloor (texture and color) to the graphic images to provide more accurate monitoring of the vehicle, manipulator and environment. The CS for SAUVIM is an extension of the NSF's DVECS project. Currently the DVECS (Distributed Virtual Environment Collaborative Simulator) system uses a cellular phone to communicate the vehicle data from the test-site to the monitoring computer located on campus for data fusion. Experiments are being conducted with the ODIN AUV. The experiments of ODIN are projected via an ElectroHome Marquee 8500 CRT projector coupled with multiple Stereographics (SG) emitters and SG CrystalEyes glasses. Finally, the VPS is in its infancy; however, several ANN methods have been tested for optimal computation time and position accuracy. Experiments have been performed in the laboratory and have generated positive results.

- SAUVIM Design (SD) – This task is the main objective of the SAUVIM project for Phase I. It is an effort to design and develop efficient, reliable hardware/software architectures of SAUVIM. Due to the immense demand of this task, it is divided into five sub-tasks, which are Reliable, Distributed Control (RDC), Mission Sensor Package (MSP), Hydrodynamic Drag Coefficient

Analysis (HDCA), Mechanical Analysis and Fabrication (MAF), and Mechanical-Electrical Design (MED).

The goal of RDC is to develop a reliable and efficient computing architecture for signal and algorithmic processing of the entire SAUVIM system. The proposed system is a multi-processor system based on a 6U VMEbus and the VxWorks real-time operating system. This system is capable of high processing throughput and fault tolerance. Currently the system consists of two VMEbuses, which are the navigation control system and the manipulator control system. The main VMEbus, or the navigation control system, has two Motorola M68060 CPU boards, a multi-port RS232 interface board, and an I/O board with a Pentium MMX processor based PC104+ board, which is connected via a RS232 port. The navigation control system handles the communication, supervision, planning, low-level control, self-diagnostics, video imaging, etc. The data exchange between the two CPUs is conducted via shared memory. The second VMEbus, or the manipulator control system, has one Motorola M68040 CPU and an I/O board. Two PC104 boards are connected serially to this CPU. The manipulator control system is independent and dedicated to the manipulator control. Many of the hardware components have been tested and are being interface with its respective software systems. Various optimization changes have been implemented to minimize communication and computation. This development will continue throughout the vehicle's development process.

The objective of the MSP is to provide semi-continuous records of SAUVIM water depth, temperature, conductivity, computed salinity, dissolved oxygen, magnetic signature of the seafloor, pH and turbidity during the survey mode. In the intervention mode, the MSP also provides compositional parameters at a selected seafloor target, including pumped samples from submarine seeps or vents. The MSP is an independent system with its own PC 104 CPU and its own power supply residing in a separate pressure vessel. All of the sensors have been purchased, and an initial field test at the Loihi Seamount has been conducted. Continual tests are being conducted to optimize the scientific sensor data-gathering capabilities.

The HDCA is used to determine the hydrodynamic coefficients via a numerical solution of full Navier-Stokes equations using PHOENICS, a commercial computational fluid dynamics (CFD) code. Initial results from the PHOENICS software have produced mixed results. The current vehicle fairing has produced a drag coefficient of 0.40; however, it has not yet been verified. Other CFD software and model testing is being conducted to verify the drag coefficient results before the implementation of the vehicle fairing on SAUVIM.

The MAF has three objectives. Its primary goal is to design and fabricate composite pressure vessels with end caps and connector openings for full ocean depths taking stress, buckling, hygrothermal effects, and fatigue analysis into account; and its two secondary goals are to design and fabricate the SAUVIM fairing and to analyze the SAUVIM frame. A thorough analysis and comparison of the Ti-6Al-4V, AS4/Epoxy, and AS4/PEEK pressure vessels manifest the advantage of composite materials in reduction of weight, size and strength. Using these results, a scaled model prototype using AS4/PEEK has been fabricated and tested. A 1/3 sized prototype is being fabricated and will also be tested. For the shallow water vehicle test, a full-sized, fiberglass pressure vessel with aluminum end caps have been manufactured and tested. These vessels are being used to determine the final hardware layout. The aluminum frame has been designed and fabricated. A full-ocean depth pressure vessel of AS4/PEEK has been developed and is in its testing phase. The initial fairing analysis has been developed and expanded. Fairing optimizations are being considered.

The MED is the integration of the mechanical and electrical components for SAUVIM. First, the design specifications were established for the fairing, frame, instrument pressure vessels, buoyancy systems, mission sensor, passive arm and robotic manipulator tasks. Second, after scrutinizing review of SAUVIM's major components - i.e. sensors, actuators and infrastructure - in terms of power consumption, compatibility, weight distribution, buoyancy distribution, hydrodynamic effects and task effectiveness, all major components have been purchased. Technical drawings of the vehicle frame, fairing, and related sub-structures have been completed. Many of the mechanical and electrical components have been fabricated and are being integrated with the overall electrical layouts.

The main body of this report is devoted to the detailed descriptions about the major technical developments and achievements during the 1997-2000 years.

Table of Contents

Figure A: SAUVIM Organizational Chart

SAUVIM   Schedule

#	Activity	Start Date	Finish Date
1	AIMP: Prototype offline genetic algorithm	6/1	9/1
2	AIMP: Conduct simulation of offline GA	9/1	3/1
3	AIMP: Design interface to SAUVIM	10/1	3/1
4	AIMP: Implement offline GA in C/C++	10/1	7/1
5	AIMP: Prepare map data	4/1	10/1
6	AIMP: Redefine the online GA	6/1	9/1
7	AIMP: Prototype online GA	9/1	12/1
8	AIMP: Conduct simulation of online GA	12/1	6/1
9	AIMP: Design interface to SAUVIM	2/1	6/1
10	AIMP: Implement online GA in C/C++	2/1	10/1
11	AIMP: Implement trajectory generation	9/1	2/1
12	AIMP: Integrate C/C++ programs	1/1	10/29
13	AIMP: Test integrated system with VR	4/1	8/6
14	AIMP: Test motion planning with SAUVIM	4/21	8/6
15	PVE: DF: Survey	6/1	9/1
16	PVE: DF: Design software	9/1	6/1
17	PVE: DF: Communication	6/1	8/6
18	PVE: SS: Survey	6/1	9/1
19	PVE: SS: Purchase, customize, or write	9/1	6/1
20	PVE: SS: Revision of VE & interpolation	6/1	11/29
21	PVE: ANN: Study problem & model	6/1	12/1
22	PVE: ANN: Survey related work & compare	10/1	2/1
23	PVE: ANN: Design and implement	2/1	2/1
24	PVE: ANN: Evaluate by simulation & refine	1/5	8/6
25	PVE: ANN: Integrate w/ other components	4/27	8/6
26	PVE: Combine DF, SS, & ANN with VR	4/27	8/6
27	PVE: Test PVE with SAUVIM	6/7	8/6
28	AORD: LR: Survey	3/2	7/3
29	AORD: LR: Design & analysis	6/1	10/2
30	AORD: LR: Fabrication	10/1	6/28
31	AORD: LR: Design test & modify	4/28	8/6
32	AORD: LR: Fixture to SAUVIM	6/3	8/6
33	AORD: HD: Survey	3/2	6/1
34	AORD: HD: Design & analysis	6/1	4/28
35	AORD: HD: Fabricate, test, & modify	10/1	11/19
36	AORD: HD: Attach to dry test setup	4/1	11/19
37	AORD: HD: Modify for SAUVIM & test	5/3	8/6

Nov 13, 2000

Figure B-1: SAUVIM: Overall Project Gantt Chart (1997-2000)

2

SAUVIM Schedule

	Activity	Start Date	Finish Date
38	AORD: HD: Attach to SAUVIM	5/25	8/6
39	AORD: PA: Survey & research	7/1	10/1
40	AORD: PA: Conceptualize & design	9/1	7/1
41	AORD: PA: Fabricate, test, & modify	6/1	7/1
42	AORD: PA: Attach to dry test setup	3/26	8/6
43	AORD: PA: Modify for SAUVIM & test	12/24	8/6
44	AORD: PA: Attach to SAUVIM	5/26	8/6
45	SD: HDCA: Shape optimization	8/1	4/1
46	SD: HDCA: Hydrodynamic coefficient analysis	4/1	10/29
47	SD: HDCA: Hydrodynamic coefficient test	2/23	8/6
48	SD: MAF: Setup ANSYS & DYNA3D	6/1	8/1
49	SD: MAF: Preliminary design	8/1	12/29
50	SD: MAF: Design refinement	1/1	9/28
51	SD: MAF: Frame design & analysis	3/15	9/28
52	SD: MAF: Scaled model: design, fabricate & test	9/25	8/6
53	SD: MAF: Final design	4/25	8/6
54	SD: MAF: Fabricate set-up modification	5/1	8/6
55	SD: MAF: Fairing design	6/1	8/6
56	SD: MAF: Full scale PV & end-cap fabrication	6/1	8/6
57	SD: MAF: Full scale PV test	6/1	8/6
58	SD: MAF: Fairing fabrication	6/1	8/6
59	SD: MAF: Additional PV fabrication	6/1	8/6
60	SD: MED: Setup work space	6/1	1/29
61	SD: MED: Make mock test site	6/16	7/7
62	SD: MED: Design vehicle	6/16	3/30
63	SD: MED: Component identification	8/11	2/26
64	SD: MED: Redesign	9/8	5/29
65	SD: MED: Process purchases	9/29	5/29
66	SD: MED: Frame fabrication	11/17	4/28
67	SD: MED: CPU, I/O, software control	11/17	8/6
68	SD: MED: Install & test sensors	11/17	8/6
69	SD: MED: Install & test video	11/17	8/6
70	SD: MED: Arm modification	4/25	8/6
71	SD: MED: Install & test manipulator	4/25	8/6
72	SD: MED: Test integrated system	8/3	8/6
73	SD: MED: Shallow water system	2/13	8/6
74	SD: MED: Sub-assembly - fabricate, fesign, etc.	2/24	8/4

Figure B-2: SAUVIM: Overall Project Gantt Chart (1997-2000)

3

SAUVIM Schedule

	Activity	Start Date	Finish Date
75	SD: RDC: Survey	8/1	12/29
76	SD: RDC: Purchase & design	11/3	2/26
77	SD: RDC: Test of VMEbus and boards & I/O	1/1	6/29
78	SD: RDC: Software architecture for vehicle/arm	6/1	9/28
79	SD: RDC: Real-Time OS programming	9/1	4/28
80	SD: RDC: Port software to Tornado PC	2/1	4/2
81	SD: RDC: Graphic simulator for VME system	3/1	12/29
82	SD: RDC: Make device driver for RTW	10/27	8/6
83	SD: RDC: Port software to RTW & debugging	3/29	11/29
84	SD: RDC: System integration	8/31	8/6
85	SD: RDC: System debugging & modification	10/27	8/6
86	SD: MSP: Survey	6/2	10/1
87	SD: MSP: Purchase & design	10/1	2/2
88	SD: MSP: Software development	2/2	6/1
89	SD: MSP: Field test & calibrate	6/1	10/1
90	SD: MSP: Integration with SAUVIM	2/1	8/6
91	SD: MSP: Shallow water test	10/1	8/6
92	ICM/FC: Manipulator survey	6/1	6/1
93	ICM/FC: Manipulator purchase & testing	6/1	8/6
94	ICM/FC: DTDS: Conceptualize & design	9/3	2/26
95	ICM/FC: DTDS: Test & modify setup	3/2	4/1
96	ICM/FC: DTDS: Attach manipulator & modify	3/1	7/29
97	ICM/FC: TM: Kinematics & dynamics	9/1	2/28
98	ICM/FC: TM: Motion coordination algorithms	3/1	7/31
99	ICM/FC: TM: Computer simulation of MC	8/1	8/6
100	ICM/FC: TM: Force control algorithm	11/1	12/31
101	ICM/FC: TM: Computer simulation of FC	12/26	8/6
102	ICM/FC: TM: Test on MC & FC	3/26	8/6
103	ICM/FC: LLC: Survey	6/2	10/1
104	ICM/FC: LLC: Design algorithm	9/1	2/26
105	ICM/FC: LLC: Implement algorithm on ODIN	12/1	10/1
106	ICM/FC: LLC: Test & modify for SAUVIM	3/1	8/6
107	ICM/FC: HLC: Survey	8/26	10/1
108	ICM/FC: HLC: Design pilot algorithm	10/1	10/29
109	ICM/FC: HLC: Implement pilot algorithm	2/3	8/6
110	ICM/FC: Combine TM, LLC, & HLC w/ veh	11/25	8/6

Figure B-3: SAUVIM: Overall Project Gantt Chart (1997-2000)

SAUVIM Schedule

#	Activity	Start Date	Finish Date
1	ONR Site Visit for Phase I Completion	5/8	5/12
2	SURT 2000 in Wailea, MAUI	6/12	6/16
3			
4	WT: Renegotiate Use of SNUG Harbor Space	2/28	3/13
5	WT: Confirmation and Selection of SNUG Space	3/13	4/24
6	WT: Set-up Infrastructure at SNUG Space	4/24	5/22
7	WT: Arrange Transportation (UH to SNUG)	2/28	5/29
8	WT: Arrange Mobilization of Frame to Dock	5/1	5/29
9	WT: Schedule Dates for Initial Wet Test	5/15	5/22
10	WT: Initial Wet Tests	5/22	12/28
11	WT: Schedule Dates for Electronics Wet Test	6/12	12/28
12	WT: Electronics Wet Tests	6/18	12/28
13	WT: Schedule Dates for Shallow Water Tests	7/3	12/28
14	WT: Shallow Water Tests	7/10	12/28
15			
16	ED: Completion of PV4 Interface Schematics	3/1	3/31
17	ED: Completion of Inter-Vessel Connections	3/1	12/28
18	ED: Fabrication of Interface Boards for PV3	3/1	4/28
19	ED: Fabrication of Auxiliary Board for PV3	3/1	11/27
20	ED: Completion of Schematic for PV4 (AC)	3/1	6/2
21	ED: Packaging of PV3 & PV4	3/1	12/28
22	ED: Completion of PV5 & PV6 Schematics	3/1	12/28
23	ED: Completion of Battery Charger	3/1	12/28
24	ED: Packaging of PV5 & PV6 (PV1 & PV2)	3/1	12/28
25			
26	MD: Batteries	3/6	12/28
27	MD: Main Rails	3/6	3/13
28	MD: HPDE Rails & Run Strips	3/13	3/20
29	MD: Tray Lockdown Mechanism	3/20	12/28
30	MD: Pressure Vessel Mounts	3/6	12/28
31	MD: Fit Saddles to PVs & Cut Notches	3/6	3/20
32	MD: Mount & Bond Neoprene to Saddle Blocks	3/20	4/3
33	MD: Space Rails, Mount Saddles, PVs & Test	4/3	12/28
34	MD: Top Foam	3/6	12/28
35	MD: Side Dorsals, Rail Mount, Notches & U-bolt	3/6	3/13
36	MD: Position & Drill Tie-Rod Holes	3/13	3/20
37	MD: Form, Cut & Bond Neoprene Pads to Foam	3/20	3/27

Nov 13, 2000

Figure C-1: SAUVIM: Sub-Task Gantt Chart (2000-2001)

5

#	Activity	Start Date	Finish Date
38	MD: Bend Al Mount Strips for Fiberglass	3/27	4/3
39	MD: Cut & Shape "Scrap Blocks" for Mounting	4/3	4/10
40	MD: Clamp Foam to Frame	4/3	4/10
41	MD: Side Foam	4/10	12/27
42	MD: Cut Blocks to Shape & Size	4/10	4/17
43	MD: Cut, Fashion & Weld L-channel Supports	4/17	5/1
44	MD: Form, Cut & Bond Neoprene Pads to Foam	5/1	5/8
45	MD: Clamp Foam to Frame	5/8	12/28
46	MD: Pressure Vessel Content & Test	3/6	12/28
47	MD: Intra-PV Wiring	9/6	12/28
48	MD: Inter-PV Wiring	9/6	12/28
49	MD: Connector Orders	3/6	3/20
50	MD: Connector Holes on Lids (Screw Taps)	3/20	12/28
51	MD: Leak Test PVs with FCR Receptacles	6/12	12/28
52	MD: Lateral Thrusters	5/22	12/28
53	MD: Fabricate Interface & Mount Frames	5/22	5/29
54	MD: PVC Interface Pipes; Cut & Mount	5/29	6/12
55	MD: Vertical Thrusters	6/12	12/28
56	MD: Fabricate Interface & Mount Frames	6/12	6/19
57	MD: PVC Interface Pipes; Cut & Mount	6/19	7/3
58	MD: Longitudinal Thrusters	7/3	12/28
59	MD: Machine Thruster Clamps	7/3	7/17
60	MD: Ballast	4/10	12/28
61	MD: Assemble Main Ballast Tray	4/10	4/17
62	MD: Fabricate Forward Mounts	4/17	4/24
63	MD: Instrumentation Racks	10/2	12/28
64			
65	MAF: Set-up Modifications with Ben Respicio	2/28	3/20
66	MAF: Design & Fabricate Bracket System (BR)	3/20	4/3
67	MAF: Determine Processing Window for Main PV	4/3	5/1
68	MAF: Manufacture Main PV	5/1	5/15
69	MAF: Machine Main PV & Titanium End-Caps	5/15	6/12
70	MAF: Test & SEM of the Main PV	6/12	12/28
71	MAF: Crash & Impact Analysis of Fairing, Etc.	3/6	12/28
72	MAF: Documentation & Grace Period	7/3	12/28
73			
74	AA: Understanding of Ansaldo Programs	3/1	5/1

Nov 13, 2000   skc

Figure C-2: SAUVIM: Sub-Task Gantt Chart (2000-2001)

SAUVIM Schedule

	Activity	Start Date	Finish Date
75	AA: Inverse Kinematic of SAUVIM System	5/1	5/22
76	AA: Workspace Analysis for the Total System	5/22	12/28
77	AA: 3D Motion Planning for the Total System	6/19	12/28
78	AA: Control & Implementation	7/11	12/28
79			
80	LLC: Cont. Dev. on Local. & Nav. Techniques	3/1	5/1
81	LCC: Mod. of Existing ODIN Code to SAUVIM	4/3	12/28
82	LCC: Control Test in Dry and Wet Environments	6/19	12/28
83			
84	RDC: Simulation System	2/28	12/27
85	RDC: Procure Hardware	2/28	3/3
86	RDC: Assemble Hardware	2/28	3/13
87	RDC: Assemble Cables & Connectors	2/28	3/13
88	RDC: I/O Test	3/13	3/20
89	RDC: OS Re-installation	2/28	3/3
90	RDC: Design GUI	2/28	3/6
91	RDC: Implement & Debug GUI	3/6	3/20
92	RDC: Test Communication between PC & VME	3/20	3/27
93	RDC: Joystick Interface	3/20	3/27
94	RDC: Integrate Interface Software	3/27	4/10
95	RDC: Test & Debug Interface Software	4/3	4/17
96	RDC: Internal Demonstration	4/17	4/24
97	RDC: Order Additional Materials	4/3	4/17
98	RDC: Hardware Reconfiguration	4/17	12/28
99	RDC: Software Test	4/24	12/28
100	RDC: Dry Test (in PV)	5/29	12/28
101	RDC: Harness	5/29	6/19
102	RDC: I/O Test	6/19	6/26
103	RDC: Software Test	6/19	12/28
104	RDC: Reliability Test	6/26	12/28
105	RDC: Wet Test	7/3	12/28
106	RDC: Communication Test	7/3	12/28
107	RDC: I/O Test	7/3	12/28
108	RDC: Sofeware Function Test	7/10	12/28
109	RDC: Joystick Control Test	7/10	12/28
110	RDC: Dead Reckoning Test	7/17	12/28
111	RDC: Task Description Language Test	7/17	12/28

Nov 13, 2000

Figure C-3: SAUVIM: Sub-Task Gantt Chart (2000-2001)

SAUVIM Schedule

#	Activity	Start Date	Finish Date
112	RDC: Auto Maneuvering Test	7/24	12/27
113	RDC: Modify & Debug Software	7/3	12/28
114	RDC: Long Term Tasks	4/24	12/28
115	RDC: Flash ROM Booting	5/1	12/28
116	RDC: Shared Memory Access	5/1	12/28
117	RDC: Image Transmission		
118	RDC: Watchdog Routine	5/1	10/2
119	RDC: Control Algorithm Interface	5/8	12/28
120	RDC: Scan Sonar Interface	5/8	12/1
121	RDC: Scan Sonar Image Processing	5/8	12/1
122	RDC: Implement Task Description Language	5/15	12/27
123	RDC: Merge Trajectory Planning Algorithm	5/15	12/28
124	RDC: Determine Control Cycle Times	5/29	12/28
125	RDC: Dead Reckoning Algorithm	4/24	12/28
126			
127	AIMP: Begin Transfering C/C++ code to the WTK	4/3	5/1
128	AIMP: Doc. & Demo. AIMP Version 7/99	5/1	5/15
129	AIMP: Continue, Debug & Test AIMP in PVE	5/8	6/5
130	AIMP: Finalize AIMP on PVE	6/5	12/29
131			
132	PVE: Optimize WTK Performance	2/28	4/3
133	PVE: Begin Incorporation of AIMP to PVE	4/3	5/1
134	PVE: Refine Video Prediction Algorithm	4/3	5/1
135	PVE: Doc. & Demo Latest Version of PVE	5/1	5/15
136	PVE: Refine AIMP in PVE	5/8	12/28
137	PVE: Test Video Recognition & Prediction	5/2	12/29
138	PVE: Begin Incorporation of Video Pred. in PVE	6/5	12/27
139	PVE: Finalize AIMP & Video Prediction in PVE	6/5	12/28
140	PVE: Re-Evaluate the Use of SGI Versus PC	3/13	12/28

Nov 13, 2000

skc

Figure C-4: SAUVIM: Sub-Task Gantt Chart (2000-2001)

8

Adaptive, Intelligent Motion Planning (AIMP)

Project Leaders: Dr. Kazuo Sugihara
Personnel: Dr. Shenyan Zhen

Objectives

This sub-project aims at developing the motion planning system for SAUVIM. It is intelligent and adaptive in the sense that the system is capable of decision-making at a task or mission level and can deal with an unknown or time-varying environment.

There are three basic objectives.
- To develop an off-line 3D motion planning algorithm.
- To develop an on-line 3D motion planning algorithm.
- To develop an adaptive, intelligent motion planning system by integrating the off-line and the on-line planning algorithms.

Current Status (Tasks Completed During 8/1/97 – 10/30/00):

Introduction

Motion planning of an autonomous underwater vehicle (AUV) can be decomposed into path planning and trajectory generation, although they are not completely independent of each other. Path planning is to compute a collision-free path in an environment with obstacles and optimize it with respect to some criterion. Trajectory generation is to schedule the movement of an AUV along the planned path over time. This paper addresses the path planning in 3D space.

An algorithm for path planning is said to be off-line if an environment is a known, static terrain and it computes a path in advance. Otherwise, it is said to be on-line. An on-line algorithm must be capable of modifying a path in response to environmental changes such as a mobile obstacle and detection of an unknown obstacle. We propose a genetic algorithm (GA) that can be used for both off-line and on-line path planning [Sugihara97, Sugihara98, Sugihara99].

The GA-based approach has two advantages. First, it is adaptive in the sense that it can respond to environmental changes and adjust a path "globally" to a new environment. Second, the dimension of space has much less effect on performance in the GA-based approach than others. Since path planning in 3D space is known to be computationally intractable, this makes the GA-based approach more attractive.

Preliminaries

Suppose that an AUV needs to move from a start point s to an end point e in 3D space. By normalizing the unit of each dimension appropriately, consider the cubical space where s and e are on vertical edges located diagonally to each other. Assume that a path between s and e is discretized with reasonable granularity as a sequence of adjacent cells in an n-by-n-by-n grid corresponding to

the 3D space. Without loss of generality, the coordinate system can be defined so that s and e are located at (0,0,a) and (n-1, n-1, b), respectively.

Note that this discretization is applied to only the representation of a path. Map data may be represented in any way as long as we can efficiently access information of a given grid cell such as whether there is an obstacle at the grid cell. There is no restriction on shapes of obstacles.

We consider two types of obstacles: Solid obstacles and hazardous obstacles. A path cannot intersect a solid obstacle while it may intersect a hazardous obstacle at the expense of extra cost in proportion to the hazardous obstacle's weight, which represents various cost factors.

The distance $d(i,j)$ from cell i to its adjacent cell j in the 3D grid is the Euclid distance from the center c_i of cell i to the center c_j of cell j. The length $length(i,j)$ from i to j is defined as $d(i,j)(1+w(c_i,c_j))$, where w denotes the average weight between the locations c_i and c_j. The length of a path between s and e is the sum of lengths between two consecutively adjacent cells on the path.

A problem of path planning in 3D space is defined as follows.

Input: n by n by n grid, start cell (0,0,a), end cell (n-1,n-1,b), obstacles and their weights
Output: A path between cells (0,0,a) and (n-1,n-1,b) such that the length of the path is minimum, subject to the following.

(a) the path does not intersect any solid obstacle and
(b) the path meets limitations on the maneuverability of an AUV such as the minimum turning radius

In 2D space, a path is said to be monotone with respect to x-coordinate (x-monotone for short) if no lines parallel to y-axis cross the path at two distinct points, i.e., the projection of the path on x-axis is non-decreasing. Similarly, y-monotone is defined.

In 3D space, a path is said to be xy-monotone if no line parallel to z-axis cross the path at two distinct points. A projection of a path on x-y plane is called xy-projection of the path, which is a path in 2D space. Similarly, xz-projection and yz-projection are defined.

Path Planning GA

A genetic algorithm (GA) [Goldberg89] for an optimization problem maintains a population of individuals, where each individual corresponds to a candidate solution and the population is a collection of such potential solutions. In GA, a binary string commonly represents an individual. The mapping between solutions and binary strings is called a coding. The number of individuals in a population is called the population size. GA repeatedly transforms the population by using a mechanism analogous to biological evolution. The mechanism includes the following steps.
1. Fitness Evaluation: The fitness corresponding to an optimization criterion (i.e., objective function) is calculated for each individual.
2. Selection: Some individuals are chosen from the current population as parents, based on their fitness values.
3. Recombination: New individuals (called offspring) are produced from the parents by applying genetic operators such as crossover and mutation.
4. Replacement: Some individuals (not necessarily parents in general) are replaced by some offspring.

The population produced at each transformation is called a generation. By giving highly fit individuals more opportunities to reproduce, the population becomes likely to include "good" individuals throughout generations.

There are 4 major components to be designed in a GA:
- coding,
- fitness function,
- configuration of genetic operators, and
- parameters of genetic operators.

The coding used in our GA decomposes a path in 3D space into three projections of the path, namely, xy-projection, xz-projection and yz-projection. Obviously, there exists at least one triple of such 3 projections, which represent an arbitrarily given path in 3D space. However, it is not always true that an arbitrarily given triple of projections represents a unique path in 3D space. To guarantee the uniqueness, we assume the following.

Assumption 1: A path in 3D space is xy-monotone.
Assumption 2: The xy-projection of the path is x-monotone and y-monotone.

Then, a binary string as described below represents each projection. Finally, the resulting 3 binary strings are interleaved bit by bit. The reason for interleaving is that crossover can transform all the projections of a path at the same time.

Since xy-projection is x-monotone (and also y-monotone), it can be represented by a row-wise (or column-wise) sequence of n-1 pairs of direction and distance such that each pair specifies a segment of the projection between two consecutive rows (or columns). Thus, xy-projection is coded into a binary string as follows. The first bit ß indicates that a path is x-monotone if ß=0 and it is y-monotone if ß=1. A block of 3+ceiling(lg n) bits represents direction and distance on each column or row. The first 2 bits of each block denote the direction, e.g., 00 (vertical), 01 (upper diagonal), 10 (horizontal) and 11 (lower diagonal) in case of ß=0; 00 (horizontal), 01 (left diagonal), 10 (vertical) and 11 (right diagonal) in case of ß=1. The other bits of the block denote the distance as a signed integer if the direction is 00; otherwise they are ignored.

To interpret binary strings as paths and evaluate their fitness values, we use the following convention, which produces more "valid" paths in generations and hence improves the performance of our GA. If consecutive blocks of a binary string make the corresponding path go beyond boundary cells, that part of the path is regarded as a straight-line short cut along the boundary cells. Note that we leave the binary string as it is, since the non-interpreted sub string may become valid and useful later if genetic operators inherit the sub string to new generations.

In our GA, the initial population is created randomly except some special strings, which correspond to the straight-line or L-shape paths between s and e in the x-monotone and y-monotone representations. Even if a random binary string has large perturbation, the convention of "chopping off a path along the boundary" often makes the random string represents a path consisting of a few line segments.

After we conducted simulation of the GA on our GA Toolkit [Smith96], we have decided the configuration of the GA consisting of the following 3 operators. First, roulette tournament selection

with geometric ranking is used to choose parents and mate them. Second, 1-point crossover is applied to the parents. Third, mutation is applied to all individuals bit by bit randomly.

On-line Path Planning

In this section, we discuss how to apply the GA presented in Section 3 to a partially known environment in real time while an AUV is moving. When the GA-based off-line path planning produces a path, a population at the last generation is regarded as the initial population of a GA for on-line path planning.

From the viewpoint of on-line path planning, environmental changes occur due to either update of map data by sensory information or the movement of an AUV. The environmental changes may cause changing the current path in order to avoid collision and improve the path with respect to an optimization criterion in a new environment. Thus, we separate two issues regarding how to incorporate sensory information into the map data and how to update a population of the GA while the AUV is moving.

At every generation in execution of the GA for on-line path planning, the GA refers to the current world model (i.e., the current map data) in order to evaluate the fitness of each individual in the current population. The world model is stored in a database on board and continuously updated with sensory information. The adaptivity of the GA realizes a modification of the current path in response to changes of the world model due to input of sensory information. We are conducting simulation to evaluate how quickly the GA adapts for environmental changes. Simulation study of the GA on our GA Toolkit suggests that the GA keeps a population diverse enough to find an alternative path at the next generation immediately after an environmental change. This feature is very important for SAUVIM.

Trajectory Generation

The path-planning program produces a path represented by a sequence of adjacent cubes in a 3D grid structure. Such a path is intuitively viewed as a corridor, which begins at the start, passes intermediate waypoints, and ends at the destination. Once the path is produced, a smooth curve inside the corridor must be generated (Figure AIMP-1).

  Input: The path, the start point, the destination, the initial velocity, and the final velocity.
  Output: A curve such that it stays inside the path and its tangent lines at the start and the destination are same as vectors of the initial and final velocities, respectively.

The Hermite curve is used to solve this problem as follows. We sequentially produce a curve between two consecutive waypoints including the start and the destination, beginning from the start. Suppose that a curve is represented in a parametric form with 4 constants a, b, c and d,

$$p(t) = a\, t^3 + b\, t^2 + c\, t + d$$

where p(t) denotes a vector of 3 coordinates x(t), y(t) and z(t) such that $0 <= t <= 1$. With the boundary conditions at the first waypoint (t=0) and the second waypoint (t=1), p(t) must satisfy the following, where v1 and v2 are the velocities at the first and second waypoints, respectively.

$$p(0) = d$$
$$p(1) = a + b + c + d$$
$$p'(0) = v1 = c$$
$$p'(1) = v2 = 3a + 2b + c$$

By solving this system of linear equations, we can determine the constant coefficients and hence compute the curve p(t), which is intuitively S-shaped.

Next, the movement of a vehicle on the curve must be scheduled. To develop the first version of software for trajectory generation, we simplify this scheduling problem by assuming that a vehicle's speed changes in the way shown in Figure AIMP-2 and the vehicle's orientation is always same as a tangent line of the curve at the current location.

Input: The generated curve, the initial speed at the start, the final speed at the destination, constant acceleration, constant deceleration, the cruising speed, and the unit time Δ in scheduling.

Output: A sequence of locations for the vehicle to be located on the curve at each time $i \Delta$ where i is a natural number.

In general, choices of a curve and a schedule on it are interrelated. Hence the curve generation and scheduling should be solved together in order to optimize them simultaneously. For example, the maximum cruising speed may depend on the curvature and the maneuverability of a vehicle (e.g., minimum turning radius). In addition, the vehicle's dynamics should be taken into account. This is one of the issues to be investigated in future.

AIMP Software

1. AIMP Software Version 1.0 alpha
   - The off-line and on-line path planning algorithms were implemented together in C.
   - A graphical user interface was implemented by using OpenGL.
   - Outputs of the path-planning program for both off-line and on-line planning were tested in experiments of the vehicle ODIN in a pool.
2. AIMP Software Version 1.0
   - A program for trajectory generation, which generates a smooth curve for a path computed by the path-planning program and schedules the movement of SAUVIM on the curve, was developed in C. Algorithms for trajectory generation will be explained below.
   - The programs for path planning and trajectory generation were integrated as software for motion planning.
3. AIMP Software Version 1.1
   - A database of mapping data on the main memory was implemented and incorporated into the motion planning software.
   - Major revisions of source code of the AIMP Software Version 1.0 were made, which greatly improved the organization and data structures of the Version 1.0.
   - Documentation was revised in accordance with *SAUVIM Software Development Process* (which will be explained below).

Screen snapshots in a demonstration of Version 1.1 are shown in Figures AIMP-3 and AIMP-4, where the submarine volcano, Loihi, was used as the initial terrain and unknown obstacles were hypothetically added in the way that they obstructed a path.

Software Development Process

In order to assure the software quality, control version upgrades, and manage the software documentation, we designed and implemented the standardized process of software development described as follows.

Every Week   (done by each member)
Take backup of everything of the current software and a progress report together with each member's activity log on ZIP disks. The backup hierarchically consists of the following.

```
sw_name/          (software name)
  ver#/           (version number)
    src/          (source code)
    doc/          (documents)
    data/         (data or examples for testing)
    demo/         (binary files or a compressed file for a demo)
    report/       (progress reports with activity log)

backup_log        (backup history on the ZIP disk)
```

Once Every One or Two Months   (done by all members)
The latest version of software is tested by a member other than its author(s) as follows.
   1. Try to reinstall the software from the backup from scratch.
   2. Try to reproduce and run a demo of the software.
   3. Give the author comments/suggestions based on this experience.
The author(s) will revise the software including documentation accordingly.

Upon the End of a Term or Substantial Progress Made   (done by a supervisor)
   1. Compile new documents and/or revise previous documents.
   2. Create a new version of software.
   3. Certify it as the latest version on the backup and keep it in duplicate.

A version upgrade should be done as follows.
1. Clean up source code of software.
   - Test whether it works after the cleanup.
   - Write informative inline comments.
   - Add the version number, author(s)' name(s), date, and copyright at the beginning of every source file.
2. Write the following documentation about the software.
   - *Requirements Specification:* Objectives, functionality (what to do, especially, input/output relationships), hardware/software environments, etc.
   - *Design Specification:* Overall architecture of your software, module structure, caller/callee relationships with data flow, algorithms, data structures, etc. Use of diagrams is strongly desired.
   - *Reference Manual:* Any implementation details, which are important for other programmers to know in order to maintain for correction, improvement and adaptation.
   - *User's Manual with README:* Instructions for installation and operation. Use of screen snapshots is strongly suggested.
   - *Testing Document (optional, but desirable):* Methods/tools for debug of the software, input/output data in testing, performance evaluation, etc.

In case of an upgraded version, *Upgrade Note* is also required and describes what are modifications, why & how the modifications are made, which parts of software and documents have major changes, etc. With the upgrade note, a person who has some knowledge about the previous version can save time to understand the upgraded version.

Future Tasks (Phase II Tasks)

The following tasks are expected in Phase II.
1. To test the AIMP software on SAUVIM in the ocean.
2. To investigate integration of the vehicle's dynamics into our GA-based motion planning.
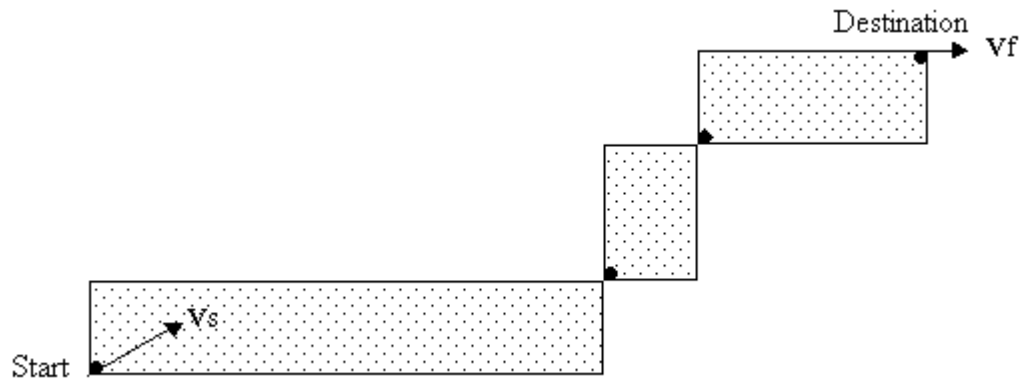
Figure AIMP-1: Inputs for generation of a curve from a path.
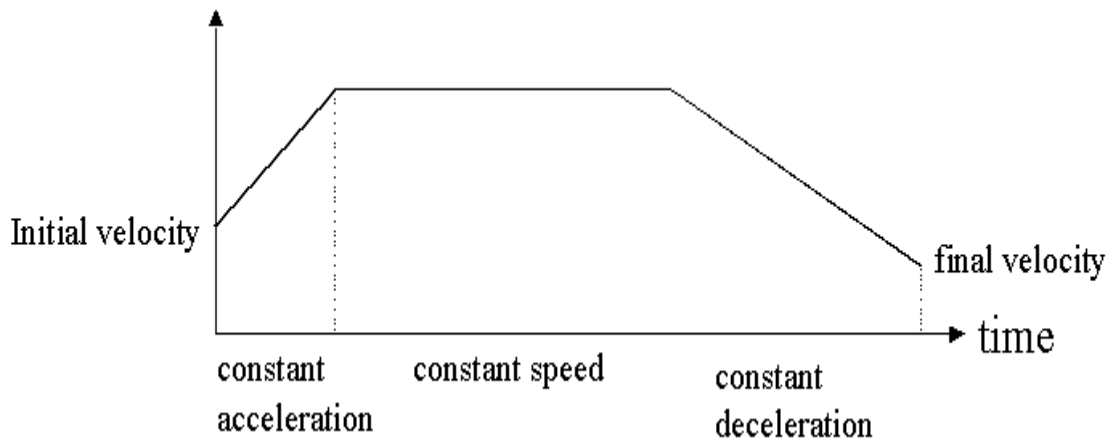
Figure AIMP-2: A schedule of speed on the curve.
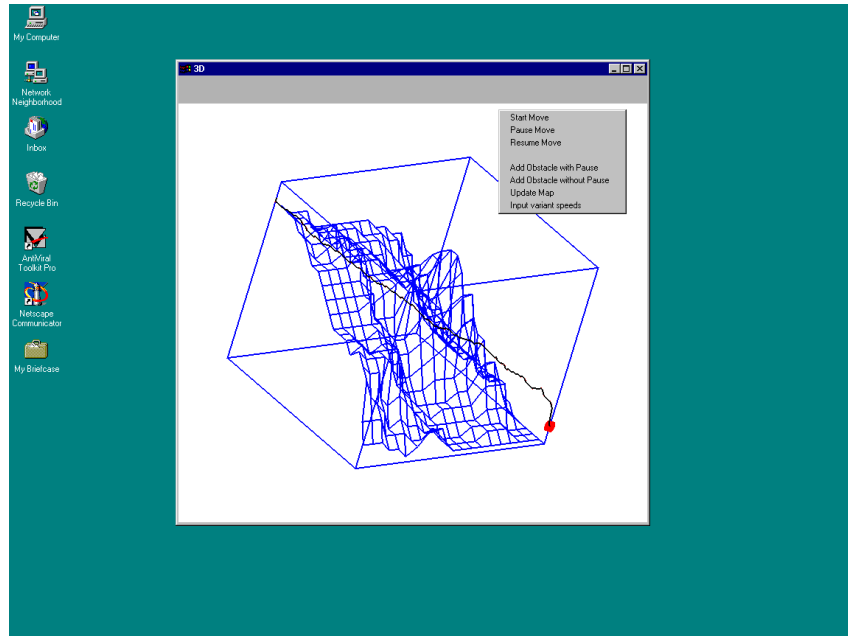
Figure AIMP-3: A screen snapshot of Version 1.1 before unknown obstacles are added.
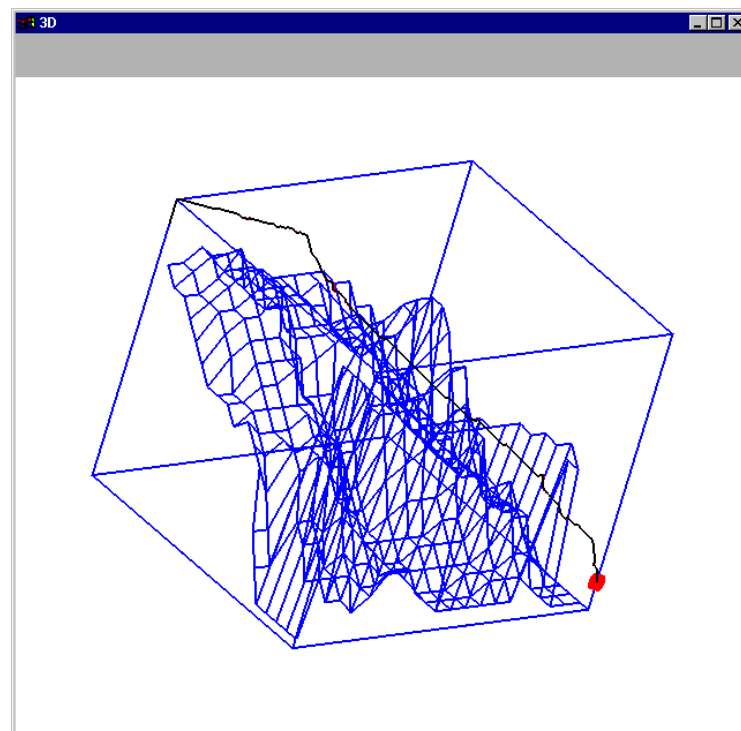
Figure AIMP-4: 3-D output after unknown obstacles are added.

Automatic Object Ranging and Dimensioning (AORD)

Project Leaders: Dr. Junku Yuh & Dr. Song K. Choi
Personnel: Mr. Oliver Easterday, Mr. Henrik Andreasson & Mr. Anders Andreasson

Objectives

To develop a multiple sensor configuration to be utilized during SAUVIM's intervention mission. The configuration will allow accurate vehicle positioning, workspace dimensioning and ranging, and manipulator homing to the task object.

A three-sensor combination is being developed to accomplish this task: 1) a passive arm sensor for vehicle positioning and station keeping, 2) a parallax-based laser ranger for workspace dimensioning and ranging, and 3) a manipulator mounted homing sensor system that will allow accurate homing of the manipulator gripper to the workspace location.

Passive Arm

The passive arm system (PA) is a multi-jointed mechanical arm that utilizes direct kinematics to sense the proximity and orientation between its two ends. Specifically, each axis of each joint senses its current angular position through the use of a potentiometer. One end of the passive arm is mounted and fixed within the forward cavity of the SAUVIM vehicle on the arm-tray, opposite to the Ansaldo robotic arm. The other end of the arm is to be attached to or placed near the task site, by means of an electro-magnet, during intervention tasks. Hence, any changes in the relative proximity between the vehicle and the task site will be sensed by angular displacements in the joints of the PA. The PA will be stored in a crutched position during cruise mode mission phases. The vehicle's robotic arm will used to crutch and un-crutch the PA as well as position it for use during active arm intervention tasks.

Laser Ranging System

The parallax based laser array ranging system (PLA) is a sensor system designed to provide the vehicle's control system with navigation information relative to a predetermined target at the task site. The operational range of this system is between 1-3 meters and it is designed to supplement the longer-range sonar systems. Mounted under the forward nosecone the sensor prototype consists of sixteen diode lasers mounted in a 4 x 4 array and one CCD camera hooked to a PC-104 computer equipped with a frame grabber. Parallax effects result in the laser dots migrating in a known pattern, depending on the distance to the occluding object. The computer can easily calculate ranges based on the relative position of the dots in the frames.

Homing Sensor System

A CCD camera will be attached to the robotic arm above the gripper and seventh joint and will be used to acquire image data for the homing sensor. The homing sensor is tasked to locate and identify shapes. Specifically, it will locate a pre-determined circular bar-code target, which will be used as a

reference point, and will determine the distance and angles between the robot arm camera and the target pattern. The initial sensor is programmed to seek, identify and reference location to circular barcode targets, later development may extend the breadth of targets

Current Status (Tasks Completed During 8/1/97 – 10/30/00):

Passive Arm

The deep-ocean passive arm is pictured in Figure AORD-1. This shows the deepwater version of the assembly. All of the aluminum parts are comprised of aluminum 6061 alloys. Two three-axis gimbal joints are in each of the two canisters. The whole assembly is around 15 lb in weight, dry and unfilled. White #9 mineral oil is the compensating fluid, which will circulate freely throughout the entire arm assembly. This is due to one cavity existing throughout the arm through the hollow arm tubes and gimbal sections, which are enclosed within neoprene bellows.

The wiring diagram for the arm is shown in Figure AORD-2. As seen from the figure the passive arm has eleven wires interconnecting it the rest of SAUVIM. As can be seen in the figure, these breakdown as follows: one signal ground line, one logic power line at 5V, seven pot data return lines, and two lines for the electromagnet power. A 50-ohm resistor is in the logic power line as a current limit should a pot reach a very low resistance. The seven 50-Kohm pots are an open-wiper design from JDK electronics company and these are all hooked in parallel between the logic rails.

How these wires are passed though the articulating joints is shown in photos of the base- and end-canister gimbals as well as elbow joints. Figures AORD-3, 4 and 5 are close-up photographs of the respective joints. From these, it can be seen that the wires are routed from slots cut in the aluminum tubing and are anchored with nylon electrical ties at both ends of the free run. Also, the free runs of wires have polyethylene spiral wrap coiled over the wires. This spiral wrap is to prevent the wires from migrating into pinch points in the joint and therefore getting severed as well as chafing on the slots cut through the arm tubing segments. The strain relief on the joints is also taken up by this armor rather than the underlying wires.

The original flexibility specified for the PA has been preserved in the pressure tolerant version. The range of swing of the base gimbals allows freedom of movement of the base leg of the PA in a cone that is ranged up to 60 degrees off the perpendicular line of the base canister. Redesign of the magnet canister allowed the same range of freedom for the lower leg of the PA. The hinge joint in its final configuration can range from a full extension (180 degrees) to a 60-degree included angle. The arm tubing sections along with the enclosed wire have been made easy to modify in length - this was done as much uncertainty about optimal lengths of the tubing segments is likely to remain until some combined arm experiments are performed.

The arm is hooked up to a 16-bit Data Translation A/D board in a 386 computer for accuracy testing as has a C-based program running. The code in its current form reports back the angles of the seven joints. Like the dry test arm, the forward kinematics solution is being sought. The same model with slight modifications should work as the two arms are topographically equivalent; the only thing that has changed is the distance of some of the segments interconnecting the joints. Figure AORD-6 is a display of the kinematics layout of the deep-ocean arm. Appendix AORD-1 is an overview of the symbolic solution matrices and the end results. The full symbolic solution is shown in Appendix AORD-2, which was obtained by use of the DERIVE software.

The next steps to in the PA development will involve sealing up the units, filling with compensating oil and performing full wet testing of the arm. This will complete the hardware development. Software development that remains is to port the dry arm code to the VME system, adjust some of the arm characteristics in the kinematics array, code optimization and to add a routine to allow for velocity tracking of the magnet head relative to the base. Repeatability and ranging error tests will complete development of this system.

Laser Ranging System

PLA system component is proceeding for the full ocean depth version. A 16-laser submergible array has been built to enable practical testing in both dry and wet setups. Proof-of-concept testing was first performed using a 4-laser array dry setup in a darkened room, Figure AORD-7. This model featured parallel-aligned lasers in a 2 by 2 array setup. The results from the 4-laser array testing are presented in Table AORD-1.

A problem encountered with the 16-laser prototype has been getting the lasers properly aligned which is absolutely necessary to be able to use the same mathematical model used in the 4-laser array setup. Allowing non-parallel lasers could resolve these manufacturing problems. Lasers tilted at specific angles can also work together and give a better resolution than the parallel could. In order to be able to handle non-parallel lasers a new math model was derived that can handle the two angles θ_1 and θ_2, see Figure AORD-8. Proof-of-concept testing was performed using Matlab-based simulations and image processing simulations. Before using the new math model on the prototype it was first tested on a one- and two-laser set up. Before trying to measure the distance, z., a calibration has to be made by measuring the two angles θ_1 and θ_2 for each laser, see Table AORD-2. The 16-laser array was then used at distances ranging between 1.85 m and 5.00 m, in a dry setup to try the new mathematical model on existing hardware. Four tests were made using four images, Tz1-Tz4. In each of these the real distance, z_r, was measured and then a Matlab simulation of the model gave the average distance, z_a, measured using the images. Testing results are presented in Table AORD-3.

Derivation of the mathematical model for parallel and skewed lasers was done by trigonometric as well by employment of similar triangle method where a pair of equivalent solutions was derived in both cases. Appendix AORD-3 is the derivation for skewed laser based on trigonometric methods.

The distance between the camera and the laser, known as "D", is important and a greater distance will give a better resolution. The prototype 16-laser array is 61 cm in extent on each side, this size will assure good resolution within the operational range. Resizing, however, will be necessary to enable positioning under the forward nosecone of the SAUVIM. By allowing tilted lasers the lasers does not have to be arranged in an array and a sufficient D can be achieved within the allowed size of the laser ranger.

Since the laser ranger has to be resized the next steep will be to evaluate the best hardware to use and how to set it up. Currently, the 16-laser prototype array employs black and white CCD camera, lights, and both red and green lasers. Evaluations on using a color CCD camera with a zoom and gated function will be carried out. The lasers will be tested regarding operational range under turbid water conditions. When the operational range has been determined the whole laser ranger can be tried underwater. The absorption and scattering processes will also be evaluated and tested which is of great importance when designing a laser ranger for an underwater environment [Caimi95].

The following software modifications are called for: reducing code latency by mapping lasers to slots on the frame grabber board, adding a moving Brownian-motion filter routine in anticipation of stirred sediment particles in the field of view. Lastly, integration of the completed system into the SAUVIM navigation CPU will have to be performed.

Homing Sensor System

Homing sensor prototype hardware fabrication is complete. Figure AORD-9 displays the components that comprise the MHS. In the center of the photograph is the PC-104 computer that is equipped with a video frame grabber, behind it and to the left is the pressure tolerant housing and bracket that clamp onto the Ansaldo arm above the wrist joint. To the right of the computer is the camera and white LED that will be used for task illumination while behind are some printed copies of the task site targets the MHS will home on. Close-up photographs of the camera and pressure housings are given in Figures AORD-10 and 11, respectively. It will be noted that the pressure housing is on a bracket that allows azimuth and elevation adjustments, this will assist in checking for optimal orientation settings as the MHS gets integrated with the Ansaldo arm controller and computer. The acrylic ring and lens mounted to the camera are to allow illumination from white LED diodes located behind the camera to diffuse and light the immediate vicinity. The lens is to narrow down the aperture of the camera as is it was found during code development that resolution was lost do to a wide camera image area.

Alpha code has been developed and loaded onto the sensor system that gives range to the targets as well as the angle off of the line centered and perpendicular to the target pattern. This code is developed in C and is resident on the PC-104 computer to avoid loading of the SAUVIM VME computers.

The major tasks that remain for these systems are to test and optimize the alpha code as well integrate the system onto the Ansaldo arm system. Testing of the homing sensor in the dry lab setup will proceed before integration onto the SAUVIM vehicle.

Future Tasks (Phase II Tasks)

C   Wet test; load forward kinematics model into C-code; and integrate to VME Arm Control CPU I/O board. Test to quantify system accuracy and repeatability.
C   Resizing the pressure housings for the diode lasers, the camera housing and building a new frame to hold the lasers and the camera.
C   Finishing modifications of software, modify from dry-test setup 4-array to operational multi laser setup.
C   Install homing sensor camera and vessel onto the Ansaldo arm, add circular barcode detection and tracking logic to skeletal image frame grabbing code. Integrate system into the DTDS setup. Test to quantify system accuracy and repeatability.

Figure AORD-1: Passive Arm (PA)

Figure AORD-2: PA wiring diagram
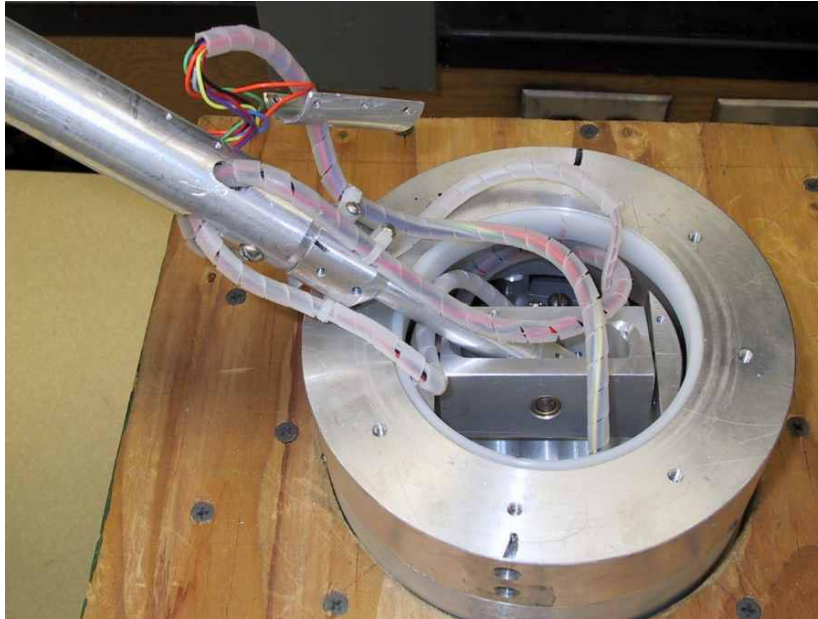
Figure AORD-3: PA close-up base gimbals joint
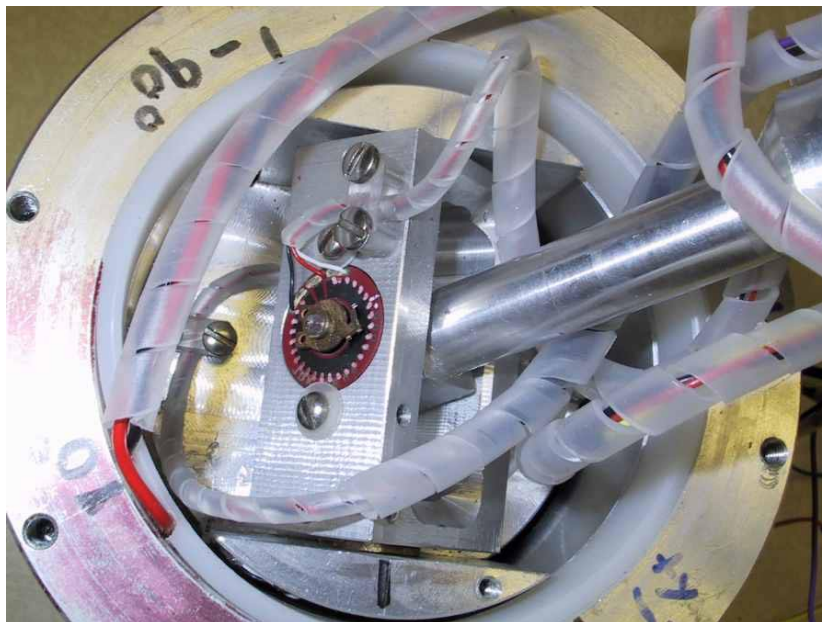
Figure AORD-4: PA close-up end gimbals joint
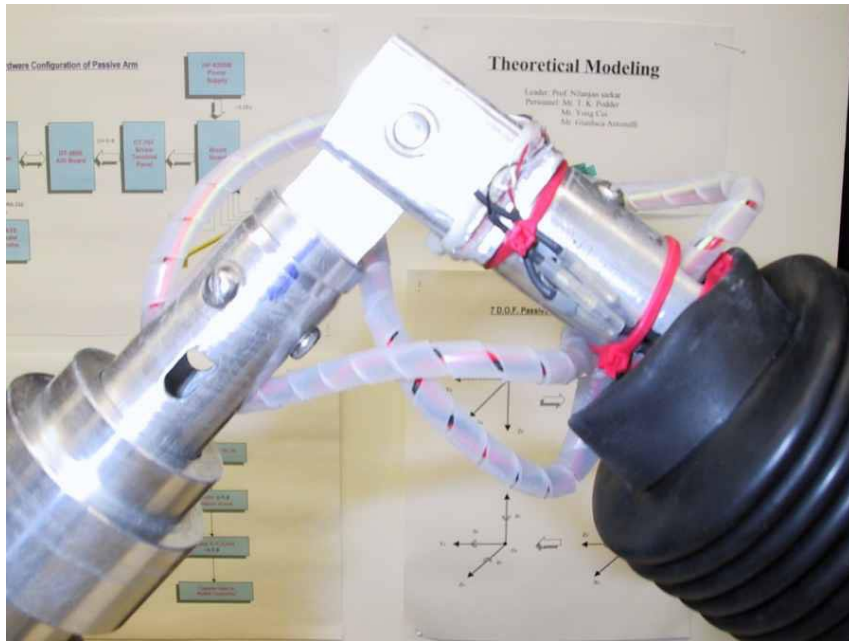
Figure AORD-5: PA close-up elbow joint
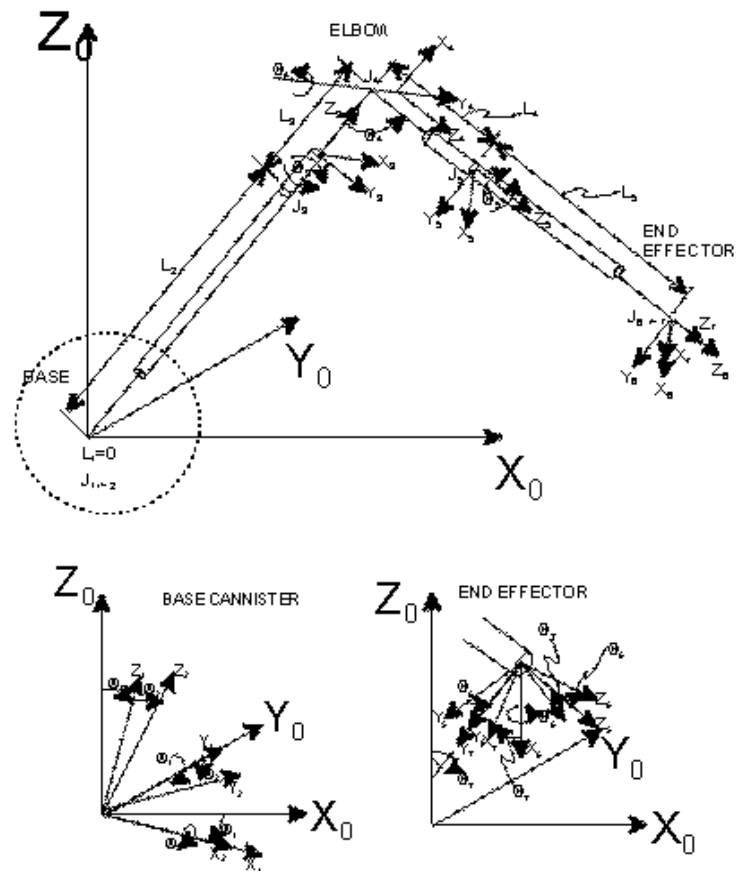
Figure AORD-6: Arm kinematics
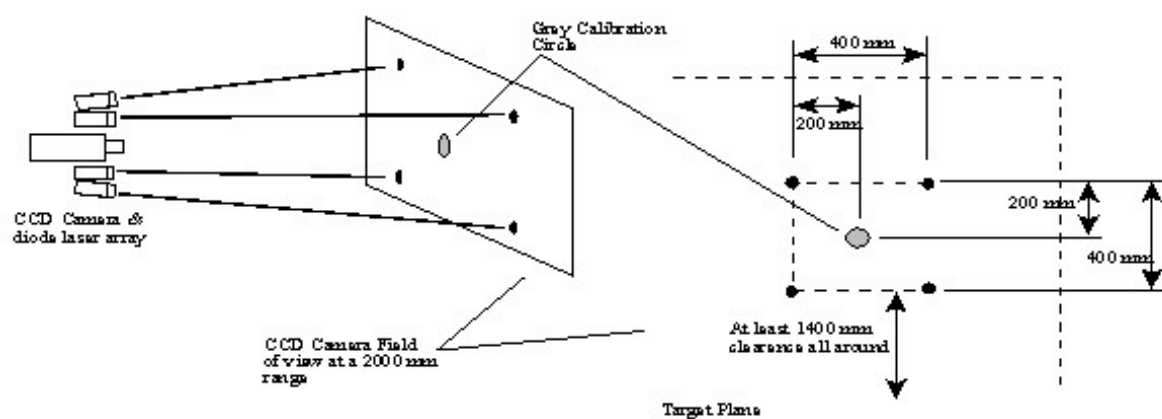
Figure AORD-7: The four-laser array set-up.
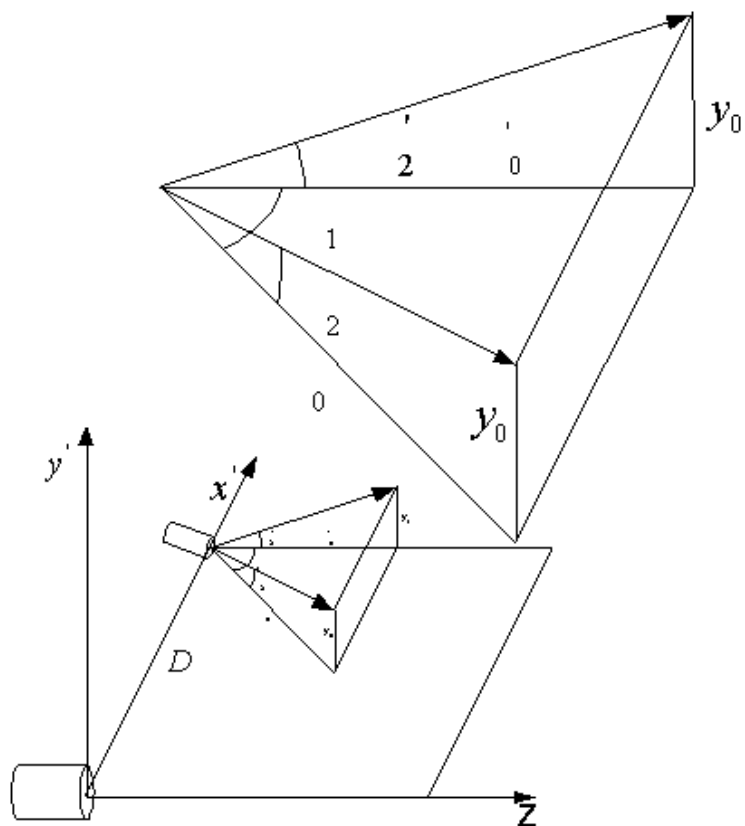
Figure AORD-8: Geometry of non-parallel laser

24
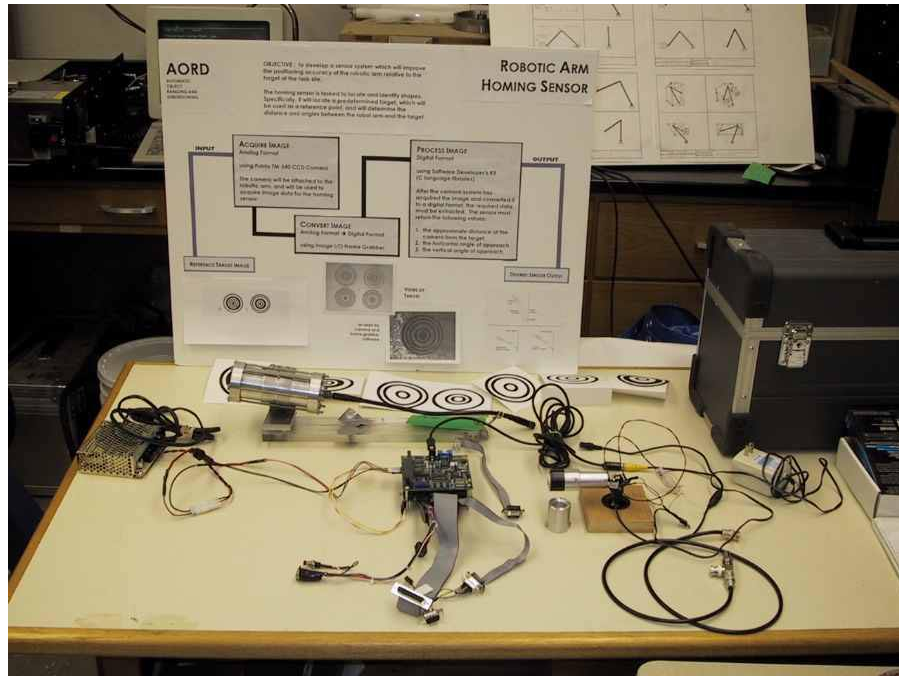
Figure AORD-9: Entire MHS System.
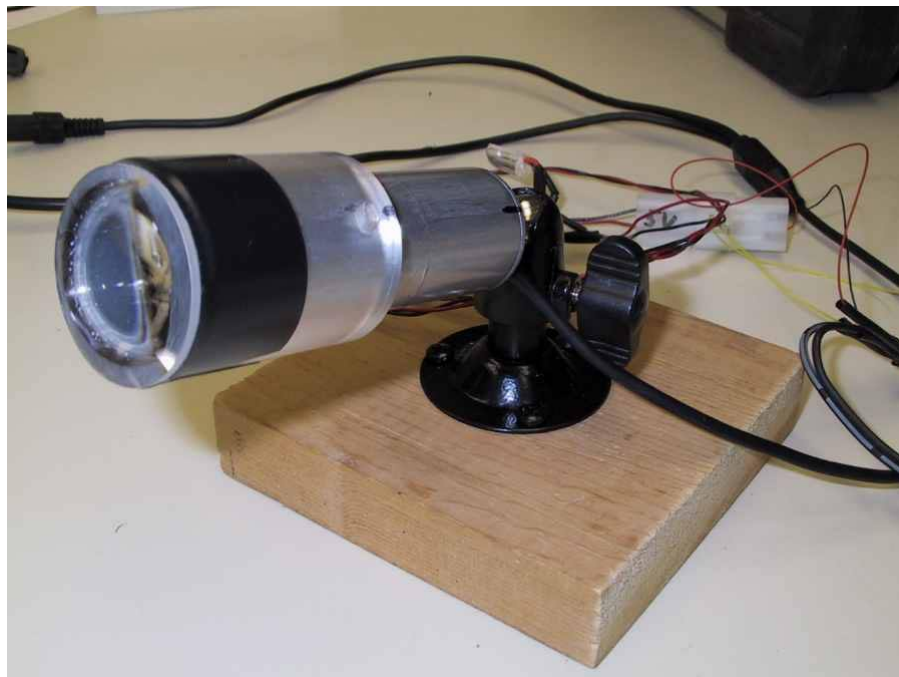
Figure AORD-10: MHS camera.

Figure AORD-11: MHS pressure vessel.

Table AORD-1: Results from four-laser array set-up

Range to Surface (cm)	Distance of Beam Separation (cm)	Angular Size of Image Field (degrees)	Angular Separation of Dots (True) (degrees)	Number of Pixels separating dots (pixels)	Range Precision across 1 pixel (cm)
10.0	4.0	30.0	22.62	386.0	0.03
25.0	4.0	30.0	9.15	156.1	0.16
50.0	4.0	30.0	4.58	78.2	0.64
100.0	4.0	30.0	2.29	39.1	2.56
150.0	4.0	30.0	1.53	26.1	5.75
200.0	4.0	30.0	1.15	19.6	10.23
250.0	4.0	30.0	0.92	15.6	15.98
300.0	4.0	30.0	0.76	13.0	23.01
400.0	4.0	30.0	0.57	9.8	40.91

Table AORD-2: Calibration of the 16-laser array

Image	z_a (m)	z_r (m)
Tz1.bmp	**3.4969**	**3.50**
Tz2.bmp	**4.5151**	**4.51**
Tz3.bmp	**2.1677**	**2.17**
Tz4.bmp	**1.8538**	**1.85**

Table AORD-3: Results from four images taken at different distances

Laser no.	θ_1 (average)	θ_2 (average)
1	-0.254	-0.590
	-0.523	-0.976
	-1.080	-0.675
	-1.083	-0.053
	0.309	-0.852
	-0.560	-0.680
	-1.195	0.074
	-1.174	0.491
	0.212	0.344
	0.333	0.241
	-0.340	0.786
	-1.252	0.176
	0.465	0.245
	0.182	0.488
	0.498	1.216
16	-0.519	0.799

Appendix AORD-1: Passive Arm Forward Kinematics Matrix

i	$"_{i-1}$	a_{i-1}	d_i	2_i	transforms-form of 2
1	0	0	0	2_1	rotation about Y_0
2	0	0	l_2	2_2	rotation about X_1, translation along Z_2
3	0	0	l_3	2_3	rotation about Z_2, translation along Z_3
4	0	0	l_4	2_4	rotation about Y_3, translation along Z_4
5	0	0	l_5	2_5	rotation about Z_4, translation along Z_5
6	0	0	l_6	2_6	rotation about X_5
7	0	0	l_2	2_7	rotation about Y_6

Transformation Matrices:

$$
{}^0_1T = \begin{bmatrix} c\theta_1 & 0 & -s\theta_1 & 0 \\ 0 & 1 & 0 & 0 \\ s\theta_1 & 0 & c\theta_1 & 0 \\ 0 & 0 & 0 & 1 \end{bmatrix}
\quad
{}^1_2T = \begin{bmatrix} 1 & 0 & 0 & 0 \\ 0 & c\theta_2 & -s\theta_2 & 0 \\ 0 & s\theta_2 & c\theta_2 & 0 \\ 0 & 0 & 0 & 1 \end{bmatrix}
\quad
{}^2_3T = \begin{bmatrix} c\theta_3 & -s\theta_3 & 0 & 0 \\ s\theta_3 & c\theta_3 & 0 & 0 \\ 0 & 0 & 1 & l_2 \\ 0 & 0 & 0 & 1 \end{bmatrix}
$$

$$
{}^3_4T = \begin{bmatrix} c\theta_4 & 0 & -s\theta_4 & 0 \\ 0 & 1 & 0 & 0 \\ s\theta_4 & 0 & c\theta_4 & l_3 \\ 0 & 0 & 0 & 1 \end{bmatrix}
\quad
{}^4_5T = \begin{bmatrix} c\theta_5 & -s\theta_5 & 0 & 0 \\ s\theta_5 & c\theta_5 & 0 & 0 \\ 0 & 0 & 1 & l_4 \\ 0 & 0 & 0 & 1 \end{bmatrix}
\quad
{}^5_6T = \begin{bmatrix} 1 & 0 & 0 & 0 \\ 0 & c\theta_6 & -s\theta_6 & 0 \\ 0 & s\theta_6 & c\theta_6 & l_5 \\ 0 & 0 & 0 & 1 \end{bmatrix}
$$

$$
{}^6_7T = \begin{bmatrix} c\theta_6 & 0 & -s\theta_6 & 0 \\ 0 & 1 & 0 & 0 \\ s\theta_6 & 0 & c\theta_6 & 0 \\ 0 & 0 & 0 & 1 \end{bmatrix}
\quad
{}^0_7T = {}^0_1T\,{}^1_2T\,{}^2_3T\,{}^3_4T\,{}^4_5T\,{}^5_6T\,{}^6_7T = \begin{bmatrix} r_{11} & r_{12} & r_{136} & p_x \\ r_{21} & r_{22} & r_{23} & p_y \\ r_{31} & r_{32} & r_{33} & p_z \\ 0 & 0 & 0 & 1 \end{bmatrix}
$$

Note: Projection of **k** along z_7 is normal to the magnet face..

Position of end gimbals wrist:

Note "c" is shorthand for "cos" and "s" is shorthand for "sin")
As to gimbals wrist position in the world coordinates the three vectors are:

$$
p_x = \{l_4 + l_5\}\left[-\left(c_1 c_3 - s_1 s_2 s_3\right)s_4 - s_1 c_2 c_4\right] - s_1 c_2\left(l_3 + l_2\right)
$$

$$
p_y = l_5\left[c_2 s_3 s_4 - s_2 c_4\right] + l_4\left[-c_2 s_3 s_4 - s_2 c_4\right] - s_2\left(l_3 + l_4\right)
$$

$$
p_z = \{l_4 + l_5\}\left[-\left(s_1 c_3 + c_1 s_2 s_3\right)s_4 + c_1 c_2 c_4\right] + c_1 c_2\left[l_2 + l_3\right]
$$

Appendix AORD-2: Passive Arm DERIVE symbolic solution

```
[T](1->0) = [["c1",-"s1",0,0],["s1","c1",0,0],[0,0,1,0],[0,0,0,1]]
 [T](2->1) = [[1,0,0,0],[0,"c2",-"s2",0],[0,"s2","c2","l1"],[0,0,0,1]]
 [T](3->2) = [["c3",0,-"s3",0],[0,1,0,0],["s3",0,"c3",0],[0,0,0,1]]
 [T](4->3) = [["c4",0,-"s4",0],[0,1,0,0],["s4",0,"c4","l2"],[0,0,0,1]]
 [T](5->4) = [["c5",0,-"s5",0],[0,1,0,0],["s5",0,"c5","l3"],[0,0,0,1]]
 [T](6->5) = [[1,0,0,0],[0,"c6",-"s6",0],[0,"s6","c6",0],[0,0,0,1]]
 [T](7->6) = [["c7",-"s7",0,0],["s7","c7",0,0],[0,0,1,"l4"],[0,0,0,1]]
 [T](1->0)*[T](2->1)*[T](3->2)*[T](4->3) =
[["c1",-"s1",0,0],["s1","c1",0,0],[0,0,1,0],[0,0,0,1]]*
[[1,0,0,0],[0,"c2",-"s2",0],[0,"s2","c2","l1"],[0,0,0,1]]*
[["c3",0,-"s3",0],[0,1,0,0],["s3",0,"c3",0],[0,0,0,1]]*
[["c4",0,-"s4",0],[0,1,0,0],["s4",0,"c4","l2"],[0,0,0,1]]

[T](4->0) =
[["c1"*"c3"*"c4"-"c1"*"s3"*"s4"+"c3"*"s1"*"s2"*"s4"+"c4"*"s1"*"s2"*"s3",
-"c2"*"s1",
-"c1"*"c3"*"s4"-"c1"*"c4"*"s3"+"c3"*"c4"*"s1"*"s2"-"s1"*"s2"*"s3"*"s4",
"c3"*"l2"*"s1"*"s2"-"c1"*"l2"*"s3"],
[-"c1"*"c3"*"s2"*"s4"-"c1"*"c4"*"s2"*"s3"+"c3"*"c4"*"s1"-"s1"*"s3"*"s4",
"c1"*"c2",
-"c1"*"c3"*"c4"*"s2"+"c1"*"s2"*"s3"*"s4"-"c3"*"s1"*"s4"-"c4"*"s1"*"s3",
-"c1"*"c3"*"l2"*"s2"-"l2"*"s1"*"s3"],["c2"*"c3"*"s4"+"c2"*"c4"*"s3",
"s2","c2"*"c3"*"c4"-"c2"*"s3"*"s4","c2"*"c3"*"l2"+"l1"],
[0,0,0,1]]

[T](1->0)*[T](2->1)*[T](3->2)*[T](4->3)*[T](5->4)*[T](6->5)*[T](7->6)=
[["c1",-"s1",0,0],["s1","c1",0,0],[0,0,1,0],[0,0,0,1]]*
[[1,0,0,0],[0,"c2",-"s2",0],[0,"s2","c2","l1"],[0,0,0,1]]*
[["c3",0,-"s3",0],[0,1,0,0],["s3",0,"c3",0],[0,0,0,1]]*
[["c4",0,-"s4",0],[0,1,0,0],["s4",0,"c4","l2"],[0,0,0,1]]*
[["c5",0,-"s5",0],[0,1,0,0],["s5",0,"c5","l3"],[0,0,0,1]]*
[[1,0,0,0],[0,"c6",-"s6",0],[0,"s6","c6",0],[0,0,0,1]]*
[["c7",-"s7",0,0],["s7","c7",0,0],[0,0,1,"l4"],[0,0,0,1]]

T(7->0) =
[["c1"*"c3"*"c4"*"c5"*"c7"-"c1"*"c3"*"c4"*"s5"*"s6"*"s7"-
"c1"*"c3"*"c5"*"s4"*"s6"*"s7"-"c1"*"c3"*"c7"*"s4"*"s5"-
"c1"*"c4"*"c5"*"s3"*"s6"*"s7"-"c1"*"c4"*"c7"*"s3"*"s5"-
"c1"*"c5"*"c7"*"s3"*"s4"+"c1"*"s3"*"s4"*"s5"*"s6"*"s7"-
"c2"*"c6"*"s1"*"s7"+"c3"*"c4"*"c5"*"s1"*"s2"*"s6"*"s7"+
"c3"*"c4"*"c7"*"s1"*"s2"*"s5"+"c3"*"c5"*"c7"*"s1"*"s2"*"s4"-
"c3"*"s1"*"s2"*"s4"*"s5"*"s6"*"s7"+"c4"*"c5"*"c7"*"s1"*"s2"*"s3"-
"c4"*"s1"*"s2"*"s3"*"s5"*"s6"*"s7"-"c5"*"s1"*"s2"*"s3"*"s4"*"s6"*"s7"-
"c7"*"s1"*"s2"*"s3"*"s4"*"s5",
-"c1"*"c3"*"c4"*"c5"*"s7"-"c1"*"c3"*"c4"*"c7"*"s5"*"s6"-
"c1"*"c3"*"c5"*"c7"*"s4"*"s6"+"c1"*"c3"*"s4"*"s5"*"s7"-
"c1"*"c4"*"c5"*"c7"*"s3"*"s6"+"c1"*"c4"*"s3"*"s5"*"s7"+
"c1"*"c5"*"s3"*"s4"*"s7"+"c1"*"c7"*"s3"*"s4"*"s5"*"s6"-
"c2"*"c6"*"c7"*"s1"+"c3"*"c4"*"c5"*"c7"*"s1"*"s2"*"s6"-
"c3"*"c4"*"s1"*"s2"*"s5"*"s7"-"c3"*"c5"*"s1"*"s2"*"s4"*"s7"-
"c3"*"c7"*"s1"*"s2"*"s4"*"s5"*"s6"-"c4"*"c5"*"s1"*"s2"*"s3"*"s7"-
"c4"*"c7"*"s1"*"s2"*"s3"*"s5"*"s6"-"c5"*"c7"*"s1"*"s2"*"s3"*"s4"*"s6"+
"s1"*"s2"*"s3"*"s4"*"s5"*"s7",
-"c1"*"c3"*"c4"*"c6"*"s5"-"c1"*"c3"*"c5"*"c6"*"s4"-
"c1"*"c4"*"c5"*"c6"*"s3"+"c1"*"c6"*"s3"*"s4"*"s5"+
"c2"*"s1"*"s6"+"c3"*"c4"*"c5"*"c6"*"s1"*"s2"-
"c3"*"c6"*"s1"*"s2"*"s4"*"s5"-"c4"*"c6"*"s1"*"s2"*"s3"*"s5"-
"c5"*"c6"*"s1"*"s2"*"s3"*"s4",-"c1"*"c3"*"c4"*"c6"*"l4"*"s5"-
```

```
"c1"*"c3"*"c5"*"c6"*"l4"*"s4"-"c1"*"c3"*"l3"*"s4"-
"c1"*"c4"*"c5"*"c6"*"l4"*"s3"-"c1"*"c4"*"l3"*"s3"+
"c1"*"c6"*"l4"*"s3"*"s4"*"s5"-"c1"*"l2"*"s3"+
"c2"*"l4"*"s1"*"s6"+"c3"*"c4"*"c5"*"c6"*"l4"*"s1"*"s2"+
"c3"*"c4"*"l3"*"s1"*"s2"-"c3"*"c6"*"l4"*"s1"*"s2"*"s4"*"s5"+
"c3"*"l2"*"s1"*"s2"-"c4"*"c6"*"l4"*"s1"*"s2"*"s3"*"s5"-
"c5"*"c6"*"l4"*"s1"*"s2"*"s3"*"s4"-"l3"*"s1"*"s2"*"s3"*"s4"],
["c1"*"c2"*"c6"*"s7"-"c1"*"c3"*"c4"*"c5"*"s2"*"s6"*"s7"-
"c1"*"c3"*"c4"*"c7"*"s2"*"s5"-"c1"*"c3"*"c5"*"c7"*"s2"*"s4"+
"c1"*"c3"*"s2"*"s4"*"s5"*"s6"*"s7"-"c1"*"c4"*"c5"*"c7"*"s2"*"s3"+
"c1"*"c4"*"s2"*"s3"*"s5"*"s6"*"s7"+"c1"*"c5"*"s2"*"s3"*"s4"*"s6"*"s7"+
"c1"*"c7"*"s2"*"s3"*"s4"*"s5"+"c3"*"c4"*"c5"*"c7"*"s1"-
"c3"*"c4"*"s1"*"s5"*"s6"*"s7"-"c3"*"c5"*"s1"*"s4"*"s6"*"s7"-
"c3"*"c7"*"s1"*"s4"*"s5"-"c4"*"c5"*"s1"*"s3"*"s6"*"s7"-
"c4"*"c7"*"s1"*"s3"*"s5"-"c5"*"c7"*"s1"*"s3"*"s4"+
"s1"*"s3"*"s4"*"s5"*"s6"*"s7",
"c1"*"c2"*"c6"*"c7"-"c1"*"c3"*"c4"*"c5"*"c7"*"s2"*"s6"+
"c1"*"c3"*"c4"*"s2"*"s5"*"s7"+"c1"*"c3"*"c5"*"s2"*"s4"*"s7"+
"c1"*"c3"*"c7"*"s2"*"s4"*"s5"*"s6"+"c1"*"c4"*"c5"*"s2"*"s3"*"s7"+
"c1"*"c4"*"c7"*"s2"*"s3"*"s5"*"s6"+"c1"*"c5"*"c7"*"s2"*"s3"*"s4"*"s6"-
"c1"*"s2"*"s3"*"s4"*"s5"*"s7"-"c3"*"c4"*"c5"*"s1"*"s7"-
"c3"*"c4"*"c7"*"s1"*"s5"*"s6"-"c3"*"c5"*"c7"*"s1"*"s4"*"s6"+
"c3"*"s1"*"s4"*"s5"*"s7"-"c4"*"c5"*"c7"*"s1"*"s3"*"s6"+
"c4"*"s1"*"s3"*"s5"*"s7"+"c5"*"s1"*"s3"*"s4"*"s7"+
"c7"*"s1"*"s3"*"s4"*"s5"*"s6",
-"c1"*"c2"*"s6"-"c1"*"c3"*"c4"*"c5"*"c6"*"s2"+
"c1"*"c3"*"c6"*"s2"*"s4"*"s5"+"c1"*"c4"*"c6"*"s2"*"s3"*"s5"+
"c1"*"c5"*"c6"*"s2"*"s3"*"s4"-"c3"*"c4"*"c6"*"s1"*"s5"-
"c3"*"c5"*"c6"*"s1"*"s4"-"c4"*"c5"*"c6"*"s1"*"s3"+"c6"*"s1"*"s3"*"s4"*"s5",
-"c1"*"c2"*"l4"*"s6"-"c1"*"c3"*"c4"*"c5"*"c6"*"l4"*"s2"-
"c1"*"c3"*"c4"*"l3"*"s2"+"c1"*"c3"*"c6"*"l4"*"s2"*"s4"*"s5"-
"c1"*"c3"*"l2"*"s2"+"c1"*"c4"*"c6"*"l4"*"s2"*"s3"*"s5"+
"c1"*"c5"*"c6"*"l4"*"s2"*"s3"*"s4"+"c1"*"l3"*"s2"*"s3"*"s4"-
"c3"*"c4"*"c6"*"l4"*"s1"*"s5"-"c3"*"c5"*"c6"*"l4"*"s1"*"s4"-
"c3"*"l3"*"s1"*"s4"-"c4"*"c5"*"c6"*"l4"*"s1"*"s3"-"c4"*"l3"*"s1"*"s3"+
"c6"*"l4"*"s1"*"s3"*"s4"*"s5"-"l2"*"s1"*"s3"],
["c2"*"c3"*"c4"*"c5"*"s6"*"s7"+"c2"*"c3"*"c4"*"c7"*"s5"+
"c2"*"c3"*"c5"*"c7"*"s4"-"c2"*"c3"*"s4"*"s5"*"s6"*"s7"+
"c2"*"c4"*"c5"*"c7"*"s3"-"c2"*"c4"*"s3"*"s5"*"s6"*"s7"-
"c2"*"c5"*"s3"*"s4"*"s6"*"s7"-"c2"*"c7"*"s3"*"s4"*"s5"+"c6"*"s2"*"s7",
"c2"*"c3"*"c4"*"c5"*"c7"*"s6"-"c2"*"c3"*"c4"*"s5"*"s7"-
"c2"*"c3"*"c5"*"s4"*"s7"-"c2"*"c3"*"c7"*"s4"*"s5"*"s6"-
"c2"*"c4"*"c5"*"s3"*"s7"-"c2"*"c4"*"c7"*"s3"*"s5"*"s6"-
"c2"*"c5"*"c7"*"s3"*"s4"*"s6"+"c2"*"s3"*"s4"*"s5"*"s7"+"c6"*"c7"*"s2",
"c2"*"c3"*"c4"*"c5"*"c6"-"c2"*"c3"*"c6"*"s4"*"s5"-
"c2"*"c4"*"c6"*"s3"*"s5"-"c2"*"c5"*"c6"*"s3"*"s4"-"s2"*"s6",
"c2"*"c3"*"c4"*"c5"*"c6"*"l4"+"c2"*"c3"*"c4"*"l3"-
"c2"*"c3"*"c6"*"l4"*"s4"*"s5"+"c2"*"c3"*"l2"-
"c2"*"c4"*"c6"*"l4"*"s3"*"s5"-"c2"*"c5"*"c6"*"l4"*"s3"*"s4"-
"c2"*"l3"*"s3"*"s4"+"l1"-"l4"*"s2"*"s6"],
[0,0,0,1]]
```

Appendix AORD-3: Derivation of the math model for skewed lasers

$$x^{'} = x_0^{'} - \tan\theta_1 \cdot z, \ \left\{x_0^{'} = D\right\} \Rightarrow$$

$$x^{'} = D - \tan\theta_1 \cdot z \tag{1}$$

$$y^{'} = y_0^{'} + \tan\theta_2^{'} \cdot z = y_0^{'} + \frac{\tan\theta_2}{\cos\theta_1}z, \ \left\{y_0^{'} = 0\right\} \Rightarrow$$

$$y^{'} = \frac{\tan\theta_2}{\cos\theta_1}z \tag{2}$$
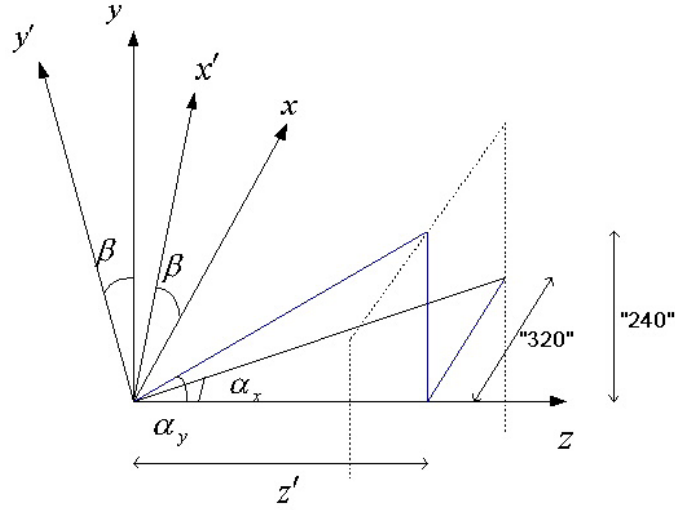
Figure A

Note that distance "320" and "240" in figure is only valid if $z = z^{'}$

Conversion from coordinate system $x^{'}$, $y^{'}$ to x, y, se figure AORD-3

$$x = \cos\beta \cdot x^{'} - \sin\beta \cdot y^{'} \tag{3}$$
$$y = \sin\beta \cdot x^{'} + \cos\beta \cdot y^{'} \tag{4}$$

Eq. (1) in (3) and eq. (2) in (4)

$$x = \cos\beta(D - \tan\theta_1 \cdot z) - \sin\beta\left(\frac{\tan\theta_2}{\cos\theta_1}\right)z \tag{5}$$

$$y = \sin\beta(D - \tan\theta_1 \cdot z) + \cos\beta\left(\frac{\tan\theta_2}{\cos\theta_1}\right)z \tag{6}$$

$X^{'}$ and $Y^{'}$ is the actual pixel value from the frame grabber. Get the origin in the middle and the y-axis in the right direction.

$$X = X^{'} - 320 \tag{7}$$
$$Y = -Y^{'} + 240 \tag{8}$$

Since the resolution is 640 x 480

31

To convert the pixel coordinates to the real coordinate system a constant $\tan \alpha$ is used, $\tan \alpha$ is different in x and y directions and is camera specific and have to be measured. In case of a zoom camera, $\tan \alpha = f(zoom - value)$. Skewing of the camera has not been under consideration in this model.

$$x = X \cdot \tan \alpha_x \cdot z \tag{9}$$

$$y = Y \cdot \tan \alpha_y \cdot z \tag{10}$$

Use eq. (5) and eq.(6) to get θ_1 and use θ_1 to calculate θ_2. These two equations is used to calibrate the lasers by measure X, Y and z.

$$\theta_1 = \tan^{-1} \left(\frac{\cos^2 \beta \cdot D - x \cdot \cos \beta + \sin^2 \beta \cdot D - y \cdot \sin \beta}{z} \right) \tag{11}$$

$$\theta_2 = \tan^{-1} \left(\frac{\cos \theta_1 \cdot D(y + \sin \beta \cdot \tan \theta_1 \cdot z - \sin \beta \cdot D)}{\cos \beta \cdot z} \right) \tag{12}$$

We now can solve out z_x and z_y since the only variable that is unknown is X and Y.

$$z_x = \frac{\cos \theta_1 \cdot \cos \beta \cdot D}{X \cdot \tan \alpha_x \cdot \cos \theta_1 + \cos \beta \cdot \tan \theta_1 \cdot \cos \theta_1 + \sin \beta \cdot \tan \theta_2} \tag{13}$$

$$z_y = \frac{\cos \theta_1 \cdot \sin \beta \cdot D}{Y \cdot \tan \alpha_y \cdot \cos \theta_1 + \sin \beta \cdot \tan \theta_1 \cdot \cos \theta_1 - \cos \beta \cdot \tan \theta_2} \tag{14}$$

The resolution for z_x and z_y depends on β therefore they have to be valued differently. Since the resolution for z_x is best (z_y worst) when $\beta = 0$ or 2π, z_y is best (z_x worst) when $\beta = \pm \dfrac{\pi}{2}$ and $\cos^2 \beta + \sin^2 \beta = 1$.

$$z = z_x \cdot \cos^2 \beta + z_y \cdot \sin^2 \beta \tag{15}$$

Intelligent Coordinated Motion/Force Control (ICM/FC)

Project Leaders: Dr. Junku Yuh & Dr. Song K. Choi

The main technical development of the ICM/FC group is described in the following sections: Manipulator Control and Test Platform, Low-Level Control and High-Level Control.   The Manipulator Control and Test Platform is the combined sections of the previous Theoretical Modeling and Dry Test Design Set-Up.

Manipulator Control and Test Platform (MCTP)

Project Leaders: Dr. Junku Yuh, Dr. Song K. Choi & Dr. Tae Won Kim
Personnel: Dr. Giacomo Marani, Mr. Jong Ho Eun & Mr. Jang-Won Lee

Objectives

The development of kinematic, dynamic, force and coordinated-motion control systems for the SAUVIM underwater robotic manipulator.

Current Status (Tasks Completed During 8/1/97 – 10/30/00):

- Specification and setup of the hardware architecture
- Board interconnections and arm cabling
- Control design and simulation
- Realization of VxWorks drivers and Maris Control Software library
- Project and realization of the Man Machine Interface (OpenGL animation and Joystick drivers)

Introduction

The *MARIS 7080* (Figure MCTP-1) is an eight-degrees of freedom redundant manipulator produced by *ANSALDO* (Italy). Seven degrees of freedom are used to control the arm positioning while the eighth degree is for controlling the gripper. Each joint is actuated by brushless motor keyed to a reduction unit by means of a spur gear. Because the manipulator is designed for underwater applications at high depths, it is oil filled to compensate the external pressure. The difference between the internal and external pressure is kept under *1 atm* by a compensating system. Moreover, the arm is protected against corrosion by means of an anodising treatment.

The manipulator is equipped with a camera installed on the gripper and other sensors can be added by means of a connector with spare channels placed on the wrist.

The arm is designed in order to guarantee high accuracy and repeatability. In order to achieve these requirements a couple of resolvers are mounted on each joint. One is set up on the motor and the second one is connected to the output axis of the joint. The resolver mounted on the output axis allows getting the arm position at the start-up of the system. The resolver mounted on the motor is used to control the joint motor. On the first four joints are also installed thermocouples in order to monitor the motor temperature during the operations. The gripper is equipped with a Hall effect sensor in order to control its motor and monitor the opening. A *JR3* force/torque sensor is installed on the wrist at the aim of getting force feedback during the manipulation.

It is possible to install other sensors by means of a connector placed on the manipulator wrist. In the MARIS 7080 some of this channels are used by a camera installed on the wrist, while the remaining one are spare for sensor that could be installed in the future.

Hardware Architecture

The control architecture of the arm is composed by the motor drivers, a VME based computing architecture on which are also installed the I/O modules and by a remote PC connected through TCP/IP sockets at aim of giving to the user a friendly interface (Figure MCTP-2).

Motor drives are a miniature PWM; full-wave, three-phase servo amplifier designed for high performance brushless servomotors. The boards used to control the joint motors implement a velocity control loop. The motor controllers provide as output an equivalent encoder signal to get the motor position. The resolution is 4096 pulses for rotation on the motor axis; the signal is acquired using an IP-Quadrature counter installed on the VME carrier board. The resolution for the arm positioning is dependent by the gear reduction and is obviously higher than the encoder resolution; the initial value of the counter is set by means of the resolvers mounted on the output axis.

The motor controllers boards can provide other signals such as the torque output or an analogue velocity feedback.

Notice that the gripper board does not implement a velocity control loop but a torque one; in this case, the Hall sensor gives the feedback. A custom board converts the Hall feedbacks in encoder signals that the IP-Quadrature counters can acquire in order to provide the gripper position feedback to the control CPU. All the motor controllers can be enabled through an external digital signal.

The computing architecture is VME based. A FORCE 68060 board is used to implement the control schemes. The board can communicate through the VME Bus to the I/O module. There are several modules; a MATRIX MD-DAADIO board is used to provide the references to the motor drivers (using the DAC channels), acquire the thermocouples signals (ADC channels) and enable the motor drivers (Digital Output signals). Two four-channel IP-Quadrature piggyback modules, which are mounted on a VME carrier board, acquire the encoder signal from the motor drivers.

Two more boards are installed on the VME Bus, one for exciting and acquiring the signals from the resolvers on the output axis, and one for the JR3 force sensor. All the modules can be accessed by the FORCE board though memory locations mapped on the VME bus.

Control Design

The arm control technique is task-oriented. This method implies the use of suitable co-ordinate transformations (in finite or differential form), from the standard joint domain to the specific task domain. Due to the complexity of the arm structure, the transformation has been computed with the aid of *RDS* package, a tool to support control development and simulation in robotics. Through a graphical interface this program can manage a generic mechanical structure organized in *open* and *branched* chains of rigid bodies. One of the most relevant features of *RDS*, used in the fast-prototyping approach, is a module for automatic generation of C-code. Results of symbolic computation are automatically translated into source code that can be compiled for PC simulation (*Simulink* specific) as well as for external hardware devices (by means of *Real Time Workshop*). At this aim it is very useful the opportunity to create blocks which input-output relation is directly definable by the user: the relation may involve any structure quantity (transformation matrixes, Jacobians, etc.).

The task level control law is computed by the control CPU and the reference signals are sent to motor drivers. The singularities in the pseudo-inverse of the Jacobian matrix are checked run-time and the

matrix is regularized; moreover a procedure to keep the arm in the best positioning in its operational area is introduced operating on the fourth joint.

The reference signals sent to the motor drivers (*ELMO* board) are velocity signals. Actually these boards implement a hardware velocity control law.

The Maris Control Software

The control software of Maris manipulator has been developed with the combined use of Simulink™[1], Real Time Workshop™[2] and Robotics Developer Studio[3] packages. This allows to hardly reducing the *time-to-run*, automating the most critical part of the development process.

In its basic conception, MCS is a Simulink library (Figure MCTP-3) specially created for the Maris manipulator. So its use is similar to any other Simulink library.

The MCS library is the root of a tree and contains following subset:

- ❑ Resolver
- ❑ DAADIO
- ❑ IP Quadrature
- ❑ Socket
- ❑ JR3
- ❑ Arm Blocks
- ❑ Build Tools
- ❑ Miscellaneous
- ❑ Demos

Subsets from 1 to 6 (Resolver, DAADIO, IP Quadrature, Socket and JR3 subsets) contain the basic drivers for all the hardware devices, while the second half of the library is a collection of more high-level blocks, specially created for using with the Maris manipulator. One of these subsets, the *Build Tools*, contains special blocks, which allow compiling and downloading the Simulink sheet in one command.

With MCS, the first step in designing a control model is to break the chain I/O↔Arm into two subparts. Each part needs to be implemented in a separate Simulink model, one running on the VxWorks target and one on a PC. The entire control model is subdivided in order to have any critical part running on the real-time target. All the input-output stuff can be left on the PC-side model. Figure MCTP-4 shows the implementation of the task space control model, where a network block performs the link between two separate models.

Man-Machine Interface

The controller, running on the *VME* based hardware, can communicate with the user interface through a network socket. The output interface consists in an *OpenGL* reconstruction of the Maris manipulator and its environment (Figure MCTP-5) and was created with the aid of OpenGL API and

---

[1] Available from *The Mathworks, Inc.*
[2] Available from *The Mathworks, Inc.*
[3] Developed by G.Marani, Italy.

Microsoft Visual C++. It is dynamically linked with the output of the position sensors in order to reproduce the exact configuration of the arm.

On the lower side of the animation window there are some virtual instruments that show the information coming from the arm sensors; eight joint meters display the joint position and issue some warning messages (visual and vocal) when a joint is running close to the mechanical stop. At this aim the analogue indicator became from green to yellow and then red while the joint approaches to the end of race.

The output of the *JR3* force sensor is displayed by means of two transparent vectors coming out from the wrist, one for the force and one for the momentum. The module of each vector is displayed on the two downright meters.

Controls on the toolbar allow setting the point of view of the scene, translating the eye in three directions. The rotation can be set with a mouse drag on the scene. These settings are automatically saved upon exiting the application.

In order to have a high frame rate the animation runs on a PC equipped with a graphic card OpenGL compatible. Anyway to improve performance on slow computers, it is possible to hide some textures or parts of the environment. For this purpose it is also possible to reduce the number of slices used in the rendering of cylinders by selecting between three different values of the resolution (high, medium and low).

An overlapped window can show the output of the camera placed on the writs. Four buttons on the main toolbar allow starting or stopping the frame grabber or zooming the image. The camera window is only available for Matrix Meteor boards.

The input commands come from a separate device that links a 3D joystick to the system and allows controlling the end-effector position and orientation.

Figure MCTP-6 shows the data flowing between these input-output devices and the controller. The network socket driver runs under *Simulink*: the data are sent to the *OpenGL* window through a *DDE* channel, and are retrieved from the joystick via a specific driver compiled in a *Simulink Mex s-function*.

Future Tasks (Phase II Tasks)

- Introduction of Collision Detection features in order to avoiding interferences with the vehicle frame.
- Identification of dynamical parameter of the wrist for introducing force feedback in the controller.
- Extension of the graphical interface with the introduction of the vehicle.
- Project and definition of a high level language for driving the arm.
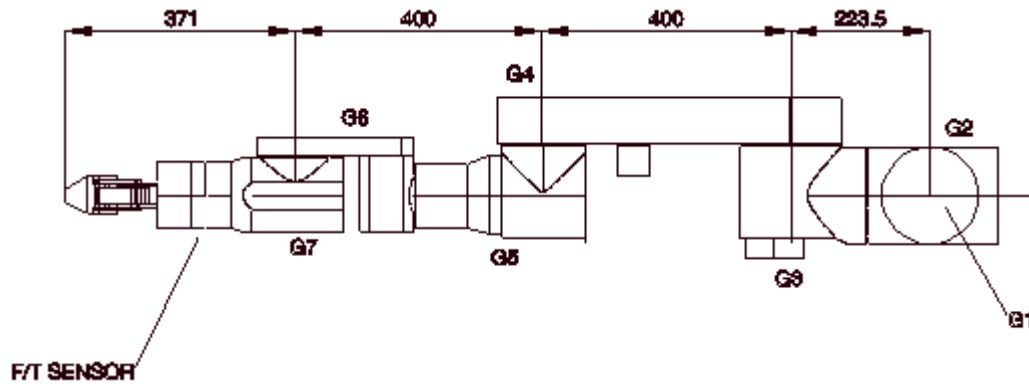
Figure MCTP-1: The MARIS 7080 Manipulator
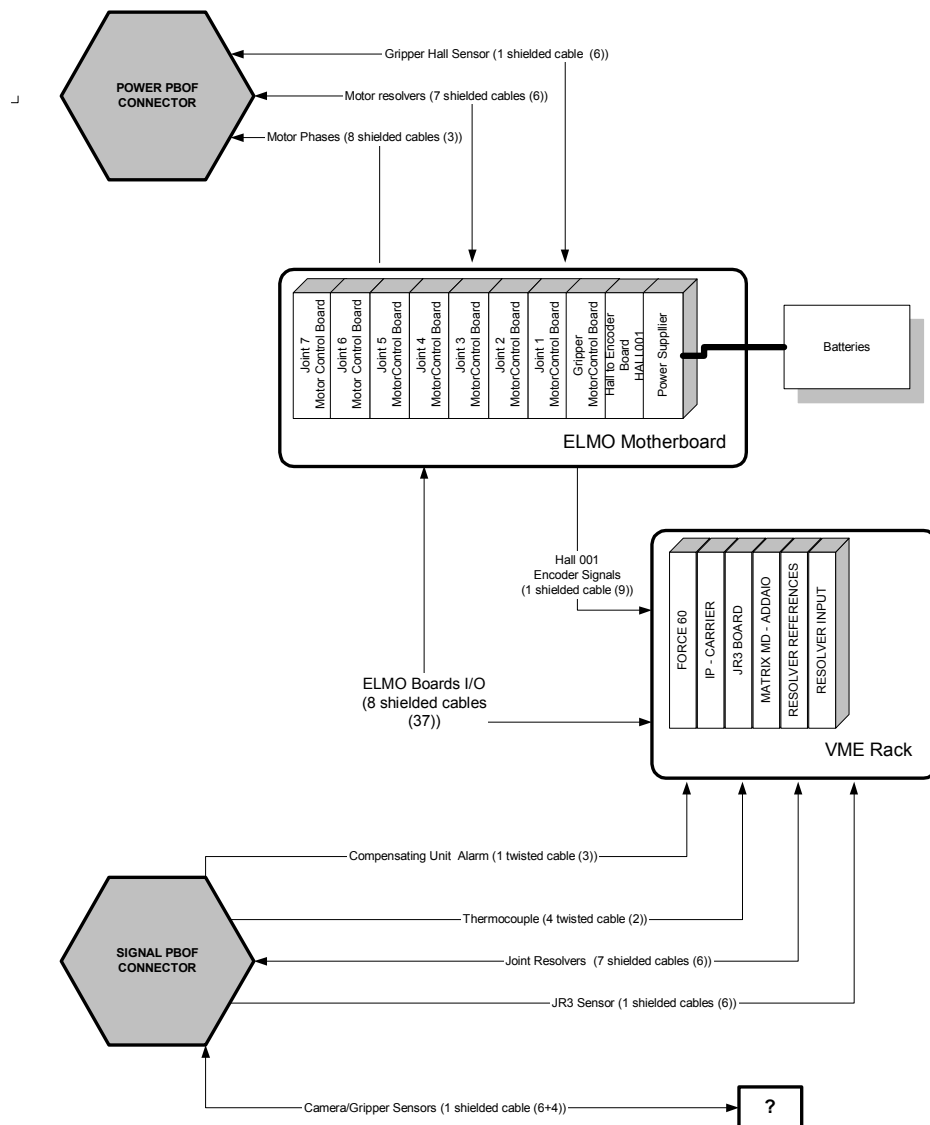
Figure MCTP –2: Manipulator control architecture
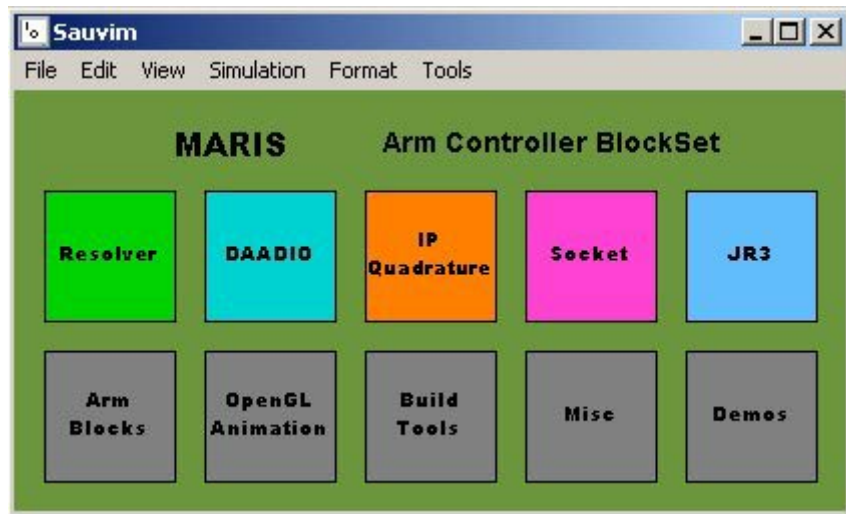
Figure MCTP –3: The Maris Control Software library
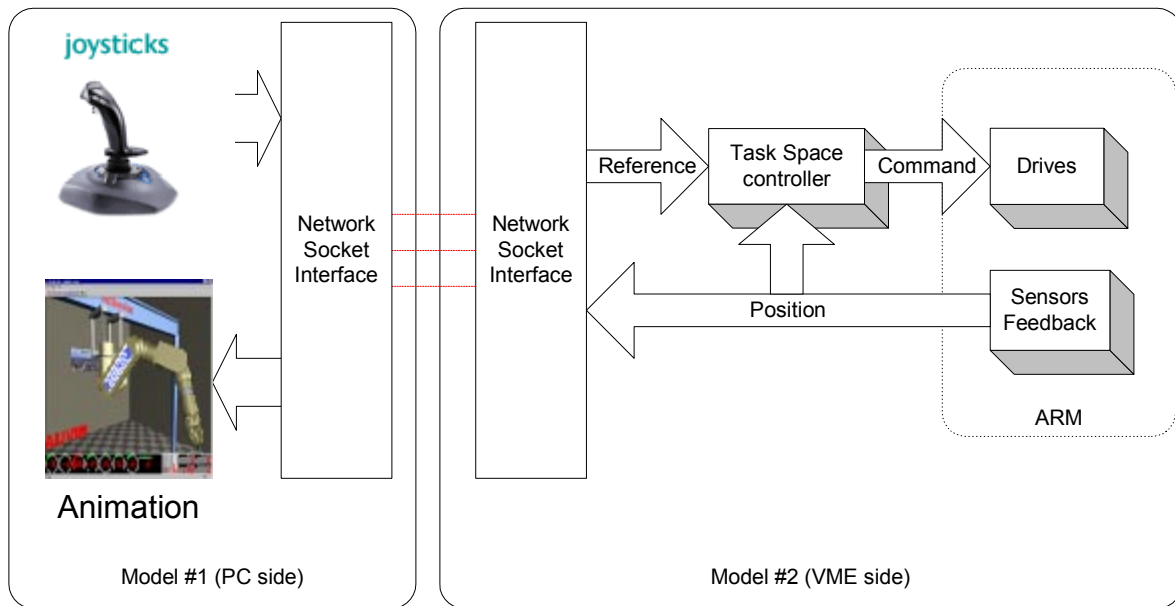
Figure MCTP –4: Task space controller implementation
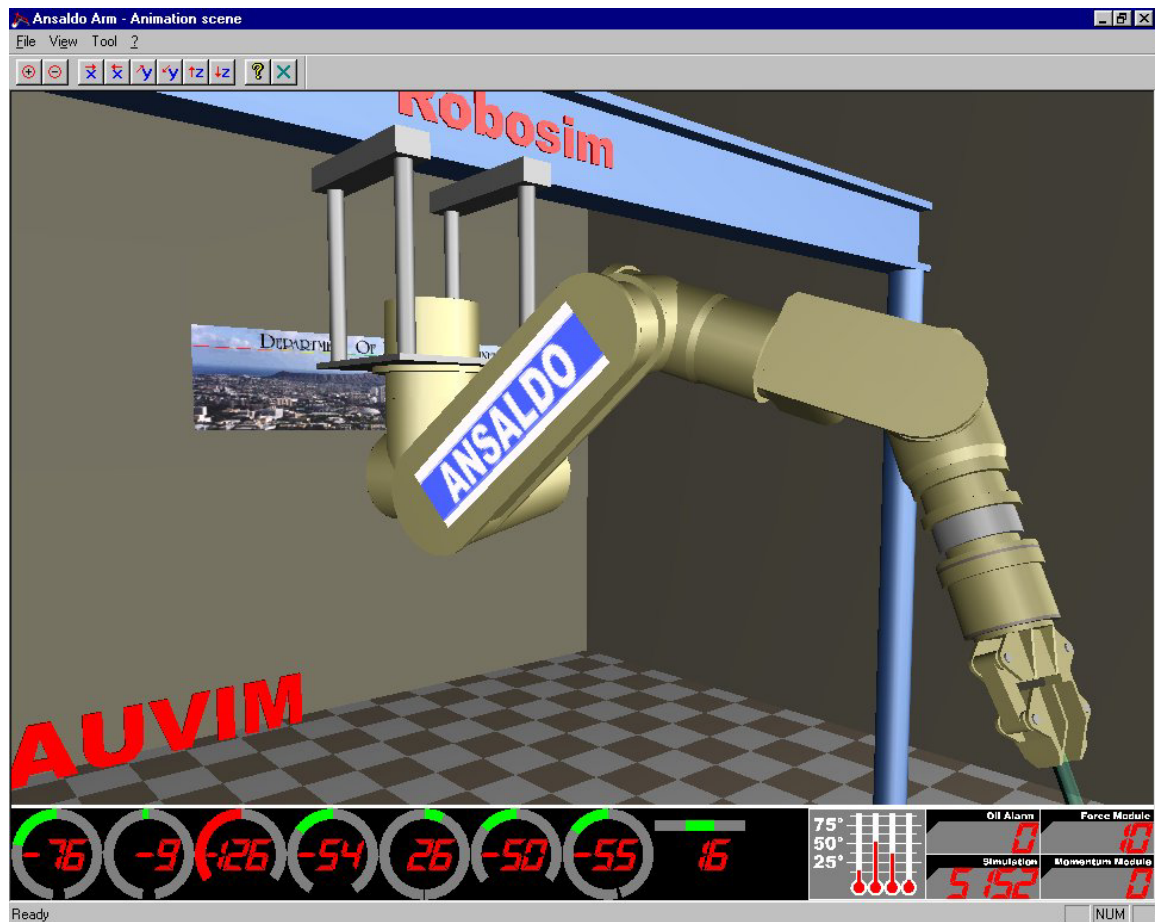
Figure MCTP –5: The OpenGL scene
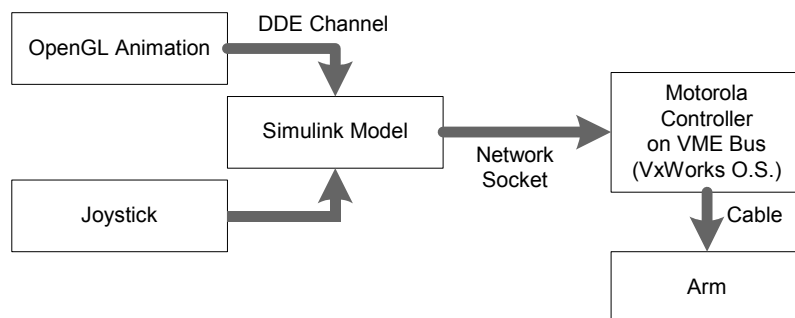
Figure MCTP-6: Data flowing

Low-Level Control (LLC)

Project Leaders: Dr. Junku Yuh
Personnel: Mr. Michael West & Mr. Side Zhao

Objectives

- To design an advanced vehicle control for navigation and hovering; and
- To design an advanced coordinated motion/force control of the vehicle and manipulator during the intervention mode.

Current Status (Tasks Completed During 8/1/97 – 10/30/00):

- Development of a non-regressor based adaptive control system algorithm for AUVs;
- Extensive simulation and testing on ODIN AUV with sonar-based position measurements;
- Development of methodology to transport algorithm and code to SAUVIM;
- Introduction of a localization technique using certainty grids; and
- Initial simulation and testing of the localization techniques.

Non-Regressor Based Adaptive Control

Introduction

Several advanced controllers for underwater robots have been proposed in the literature. Among them are sliding mode control [Cunha95, Healey93, Dougherty90], neural network based control [Ishii94], fuzzy logic control [DeBitetto94], and hybrid adaptive control [Tabaii94]. Cunha 1995 presented an adaptive control scheme for dynamic positioning of remotely operated vehicles (ROV) based on a control algorithm called Variable Structure Model-Reference Adaptive Control (VS-MRAC). In this scheme, each degree of freedom of interest is controlled by a single loop VS-MRAC controller. Healey 1993 used the sliding mode method to control the underwater vehicle and separated the system into non-interacting (or lightly interacting) subsystems, grouping certain key motion equations together for separate functions of steering, diving, and speed control. The design and testing of the flight control system of an advanced unmanned underwater vehicle (UUV) also using sliding mode methods with several single-input single-output (SISO) controllers was presented in [Dougherty90]. Ishii 1994 proposed a neural network based control system called "Self-Organizing Neural-Net-Controller System" (SONCS) for autonomous underwater vehicles (AUV) and examined its effectiveness through application to heading keeping control of an AUV called "Twin-Burger." In their study, a quick adaptation method of the controller called "Imaginary Training" was used to improve the time-consuming adaptation process of SONCS. A simple 14-rule fuzzy logic controller was developed and simulated for the depth control of a UUV in the study of Debitetto 1994. In the hybrid adaptive control (suggesting that the procedure is a mixture of continuous and discrete operations) of AUV done by Tabaii 1994, the control system was simulated in the continuous domain while the control and identification section was discrete.

In this study, a new adaptive control scheme for underwater robots was experimentally implemented on the Omni-Directional Intelligent Navigator (ODIN) (Figure LLC-1). ODIN is a 6 degrees-of-freedom, autonomous underwater robot with 8 thrusters; various navigation sensors such as sonar, a

pressure sensor, and an inertial navigation system (INS); and an on-board CPU with VxWorks OS in VMEbus. A detailed description is available at in reference [Kawaguchi96] or at the laboratory website "http://www.eng.hawaii.edu/~asl/odin.html website."

The presented control scheme is different from conventional adaptive control schemes in that it estimates a set of combinations of unknown bounded constants of system parameter matrices rather than estimating each parameter individually. And the presented adaptive law adjusts the controller gains based on the performance of the system instead of the knowledge of the dynamic model. Its computational requirement does not depend on the number of unknown system parameters. Therefore, the presented adaptive control system is structurally simple and computationally efficient. Stability analysis by the Lyapunov method proves that the tracking error can asymptotically converge to zero. Results from wet experiments show that the controller can achieve high-performance trajectory tracking in the presence of model uncertainties, measurement noises, and external disturbances.

Navigation and Control

Figure LLC-2 shows a general overview of an underwater robot's (vehicle) navigation and control systems. The task/motion planning and trajectory generator module provides the desired vehicle position as a function of time. The controller then computes desired vehicle force/torque, by comparing the desired vehicle position with the current position estimate based on the sensor measurements. The corresponding value of each thruster force to provide the desired vehicle force/torque is computed using a thruster control matrix (TCM). TCM's elements are geometry dependent and can be computed in advance for each vehicle. Then, the desired input voltage to each thruster driver can be computed by using a thruster model. Input to the thruster model is the input voltage to the thruster driver and its output is the thruster force. A thruster system has highly nonlinear dynamics. Therefore, a simple thruster static model (TSM) is often used to compute the desired input voltage to each thruster driver, assuming that a time constant of the thruster system is much smaller than a time constant of the overall control system. In this study, a simple linear TSM of ODIN, which was experimentally obtained, was used. A pressure sensor was used to measure its position in z and its velocity was estimated by Kalman filter. Eight sector sonar on ODIN were used to determine its position in x and y coordinates defined in a water tank. As shown in Figure LLC-2, the raw sonar measurements were processed through the pre-processing filter to remove false readings; the function filter was used to estimate x and y position with INS outputs; and the Kalman filter was used to estimate velocities in x and y. These estimates were used in the control system. As this paper focuses on the control system, detailed description of the navigation system is omitted here. Detailed information about the navigation systems and filters used on ODIN is available in ref. [Nie99]. Figures LLC-3a, b & c show effectiveness of the navigation system with three filters shown in Figure LLC-2. Figure LLC-3a shows input signals to the navigation system, which are raw data of one sonar with lots of false readings and noise; Figures LLC-3b & 3c show position and velocity estimates of the Kalman filter, respectively, which are outputs of the navigation system.

Adaptive Control System

The presented control system is based on the adaptive control with bound estimation developed by Yuh (Yuh96, Choi96). In general, underwater vehicles can be represented by the following vector equation:

$$\mathbf{M}_v \dot{\mathbf{v}} + \mathbf{C}_v(\mathbf{v})\mathbf{v} + \mathbf{D}_v(\mathbf{v})\mathbf{v} + \mathbf{g}_v(\boldsymbol{\eta}) = \boldsymbol{\tau}_v \qquad (1)$$

$$\dot{\boldsymbol{\eta}} = \mathbf{J}(\boldsymbol{\eta})\mathbf{v} \qquad (2)$$

where $\mathbf{v}$ = the linear and angular velocity vector with coordinates in the body-fixed frame, $\boldsymbol{\eta}$ = the position and orientation vector with coordinates in the earth-fixed frame, $\mathbf{M_v} = \mathbf{M_{RB}} + \mathbf{M_A}, \mathbf{C_v}(\mathbf{v}) = \mathbf{C_{RB}} + \mathbf{C_A}$, $\mathbf{M_{RB}}$ = rigid body inertia matrix, $\mathbf{M_A}$ = added inertia matrix; $\mathbf{C_{RB}}(\mathbf{v})$ = rigid body Coriolis and centripetal matrix, $\mathbf{C_A}(\mathbf{v})$ = hydrodynamic Coriolis and centripetal matrix, $\mathbf{D_v}(\mathbf{v})$ = hydrodynamic damping and lift matrix, $\mathbf{g_v}(\boldsymbol{\eta})$ = gravitational forces and moments vector, $\boldsymbol{\tau_v}$ = control inputs (forces and moments) vector, and $\mathbf{J}$ = transformation matrix between vehicle and fixed frames.

Equation (1) can also be written in earth-fixed coordinates as follows:

$$\mathbf{M}\ddot{\boldsymbol{\eta}} + \mathbf{C}(\mathbf{v},\boldsymbol{\eta})\dot{\boldsymbol{\eta}} + \mathbf{D}(\mathbf{v},\boldsymbol{\eta})\dot{\boldsymbol{\eta}} + \mathbf{g}(\boldsymbol{\eta}) + \mathbf{u_d} = \boldsymbol{\tau} \qquad (3)$$

where $\mathbf{M}(\boldsymbol{\eta}) = \mathbf{J^{-T}M_vJ^{-1}}$, $\mathbf{C}(\mathbf{v},\boldsymbol{\eta}) = \mathbf{J^{-T}}[\mathbf{C_v}(\mathbf{v}) - \mathbf{M_vJ^{-1}\dot{J}}]\mathbf{J^{-1}}$, $\mathbf{D}(\mathbf{v},\boldsymbol{\eta}) = \mathbf{J^{-T}D_v}(\mathbf{v})\mathbf{J^{-1}}$, $\mathbf{g}(\boldsymbol{\eta}) = \mathbf{J^{-T}g_v}(\boldsymbol{\eta})$, and $\mathbf{u_d}$ represents a class of unmodeled effects which are bounded by

$$\|\mathbf{u_d}\| \leq d_0 + d_1\|\dot{\mathbf{e}}\| + d_2\|\mathbf{e}\| \qquad (4)$$

where d_i $i=0, 1, 2$ are positive constants and the tracking error vector $\mathbf{e}$ is defined as

$$\mathbf{e} = \boldsymbol{\eta_d} - \boldsymbol{\eta} \qquad (5)$$

where $\boldsymbol{\eta_d}$ is a desired value of $\boldsymbol{\eta}$.

The system matrices of the vehicle are assumed to be bounded by

$$\|\mathbf{M^{-1}}\| \leq \alpha, \quad \|\mathbf{M}\| \leq \beta_1, \quad \|\mathbf{C+D}\| \leq \beta_2, \quad \|\mathbf{g}\| \leq \beta_3, \quad \lambda_{min}(\mathbf{M^{-1}}) \rangle \gamma \qquad (6)$$

where α, β_i, and γ are positive constants.

Instead of mathematically proving Eq. (6), we will show how to estimate

$$\theta_i = \frac{\alpha(\beta_i + d_{i-3})}{\gamma} \quad i = 1, ..., 5 \qquad (7)$$

where $\beta_4 = \beta_5 = \dfrac{\varepsilon}{\alpha}$, ε is a positive constant, and $d_i = 0$ for $(i-3) < 0$.

Consider the following control law:

$$\boldsymbol{\tau} = \mathbf{K_1}\ddot{\boldsymbol{\eta}}_d + \mathbf{K_2}\dot{\boldsymbol{\eta}} + \mathbf{K_3} + \mathbf{K_4}\dot{\mathbf{e}} + \mathbf{K_5}\mathbf{e} = \sum_{i=1}^{5}\mathbf{K_i}\boldsymbol{\Phi_i} \qquad (8)$$

where $\boldsymbol{\Phi_1} = \ddot{\boldsymbol{\eta}}_d$, $\boldsymbol{\Phi_2} = \dot{\boldsymbol{\eta}}$, $\boldsymbol{\Phi_3} = 1$, $\boldsymbol{\Phi_4} = \dot{\mathbf{e}}$, $\boldsymbol{\Phi_5} = \mathbf{e}$, and $\mathbf{K_i}$ are control gain matrices.

From Eqs. (3) and (8), the error equation can be obtained as follows

$$\ddot{\mathbf{e}} = \mathbf{M}^{-1}(\mathbf{M}-\mathbf{K}_1)\ddot{\boldsymbol{\eta}}_d + \mathbf{M}^{-1}(\mathbf{C}+\mathbf{D}-\mathbf{K}_2)\dot{\boldsymbol{\eta}} + \mathbf{M}^{-1}(\mathbf{g}-\mathbf{K}_3) + \mathbf{M}^{-1}\mathbf{u}_d - \mathbf{M}^{-1}\mathbf{K}_4\dot{\mathbf{e}} - \mathbf{M}^{-1}\mathbf{K}_5\mathbf{e}$$
$$= \mathbf{M}^{-1}\sum_{i=1}^{5}(\mathbf{P}_i - \mathbf{K}_i)\boldsymbol{\Phi}_i + \mathbf{M}^{-1}\mathbf{u}_d \qquad (9)$$

where $\mathbf{P}_1 = \mathbf{M}, \ \mathbf{P}_2 = \mathbf{C}+\mathbf{D}, \ \mathbf{P}_3 = \mathbf{g}, \ \mathbf{P}_4 = \mathbf{P}_5 = 0.$

Theorem: The tracking error **e** will asymptotically converge to zero with the following adaptive controller:

$$\mathbf{K}_i = \frac{\hat{\theta}_i \, \widetilde{\mathbf{e}} \boldsymbol{\Phi}_i^{\mathrm{T}}}{\|\widetilde{\mathbf{e}}\| \|\boldsymbol{\Phi}_i\|} \qquad (10)$$

$$\dot{\hat{\theta}}_i = \mathbf{f}_i \|\widetilde{\mathbf{e}}\| \|\boldsymbol{\Phi}_i\| \quad i=1,\dots,5 \qquad (11)$$

where $\mathbf{f_i}$ are positive constants, $\hat{\theta}_i$ are estimates of θ_i, and

$$\widetilde{\mathbf{e}} = \dot{\mathbf{e}} + \sigma\mathbf{e} \qquad (12)$$

where σ is a positive constant.

Proof: Consider the following Lyapunov function candidate:

$$V = \frac{1}{2}\widetilde{\mathbf{e}}^{\mathrm{T}}\widetilde{\mathbf{e}} + \frac{1}{2}\sum_{i=1}^{5} f_i^{-1}\gamma(\theta_i - \hat{\theta}_i)^2 \qquad (13)$$

Differentiating Eq. 13 along Eq. 9 with respect to time yields

$$\dot{V} = \widetilde{\mathbf{e}}^{\mathrm{T}}\ddot{\mathbf{e}} + \sigma\widetilde{\mathbf{e}}^{\mathrm{T}}\dot{\mathbf{e}} - \sum_{i=1}^{5} f_i^{-1}\gamma(\theta_i - \hat{\theta}_i)\dot{\hat{\theta}}_i$$
$$= \left[\widetilde{\mathbf{e}}^{\mathrm{T}}(\mathbf{M}^{-1}\sum_{i=1}^{5}\mathbf{P}_i\boldsymbol{\Phi}_i + \mathbf{M}^{-1}\mathbf{u}_d) + \sigma\widetilde{\mathbf{e}}^{\mathrm{T}}\dot{\mathbf{e}} - \sum_{i=1}^{5} f_i^{-1}\gamma\theta_i\dot{\hat{\theta}}_i\right] + \left[-\widetilde{\mathbf{e}}^{\mathrm{T}}\mathbf{M}^{-1}\sum_{i=1}^{5}\mathbf{K}_i\boldsymbol{\Phi}_i + \sum_{i=1}^{5} f_i^{-1}\gamma\hat{\theta}_i\dot{\hat{\theta}}_i\right] (14)$$

With the adaptive controller Eq. (10), Eq. (11) and $\varepsilon > \sigma,$ the equation in the first bracket of (14) becomes

$$\widetilde{\mathbf{e}}^{\mathrm{T}}(\mathbf{M}^{-1}\sum_{i=1}^{5}\mathbf{P}_i\boldsymbol{\Phi}_i + \mathbf{M}^{-1}\mathbf{u}_d) + \sigma\widetilde{\mathbf{e}}^{\mathrm{T}}\dot{\mathbf{e}} - \sum_{i=1}^{5} f_i^{-1}\gamma\theta_i\dot{\hat{\theta}}_i$$
$$= \widetilde{\mathbf{e}}^{\mathrm{T}}\sum_{i=1}^{3}\mathbf{M}^{-1}\mathbf{P}_i\boldsymbol{\Phi}_i - \sum_{i=1}^{3}\alpha\beta_i\|\widetilde{\mathbf{e}}\|\|\boldsymbol{\Phi}_i\| + \sigma\widetilde{\mathbf{e}}^{\mathrm{T}}\dot{\mathbf{e}} - \varepsilon(\|\widetilde{\mathbf{e}}\|\|\dot{\mathbf{e}}\| + \|\widetilde{\mathbf{e}}\|\|\mathbf{e}\|) + \widetilde{\mathbf{e}}^{\mathrm{T}}\mathbf{M}^{-1}\mathbf{u}_d - \alpha(d_0\|\widetilde{\mathbf{e}}\| + d_1\|\widetilde{\mathbf{e}}\|\|\dot{\mathbf{e}}\| + d_2\|\widetilde{\mathbf{e}}\|\|\mathbf{e}\|)$$
$$\leq \sum_{i=1}^{3}(\|\mathbf{M}^{-1}\|\|\mathbf{P}_i\| - \alpha\beta_i)\|\widetilde{\mathbf{e}}\|\|\boldsymbol{\Phi}_i\| + (\sigma-\varepsilon)\|\widetilde{\mathbf{e}}\|\|\dot{\mathbf{e}}\| - \varepsilon\|\widetilde{\mathbf{e}}\|\|\mathbf{e}\| + (\|\mathbf{M}^{-1}\| - \alpha)(d_0 + d_1\|\dot{\mathbf{e}}\| + d_2\|\mathbf{e}\|)\|\widetilde{\mathbf{e}}\| \leq 0 \qquad (15)$$

and the equation in the second bracket becomes

$$-\widetilde{\mathbf{e}}^{\mathrm{T}}\mathbf{M}^{-1}\sum_{i=1}^{5}\mathbf{K}_i\boldsymbol{\Phi}_i + \sum_{i=1}^{5} f_i^{-1}\gamma\hat{\theta}_i\dot{\hat{\theta}}_i = \sum_{i=1}^{5}(-\frac{\widetilde{\mathbf{e}}^{\mathrm{T}}\mathbf{M}^{-1}\widetilde{\mathbf{e}}}{\widetilde{\mathbf{e}}^{\mathrm{T}}\widetilde{\mathbf{e}}} + \gamma)\|\widetilde{\mathbf{e}}\|\|\boldsymbol{\Phi}_i\|\hat{\theta}_i \leq \sum_{i=1}^{5}(-\lambda_{\min}(\mathbf{M}^{-1}) + \gamma)\|\widetilde{\mathbf{e}}\|\|\boldsymbol{\Phi}_i\|\hat{\theta}_i \leq 0 \ (16)$$

From Eqs. (14), (15) and (16), we can conclude that $\dot{v} < 0$ for all $\tilde{e} \neq 0$. Therefore, the tracking error e will asymptotically go to zero from Eq. 10.

The adaptive controller is described by Eqs. (8), (10) and (11). However, the direct use of the controller of Eq. (10) would generate large control input signals at near zero values of the denominator. To avoid this problem, the following modified controller is used:

$$\mathbf{K}_i = \frac{\hat{\theta}_i \tilde{e} \mathbf{\Phi}_i^{\mathrm{T}}}{\| \tilde{e} \| \| \mathbf{\Phi}_i \|} \quad \text{for } \| \tilde{e} \| \| \mathbf{\Phi}_i \| > \delta_i$$

$$\mathbf{K}_i = \frac{\hat{\theta}_i \tilde{e} \mathbf{\Phi}_i^{\mathrm{T}}}{\delta_i} \quad \text{for } \| \tilde{e} \| \| \mathbf{\Phi}_i \| \leq \delta_i$$

(17)

where $i = 1,...,5$ and δ_i is a positive constant.

The modified controller of Eq. (17) may not guarantee asymptotic stability; however, tracking errors are bound by small values of δ_i. To reduce the error, a term $k_1 \int e dt$ is added to Eq. (8), where k_1 is a small constant.

Influence and Control parameters

There are four parameters that affect the performance of the adaptive controller: adaptation gain (f) in Eq. (11), sigma (σ) in Eq. (12), threshold (δ) in Eq. (17), and I-control gain (k_I). One can note the following, σ affects the time constant of the overall control system. The adaptation gain f affects the adaptation period. Appropriate values of the threshold δ would keep the denominator in Eq. 17 from becoming the near zero value that may cause high gain values and large control signals beyond saturation limits. Appropriate small values of the I-control gain k_I would help reduce the steady state errors due to δ without affecting the overall stability.

Effects of these parameters were investigated by experiments on ODIN. The desired path for ODIN has three segments. Segment 1: ODIN moves down from the surface with the position control in the z direction only (Z: 0 to 2 m). Segment 2: ODIN then moves in the y direction with position control in all 6 dof, tracking in y (y: 2.5 to 4.5 m) and regulation in x at 2.5 m, z at 2 m, pitch at zero degree, roll at zero degree, and yaw at zero degree. Segment 3: ODIN then moves in the x direction with position control in all 6 dof, tracking in x (x: 2.5 to 4.5 m) and regulation in y at 4.5 m, z at 2 m, pitch at zero degree, roll at zero degree, and yaw at zero degree. The desired trajectory for each segment of the path was generated using a trapezoidal velocity profile. Since there was no position control in the x and y directions during segment 1, ODIN was usually away from the desired initial location of segment 2 at (x, y)= (2.5m, 2.5m) after segment 1. As can be seen from experimental results in Figures LLC-4 to 6, ODIN tried to move to the desired x and y location (2.5m, 2.5m) as soon as segment 2 started with control in all 6 dof. During experiments, all control gains were initially set to 0.

Case 1: Effect of σ was tested with three different values of σ = 1, 2 and 3. The same values of (f, δ, k_I)=(0.9,55,0.008) were used for each σ. It can be seen from Figure LLC-4 that the tracking in the x-y plane is much better when sigma = 2 (Figure LLC-4b) than when sigma = 1 (Figure LLC-4a). However, when sigma increases to sigma = 3, the performance degrades. This is because when

sigma is too large, it leads to very large voltage input, reaching the saturation limit of the motor. Oscillation is observed in Figure LLC-4c.

Case 2: Effect of f was tested with three different values of f = 0.2, 0.5, and 0.9. The same values of (σ, δ, k_I)=(2,55,0.008) were used for each f. Figure LLC-5 shows that the performance gets better when adaptation gain f increases from f = 0.2 (Figure LLC-5a) to f = 0.5 (Figure LLC-5b) and to f = 0.9 (Figure LLC-5c).

Case 3: Effect of δ was tested with three different values of δ = 55, 60, and 65. The same values of (σ, f, k_I)=(2,0.9,0.008) were used for each δ. As shown in Figure LLC-6, tested values of δ provide almost the same performance even though it was observed during the wet experiment that δ=0 caused instability of the system.

Case 4: During wet tests to investigate effect of k_I, the following values for other parameters were used: (σ, f, δ)=(2,0.9,55). The influence of I-control gain k_I is shown in Figure LLC-7. It was observed in earlier tests that there were almost no steady state errors in x, y and other angles with or without k_I but large steady state errors in the z direction without k_I. Therefore, k_I was used only for the z direction. Figure LLC-7 shows that the steady state errors are reduced significantly with k_I = 0.008 (Figure LLC-7b) compared to steady state errors with k_I = 0 in (Figure LLC-7a).

Conclusion

This section described a new multi-input multi-output (MIMO) adaptive controller using bound estimation for underwater robots and presented experimental results of the control system on ODIN. Results show that the control system did not require any prior information about the system dynamics and yet could provide high performance in the presence of noise and unmodeled dynamics. Even though a very simple static thruster model was used as part of the control system, the adaptive controller could still provide good performance. No information about the ODIN's hydrodynamics was required in the adaptive controller design, yet it still provided good performance. Conventional linear controller with zero or poorly tuned gains cannot provide good performance and may even result in instability while the presented adaptive control performed well with gains initially set to zero. The fine-tuning of PID-type controller gains for the underwater robot system is very difficult if not impossible. It is not only due to the robot's highly nonlinear and time-varying dynamics but also because the operator may not have full access to the robot's on-board control unit while the robot is in water.

Based on a theoretical model and experimental results, ODIN's dynamic model was obtained and computer simulator software for ODIN, *OdinSim* was also developed in Matlab as well as in C language, including all modules shown in Figure LLC-2. Future research will be on integration of a GA-based motion planner [Sugihara98] with the presented navigation and control system and its implementation on ODIN.

Localization using Certainty Grids

Introduction

A largely unexplored area of underwater navigation is the ability to estimate the autonomous underwater vehicles' (AUV) position given an a priori map of the vehicles working space. In other words, the AUV must be able to determine from a small number of sensor readings its current position given a map made previously from a large set of readings. We will explore this problem of localization of the vehicle using the certainty grid technique developed by Elfes 1987 and Moravec 1989.

Currently, most AUV localization techniques are "geometric" based and require constructing point, line, or other surface descriptions from sense data at an early stage of processing [Faugeras93]. Leonard 1997 uses a technique called concurrent mapping and localization (CML), which tracks the vehicle and a set of proposed features through time. Leonard's system theoretically will produce very accurate results even without an a priori map of the environment; however, the technique requires the use of very expensive underwater navigation sensors (such as the Navy's high resolution array (HRA) imaging sonar [Nussbaum96]). The technique also suffers with the lack of features to reference, i.e. a sandy bottom. Healey 1996 and McLain 1996 have investigated other "geometric-based" techniques for AUV localization. However, they have the disadvantage of having to process a tremendous amount of data about the geometric extensions in a very short amount of time. Thus, the technique is susceptible to errors if the underwater sensors are not clean.

The technique that we wish to demonstrate uses the evidence grid approach. The technique allows the use of fairly inexpensive wide beam angle sonar's. These underwater sensors are known for having transient mis-readings. Instead of registering objects, the grid method accumulates occupancy evidence from an array of spatial locations and slowly resolves the ambiguities as the AUV travels [Moravec96]. It has proved tremendously successful for land based mobile robots. Stewart 1988 considered concurrent mapping and positioning of underwater vehicles using a grid-based technique. Aramaki 1996 used a grid-based technique with their "Twin Burger" underwater vehicle.

Mathematical Approach for Certainty Grid

Certainty grids (or occupancy grids) are mapped regions of space divided into cells, where each cell represents the probability of being occupied or empty. The implementation of the certainty grid algorithm requires a sensor map (Figure LLC-8) and an update rule. The update rule assigns a value between 0 and 1 based on the probability that the grid is occupied.

In order to determine the occupancy probability, Moravec 1996 used a Bayesian model updating formula. The Bayesian sequential update formula may be written as

$$p(A \mid B_k) = \frac{p(b_k \mid A \wedge B_{k-1})}{p(b_k)} \times p(A \mid B_{k-1})$$

Now, let's substitute o for A, which corresponds to the current certainty value of the cell. Next, let B_k correspond to R_k, the sequence of all the range reading obtained so far. Finally, let b_k correspond to r_k, a single range reading. The Bayesian update rule is rewritten as the following

$$p(o \mid R_k) = \frac{p(r_k \mid o)}{p(r_k)} \times p(o \mid R_{k-1})$$

The quantity $p(r_k \mid o)$ determines the probability of getting a given range reading given the cell is occupied. This is the sensor model, which was shown in Figure LLC-1. The quantity $p(r_k)$ is the probability of getting a range reading independent of the occupancy of the cells.

Future Tasks (Phase II Tasks)

- Complete testing of control systems on the ODIN AUV.
- Continue development of the localization algorithm.
- Test the localization algorithm to the ODIN AUV and test.
- Refine and combine the vehicle control and manipulator software.
- Import software to SAUVIM.

Figure LLC-1: ODIN AUV
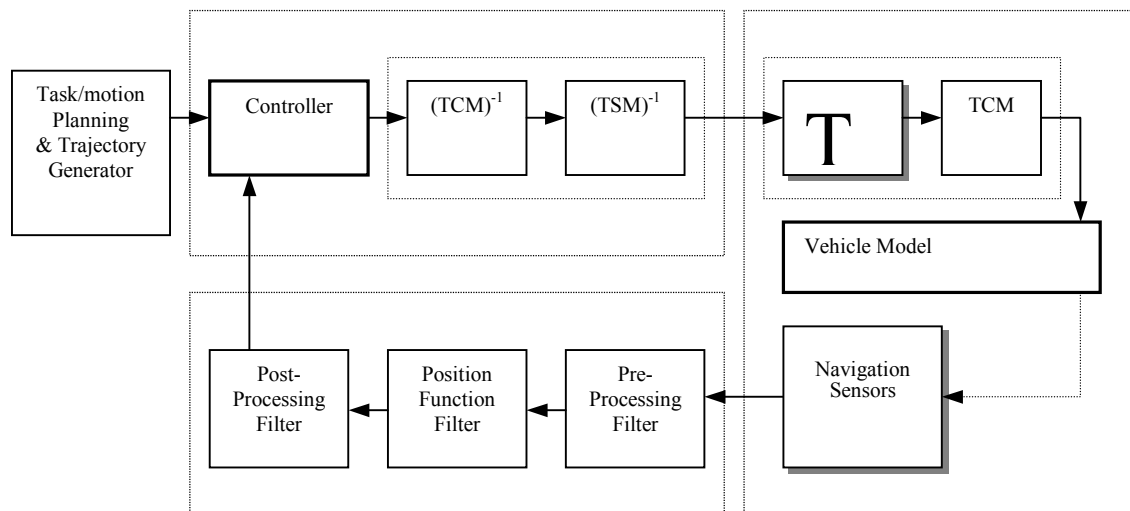
Figure LLC-2: Block diagram of navigation and control system
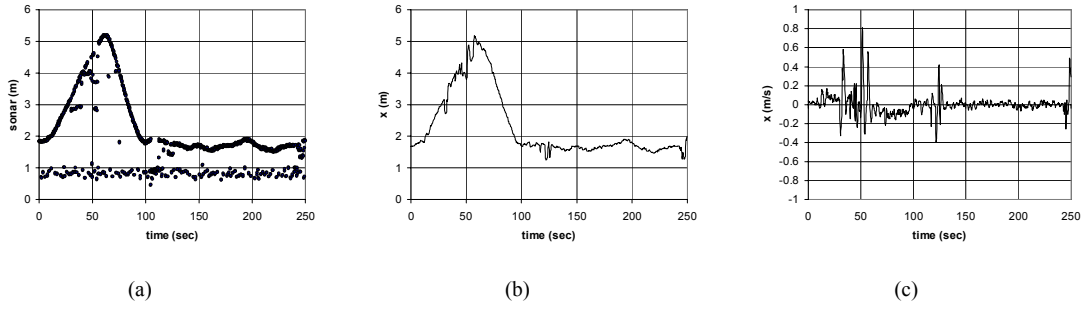
Figure LLC-3: (a) Unfiltered sonar signal, (b) Position from Kalman filter,
(c) Velocity from Kalman filter.
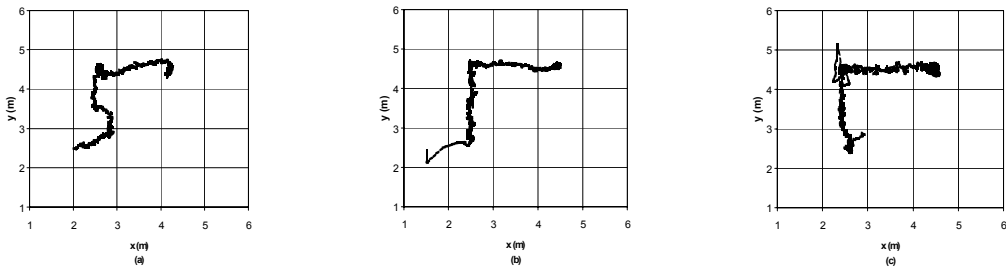
Figure LLC-4: Influence of control parameter sigma. (a) sigma =1, (b) sigma =2, (c) sigma=3.
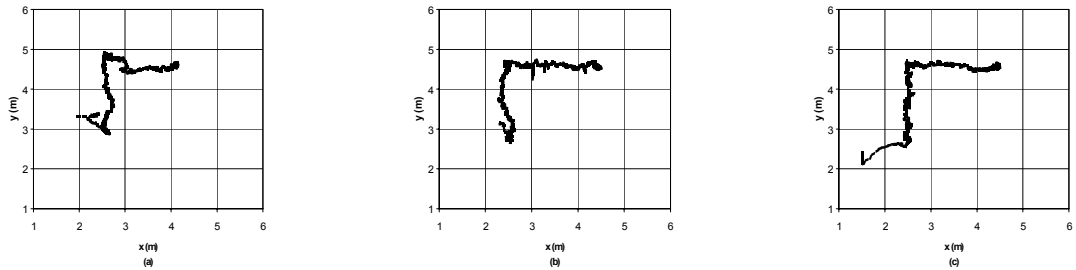
Figure LLC-5: Influence of control parameter f. (a) f=0.2, (b) f=0.5, (c)=0.9.
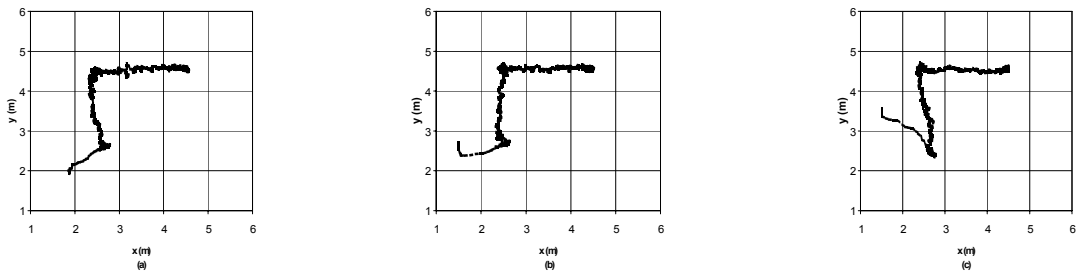
Figure LLC-6: Influence of control parameter threshold: (a) threshold=55, (b) threshold=60, &
(c) threshold=65.
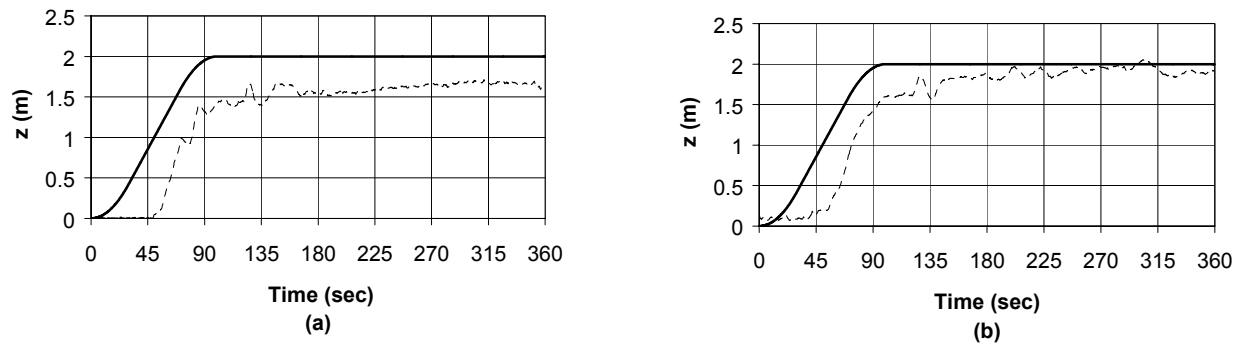
Figure LLC-7: Influence of control parameter k_I in z direction. (a) $k_I = 0$, (b) $k_I = 0.008$.
(Desired trajectory -- Actual trajectory)
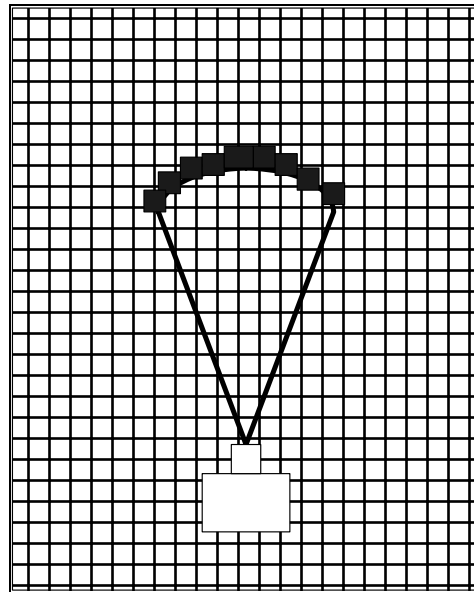
Figure LLC-8: Sonar Senor Model

High-Level Control (HLC)

Project Leaders: Dr. Junku Yuh, Dr. Kazuo Sugihara & Dr. Song K. Choi
Personnel: Mr. Side Zhao

Objectives

The objective is to develop an event-driven supervisory control module that minimizes human involvement in the control of underwater manipulation tasks.

Current Status (Tasks Completed During 8/1/97 – 10/30/00):

From a human viewpoint, a mission is always composed of two parts: the goal and the method of accomplishment. Other words, "what do I need to do" and "how do I do it". Following this strategy, a new architecture of vehicle control, named Intelligent Task-Oriented Control Architecture (ITOCA), is developed for SAUVIM. ITOCA is an effective and efficient operation running on the VxWorks real-time operating system (RTOS) environment. ITOCA is four layers: Planning Layer; Control Layer; Execution Layer and Evaluation Layer. Every mission is broken into many smaller missions, and the simplest mission is considered a task. The combination of different tasks in different sequences accomplishes various missions.

The planning layer consists of the plan supervisor and task supervisor. The plan supervisor decomposes the given mission into the sequence of several sub-goals. The task supervisor sequences task modules for each sub-goal. Common sub-goals and task modules are pre-programmed in database along with a world model that is continuously updated using sensor data. The control layer handles various control actions, such as the adaptive and intelligent motion control and the manipulator force/position control, based on the sequence of tasks. The execution layer includes permanent tasks independent of specific missions. These tasks are interrupt handling, shared memory control, navigation sensor handling, servo control, and communication. The evaluation layer checks the status of the vehicle/manipulator performance by comparing actual performance based on sensor feedback with desired performance given by the plan supervisor and task supervisor. This layer makes a decision for the modifications of sub-goal planning and task sequences or the suspension of the mission from fatal errors.

Advancements, in the SAUVIM software modules of motion planning and control, include: off-line and on-line motion planning modules based on GA; a low-level control module using a new non-regressor based adaptive control scheme; and a redundancy resolution control module for the vehicle and manipulator system.

Future Tasks (Phase II Tasks)

- Refinement of ITOCA and development of generic ITOCA command language.
- Software implementation of preliminary version of ITOCA.
- Testing of ITOCA and refinement..
- Implementation in to the SAUVIM software.

Predictive Virtual Environment (PVE)

Project Leader: Dr. Song K. Choi & Dr. Kazuo Sugihara
Personnel: Mr. Scott Menor & Mr. Alexander Nip

Objectives

This sub-project aims at applying virtual reality (VR) to the construction of the predictive virtual environment that presents a supervisor with the current situation of SAUVIM as accurately and realistically as possible.

The basic four objectives are:

- To develop software for data fusion of map data and online sensory information;
- To develop software to smooth out a jerky virtual environment due to delayed information from limited bandwidth of communication;
- To develop a learning algorithm for prediction of the current situation from the delayed information acquired by SAUVIM; and
- To integrate the above software modules and interface them with SAUVIM communication for the PVE.

Current Status (Tasks Completed During 8/1/97 – 10/30/00):

Introduction

Even with the increased interest in the development of underwater robotic technology, the design, fabrication and analysis of AUVs are very difficult and expensive. The unpredictable, hazardous underwater environment is unforgiving and remote. With great limitation in communication, an AUV must operate in a fully autonomous or near autonomous modes. This limitation immensely complicates the diagnosis and evaluation of AUV's many subsystems. In order to ensure reliability in these systems, it is imperative to obtain and maintain accurate software and hardware. For this purpose, it is imperative to test and re-test these systems under severe or extreme conditions in a controlled laboratory environment before operational or sea-trial deployment. Many military, scientific and commercial tasks in the ocean often require multi-national operations. It is necessary to rehearse the operations before the actual operation, establishing operational strategy and ensuring the success of the operation. The Distributed Virtual Environment Collaborative System (DVECS), a virtual reality monitoring system for the Semi-Autonomous Underwater Vehicle for Intervention Missions (SAUVIM), provides an excellent tool for these needs.

Several universities have conducted research in the graphic simulator arena. To mention a few, they are: (1) the Naval Postgraduate School and their NPS AUV Integrated Simulator for their NPS AUV [Brutzman92]; (2) the University of Tokyo and their Multi-Vehicle Simulator for their Twin-Burger AUV [Kuroda95]; and (3) the Autonomous Undersea Systems Institute and their Cooperative AUV Development Concept [Chappell99]. Both the NPS and UT systems were developed on the IRIX environment of the Silicon Graphics workstation, while the AUSI system runs on the Win32 environment of an Intel based system.

The DVECS was developed with objectives of reducing the time required for the tedious aspects of pre-testing the software and hardware before deployment and the collaboration of various AUVs without having to consider the transportation of these vehicles. Much of DVECS is based and developed on a 3-dimensional graphic test platform for underwater vehicles by Yuh, Adivi and Choi [Yuh92]. The DVECS utilizes a similar hierarchical architecture of this test platform combined with the UT's MVS simulation system. The DVECS also utilizes various wireless communications methods - radio frequency link, commercial cellular telephone, wireless Ethernet, and asynchronous transfer mode - for data transfer. Finally, the DVECS incorporates a projection VR system combined with polarized eyewear and emitter system.

Distributed Virtual Environment Collaborative Simulator (DVECS)

The design, testing and operation of AUVs and their control systems can benefit considerably from interactive, 3-dimensional (3D) computer simulations. In particular, developing and testing complex systems that involve multiple autonomous underwater robots operating in an uncontrolled environment is considerably safer in a controlled synthetic environment than a real environment, as research vehicles are not placed at risk of loss or damage. Mission planning, monitoring and analysis can also benefit from an interactive, 3D virtual environment since its performance can be tested prior to actual sea-trials. For these reasons, the Distributed Virtual Environment Collaborative Simulator (DVECS) was developed to be used in hybrid synthetic simulations for testing real and virtual vehicles in a common environment and for mission collaboration, planning, monitoring and analysis of existing unmanned underwater vehicles (UUVs), as described in Figure PVE-1.

UH's DVECS and UT's MVS are based on a similar concept to achieve this collaboration effort. The DVECS architecture is designed to operate in a networked environment such that each component of the simulation can be run on a separate system, processor or virtual machine within a single computer; thus, distributing the computation load.

This feature offers several advantages over a single system layout. First, it is possible to modify or create new components with minimal restrictions on internal architecture. As long as each component adheres to certain prescribed requirements for communication, language and operating system, the design and implementation of each component is irrelevant to the rest of the system.

Second, users can design and test their AUV simulations across the Internet using common servers. This allows computationally intensive 3D simulation of interaction between multiple objects in the virtual world to be simulated on one or more centralized high performance computers, while the processing requirements for the user's AUV simulations are no more than what their physical AUVs would normally require. Thus, this optimizes the computation time and allows users to accurately evaluate their vehicle's computation performance and requirements.

Finally, multiple simulated or physical entities can interact over a networked environment without requiring them to share code or knowledge of each other's capabilities so proprietary algorithms can be tested in a common environment without making them public. This allows for collaboration from many different sectors of the underwater community that wish to "evaluate" their AUV in conjunction with pre-tested AUVs, as shown in Figure PVE-2.

Communication

One key feature of the DVECS is that multiple simulated and real systems must be able to interact with one another. In order to accomplish this, communication between the various components is

essential. Within the DVECS environment, TCP socket streams convey messages from one component to another. These messages or data are used in the various sub-systems - graphics module, numerical module, navigation module, etc. - to exactly determine the position of the AUV within the virtual environment. In addition, a simple network reflector interface that allows a simulated entity within the DVECS to be controlled by telemetry data from an external component is used to garner data from the UH AUV, ODIN (Omni-Directional Intelligent navigator) [Choi95]. This interface can be used to monitor a physical or simulated vehicle either directly over a network or with an additional software reflector if the communications system does not include network support.

Wireless communication between a vehicle in the field (ODIN) and the DVECS, for use as a monitoring or testing system, can thus be accomplished either of two methods. First, it is possible by a serial data link that connects to an intermediate interface that relays data between our TCP packets and the serial link, or second, by a direct network connection over a wireless link with an interface either on board the AUV or at the test site. Either system is completely transparent to the DVECS and the communications delay created by adding additional reflectors is typically negligible.

Typically for ODIN, the transfer of data between the test vehicle and the monitoring laptop is via a radio frequency (RF) modem. The transfer of data from the monitoring laptop to the DVECS is via a cellular phone or a wireless Ethernet connection.

For interactive vehicle testing in a hybrid, simulated synthetic environment, combining the actual and the virtual sensor measurements generates the synthetic sensor data. This is easiest for range data, such as from sonar, in which the synthetic range is simply the minimum of the actual and virtual sensor data.

Sensor Fusion

UUVs with even a modest number of sensors can generate an enormous amount of data that can be difficult for an operator or observer to easily interpret. For this reason, it is desirable to combine data from a variety of sensors and present it in a clear, easily understandable way. Within the DVECS, it includes a sensor fusion system that can apply sensor data to surfaces in the virtual world that represents actual objects in the real environment of the AUV.

An obvious way to apply sensor data to the surfaces in the virtual world is to use tomographic methods, solving the inverse problem for the sensors. Unfortunately, even for sensors such as cameras under non-reflective and non-refractive conditions where the light paths are all straight lines between the sensor and the object being sensed, directly solving the inverse problem can be computationally intensive and require a significant amount of processing time. For other sensors, such as sonar in water, where multi-path effects become important and with refractive media, the paths are not straight lines and directly solving the inverse problem at reasonable resolution within a reasonable amount of time is impractical on current computers.

In order to overcome these problems, the use of texture mapping of images generated from the sensor data was selected. The DVECS achieves this by generating a 'sensor space' coordinate system on the geometries, combining sensor data into texture images and applying the textures to the surfaces of the geometries.

There are several benefits of using texture mapping over directly solving the inverse problem. First, generating and manipulating the texture images can be done with commonly available image

processing routines. This has the advantages that these routines can be highly optimized so processing time is minimal and that these routines are well tested, existing code considerably simplifying and shortening design and implementation.

Second, computing the sensor space parameterization of the geometries typically involves solving relatively simple equations at a small number of points on the geometry so does not require a significant amount of processing time. For a simple optical camera in non-refractive media imaging a non-reflective surface, the form of this parameterization is very simple. For simplicity, adopt a sensor space coordinate system where the origin is the focal point, forward distance from the focal point away from the vehicle is the positive z direction, up is positive y and when facing positive z and oriented with positive y up, horizontal left is positive x. As indicated in Figure PVE-3, given a point, p, on geometry G, if the corresponding view plane then is parameterized by the coordinates [u,v,L], for fixed L and point p has coordinates [x,y,z] then the parameterization of p has the simple form,

$$[u,v]^T = \frac{L}{z}[x,y]^T .$$

Although the actual parameterization will take on a more complicated form for more complicated sensor problems, in many cases, this approximation can be used quite effectively. Unfortunately, obvious problems arise with discontinuities and multiple representation of a given area in multi-path problems or in media with variable refractive index. In principle, however, many of these problems may be dealt with by using image-processing techniques at the stage of generating the textures. The video to graphic overlay can be seen in the upper right hand window in Figure PVE-4.

Finally, most commonly available high performance graphics hardware includes texture-mapping optimization, so scenes with complex geometries and high resolution, high detail textures can be rendered in real time.

Graphic Prediction

Due to the overwhelming delay in the data transmission and the lack of desired bandwidth from acoustic underwater communication signals, it is imperative that a prediction method be utilized to provide relatively "smooth" graphic motions in the monitoring system. In most cases, a "smooth" (real-time) video is considered to be 30 frames per second; however, in underwater communication cases, the data transfer rate is approximately one frame per 3 seconds.

The graphic prediction system uses an Artificial Neural Network (ANN) of back-propagation methodology of three hidden layers. The system utilizes a four-ANN combination where each recognizes particle motions from each edge of the video screen (top, bottom, right and left sides). To perform these experiments, an extensive, random video of 20-30 second length per particle motion was created in advance. After multiple experiments of multiple random particle motions where 25% of the total motion data were used for training and 75% of the total motion data for prediction, the ANN performed to within 5% errors of each motion; however, the total time (training and prediction) result in a ballooning effect. Once an optimal performance level is reached, additional experiments will be conducted for higher performance. The next experiments will involve shape recognition algorithms and a database lookup tables for possible, standard motions. Additional results will be published in future publications.

Virtual User Interface

As mentioned before, the DVECS uses a Silicon Graphics workstation setup. This dual workstation setup comprises of an Onyx and an Indy. It interfaces with an ElectroHome Virtual Reality Projection unit and Stereographics CrystalEyes eyewear and emitter system.

The DVECS software is a multi-layered C++ program modularized by its subsystems and utilizes the inheritance properties. It uses OpenGL graphics libraries to generate the background, vehicle and obstacles, and uses Open Inventor 3D toolkit protocols to create the 3-dimensional, virtual images.

The DVECS consists of three windows. They are the Main View Window, Main Menu Bar Window, and Main Control Panel Window (Figure PVE-5).

The Main View displays the virtual environment with the vehicle being tested. The background environment can be modified to represent an area being used, such as the UH dive well, or can used pre-mapped seafloor data to represent a specific deployment area. The window allows instantaneous change in viewpoints and magnification.

The Main Menu Bar allows access to the background, multiple vehicles or obstacles. This is a simple, pull-down menu layout allowing for access to a specific object's properties - dimension, location and attributes.

The Main Control Panel allows access to different environments or simulations, mission controls (start, stop, pause), placement of grid layout, modification of object labels, and control of the sensor and thruster data. It also allows monitoring of system messages, warnings, etc.

Figure PVE-6 shows the Main View of the DVECS running an ODIN test in the UH dive well; Figure PVE-7 shows ODIN avoiding a virtual obstacle; and Figure PVE-8 shows the sonar array of ODIN as seen in DVECS. When an AUV is ready to be deployed, a scene similar to Figure PVE-4 can be observed.

Future Tasks (Phase II Tasks)

- To implement graphic-scene prediction software based on the designed ANN.
- To integrate various software modules in the overall PVE system.
- To improve communications methods for open oceans.
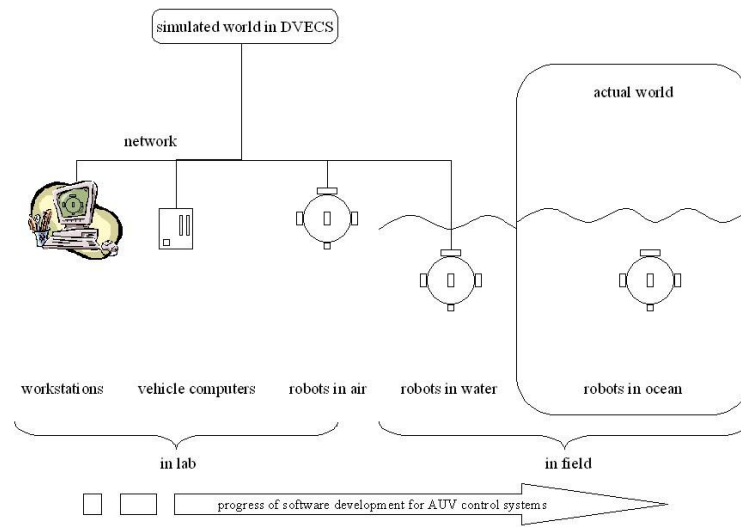
Figure PVE-1: DVECS development environment
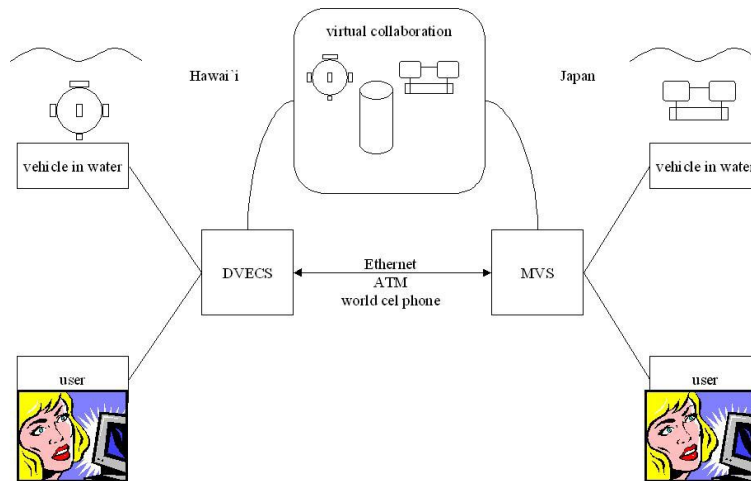
Figure PVE-2: DVECS and MVS Collaboration
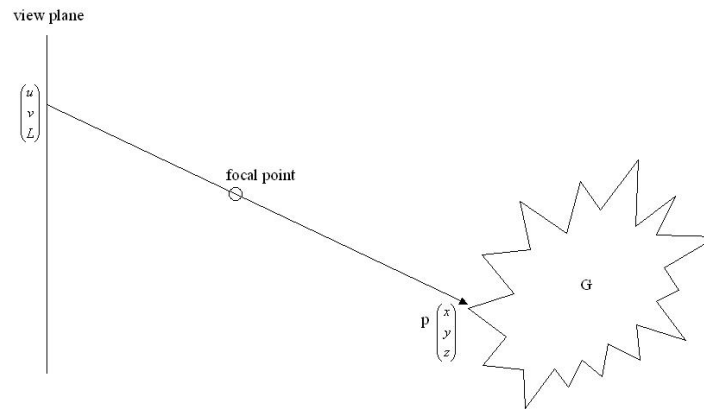
Figure PVE-3: The sensor space parameterization
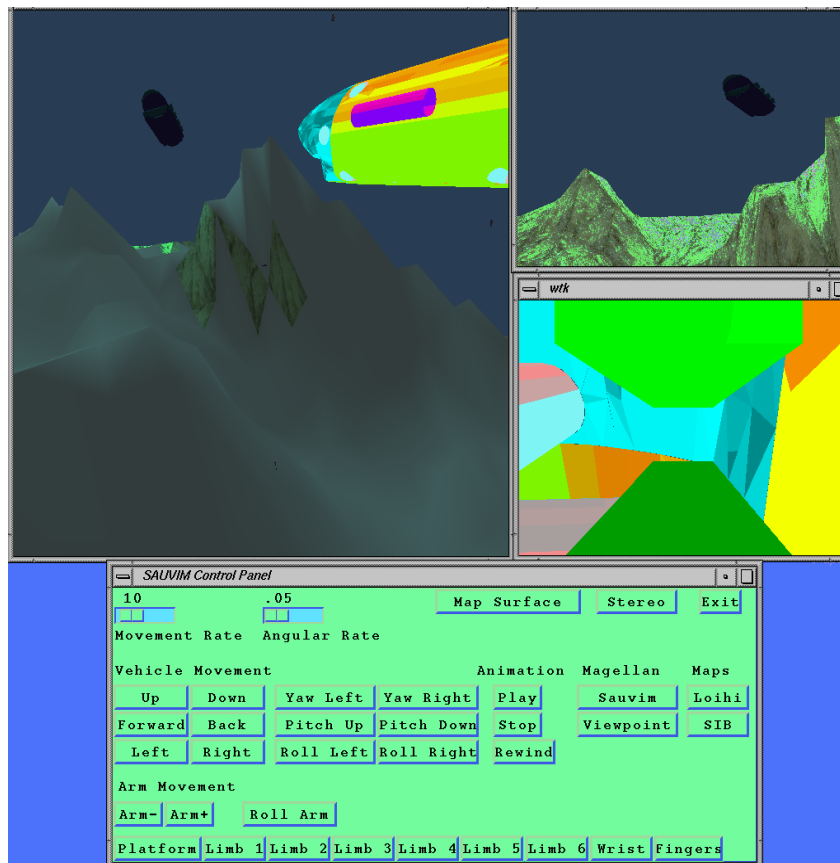
Figure PVE-4: DVECS for AUV in an undersea environment testing and evaluation
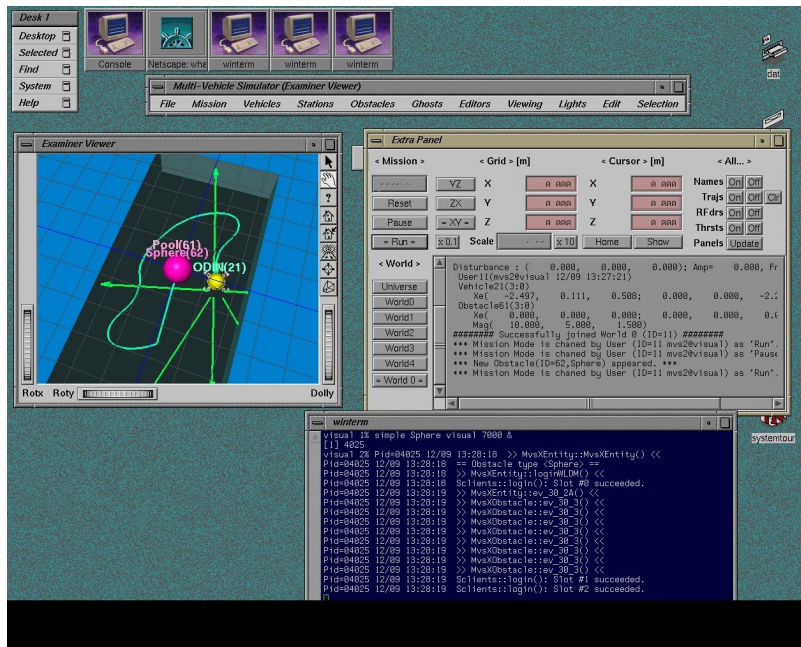
Figure PVE-5: Overview of DVECS graphic interface for a pool test
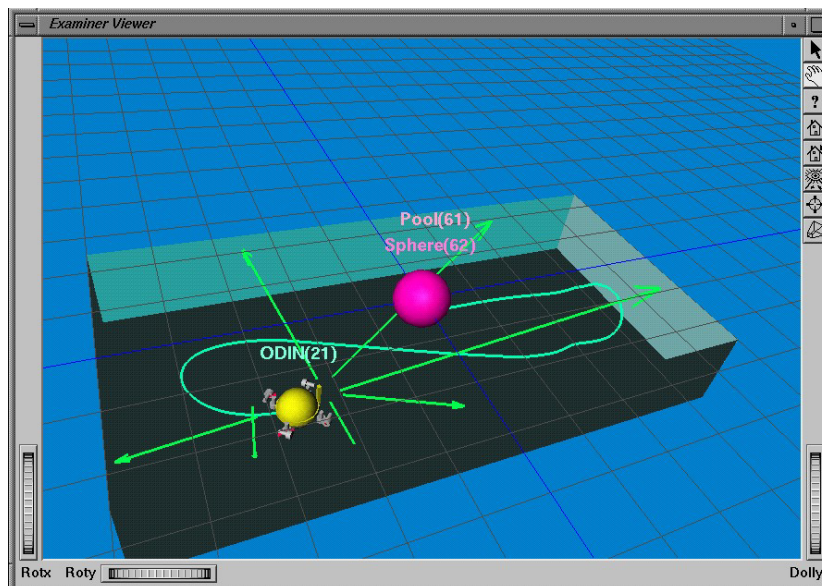
Figure PVE-6: ODIN pool test as observed on DVECS
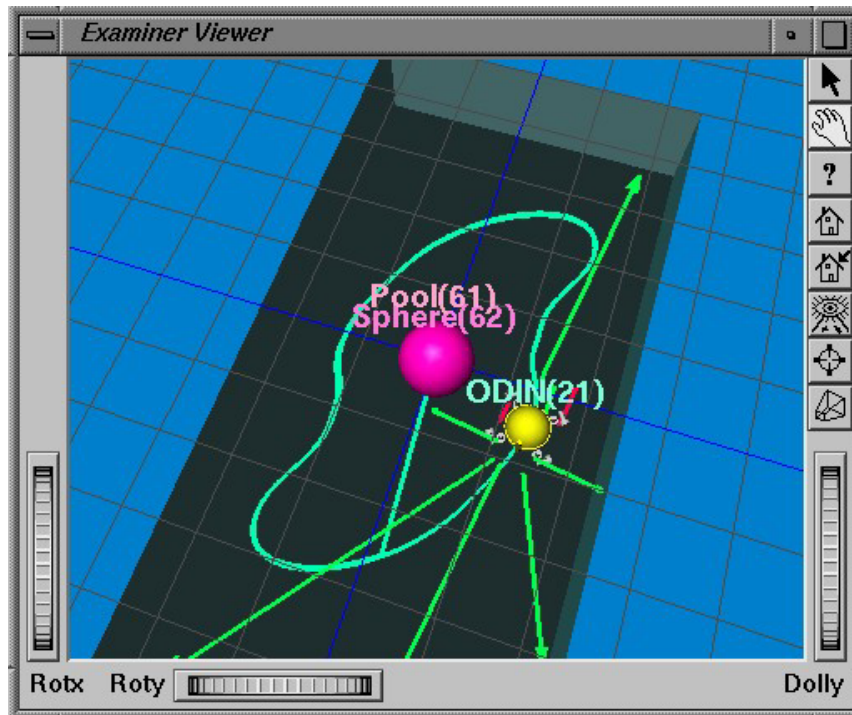
Figure PVE-7: ODIN avoiding an obstacle in DVECS
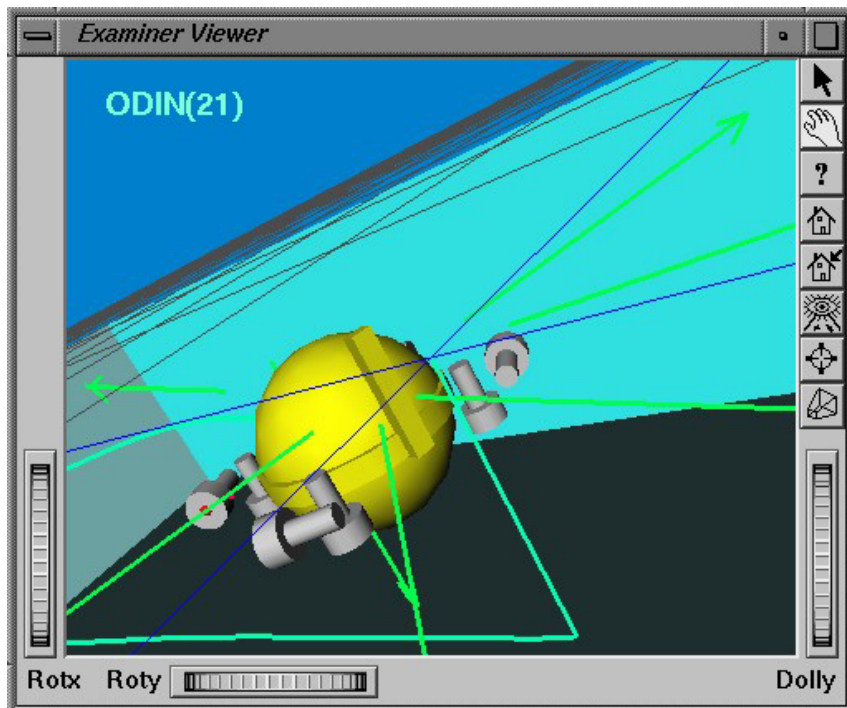
Figure PVE-8: DVECS representation of ODIN sonar sensors.

SAUVIM Design (SD)

Project Leaders: Dr. Tae W. Kim, Dr. Song K. Choi, Dr. Junku Yuh, Dr. Mehrdad Ghasemi Nejhad, Dr. Gary McMurtry, Mr. Oliver Easterday & Mr. Gus Coutsourakis

The main technical development of the SD group is described in the following sections: Reliable, Distributed Control, Mission Sensor Package, Hydrodynamic Drag Coefficient Analysis, Mechanical Analysis & Fabrication, and Mechanical-Electrical Design.

Reliable Distributed Control (RDC)

Project Leader: Dr. Tae Won Kim
Personnel: Mr. Jang-Won Lee and Mr. Mick West

Objectives

The objective is to develop a reliable & efficient computing architecture for signal and algorithmic processes of the entire SAUVIM system.

Current Status (Tasks Completed During 8/1/97 – 10/30/00):

- VMEbus-based multiprocessor system with commercialized real-time O.S., VxWorks, was designed and implemented to produce high processing throughput and fault tolerance capability.
- Dry test system to evaluate the supervisory control S/W was developed and tested.
- Hierarchical S/W structure, incorporating real-time processing and event handling, was developed.
- Evaluation of CPU boards, I/O boards, sensors, and actuators was conducted to confirm its response time, characteristics, computation capability, and so on.
- Third party device drivers were interfaced under VxWorks environment.
- Communication interface among multi-CPUs (MC68060's and PC104 Pentium) was implemented via Ethernet and serial communication line.
- Interface between control system and human operators was designed and implemented.
- Task description language(TDL) was designed and implemented with VxWorks. The communication between TDL and supervisory controller is under development.

Structure of SAUVIM Control System

As shown in Figure RDC-1, the SAUVIM controller consists of multiple CPU boards and I/O boards to distribute tasks among multiple components. The basic idea of design is to make multiple components work in harmony and perform specific tasks based on their capabilities. The systems communicate via VME buses or Ethernet lines depending on the time dependencies of tasks. The entire controller system will be installed in two separate pressure vessels based on control objects. The first pressure vessel will contain hardware components for navigation of the vehicle. The second pressure vessel will house underwater manipulator controller and related components. These two pressure vessels are connected with Ethernet cables. Though Ethernet link is known to have a little delay in communication, we found that the communication delay is negligible in our configuration.

Navigation Control System Hardware

Navigation control system consists of four CPU boards and multiple I/O boards. Two of CPU boards are Force Computer SYS68K-60Ds based on Motorola MC68060 processor. The two other board are PC104 boards based on Intel Pentium MMX processor. Two MC68060 CPU boards are installed in a VME bus chassis and they are connected with VME bus. The PC104 boards communicate with other CPU boards via Ethernet link. Two MC68060 boards handle main tasks for vehicle navigation and PC104 boards support those two MC68060 boards. Two multifunctional AD/DA/DIO boards are

used for interfacing vehicle's sensors and actuators. One intelligent multi-port serial communication board is installed to handle communication between CPU chassis and sensors with RS-232 or RS-485 interfaces. A small network hub will be installed in the navigation pressure vessel to handle Ethernet communications among all CPU boards in control system. Because of the network hub, two MC68060 boards can have Ethernet connection beside the VME bus connection.

The Force SYS68K-60D board has a shard DRAM onboard. The shared memory is used for task synchronization and data exchanges between two navigation CPUs.

A frame grabber card is installed on one of PC104 board to capture images from the cameras. Theoretically, up to 4 cameras can be connected to the frame grabber. One of serial ports in the same board will be used to receive data from scan sonar. The scan sonar transmits data at 115.2Kbps via RS-485 interface, this speed can be handled only in PC104's serial ports. Because the serial ports of the board are RS-232 type, a RS-485 to RS-232 converter will be used. The other PC104 boards will control laser range detector and return results from the sensor to the main MC68060 processor boards

Each multifunctional analog and digital I/O board, MD-DAADIO, has 32 ADCs, 8 DACs, and 48 digital I/O channels. The ADC and the DI port A (8 bits) of the MD-DAADIO can be driven with an interrupt service routine. Compared to the previous configuration, another multifunctional I/O board has been added for future expandability. Specific pin layout design is finished, but it can be changed during vehicle construction.

The intelligent serial communication board, MVC16, has 16 serial communication channels. These channels can be set up as RS-232, RS-422 or RS-485 using jumpers. In our configuration, MVC16 board has 12 RS-232 channels and 4 RS-485 channels. This board has own processor with 128Kbyte buffer memory. It does not require main CPU board's processor time to handle communication.

Manipulator Control System

Similar with navigation control system, manipulator control system has its own pressure vessel and power supply. The robot controller uses one Force SYS68K-60D processor board. One PC 104 boards is installed for homing devices. The PC104 for homing device is installed in the manipulator pressure vessel because of space limit of other pressure vessel housing navigation control system. The manipulator control system communicates with the navigation control system via Ethernet. In previous reports, we mentioned about Ethernet's inherent communication delay, but it is found negligible after simulation and experiment. The same multifunctional analog and digital I/O board is used to control brushless DC servomotors of the manipulator. Two IP Quadrature counters are installed on a carrier board in the VME chassis for detecting seven resolver signals from the motors and one encoder signal from hall sensor in the gripper. A 6-degree of freedom force/torque sensor, JR3, is mounted at the wrist of the robot manipulator, and its controller is installed in the VME bus.

Figure RDC-1 shows the I/O boards and the external components for the manipulator controller. The homing sensor is interfaced with the RS-232 ports of the manipulator controller.

The manipulator control architecture is developed by the Theoretical Modeling and Low Level Control group and in cooperation with University of Genoa in Italy.

Attitude Heading Reference System: AHRS-BA303

AHRS is a low-cost reference navigation sensor. It uses a solid-state gyro system for an attitude gyro and a slaved heading gyro. It corrects errors with a closed loop system and adjusts biases from earth rotation and instrument offsets automatically. The attitude and heading signals are compared with two vertical reference pendulums and a triaxial fluxgate magnetometer to derive short-term absolute errors. To get the reliable data, moving average and min/max cancellation methods are used. The detailed specification of AHRS-BA303 is provided in Table RDC-1.

Altimeter: Tritech PA200

SAUVIM will be equipped with seven range sonar sensors, Tritech PA200. One is for altitude (vertical) and the others are for range measuring. These sensors have RS-485 serial communication interfaces. And, star topology is used for physical connection, because it doesn't affect the rest of the connection, and it's easy to add and remove nodes. Table RDC-2 shows the specification of PA200 sensors.

Electronic Compass Sensor: TCM2

TCM2 is an electric compass sensor module. It has a three-axis magnetometer and two-axis tilt sensor. In addition to compass heading, the TCM2 supplies pitch, roll, magnetic field data and temperature information. This sensor can be used as a backup sensor for the AHRS-BA303 sensor. And, it also uses moving average and min/max cancellation methods to have noise immunity. The detailed specification of TCM2 is shown in Table RDC-3.

Scan sonar: Imagenex 881 high resolution imaging sonar

The Imagenex sonar is an image scanning sonar. It will provide scanned images around the vehicle. The scanned images can be used for object avoidance or target detecting. However, actual implementation will be done in the future. The sonar consists of two parts. One is a sonar module with a rotating sonar head. The other is a digital signal-processing module, which processes sonar signal and transmits processed data via RS-485 interface. Two modules are connected with an oil-filled underwater cable. The processing module is connected to the pressure vessel of the navigation control system with a 4-conductor underwater cable. Table RDC-4 shows specification of the Imagenex 881 sonar.

Software Architecture

There are several objective of software design for the SAUVIM. First, the whole software system is designed to be modularized so that anyone can implement his or her own control algorithm easily and additional functions can be easily added. Second, the tasks should be distributed among processor boards. The tasks should be performed in harmony with other tasks. Third, the system should provide fault-tolerant and/or fault-recovery functions to guarantee return of the vehicle in case of emergency.

To fulfill those requirements, the whole software was designed to have three layers, *Application layer*, *Real-time layer*, and *Device layer*, as shown in Figure RDC-2.

The first layer of SAUVIM software, *Application Layer*, consists of application software, application task manager, and sub-task modules. Application software includes hardware independent high-level modules such as interface module for human operators, interpreter for task description language, and control algorithm for SAUVIM. Actual processing module for application software is sub-task module that includes all software modules for high-level processing. The application task manager is

in charge of connecting between the application software and the sub-task modules by using task-managing method such as creation and deletion of tasks, and communication and synchronization between tasks.

The second layer of SAUVIM software, *Real-Time Layer*, consists of system configurator, real-time object manger, and real-time operating system. The main role of system configurator is mapping between hardware-independent application software and real hardware-related modules. It can map real world human-friendly data to actual value for specific hardware. It can also map actual raw sensor data to human-friendly meaningful value such as depth or speed of vehicle. The real-time object manager provides system services tuned to the domain of object-oriented application. These services include management of object-oriented modules for real-time tasks. And the real-time object manager is used on top of a commercial RTOS(real-time operating system). Most of commercial RTOS vendors support and provide this real time object-related modules as an option.

The third layer of SAUVIM software, *Device Layer*, is the only hardware dependent part. Most of software modules in this layer are directly connected to hardware to send command data for actuators and get actual data from sensors. Instead of actual hardware device driver, virtual device driver can be used to emulate hardware for testing purpose or isolate software from hardware.

Navigation Control System Software

The entire software is being developed based on commercial 32-bit real-time operating systems, VxWorks and QNX. Two different operating systems are selected based on the capabilities of hardware and cost. As shown in Figure RDC-3, tasks are distributed in processor boards based on hierarchical software architecture.

The primary CPU board has several main functions. First, it harmonizes requests and responds from different systems distributed in multiple pressure vessels. For example, when the manipulator control system requests the navigation control system to move the vehicle after failing to reach an object within arm range, it responds to the request and determines what to do. Second, it reports status of vehicle to the supervisor using communication lines. Third, it performs high-level control like path planning and task planning. It plans tasks based on the task description language. Based on the interpretation of the task description language, it executes necessary tasks or requests other processor boards to perform necessary functions to fulfill its objective.

The second navigation CPU synchronizes tasks between two processor boards with its built-in shared memory and communicates with other boards via VME bus or Ethernet. It collects and keeps data required to operate vehicle in the shard memory. It provides the data in response to internal request or external request from other processor boards. The second CPU mainly processes device handling and data handling routines. It communicates with external devices using I/O device drivers for specific hardware. Current status of external devices is saved in the shared memory in the second CPU board for the first navigation CPU.

PC104 with frame grabber and scan sonar handle image capturing and scan sonar signal interpretation. It also serves the control system as a file server. It stores data gathered mainly from second navigation CPU and other during mission on a solid-state disk drive. This data can be reviewed after experiments. PC104 system uses QNX for its operating system. Several operating system was considered for candidates. QNX was selected for low costs and its good capabilities with reliability on x86 compatible CPU based processor boards.

Currently, basic functions are implemented and tested with dry test setup. During test, minor problems were found and they are under investigation.

Manipulator Control System Software

The control software is under development by cooperation with University of Genoa in Italy and the Theoretical Modeling and Low-Level Control group. In the case of failure in the navigation control system, some redundant critical functions are implemented in the software. For example, weight drop task will be implemented in the manipulator control system.

Communication of two systems

The communication between the navigation control system and the manipulator control system is at design state. Basic idea of design is drafted, but it still needs experiment and modification.

Task Description Language (TDL)

TDL is designed to provide high-level task describing tool like a command script language or MatLab script language. It can handle complex tasks with pre-defined simple commands. The primitive of TDL is as follows;

1. Vehicle Motion

- 6 DOF motion
- Use relative/absolute Pose
- Position/ Orientation/ Pose
- Speed (SP)

♦ Relative motion (w.r.t. body-fixed frame)
movev.r *position_variable* **[with sp=*speed*]**
movev.r *pos1, pos2, pos3* **[,** *ori4, ori5, ori6*] **[with sp=*speed*]**

♦ Absolute motion (w.r.t. earth-fixed frame)
movev.a *position_variable* **[with sp=*speed*]**
movev.a *pos1, pos2, pos3* **[,** *ori4, ori5, ori6*] **[with sp=*speed*]**

pos = float, integer, * (current position ; valid for absolute motion)
ori = float, integer, * (current orientation ; valid for absolute motion)
speed = float, integer   [absolute value]
        (float, integer) + %   [relative value]

♦ Fin motion
fin #*number*, *angle* [with sp = *speed*]

number = integer (1 ~ 3)
angle = integer (-90 ~ 90)
speed = float, integer (default = pre-defined speed)

2. Robot Motion

- 7 DOF
- Relative/Absolute Pose in 6 DOF (in Cartesian Space)
- Relative/Absolute Pose in 7 DOF (in Joint Space)
- Position/ Orientation/ Pose
- Speed (SP)
- By-pass level (PL)

♦ Relative motion (in Cartesian space)
  mover.r *position_variable* **[with sp=*speed*]**
  mover.r *pos1, pos2, pos3* **[,** *ori4, ori5, ori6*] **[with sp=*speed*]**

♦ Absolute motion (in Cartesian space)
  mover.a *position_variable* **[with sp=*speed*]**
  mover.a *pos1, pos2, pos3* **[,** *ori4, ori5, ori6*] **[with sp=*speed*]**

♦ Relative motion (in Joint space)
  movej.r *joint_variable* **[with sp=*speed* [%]]**
  movej.r *ang1, ang2, ang3, ang4, ang5, ang6, ang7* **[with sp=*speed* [%]]**

♦ Absolute motion (in Joint space)
  movej.a *joint_variable* **[with sp=*speed* [%]]**
  movej.a *ang1, ang2, ang3, ang4, ang5, ang6, ang7* **[with sp=*speed* [%]]**

  pos = float, integer, * (current position ; valid for absolute motion)
  ori = float, integer, * (current orientation ; valid for absolute motion)
  ang = float, integer, * (current orientation ; valid for absolute motion)
  speed = float, integer   [absolute value]
            (float, integer) + %   [relative value]

♦ Force control command : T.B.D.

♦ Gripper command : T.B.D.

3. Sensing

- Analog
    o Input
        ▪ PV temperature
        ▪ Motor temperature
        ▪ Motor current
        ▪ Depth/Pressure
    o Output
        ▪ Thruster command

    ain #*port_number*
    aout #*port_number, floating_value*

69

- Digital
  - input
    - Limit switch
    - Leakage sensor
  - Output
    - Weight release
    - light

  dio #*port_number*
  dout #*port_number*, *binary_value*

- Communication-based sensors
  - INS
  - Altimeters

➔ Also, it is possible to use ***internal state variable*** to read/write the data

4. Arithmetic Operations

- Basic Operations : **+, -, /, *, %, DIV**
- Trigonometric Functions : **sin, cos, tan, asin, acos, atan, hsin, hcos, htan**
- Etc : **sqrt, log, exp**
- Use ( ) to change operation priority

5. Logical Operations

- Byte-wire operations: and (&&), or (||), not (!)
- Bit-wise operations : and (&), or (|), not (~), ex-or (^)
- Comparisons : <, >, <=, >=, ==, !=

6. Flow Operations

- **IF** (*logical expression*)
  statements
  ELSE
  statements
ENDIF
- **DO**
  statements
  WHILE (*logical expression*)
- **WHILE** (*logical expression*)
  statements
ENDWHILE
- **FOR** (initialization; condition ;)
  statements
  ENDFOR
- **SWITCH** (values)

CASE values : statements
    BREAK
DEFAULT : *statements*
    BREAK
ENDSWITCH

7. File Operations

- Open/Close
    o **open.***file_number file_type filename*
    o **close.***file_number*
    o **close.*** → close all open files

    ex) open.1w data.dat → open *data.dat* for writing with file ID #1
        close.2 → close file ID #2
        close.* → close all files

- Read/Write data
    o **write.***file_number variables/IO_data* [**with period =** *time*]
    o **read.***file_number variables*

- File management
    o **type** *filename*
    o **dir [***filename***]**
    o **del** *filename*
    o **copy** *filename1 filename2*

8. ETC

- Define/Alias
    o **define** *name value*

- Change status of internal flags
    o **set** *flags* **ON/OFF**
    o **get** *flags*

    flags
        ▪ **stop_e**   : stop at error (default)
        ▪ **stop_w**   : stop at warning
        ▪ **verbose_e** : display error message (default)
        ▪ **verbose_w** : display warning message
        ▪ **coord_a** : absolute coordinate
        ▪ **coord_r** : relative coordinate
        ▪ **debug**   : display debug message (default : off)

- Set/get warning or error range of internal state variables
    o **set** *internal_state_variable* **warning/error at (** *lower limit***:** *upper limit* **)**
    o **get** *internal_state_variable*

internal_state_variable : pre-defined variable (see Variable)
lower limit, upper limit : integer, float

- **//** : remark

- **printf( )** : print out. Usage is same as C.

- **goto [*number*]**

- Variable
    - o Use the first character in the variable as an identifier of the variable type.
        - ▪ I*** : integer variable
        - ▪ F*** : floating variable
        - ▪ L*** : logic variable
        - ▪ J*** : joint variable
        - ▪ C*** : Cartesian variable

        Ex) I_var   = 34
             F_value = 34.56
             L_value = 1
             J_angle = (23.4, 32.34, 0.32, 78.3, 28.3, 39.5, 34.2)
             C_pos   = (10.2, 32.32, 45.3, 10.2, 1.23, 0.34)

    - o Use array with [ ]

    - o Pre-defined internal state variables

        ain_pv_temp   = ain#1
        ain_mot_temp   = ain#2
        ain_mot_cur   = ain#3
        ain_depth   = ain#4
        ain_battery   = ain#5

        aout_th_1 ~ 8   = aout#1 ~ 8
        ➔ **thruster_1~8**

        din_fin1_limit_h   = din#1
        din_fin1_limit_n   = din#2
        din_fin1_limit_l   = din#3

        for INS
                ins_bank, ins_elev[ation], ins_head[ing], ins_xv, ins_yv, ins_zv
        for Altimeter
                alti[meter]_1 ~ 4

    - o Pre-defined internal variables

speed.v = *value* [%]
speed.r = *value* [%]

- Wait or delay process
  - **delay *time***
    time : msec

- Save/Load program file
  - **save [*filename*]**
  - **load *filename***

- Start interpreter
  - **run [*filename*]**

Future Tasks (Phase II Tasks)

- Integration of higher-level control routine into existing software.
- Design and implementation of communication between navigation control system and manipulator control system.
- Actual water test with current software architecture.
- Refinement and debugging of software.
- Upgrade TDL to describe tasks easily.
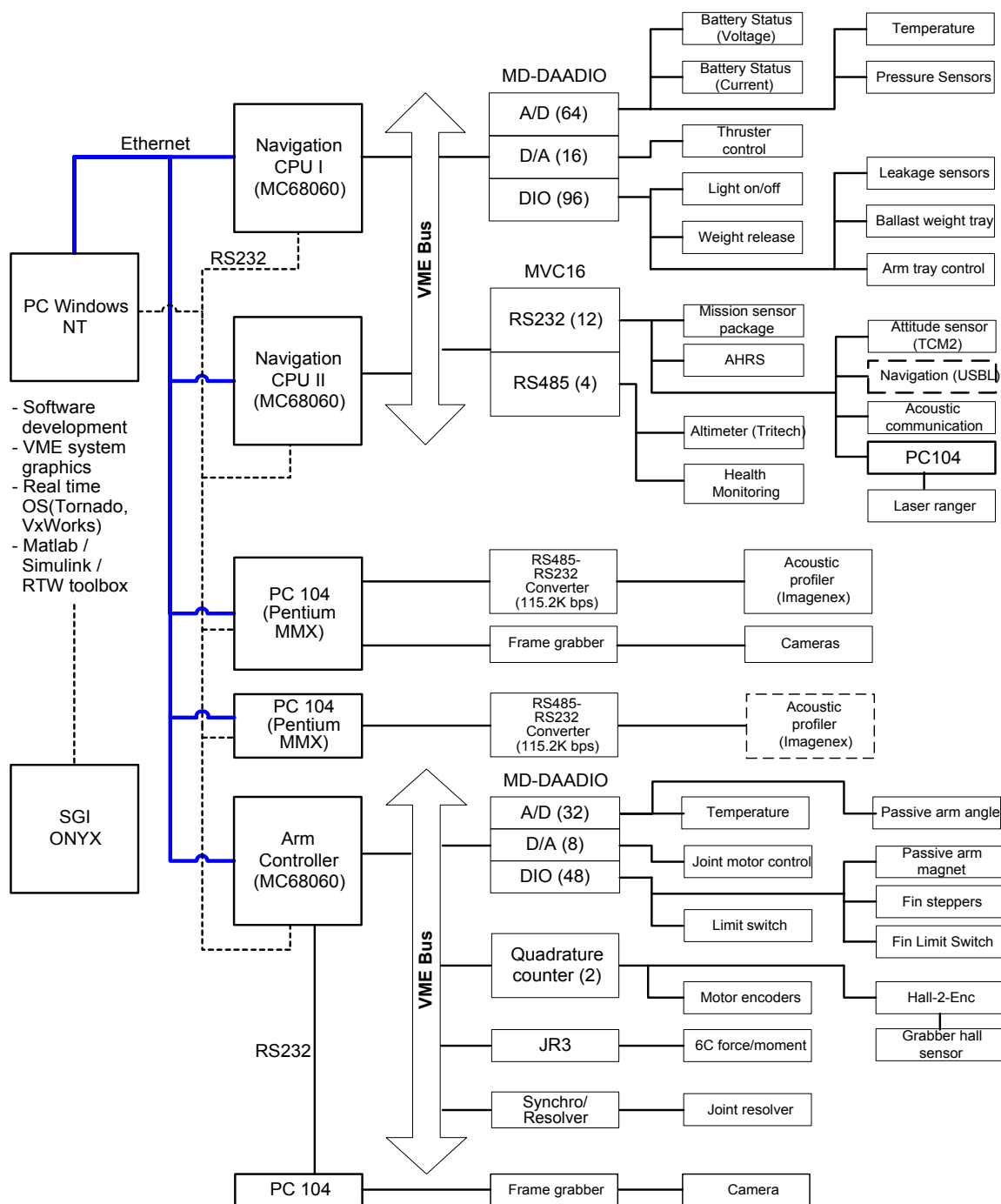
Figure RDC-1: System diagram of SAUVIM.
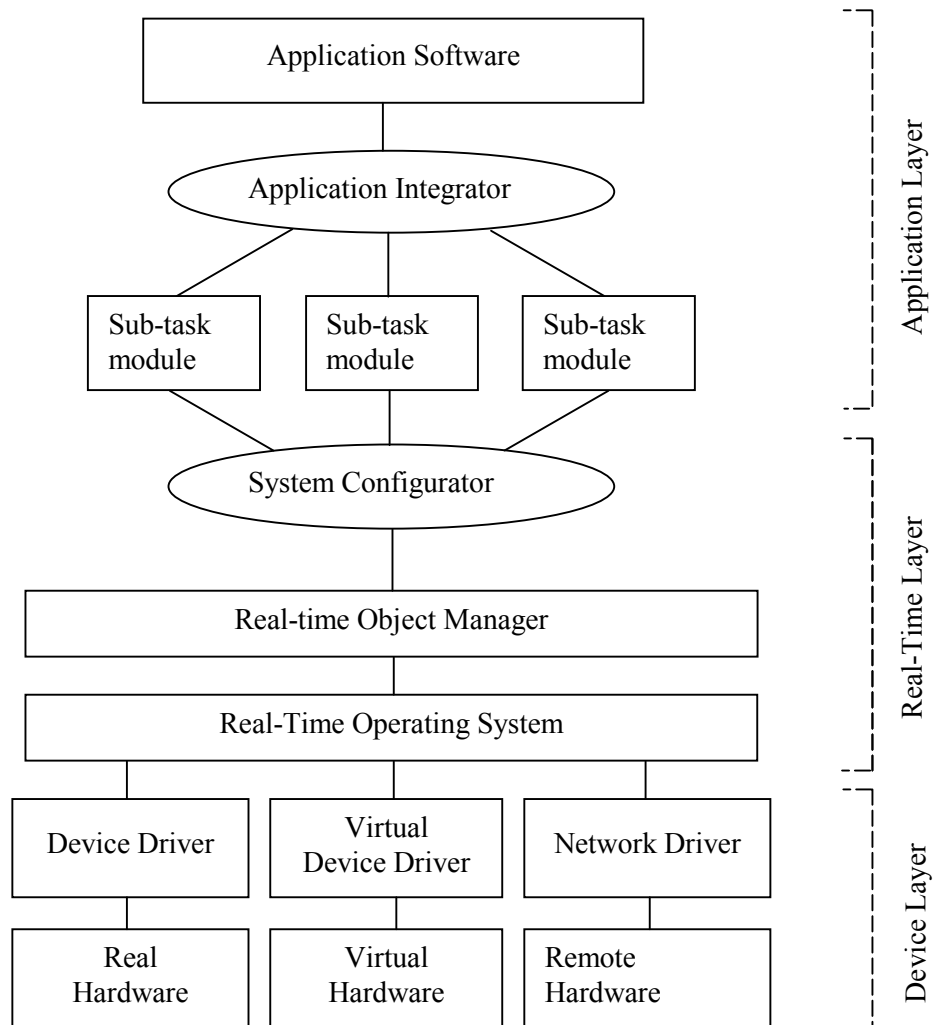
Figure RDC-2: Software hierarchy for SAUVIM controller

Second Navigation CPU   Primary Navigation CPU

```
┌─────────────────────────────────────────────┐    ┌──────────────────────┐
│  ┌───────────────────┐   ┌───────────────┐   │    │  ┌────────────────┐  │
│  │ Initialize Routine│   │ Task Manager  │   │    │  │Initialize Routine│ │
│  └───────────────────┘   └───────────────┘   │    │  └────────────────┘  │
│                                               │    │  ┌────────────────┐  │
│                                               │    │  │  Task Manager  │  │
│                                               │    │  └────────────────┘  │
│  ┌───────────────┐       ┌──────────────┐    │    │  ┌────────────────┐  │
│  │               │       │Shared Memory │    │VME │  │                │  │
│  │- Hardware     │ <===> │(Maintains all│<==Bus==> │  │ Higher Level   │  │
│  │  Device       │       │the data req..│    │    │  │ Routine (User  │  │
│  │  Drivers      │       │...)          │    │    │  │ Functions)     │  │
│  │- Data Handling│       │              │    │    │  │                │  │
│  │  Routines     │       │              │    │    │  │                │  │
│  └───────────────┘       └──────────────┘    │    │  └────────────────┘  │
└──────────│────────────────────────────────────┘   └──────────│───────────┘
           │ VME Bus                                            │
           │                  ┌────── Ethernet ─────────────────┤
           ▼                  ▼                                 ▼
  ┌───────────────┐   ┌───────────────┐           ┌──────────────┐
  │ AD/DA/DIO     │   │   Console     │           │              │
  │ Board         │   │for Human      │           │   Arm CPU    │
  │ Multi Serial  │   │Operator       │           │              │
  │ Communication │   │(Windows       │           │              │
  │ Board         │   │program)       │           │              │
  └───────────────┘   └───────────────┘           └──────────────┘
```

Figure RDC-3: Software architecture of the navigation control system.

Table RDC-1. Specification of AHRS-BA303

Item	Range	Accuracy	Sensitivity	Remarks
Pitch rate	±100°/s	Static: ±0.2°/s Dynamic: ±2% digital ±6% analog	10 °/s/V	Positive for nose up
Roll rate	±100°/s			Positive for roll to right
Yaw rate	±100°/s			Positive for right turn
Heading rate	±100°/s			Positive for right turn
Bank	±180°	Static: ±0.5°/s Dynamic: ±2%	18 °/V	Positive for bank to right
Elevation	±90°			Positive for nose up
South heading	0 - 360°	Static: ±1°/s Dynamic: ±2%		S=0V, E=-5V, W=5V, N=±10V
North heading	0 - 360°			N=0V, E=5V, W=-5V, S=±10V
Velocity input	-400 – 400 Km/hr		40 Km/hr/V	Forward velocity
Error correction time		15 seconds		

Table RDC-2. Specification of Tritech PA200

Frequency and beam width	200 kHz and 20 degrees
Measurement range	100 meters
Operating depth	6800 meters
Input voltage	12 VDC
Interface	RS-485, 9600 bps, 8 data bits, 1 stop bit, no parity
Head RS-485 Termination	220 Ω (Sensor A only)
Command	*, or 'A', 'B', 'C', 'D', 'E', 'F', 'G'

Table RDC-3. Specification of Precision Navigation TCM2

Heading information	Accuracy when level	±0.5° RMS
	Accuracy when tilted	±1° RMS
	Resolution	0.1°
	Repeatability	±0.1°
Tilt information	Accuracy	±0.2°
	Resolution	0.1°
	Repeatability	±0.2°
	Range	±20°
Magnetic field information	Accuracy	±0.2 μT
	Resolution	0.01 μT
	Repeatability	±0.2 μT
	Range	±80 μT
Temperature information (sensor is un-calibrated)	Accuracy after calibration	±1°C, ±2°F
	Resolution	1°C, 2°F
	Range	-20°C to 70°C
Power requirement	Supply voltage	+5 VDC regulated 6 to 18 VDC unregulated
	Current	Standard mode: 15-20 mA Low-power mode: 7-13 mA Sleep mode: 2.5 mA
Interface	Digital	RS-232C, NMEA0183
	Analog	0-5V linear, 19.53 mV resolution (256 discrete levels), 0-5 Quadrature (sine and cosine)

Table RDC-4. Specification of Imagenex 881

Frequency	675 kHz
Transducer	Imaging/profiling
Power supply	22 – 48 VDC at 1 Amp max.
Interface	RS-485 (115200 bps, 8 data bits, 1 stop bit, no parity)
Operating range	5 – 200 meters 15 – 600 feet Default: 50m (150ft)
Sector size	Scan with angle Sector mode: 0 to 180° in 3° increments. Default: 180° Polar mode: 0 to 360° in 3° increments Default: 360°
Speed	Step size angle Slow: 0.3°/step Med: 0.6°/step Fast: 0.9°/step Faster: 1.2°/step Fastest: 2.4°/step Default: fast
Transmit pulse length	0 to 255 μs in 5 μs increments

Mission Package Sensors (MSP)

Project Leaders: Dr. Gary M. McMurtry
Personnel:　　　Mr. Yann Douyere

Objectives

The SAUVIM Mission Sensor Package for Phase 1 is designed to provide semi-continuous records of AUV water depth (pressure), water temperature, conductivity, computed salinity, dissolved oxygen, pH and turbidity for at least eight hours. These parameters as well as the magnetic signature of the seafloor can be acquired by the SAUVIM in survey mode. In intervention mode, the Mission Sensor Package will provide AUV water depth (pressure) and the water temperature and compositional parameters at a selected seafloor target, including pumped samples from submarine seeps or vents.

Current Status (Tasks Completed During 8/1/97 – 10/30/00):

The system-wiring layout is presented in Figure MSP-1. A CAD drawing of the package is also available. Ambient seawater or submarine vent/seep waters will enter the Teflon sensor plenum through a short length of Teflon tubing, which will contain a tributal tin marine anti-foulant. The Teflon entry nozzle will be screened and will face the forward direction of the AUV, allowing waters to passively enter the sensor housing when the AUV is running or to be pumped across the sensors when the AUV is station keeping. Otherwise, the Sea Bird Electronics impeller pump will remain off to conserve power. The Ocean Sensors model OS 200 CTD is a small, compact and low power instrument used to acquire data in remote oceanic; the sensor head is 2.25 inches in diameter (OD) and will house the conductivity cell, thermistor temperature probe, pressure, pH and dissolved oxygen sensors. The ranges for the sensors are: pressure, 0 - 6000 dBARS; temperature, -2 - 100° C; conductivity, 0.5 - 65 mS/cm; salinity (computed), 2 - 42 PSU; pH, 0 - 14 pH units; dissolved oxygen, 0 - 15 ml/l. All sensors are rated to 6000 meters.

The Ocean Sensors OS-200 CTD electronics have been custom modified to slave to our CPU (via RS-232 link) and allow up to eight additional analog inputs. Additional space within the command or CPU housing will be set aside for future sensor additions. The Sea Tech Light Back-Scattering Sensor (LBSS) will the measuring by a high-gain (to 33mg/l) the particle concentrations or turbidity levels in the surrounding. The LBSS or nephelometer will be externally mounted to the AUV so that its frame will not obstruct the light emitting diodes during its time of operation.

The PC/104 CPU module, manufactured by AMPRO computer Inc, provides for a 25 MHz 386SX processing power in a compact, pre-configured subsystem module. The CPU card is interfaced with a serial communication card that offers two independent RS-232 serial ports, which are used to converse directly with the OS-200 CTD and the magnetometer. A number of C-based programming files were created to open or close the ports when necessary. All the information that is extracted from the sensors is directly saved within the hard drive so that they can be extracted and analyzed.

The magnetic signature of the seafloor will be measured with an Applied Physics Systems model 544 Micro Angular Orientation Sensor. The unit contains both a 3-axis fluxgate magnetometer and a 3-axis accelerometer. These sensors are sampled by an internal ADC and microprocessor subsystem, which outputs 16-bit digital data representing the magnetometer and accelerometer readings via an RS-232 cable to the CPU. Ideally, to minimize the AUV magnetic background, this small (0.75" x

0.75" x 4.6") sensor should be placed as far away from magnetic-field generating devices (e.g., motors, spinning propellers, circuit boards, hard disks) as practicable. To date, we plan placement of this sensor in the nose faring of the AUV. The angular orientation sensor is housed within a 1-inch OD cylindrical pressure vessel (6000-m capable) made low-Fe grade-2 titanium.

For a 6000-m depth capability, we have constructed a 7071-grade titanium pressure housing for the external power supply, Intel 386-based CPU and associated electronics, and the internal battery. Currently, we use a PC/104 card stack for the CPU and serial I/O, and a 128 MB Quantum IDE hard drive for program and data storage. System power will be provided at 12 VDC via a DC-DC converter from 24VDC rechargeable lead-acid batteries within the main body of the AUV. The external power is supplemented by a small rechargeable sealed 12VDC lead-acid battery within the pressure housing that can also act as an uninterruptible power supply (UPS) in case of external power failure. Communications (system command uploads and downloads data) to the surface and other AUV CPUs will be via RS-232 link. We plan to mount the CTD and CPU housings of the mission sensor package within the AUV forward of the battery pods and high enough above the skids to minimize damage on the seafloor. The magnetometer will reside within the faring of the AUV body as far forward as possible to isolate it from the motors.   The nephelometer will point down immediately below the CTD and CPU housings. When station keeping, the AUV manipulator will be able to pull the nozzle out toward any vent or seep for better sampling.

Future Tasks (Phase II Tasks)

We will be looking forward to replace the existing Quantum hard disk drive with a new flash disk drive with a capacity of 64MB. The flash disk is based upon flash technology and is intensive to tremors, vibrations, fluctuations in temperature and magnetic fields, making it an ideal and reliable components in our future missions.

We will have to run bench-top demonstration of the existing hardware and software in order to see the overall performance of the system. The system will be running off the lead acid battery in order to measure the running time of the equipment and to calculate more precisely the energy budget for the MSP. Once all of the above will be accomplished and upon satisfaction of the obtained data, the CTD and the remaining sensors (i.e. nephelometer, magnetometer, etc.) and utility instruments (pump) will be calibrated and tested in shallow water. We are planning to gather information off the computer and create an interface using LabView in order to visualize the sensor outputs.

The next part of the project, will be the to interface with the other project team members to begin system integration with SAUVIM. We are ultimately planning to be linked to the SAUVIM computer via a RS-232 data connection in order to send, receive and compare multiple sensor data. This link is extremely critical in our mission due to data exchange. Furthermore, we will need to tap our equipment to a 24VDC power supply in order to get power feed during the mission. Should any power problem occur, our back up battery, located within the pressure housing will feed our equipment without power interruption.
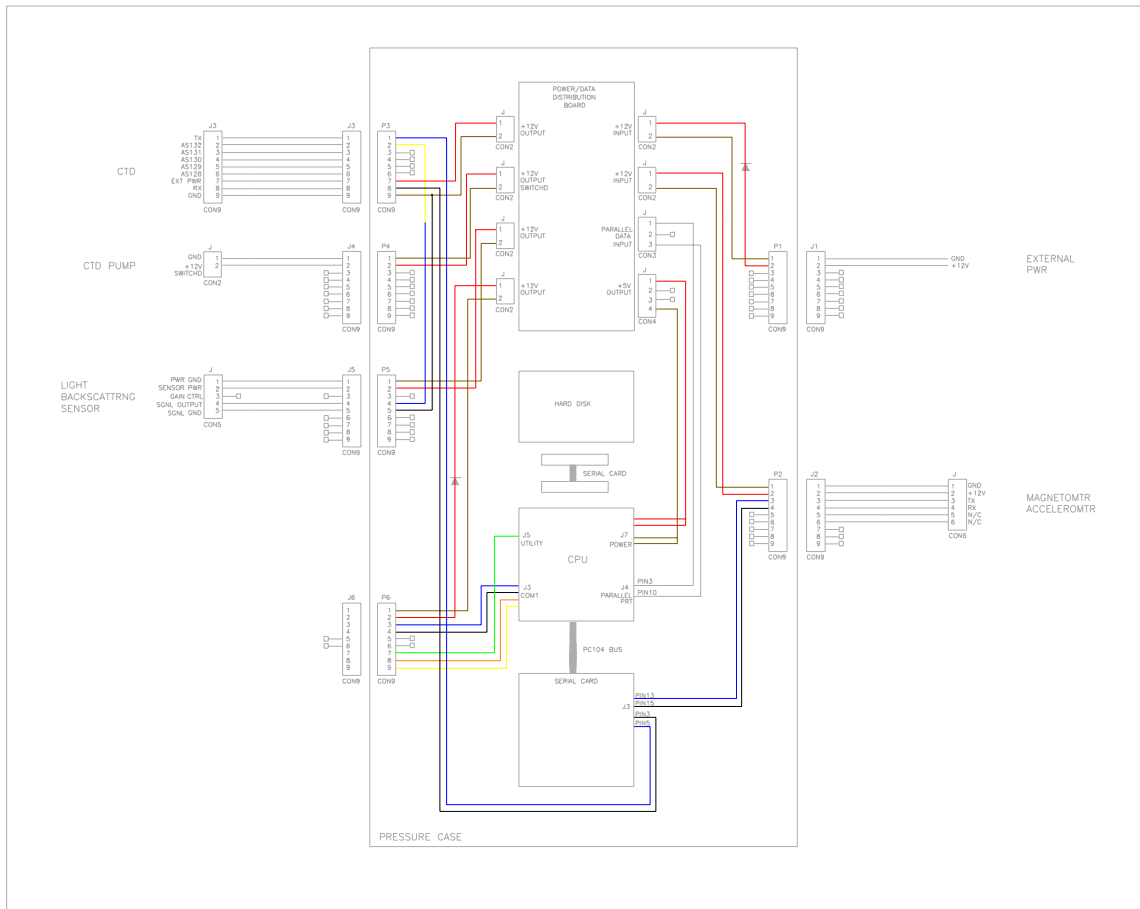
Figure MSP-1: MSP Configuration and Wiring Diagram

Hydrodynamic Drag Coefficient Analysis (HDCA)

Project Leader: Dr. Junku Yuh & Dr. Song K. Choi
Personnel: Mr. Brian Lau & Mr. Oliver Easterday

Objectives

- Determination of the hydrodynamic coefficient via numerical solution of full Navier-Stokes equations using commercial CFD code, PHOENICS.
- Provide design recommendations for the vehicle fairing from the hydrodynamic results.
- Perform experiments to verify and confirm the CFD results.

Current Status (Tasks Completed During 8/1/97 – 10/30/00):

The CHAM PHOENICS software generated various hardware and software errors when an attempt was made to numerically obtain a reasonable drag number for a known object. Further testing of the software will have to be conducted to confirm and verify other standardized numerical results with empirical data in references.

However, using standardized methods to calculate the coefficient of drag (C_d) of an object or a vehicle, the formula,

$$C_d = F/0.5*\rho*A*V^2,$$

where F is the force in the direction of the flow direction being tested, ρ is the fluid density, A is the frontal area of an object or vehicle, and V is the fluid velocity was used. For the SAUVIM, a coarse grid of *10x10x10* as provided by CHAM was used, and setting ρ as 998 kg/m^3, V = 3m/s, and SAUVIM frontal area of 10 m^2, the software generated a drag coefficient of 0.40.

Future Tasks (Phase II Tasks)

- Fabricate SAUVIM model for testing.
- Compare CFD results to actual test data.
- Correct and modify CFD codes for future use.

Mechanical Analysis and Fabrication (MAF) Group

Project Leader: Dr. Mehrdad Ghasemi Nejhad
Personnels: Dr. Ali Yousefpour, Mr. Robert Ng, Mr. Mark Uyema, Mr. Saeid Pourjalali, Ms. Melanie Yamauchi & Mr. Reid Takamiya

Objectives

Mechanical Analysis and Fabrication (MAF) group is responsible for designing, analyzing, manufacturing, and testing of pressure vessels and flooded fairing as well as analyzing the metallic frame of the vehicle.

Current Status (Tasks Completed During 8/1/97 – 10/30/00):

1. DESIGN AND ANALYSIS OF PRESSURE VESSEL

To design the pressure vessels for the SAUVIM project various finite element analyses for different modes of failure have to be performed. The structure is mainly analyzed for stress and buckling mode of failure. Design constraints of the pressure vessels are: an effective length of 18", an inner diameter of 13", and a design pressure of 8,976 psi, which corresponds to 20,013 feet (6,100 meters) depth. It should be noted that the operating depth of the vehicle is 19,685 feet (6,000 meters), which corresponds to a pressure of 8,840 psi. Figure MAF-1 shows the development methodology for the pressure vessels employed herein. Two modes of failure are considered, and they are i) stress and ii) buckling analyses taking hygrothermal effects into account. Ti-6Al-4V, Graphite/Epoxy, and APC-2/AS4 are three candidate materials for the pressure vessels. The results of the analyses reveal the most desirable material and required thickness of the pressure vessels. Next, end-caps are designed. Then, detailed analysis of the pressure vessels and the end-caps are performed. Finally, the pressure vessel and end-caps are fabricated and tested.

1.1. Candidate Materials and Material Properties

Ti-6Al-4V, Graphite/Epoxy, and APC-2/AS4 are three candidate materials for the pressure vessels. Ti-6Al-4V is a popular material for manufacturing pressure vessels for underwater vehicles. It is a lightweight material, and due to its excellent corrosion resistance, it is the best metallic material for marine structures. Ti-6Al-4V has a relatively high strength-to-weight ratio, good high-temperature properties, and high mechanical performance (Askeland84). Table MAF-1 gives the mechanical properties of Ti-6Al-4V.

APC-2/AS4 thermoplastic composite and Graphite/Epoxy thermo set composite are the two candidate composite materials. Both of these materials have high specific properties, good corrosion resistance, and low density. Table MAF-2 gives unidirectional mechanical properties for these materials (ICI Thermoplastic Composite92, Mallick93).

1.2. Analysis Procedure

Figure MAF-2 shows the analysis procedure for designing a pressure vessel. Stress and buckling analyses taking hygrothermal (i.e., moisture and temperature) and end-cap effects into account are performed to achieve an optimum wall thickness for the pressure vessel. The following explains the analysis procedure flowchart in Figure MAF-2. Stress analysis is used for the structure to determine the required wall thickness for the pressure vessel according to the design constraints at room temperature, 70°F. A stress factor of safety of around two is required. Von Mises failure criterion is considered for the metallic pressure vessel. For the composite pressure vessel, Maximum Principal Stress criterion is considered. The stress analysis is also preformed considering thermal effects, i.e., extreme temperatures of 32°F and 140°F, for the metallic pressure vessel. The hygrothermal effects, i.e., extreme temperatures of 32°F and 140°F as well as the maximum moisture absorption, are considered for the stress analysis of composite pressure vessels. In the case of the metallic pressure vessel, the moisture effect is zero. Next, non-linear buckling analysis is performed considering hygrothermal and end-cap effects to investigate the stability of the pressure vessel under the design constraints. To perform the non-linear buckling analysis, an eigenvalue buckling analysis is first employed to determine the first buckling mode shape and bifurcation pressure of the pressure vessel. These results are then used in the non-linear buckling analysis. Buckling factor of safety of at least two is required for the pressure vessel. Finally, the non-linear stress analysis considering hygrothermal and end-cap effects are also performed to investigate the linear nature of the problem.

1.2.1. Hygrothermal Effects

The effects of temperature and moisture (hygrothermal) were considered in the design of the pressure vessels. Two extreme cases were considered. For the metallic pressure vessel, the extreme temperatures were a) 32°F and b) 140°F and the moisture effect was zero. For the composite pressure vessel, in addition to the thermal effect, the effect of moisture absorption was also considered. Coefficient of Moisture Expansion (CME) is not an input material property for a composite material in ANSYS finite element software. To apply the effect of moisture absorption, the CME was modeled as an equivalent Coefficient of Thermal Expansion, CTE, and is introduced here as the Moisture Equivalent Coefficient of Thermal Expansion, MECTE.

1.2.2. Moisture Equivalent Coefficient of Thermal Expansion, MECTE

The MECTE was evaluated and then combined with the CTE of the composite material to give a Modified Coefficient of Thermal Expansions (MCTE), which was used in the analysis. The hygrothermal effects in principal directions are dilatational and can be shown by the following equation:

$$\varepsilon_i = \alpha_i \Delta T + \beta_i \Delta m \quad (i=1, 2, 3) \tag{1}$$

where

       ε_i= Strain due to hygrothermal effects
       α_i= Coefficient of thermal expansion , CTE
       β_i= Coefficient of moisture expansion, CME
       ΔT= Change of temperature
       Δm= Change in percentage weight

It can be assumed that the ε_i is equal to the MCTE, $\overline{\alpha}_i$, times ΔT (see Equation 2):

$$\varepsilon_i = \overline{\alpha}_i \Delta T = \alpha_i \Delta T + \beta_i \Delta m \qquad (i=1, 2, 3) \qquad\qquad (2)$$

By dividing Equation 2 by ΔT, the MCTE, which also includes the effect of moisture absorption, MECTE, can be obtained as,

$$\overline{\alpha}_i = \alpha_i + \beta_i \frac{\Delta m}{\Delta T} \qquad (i=1, 2, 3) \qquad\qquad (3)$$

The MCTE for the extreme temperatures and maximum moisture absorption were determined using Equation 3. In Equation 3, the LHS is MCTE, the first term on the RHS is CTE, and the second term on the RHS is MECTE. The maximum value for Δm is 0.23% for APC-2 (thermoplastic resin) and 5% for Epoxy (thermo set resin) (ICI Thermoplastic Composite92, Mallick93). α_i and β_i for the APC-2/AS4 and Graphite/Epoxy are given in Table MAF-2 (ICI Thermoplastic Composite92, Mallick93). Table MAF-3 gives the MCTE at 140°F and 32°F, for both composite systems.

1.3. Stress Analysis

Finite Element Analysis (FEA) was performed to determine the required thickness of the pressure vessel. Due to the axi-symmetric geometry, material properties, loading, and boundary conditions, ten degrees wedge of the pressure vessel was modeled (see Figure MAF-3). Modeling wedge section of the pressure vessel reduces the computational time and memory requirements significantly. A cylindrical coordinate system was used with its origin at the center of the pressure vessel and X≡R, Y≡θ, and Z≡Z. Axi-symmetric boundary conditions were applied at Y=0° and Y=10° planes, a symmetric boundary condition was applied at the Z=0 plane (see Figure MAF-3). Hydrostatic pressure was applied. Also, the end-cap was simulated as radial simply supported boundary and axial hydrostatic pressure load conditions at the other end of the model.

1.3.1. Effects of End-cap

A contoured-end plug-supported end-cap was considered for the pressure vessel. A large radius circular taper, R, is incorporated into the end-cap to control both bending and shear stresses near the cylinder ends (see Figure MAF-4). The cylinder ends can conform to the circular tapered section as pressure increases which reduces the stress concentration at the ends and enhances the performance of the pressure vessel (Leon95; Yousefpour00a).

The contoured-end plug-supported end-cap was modeled as radial displacements at the cylinder end. A parametric study was performed to determine the optimum radius circular taper, R, based on the stress factor of safety (Yousefpour00a). The length of the tapered section was also optimized and found to be 1.5". This length was also required to place two radial O-rings for sealing purposes. To calculate 'R', an edge simply supported pressure vessel with 21" in length was modeled and analyzed under a hydrostatic (i.e., radial and axial) design pressure of up to 10,300 psi corresponding to 7,000 meters depth. Table MAF-4 gives the selected thickness for the pressure vessels, which were determined by trial-and-error based on a factor of safety of around 2. The radial displacement, d, at 1.5" from the cylinder end was determined (see Figure MAF-4). Figures MAF-5, MAF-6, and MAF-7 show the radial displacements from the end to the mid-length of the 21" long Ti-6Al-4V, APC-2/AS4, and Graphite/Epoxy cylinders with edge simply supported boundary condition, respectively.

86

Table MAF-4 also gives the selected thickness and the corresponding 'd' values for the candidate materials.

Although the maximum deflections of all pressure vessels, at the mid-length (see Figures MAF-5, MAF-6, and MAF-7), were close, however the 'd' and thickness values for the Ti-6Al-4V were smaller than those for the composite pressure vessels. This is believed to be due to a higher flexural rigidity of the Ti-6Al-4V pressure vessel. $D_{zz}=3.041 \times 10^6$ lb-in for the composite and $D_{zz}=Eh^3/12(1-\nu^2)=3.7 \times 10^6$ lb-in for Ti-6Al-4V, in this case. Simple trigonometry was applied to calculate 'R' for the given 'd'. For parametric analysis, different percentages of 'd' were considered and corresponding R's were calculated and applied to the finite element model as radial displacement boundary conditions. The curve of the end-plug is part of a circle with radius R. Figure MAF-8 shows the end-cap and its plug circle with radius R. Assume the X-Y coordinate system at the center of the circle. The equation of circle can be written as:

$$X^2 + Y^2 = R^2 \qquad\qquad (4)$$

Since X=a and Y=R-d is a point on the circle, Equation 4 can be written as:

$$a^2 + (R-d)^2 = R^2 \qquad\qquad (5)$$

After simplifying Equation 5, the radius R can be obtained from the following equation:

$$R = \frac{a^2 + d^2}{2d} \qquad\qquad (6)$$

It should be noted that 'a' is equal to 1.5" and 'd' is radial displacement at 1.5" from the cylinder end. Table MAF-5 gives the radius of the end-cap circular taper, R, for different percentages of 'd' for the candidate materials. Zero percentage of 'd' means no tapered on the end-cap. Von Mises failure criterion was considered for metallic pressure vessel (Shigley89). For the composite pressure vessel, Maximum Principal Stress criterion was considered (Vinson87; Mallick93). Figures MAF-9, MAF-10 and MAF-11 show the stress factor of safety of the pressure vessels as a function of the different percentages of 'd' for the candidate materials. The results revealed an optimum 'R' for each pressure vessel. Maximum factor of safety of 1.96 was obtained for Ti-6Al-4V pressure vessel at the circular tapered radius of 420", which corresponds to 20% 'd' value (see Table MAF-5). For the APC-2/AS4 and AS4/Epoxy the maximum factor of safety was 1.96 (R= 131" and d=40%) and 1.90 (R= 135" and d=40%), respectively. The results clearly show that the optimum radius circular taper, R, which is incorporated into the end-caps, increases the performance of the pressure vessel, when the optimum percentage of 'd' value is selected.

1.3.2. Stress Analysis of Ti-6Al-4V Pressure Vessel

Table MAF-6 presents the results of stress analyses for the Ti-6Al-4V pressure vessel with the optimum R, 420", and wall thickness of 1.35" at 32°F, 70°F, and 140°F under a design pressure of 10,300 psi. Desired stress factor of safety was achieved for each case. The results revealed that the thermal effects did not cause significant effects on the performance of the pressure vessel. The maximum Von Mises stress and strain occur at the end-cap and maximum deflection happens at the mid-length for different temperatures (see Table MAF-6).

Figures MAF-12 and MAF-13 show the strain and stress distributions through the thickness at the mid-length of the Ti-6Al-4V pressure vessel at 70°F, respectively. The results of stress had the same trend as the verification model for the metallic pressure vessel. Both axial and hoop strain were compressive however the radial strain was tensile although the whole structure was under hydrostatic pressure (see Figure MAF-12). This was due to the axial pressure and Poisson's ratio effects. Compressive axial, hoop, and radial stresses should cause compressive axial, hoop, and radial strains. However, the compressive radial strain, due to compressive radial stress (see Figure MAF-12), was smaller than axial pressure and Poisson's ratio effects. The results would be the extensional radial strain through the thickness at the mid-length of the pressure vessel. It should also be mentioned that radial stress satisfies the radial stress boundary conditions at the inner (zero stress) and outer (external pressure) radii.

1.3.3. Stress Analysis of Composite Pressure Vessels

A symmetric sub-laminate configuration of $[90/90/0/0/90/90]_s$ was chosen for the composite pressure vessels. The symmetric cross-ply lay-up configuration for the composite pressure vessels eliminates extension-bending, extension-shear, and bending-twisting couplings in the structure. The 2:1 hoop-to-axial ply ratio is chosen since the theoretical hoop stress for metallic pressure vessel is twice of the axial stress (Hyer, 1989).

Table MAF-7 gives the stress analysis results for APC-2/AS4 and Graphite/Epoxy pressure vessels considering hygrothermal effects. Modified Coefficient of Thermal Expansion (MCTE) was used for 32°F and 140°F cases with the maximum moisture effect (see Table MAF-3). The results revealed that the hygrothermal effects did not cause significant difference on the performance of the APC-2/AS4 pressure vessel. However, the hygrothermal effects were severe on the performance of the Graphite/Epoxy. This was due to the high moisture absorption of the Epoxy in the water, i.e., $\Delta m=5\%$. The maximum radial and axial stresses and strains occur at the end-cap of the pressure vessel. The maximum hoop stress and strain happen at the mid-length of the composite pressure vessels. The maximum displacement occurs in the axial direction of the composite pressure vessels. These locations were the same at different temperatures.

Figures MAF-14, MAF-15, MAF-16, and MAF-17 show the strain and hoop, axial, and radial stress distributions through the thickness at the mid-length of the APC-2/AS4 pressure vessel under a design pressure of 10,300 psi, respectively. The results had the same trend as Hyer's solution (Hyer88; Yousefpour00a). It should be noted that the radial strain was tensile at the inner radius and became compressive at the outer radius (see Figure MAF-14). However, the radial strain was tensile for the metallic pressure vessel through the thickness (see Figure MAF-12). For the same reason that explained for the metallic pressure vessel, the radial strain was tensile close to the inner radius. However, the compressive radial strain, due to the hydrostatic pressure, overcomes the Poisson's ratio effect close to the outer radius. This resulted in the compressive radial strain close to the outer radius. The discontinuity of the radial strain was due to the layer interfaces and element boundaries (see Figure MAF-14). In the hoop direction, fibers in 90-degree layers took most of the loads and 0-degree fibers carried less loads (see Figure MAF-15), and in the axial direction, fibers in 0-degree layers took most of the load and 90-degree fibers carried less loads (see Figure MAF-16). It should be noted that the right choice of 2:1 fibers in the hoop direction resulted in an efficient structure where all fibers in hoop (90° layers in Figure MAF-15) and axial (0° layers in Figure MAF-16) directions carry equivalent loads, unlike a metallic structure where stress in hoop direction is twice of that in axial direction. Radial stresses also satisfy radial stress boundary conditions. Stress discontinuities, which are due to the lay-up configuration, are clearly observed in Figures MAF-15,

MAF-16, and MAF-17. Figures MAF-18, MAF-19, MAF-20, and MAF-21 show the strain and stress distributions of the Graphite/Epoxy composite pressure vessel. Similar trend as APC-2/AS4 pressure vessel was observed for the Graphite/Epoxy pressure vessel. Mesh convergence study was performed for all stress analyses with a convergence criterion of 5%.

1.4. Buckling Analysis

Buckling phenomenon occurs in a pressure vessel under a hydrostatic pressure when most of its strain energy, which is stored as membrane energy can be converted to the bending energy (Bushnell85), which requires large deflections. Two types of buckling analyses: a) bifurcation buckling or eigenvalue buckling analysis and b) non-linear buckling analysis were performed in this work.

1.4.1. Eigenvalue Buckling Analysis

In the eigenvalue buckling analysis, the theoretical buckling pressure for an ideal linear elastic structure is calculated. At the eigenvalue buckling pressure (the bifurcation pressure), the deformation starts to follow a new pattern on the load-deflection curve, which is different from the pre-buckling pattern (Bushnell85).

The finite element eigenvalue buckling analysis of the metallic and composite pressure vessels were performed using ANSYS, 1999. The wall thicknesses of the metallic and composite pressure vessels were the same as those were determined in the stress analyses. Figure MAF-22 shows a typical first buckling mode shape of the Ti-6Al-4V pressure vessel. A typical first buckling mode shape of the composite pressure vessels, i.e., APC-2/AS4 and Graphite/Epoxy, is shown in Figure MAF-23.

Due to the axi-symmetric geometry, material properties, loading, and boundary conditions, one-sixth and one-fourth (to include the snap-through portion within the model) of the metallic and composite pressure vessels were modeled and are given in Figures MAF-24 and MAF-25, respectively. A cylindrical coordinate system was used with its origin at the center of the pressure vessel and $X \equiv R$, $Y \equiv \theta$, and $Z \equiv Z$. Axi-symmetric boundary conditions were applied at the Y=0º and Y=120º planes and symmetric boundary condition was applied at the Z=0 plane for the Ti-6Al-4V pressure vessel (see Figure MAF-24). For the composite pressure vessels, axi-symmetric boundary conditions were applied at the Y=0º and Y=180º planes and symmetric boundary condition was applied at the Z=0 plane (see Figure MAF-25). The effect of the end-cap was modeled as radial plug simply supported boundary condition at the other end (see Figure MAF-24 and Figure MAF-25). Figures MAF-26 and MAF-27 show the typical first modal shape of one-sixth and one-fourth of the Ti-6Al-4V and composite pressure vessels under external radial pressure, respectively. Table MAF-8 gives the bifurcation pressure of the pressure vessels with pre-determined thicknesses that were obtained from the stress analyses. The bifurcation pressure of the pressure vessels was considerably higher than a design pressure of 10,300 psi.

1.4.2. Non-Linear Buckling Analysis

Non-linear buckling pressure can be evaluated using non-linear stress analysis by observing the first change in the slope (i.e., stiffness of the structure) in the load-deflection curve (Bushnell85). The wall thickness of the pressure vessels that were calculated in the stress analyses was used in non-linear buckling analysis. Also, same optimized tapered end-cap boundary conditions established in

the stress analysis was used in this section. To employ the non-linear buckling analysis small out-of-plane perturbations were applied to the model (geometric imperfections) to make the structure unstable as the pressure increases. The perturbations can be small out-of-plane forces, or specified displacements (see Figures MAF-24 and MAF-25). The mode shape obtained from the eigenvalue buckling analysis was used to predict the location and magnitude of the perturbations to stimulate the desired buckling response (see Figures MAF-26 and MAF-27). The non-linear buckling analysis was performed for Ti-6Al-4V, APC-2/AS4, and Graphite/Epoxy taking hygrothermal and end-cap effects into account, and was found that all three materials had a minimum buckling factor of safety of 3.6. The end-cap was modeled as radial tapered simply supported (for the circular tapered plug portion) and axial external pressure under a hydrostatic pressure.

1.5. Non-Linear Stress Analysis

Non-linear stress analysis was applied to the pressure vessel models that were developed from linear stress analysis to investigate the linear behavior of the structure. The results of the non-linear stress analyses for the Ti-6Al-4V pressure vessel is given in Table MAF-9. Table MAF-6 gives linear stress analysis results. The results are identical. Table MAF-10 gives the results on the non-linear stress analysis for the composite pressure vessels. Table MAF-7 gives linear stress analysis results. The results were in good agreement. Generally, the non-linear stress analysis results revealed the linear nature of the stress problem.

1.6. Hygrothermal Effects on the Pressure versus Radial Displacement

Typical pressure vs. radial displacement curve at the mid-length of Ti-6Al-4V, APC-2/AS4, and Graphite/Epoxy pressure vessels taking hygrothermal and end-cap effects into account are shown in Figures MAF-28, MAF-29, and MAF-30, respectively. It can be observed that the thermal effects did not cause significant difference on the performance of the metallic pressure vessel. The thermal effects just shifted the stability curve parallel to the room temperature (70°) stability curve either upward (for 140°F) or downward (for 32°F) (see Figure MAF-28). These results were also true for the APC-2/AS4 pressure vessel. However, hygrothermal effects in the APC-2/AS4 pressure vessel were less than thermal effects in the metallic pressure vessel. At a given pressure, the radial displacement is lower for higher temperature since the effect of higher moisture and temperature in the radial direction is the opposite of the hydrostatic pressure. The hygrothermal effects were more sever in the Graphite/Epoxy pressure vessel. This was due to high moisture absorption, $\Delta m = 5\%$, of the Epoxy resin (see Figure MAF-30).

1.7. Material Selection

APC-2/AS4 was chosen as the material for the pressure vessel. This material has following characteristics: i) high strength and stiffness, ii) low coefficient of moisture absorption, iii) excellent corrosion and solvent resistant, iv) good thermal conductivity in fiber direction, v) low density, vi) high fracture toughness, vii) high damage tolerance, viii) high impact resistant, ix) good fatigue resistance, x) recyclable, xi) reprocessable, xii) repairable, xiii) reshapable, xiv) reformable, and xv) ease of fabrication (ICI Thermoplastic Composite, 1992). In addition, the extra damping and lower electromagnetic observable inherent in the APC-2/AS4 further enhance its performance (ICI Thermoplastic Composite, 1992). These feature are desirable in order to decrease the weight of the vehicle, increase the speed and operating depth, and increase the serviceability and survivability of the vehicle, and provide a safe operation. The comparison of the APC-2/AS4 and Ti-6Al-4V pressure vessels shows that although the wall thickness of the APC-2/AS4 pressure vessel is greater

than Ti-6Al-4V but its density is almost three times less than that for Ti-6Al-4V (see Table MAF-11). The dry weight of APC-2/AS4 pressure hull is 91 lbs and that for Ti-6Al-4V pressure hull is 204 lbs. This result shows that the APC-2/AS4 pressure hull is 2.24 times lighter than Ti-6Al-4V pressure hull. In the water, disregarding the weight of the end-caps (which would be the same for both), the APC-2/AS4 composite pressure hull is weight-less and has the buoyancy force (upward) of 58 lbs. However, the Ti-6Al-4V pressure hull wet weight (downward) in the water is 69 lbs. Lower weight of the APC-2/AS4 pressure vessel reduces the total dry weight of the vehicle and the energy consumption of the vehicle (mainly from batteries) as well as the cost. Roughly for every wet lb. of the vehicle 3 dry lbs. of synthetic foam is needed to maintain a buoyant vehicle. The APC-2/AS4 pressure hull has the same weight as the Graphite/Epoxy pressure hull. The hygrothermal effects are negligible for the APC-2/AS4 pressure vessel (see Table MAF-3 and Figure MAF-29). The hygrothermal effects did not change the factor of safety of the APC-2/AS4 pressure vessel (see Table MAF-7 and Figure MAF-30) considerably. However, the hygrothermal effects were severe in Graphite/Epoxy pressure vessel (see Figure MAF-7 and Figure MAF-30). This was due to the higher moisture absorption of Epoxy (thermo set resin) over that of APC-2 (thermoplastic resin). The thermal effect is more considerable in the metallic pressure vessel than hygrothermal effects in the APC-2/AS4 pressure vessel (see Tables MAF-6 and MAF-7), and they were both affected less compared with Graphite/Epoxy (see Figures MAF-28, MAF-29, and MAF-30). Manufacturing of APC-2/AS4 pressure vessel is comparable to the Ti-6Al-4V and the final composite product needs less machining than the Ti-6Al-4V pressure vessel. It should be noted that the material waste during the manufacturing for Ti-6Al-4V pressure hull is much more sever than that for the APC-2/AS4. Manufacturing of thick APC-2/AS4 pressure hull is easier than that of thick Graphite/Epoxy pressure hull. The Graphite/Epoxy is a thermo set composite and due to its exothermic property, it is not suitable for the manufacture of thick-section composite structures. Also, since the thermo set pressure hull needs to be cured in the autoclave after the winding, the final product gains large residual stresses, which reduce the performance of the structure. However, the thermoplastic composite has endothermic property, and an in-situ thermoplastic filament winding technique can be used to manufacture the thick-section thermoplastic pressure hull. The consolidation can be achieved during the winding using in-situ heat sources and a consolidation pressure roller. On-line consolidation considerably reduces the residual stresses in the structure (Nejhad92a, Nejhad92b, Nejhad94), which yields final products with better quality and performance. No post-curing is necessary for the thermoplastic composite when is processed in-situ. In addition, in a thermo set wet filament winding, particularly for thick section composites, the tension build-up causes a fiber migration towards the mandrel which, in turn, leads to fiber waviness under pressure, due to the slacks created by the fiber migration. The fiber waviness is not desirable since it can trigger fiber micro buckling under local compressive loads, which is the case for a pressure vessel under external hydrostatic pressure. A micro buckling phenomenon can lead to a premature catastrophic failure of the pressure vessel.

1.8. Design of Titanium End-caps

End-caps are required to close the ends of the APC-2/AS4 pressure vessel. Under ocean hydrostatic pressure, the pressure vessel and end-caps are under radial and axial pressure, and they mutually affect each other. Finite Element Analysis (FEA) was performed to study the stress distributions in metallic end-caps with maximum six holes for connectors and one hole for a vacuum valve, i.e., a total maximum holes of seven. The diameter of each hole was one inch. Due to axi-symmetric geometry, material properties, loading, and boundary conditions, 51.43 degrees wedge of the end-cap was modeled in the FEA. A cylindrical coordinate system was used, $X \equiv R$, $Y \equiv \theta$, and $Z \equiv Z$, (see Figure MAF-31). Axi-symmetric boundary conditions were applied at $Y=0°$ and $Y=51.43°$ planes.

Hydrostatic pressure was applied at the exposed surfaces of the end-cap. Also, simply supported boundary condition was applied at the axial mating surfaces of the end-cap and pressure hull. The radial stress calculated from the pressure vessel analysis was applied at the radial mating surfaces of the end-cap and pressure hull. Von-Mises failure criterion (Shames, 1989) was considered for the design of the metallic end-cap. The end-cap is made of Ti-6Al-4V (see Table MAF-1) and is designed for 10,300 psi with a stress factor of safety of about two. Figure MAF-31 shows the Von-Mises stress distribution for the end-cap. The maximum stress of 60,731 psi occurs at the holes. Figure MAF-32 shows the deformation of the end-cap. The maximum deformation of 0.022 inches happens at the center of the end-cap. The dimensions of the end-cap and locations of the connectors are shown in Figure MAF-33.

1.9. SAUVIM Pressure Vessel Design

In the pervious section APC-2/AS4 was selected as the material of choice for the deep ocean pressure vessel up to a design depth of 7,000 m (corresponding to 10,300 psi). The SAUVIM vehicle will operate up to 6,000 m depth. Therefore, this section presents the design of the SAUVIM pressure vessels for a design depth of 6,100 m, which corresponds to 8,976 psi. The pressure vessels for the SAUVIM vehicle have two different sizes. The design constraints of the pressure vessels are: total lengths of 21" and 19", an inner diameter of 13", and a design pressure of 8,976 psi which corresponds to 20,013 feet (i.e., 6,100 meters) depth. Symmetric sub-laminate configuration of $[(90/90/0/0/90/90)_s]_4$ is chosen for the composite pressure vessel. The symmetric cross-ply lay-up configuration for the composite pressure vessels eliminates extension-bending, extension-shear, and bending-twisting couplings in the structure. The 2:1 hoop-to-axial ply ratio is chosen since the theoretical hoop stress for metallic pressure vessel is twice of the axial stress (Hyer, 1988). The thickness of a lamina is 0.0055". Stress analysis was performed to determine the required thickness of the pressure vessels with tapered end-cap for SAUVIM vehicle. The thickness was determined by trial-and-error based on a factor of safety of around 2. The thickness of the pressure vessel was selected to be 1.188". The material property of APC-2/AS4 is given in Table 3.2. APC-2/AS4 material is selected employing in-situ thermoplastic composite filament winding technique to manufacture the pressure hull.

A contoured end-plug end-cap was considered (see Figure MAF-4). The goal of using this end-cap is to improve the performance of SAUVIM pressure vessels by reducing the bending and shear stresses at the ends. A parametric study is performed to determine the optimum value for the tapered radius for the 21" and 19" pressure vessels (see section 2.3.1). The length of the plug is optimized and found to be 1.5" (Yousefpour00a). This length was also required to place two radial O-rings for sealing purposes. Stress analysis was performed to determine the required thickness of the pressure vessels with tapered end-cap for SAUVIM vehicle. The thickness was determined by trial-and-error based on a factor of safety of around 2. The thickness of the pressure vessel was selected to be 1.188". The methods were explained in section 2.3.1. For the tapered end-caps, the radial displacements, d, at 1.5" from the end of the 21" and 19" cylinders were 0.024" (see Figure MAF-34). The values were obtained from edge simply supported model (see section 2.3.1). Table MAF-12 gives the taper radius of the end-cap with the corresponding stress factor of safety for different percentage of 'd'. Zero percentage of 'd' means the end-cap has no tapered radius and yields identical plug boundary conditions.

Maximum factor of safety of 1.67 was obtained for 21" and 19" pressure vessels at the circular tapered radius of 115" which corresponds to 40% 'd' value (see Table MAF-12). The results clearly show that the optimum radius circular taper was incorporated into the end-cap, enhanced the performance of the pressure vessel compared with a plug end-cap with no taper. Table MAF-13

gives the stress analysis results for APC-2/AS4 pressure vessels with optimum tapered radius, 115"
with a wall thickness of 1.188" at 32°F, and 70°F, and 140°F under a design pressure of 8,976 psi.
The results revealed that the hygrothermal effects did not cause significant difference on the
performance of the pressure vessels. For the pressure vessels with tapered end-caps, the maximum
radial and axial stresses and strains occur at the end-cap

As mentioned before, in the eigenvalue buckling analysis, the theoretical buckling pressure for an
ideal linear elastic structure is calculated. At the eigenvalue buckling pressure (the bifurcation
pressure), the deformation starts to follow a new pattern on the load-deflection curve, which is
different from the pre-buckling pattern (Bushnell, 1985). First mode shapes of the 21" and 19"
composite pressure vessels for SAUVIM are shown in Figures MAF-35 and MAF-36, respectively.
Due to the axi-symmetric geometry, material properties, loading, and boundary conditions, one-sixth
of the composite pressure vessels were modeled (see Figure MAF 37 and MAF-38). Table MAF-
14gives the bifurcation pressure of the pressure vessels for SAUVIM with pre-determined thickness
(i.e., 1.188") that was obtained from the stress analyses. The bifurcation pressures of the pressure
vessels were considerably higher than the design pressure of 8,976 psi.

As mentioned before, non-linear buckling pressure can be evaluated using non-linear stress analysis
by observing the first change in the slope (i.e., stiffness of the structure) in the load-deflection curve
(Bushnell85). The wall thickness of the pressure vessels that were calculated in the stress analyses
was used in the non-linear buckling analysis. Also, same optimized tapered end-cap boundary
conditions established in the stress analysis was used in this section. Since the eigenvalue buckling
pressure was very high, the non-linear buckling analysis was performed up to 17,952 psi, which gave
a minimum buckling factor of safety of two for the pressure vessel. The pressure-displacement curve
of the 21" and 19" APC-2/AS4 pressure vessels with optimum tapered radius taking hygrothermal
effects into account are shown in Figures MAF-39 and MAF-40, respectively. The results show that
the pressure vessels did not lose their stability up to 17,952 psi. It can be observed that the
hygrothermal effects did not cause significant difference on the performance of the pressure vessels.

Non-linear stress analysis was applied to the pressure vessel models for SAUVIM to present the
linear behavior of the structure. Table MAF-15 shows the results on the non-linear stress analysis for
the composite pressure vessels. The results were in good agreement (see Table MAF-13). Generally,
the non-linear stress analysis results revealed the linear nature of the stress problem.

1.10. Design of Titanium End-cap for SAUVIM

One size end-cap was designed for 21" and 19" pressure vessels with optimum tapered radius for
SAUVIM. Finite Element Analysis (FEA) was performed to determine the stress distributions in
metallic end-caps with maximum six holes for connectors and one hole for vacuum valve, i.e., a total
maximum holes of seven. The diameter of each hole was one inch. The end-cap was made of Ti-
6Al-4V and designed for 8,976 psi with a stress factor of safety of about 2. Figure MAF-41 shows
the Von-Mises stress distribution of the end-cap. The maximum stress of 60,880 psi occurs at the
holes. Figure MAF-52 shows the deformation of the end-cap. The maximum deflection of 0.024
inches happens at the center of the end-cap. The dimensions of the end-cap and locations of the
connectors are shown in Figure MAF-43.

1.11. Scaled Thermoplastic Composite Pressure Vessel and End-caps

The analyses for the metallic and composite pressure vessels revealed that APC-2/AS4 pressure vessel in general has advantages over the Ti-6Al-4V and Graphite/Epoxy pressure vessels. An APC-2/AS4 scaled pressure vessel was designed. The length and inner diameter of the scaled pressure vessel were chosen to be approximately one-third of those for the main pressure vessel - the design of which was reported earlier. The length and inner diameter of the scaled pressure vessel were 6.625" and 4.18", respectively. The thickness of the scaled pressure vessel was fixed and chosen to be 0.24" in order to have a thick wall pressure vessel. A symmetric cross-ply sub-laminate configuration of [90/90/0/0/90/90]$_s$ was chosen for the composite scaled pressure vessel to avoid extension-bending, extension-shear, and bending-twisting couplings in the structure. The 2:1 hoop-to-axial ply ratio is chosen since the theoretical hoop stress for metallic pressure vessel is twice of the axial stress (Hyer88). Finite element analyses were performed on the scaled model pressure vessel using ANSYS software. Due to axi-symmetric geometry, material properties, loading, and boundary conditions, ten degrees wedge of the circular cylinder was modeled in the FEM stress analysis. Cylindrical coordinate system was considered. Modeling a wedge portion of the pressure vessel reduces the computational time and memory requirements significantly. The stress analysis revealed that the scaled model, with end-caps in place and modeled as simply supported boundary conditions, could sustain a pressure up to 3,500 psi with a stress factor of safety of about 2.2 using Maximum Principal Stress failure criterion (Vinson87). For the scaled model a plug-supported end-cap was used. Figures MAF-44, MAF-45, and MAF-46 show the radial, axial, and hoop stress distributions, respectively. Also, Figures MAF-47, MAF-48, and MAF-49 show the radial, axial, and hoop strain distributions, respectively.

The maximum radial stress and strain occur at the end-cap of the scaled pressure vessel, i.e., -5,665 psi and 0.00372 in/in, respectively. The maximum axial stress and strain occur at the end-cap of the scaled pressure vessels, i.e., -11,365 psi and -0.00308 in/in, respectively. The maximum hoop stress of -51,682 psi, and maximum strain of -0.00252 in/in, happens at the inner surface at the mid-length of the scaled pressure vessels. The maximum displacement of 0.00716" occurs in the axial direction of the composite pressure vessels. At the mid-length of the scaled pressure vessel, the radial stress and strains are -3,119 psi and 0.00134 in/in, respectively. The axial stress and strain are -50,801 and -0.00214 in/in, respectively, at the mid-length of the scaled pressure vessel. The hoop stress and strain are -52,924 psi and -0.00251 in/in at the mid-length of the scaled pressure vessel. The maximum defection at the mid-length is 0.00527".

Figure MAF-50 shows the first mode of the buckling shape for the scaled pressure vessel. Due to the axisymmetric geometry, material properties, loading, and boundary conditions, one-sixth of the scaled pressure vessel (i.e., one-third circumferentially and one-half axially) was modeled and the cylindrical coordinate system was considered (see Figure MAF-51). The eigenvalue buckling pressure for the pressure vessel was about 13,942 psi. Non-linear buckling analysis (ANSYS99) was performed on the structure to investigate the stability of the scaled pressure vessel up to 7,000 psi pressure, with end-caps in place modeled as radial simply supported and axial external pressure boundary conditions. The mid-length pressure-deflection curve of the APC-2/AS4 scaled pressure vessel is shown in Figure MAF-52. It was found that the scaled pressure vessel would not lose its stability up to 7,000 psi.

A plug-supported end-cap with a hole at the center for a connector was considered for the scaled pressure vessel. The end-cap was made of stainless steel and designed for 3,500 psi with a factor of safety of about three. The stainless steel has Young's Modules of 30 Msi, Poisson's ratio of 0.3, and yield strength of 40 Ksi. Figure MAF-53 shows the Von-Mises stress distribution of the scaled end-cap. The maximum stress of 13,086 psi occurs at the center holes. Figure MAF-54 shows the displacement of the scaled end-cap. The maximum displacement is radial and happens at the center

of the end-cap around the hole and is 0.00054 inches. The dimensions of the end-cap are shown in Figure MAF-55. The end-cap has two radial O-rings for sealing.

2. Manufacturing of the Pressure Vessel

The APC-2/AS4 thermoplastic composite was chosen as the material system for the manufacture of composite pressure vessels for the SAUVIM underwater vehicle. This was due to superior mechanical properties, performance, and ease of fabrication of the APC-2/AS4 thermoplastic composite over the Graphite/Epoxy and Ti-6Al-4V, as explained earlier. The Cytec Fiberite, Inc produces the APC-2/AS4. This composite is available in form of unidirectional tape with various width and grade (ICI Thermoplastic Composite92). To manufacture the pressure vessel a symmetric sub-laminate configuration of [90/90/0/0/90/90]$_s$ was chosen. The pressure vessel was fabricated using in-situ thermoplastic composite filament winding/tape-laydown. Unidirectional tapes with thickness of 0.005" and width of 0.24" were used.

2.1. Manufacturing Equipment and Set-up

Figures MAF-56 and MAF-57 show the schematic of the in-situ thermoplastic composite filament winding/tape-laydown set-up for the scaled and main pressure vessels, respectively. The tensioner assembly consists of tape supply roller, tensioner rollers, sensing unit cable, air cylinder and festoon. The purpose of applying suitable tension in the tape during winding is to achieve a good compaction during fabrication, and increase the quality of final composite parts. Next, the tape is guided through the bracket system. A bracket system is designed to hold the pay-out eye system, compaction system, and nip-point heater. The tape passes through the pay-out eye system and winds over the mandrel. The nip-point infrared heater is located in such a way to melt the incoming composite tape as well as the surface of the substrate (Werdermann89) (see Figure MAF-56). For the main pressure vessel set-up, three local infrared heaters were used. Two of the local heaters melt the substrate and the third one melts the incoming tape and partially substrate (see Figure MAF-57). The bracket system is mounted on the translation stage, which gives the translational motion to the bracket system, and the mandrel, on one end, is connected to the rotary motor, which gives rotary motion (see Figures MAF-56 and MAF-57). A motion controller can be programmed to control the motion of the rotary and translational motor to yield a desired winding speed and path. The photographs of the filament winding set-up for the scaled and main pressure vessels are given in Figures MAF-58 and MAF-59.

The compaction system consists of an air cylinder, a pressure gage, and a compaction roller. The compaction roller is made of stainless steel with diameter of 3" and thickness of 0.9". The compaction roller can apply pressures up to 1,180 lb/linear-inch on the lay-down point to facilitate the bonding between the layers. The mandrel of the scaled pressure vessel is made of stainless steel and that for the main pressure vessel is made of aluminum. The mandrel for the scaled pressure vessel is 9" long with 4.12" outer diameter. The mandrel for the main pressure vessel is 36" long with an outer diameter of 12.92". The mandrels are tapered with a slope of 0.056 degrees to slip off the mandrel the wound thermoplastic composite part after its manufacturing. The mandrel is placed between two couplings, which are attached to a bearing at each end, and the whole system is connected to a rotary motor. The translational and rotational motions of the translation stage and rotary motor are controlled by a multi-dimensional motion programmable controller (Aerotech92). The program was written in G-code machine language to wind the tape on the mandrel. The winding speed for the scaled pressure vessel was 157 in/min. The scaled pressure vessel was manufactured in 8 hours. The winding speed of the main pressure vessel was 212 in/min. The time of manufacturing of the main pressure vessel is about 90 hours.

Two infrared strip heaters are set up at both sides of the mandrel to maintain the temperature of mandrel and composite shell around 50°C-70°C (see Figures MAF-56 and MAF-57) to facilitate the processing (Nejhad93). The temperature of the infrared heaters can be adjusted by power controllers. To monitor and control the temperature of the mandrel and composite shell a thermocouple and an infrared pyrometer were used.

2.2. Fabrication Methodology and Steps

The pressure vessel was manufactured using in-situ thermoplastic filament winding and tape placement technique. This method consists of three steps: (i) pre-heat the composite tape and mandrel/substrate, (ii) apply enough heat at the lay-down point during winding, and (iii) apply enough pressure on the lay-down point for consolidation purpose (Werdermann89; Aerotech92; Sonmez97). In the first step, the incoming pre-preg composite tape is preheated by passing through the preheating infrared heaters, and then is wound/laid-down on the mandrel (Nejhad97). Infrared heaters on sides of the mandrel also keep the temperature of the mandrel and composite substrate around 50°C-70°C and below the glass transition temperature to facilitate winding (Nejhad93; Sonmez97). While the tape is being wound/laid-down on the mandrel, the local nip-point infrared heater supplies heat to the mating surfaces of the incoming tape and the substrate. The temperature at the lay-down point should be around processing temperature in order to melt the matrix. The processing temperature for APC-2 matrix is around 450°C (ICI Thermoplastic Composite92). The processing temperature is controlled by the winding speed and heat intensity, which can, in turn, affect the size of the processing window (Nejhad91a, Nejhad91b). The larger the size of the processing window, the easier it is to control the processing and quality of the manufactured parts (Nejhad93). Finally, the compaction roller should apply enough pressure on the lay-down point to consolidate the incoming composite layer to the previous layer on the substrate to facilitate the consolidation procedure. Heat flux, tape/tow/substrate preheating, winding speed, and pressure are four most important parameters for in-situ manufacturing of thermoplastic composites. These parameters must be adjusted accurately to manufacture high quality structure and achieve high production rate by enlarging the processing window and operating within it.

To determine the processing condition for the manufacturing of the APC-2/AS4 pressure vessel, a case study was performed (Yousefpour99, Yousefpour00b). In this study, mechanical performances of APC-2/AS4 thermoplastic composite C-ring samples with different processing conditions were investigated and experimental results were compared with numerical results using Finite Element Method (FEM). The manufactured samples had final average inner radius of 2.13", thickness of 0.11" and width of 0.26". The effects of tape preheating, mandrel/substrate preheating, and on-line consolidation pressure on the mechanical performances of the parts were studied. Mandrel/substrate preheating was found to be necessary for good quality manufacturing. Ten sets of samples, with five samples per set, were manufactured using in-situ thermoplastic composite filament winding. For the first five sets, tape preheating below Glass Transition Temperature (T_g) at 110°C was used, however the consolidation pressure for various sets was 30, 70, 105, 140, and 175lb/linear-inch. Same pressures were used for the next five sets while the tape was preheated above T_g at 170°C. T_g for APC-2 is 140°C. C-ring tests were performed to evaluate failure stress, strain, and deflection of C-rings at room temperature. All C-ring tests were performed on an Instron machine. Samples failed in compression at inner radius. It was found that samples with tape preheating below T_g had superior mechanical performance than those with tape preheating above T_g. This could be due to twisting of filaments within the tape during preheating which led to the low quality of samples and possible immature failure. Also, it was found that samples made with consolidation pressures of 70 and 105 lb/linear-inch had better mechanical performances than other samples. It is believed that

consolidation pressures of 70 and 105 lb/linear-inch were optimum consolidation pressures and caused good mechanical performances and quality. Scanning Electron Microscopy was conducted on the samples for quality control. The manufactured samples were found to be uniform microscopically. Non-linear Finite Element Analysis (FEA) associated with contact element was performed to simulate the C-ring testing and determine the mechanical performance of the C-rings. It was found that the results of FEA were in good agreement with the experimental and analytical results. The preheating and consolidation pressure affect the quality of the parts, which, in turn, affects the failure load and strength that can be measured experimentally and be used in the FEA. It can be concluded that using FEA in conjunction with failure load as input to model can present the real mechanical performance of the parts. These results were used to determine the optimal processing parameters for the manufacture of the APC-2/AS4 pressure vessels.

3. Testing of Scaled Pressure Vessel

An APC-2/AS4 scaled pressure vessel was designed for the hydrostatic pressure of 3,500 psi. The length and inner diameter of the scaled pressure vessel were chosen to be approximately one-third of the main pressure vessel for the SAUVIM. The length and inner diameter of the scaled pressure vessel were 6.625" and 4.18", respectively. The thickness of the scaled pressure vessel was fixed and chosen to be 0.24" in order to have a thick-walled pressure vessel. A symmetric sub-laminate configuration of [90/90/0/0/90/90]$_s$ was chosen for the composite scaled pressure vessel. The 2:1 hoop-to-axial ply ratio is chosen since the theoretical hoop stress is twice of axial stress (Hyer, 1988). Figure MAF-60 gives a photograph of the scaled pressure vessel with its stainless steel end-caps and tie-rods. The scaled pressure vessel was instrumented with eight strain gages. Figure MAF-61 shows the strain gage locations. Four strain gages were located close to the cylinder end to monitor the strain near the end closure. Two of those strain gages were positioned in the axial and the other two in the hoop direction. Other four strain gages were located at the mid-length of the pressure vessel with two strain gages in the axial and two in the hoop direction. The scaled pressure vessel was tested under hydrostatic pressure up to 3,500 psi, in the Hawaii Institute of Geophysics Laboratory Pressure Chamber with maximum pressure testing capability of 10,000 psi. After attaching the strain gages and wiring them, each wire was connected to a 16-pin connector, which was located on one of the scaled pressure vessel's end-cap (see Figure MAF-62). Another 16-pin connector was attached to the end-cap of the pressure chamber (see Figure MAF-63), which had wires out from the other side of the pressure chamber's end-cap. The wires were connected to a Signal Conditioning Board. The Signal Conditioning Board was connected to a Data Acquisition Board, which was installed on a PC. LabView software was used to collect the strain gage data. The two connectors were connected by a cable. The connectors and the cable were designed specifically for high-pressure applications. Figure MAF-64 shows the photograph of the scaled pressure vessel, the high-pressure chamber, and the connection cable. The scaled pressure vessel was placed in the pressure chamber and pressurized. The pressure was raised with an increment of 350 psi every 5 minutes with a dwell time of 10 minutes per step. After staying 30 minutes at the maximum pressure, the pressure was dropped to 1,750 psi and again increased to 3,500 psi with the same manner as before. After staying for 30 minutes at the maximum pressure, the pressure was released to the atmosphere pressure and the pressure vessel was taken out. At the end of the test, the pressure vessel was intact and no leak was observed. Figure MAF-65 gives the photograph of the scaled pressure vessel after the test.

Figures MAF-66 and MAF-67 show the comparison of the axial and hoop strain results, respectively, from the experiment and FEA for the strain gages close to the end-cap. There are good agreements between the experimental and numerical results. These figures show that the experimental strain results are slightly smaller than the FEA results. This reveals that the FEA results are accurate or somewhat conservative. The same conclusions can be made for the axial and hoop strain results from experiment and FEA at the mid-length of the scaled pressure vessel shown in Figures MAF-68 and MAF-69, respectively. The main pressure vessel will be tested in near future.

4. Design, Analysis, Manufacture, and Test of Shallow Water Composite Pressure Vessels Using E-glass/Epoxy Woven for SAUVIM

For the Phase-I of the SAUVIM project, the vehicle will be operated and tested in the shallow water (less than 300 feet under water). Six E-glass/Epoxy shallow water composite pressure vessels with internal length of 18" and inner diameter of 13" were designed for an external hydrostatic design pressure of 165 psi. Buckling and stress finite element analyses were performed for the design of the pressure vessels. An eigenvalue buckling analysis was performed to determine a bifurcation

buckling pressure and a modal shape of the structure for a wall-thickness of 0.304 inches. These results were used to perform a non-linear buckling analysis. The buckling pressure was determined to be 215 psi. Stress analysis was performed to investigate the stress response of the structure with the wall-thickness of 0.304" under the design pressure. Maximum stress criterion was used and a stress factor of safety of 11.95 was achieved. End-caps were designed using Aluminum 6061-T6 employing Von Mises criterion. The end-caps have seven holes, which are used to place the connectors and vacuum bolt. The stress factor of safety of two was achieved for the end-caps (Ng00a; Yousefpour00).

Tube roll-wrapping with wet-laying technique was used to fabricate the pressure vessels. This technique consisted of several steps, namely set-up preparation, fabric impregnation, fabric rolling, shrink taping, curing/cooling, and post-processing (Ng00a, Ng00b). The total time of manufacturing was 7 hours for each pressure vessel. The finial products needed minor machining. The final length, inner diameter, and thickness of the pressure vessels were 19.5", 13", and 0.324", respectively. Aluminum 6061-T6 end-caps with 1.125" thickness were fabricated. An axial washer and two radial O-rings were used to seal the pressure vessel/end-caps interfaces. The pressure vessels and end-caps were assembled using six tie-rods. Six pressure vessels were tested at the design pressure of 165 psi inside a high-pressure water-filled chamber. The pressure vessels were intact and no leakage was observed. Figure MAF-70 shows a shallow water pressure vessel with its end-caps and tie rods (Ng00a).

5. Finite Element Analysis of the Frame

Two SAUVIM groups, namely, Mechanical-Electrical Design (MED) and Mechanical Analysis and Fabrication (MAF) groups were involved in the design, analysis, and test of the frame for SAUVIM project. MED group was responsible to identify the required components and develop the preliminary conceptual design of the frame based on the most desired component layout as well as the fabrication considerations of the frame. Several frame designs were proposed at this stage. Material selection and FEA of the frame were MAF group responsibilities. MAF group performed FEA on the frame structure and studied the behavior of the frame structure under different loading conditions. MAF group recommended the necessary changes in the design of the frame to the MED group according to the FEA study. The MED group implemented the changes and came up with a modified design for the frame. This sequence was repeated till the optimum design was achieved. The MAF group presented the final FEA results and determined the final size and shape of all required structural members of the frame to the MED group. Then, the MED group sent the drawing of the frame with all required information to a machine shop for fabrication. Finally, MED group performed a number of non-destructive tests such as X-ray radiography and penetration tests to evaluate the quality and strength of the critical locations such as welded joints.

5.1. Mechanical Design of the Frame

The frame of an underwater vehicle serves as a carriage on which thrusters, batteries, pressure vessels, robotic arms, foams, and accessories are firmly attached. Therefore, all loads on the vehicle are carried by the frame. Three types of loads are applied to the frame - static loads (e.g., weight of the components and frame itself), bouncy forces, and dynamic loads (e.g., the thruster forces). To design the frame for SAUVIM, several steps were taken. The following gives these steps:

- Identification of the components and component layout for the vehicle (see Figure MAF-71).

99

- Development of a conceptual design for the frame using component layout.
- Selection of material.
- Analysis of the frame structure using Finite Element Method.
- Fabrication of the frame.

5.2. Components Identification

The MED group identified all the required components that would be installed on the frame. Table MAF-16 shows a list of major components for the vehicle. After identifying the components, a few component layouts were proposed. The component layout presents the locations of the components on the frame and is a benchmark for the design of the frame. A few issues were considered during the component layout design. First, it was desired to place components such that the applied loads on the frame would be distributed on the structure uniformly. Second, the components, such as pressure vessels and batteries, which needed to be accessible, were located at reachable locations for possible services or exchanging.

5.3. Conceptual Design of the Frame

The MED group, based on their desired component layout, proposed a preliminary design of the frame. In the component layout, locations, weights, and volumes of the components were specified. Figure MAF-72 shows a preliminary design of the frame based on the desired component layout. Figure MAF-73 shows the final frame design. The following issues were considered during the final frame design:

- Use of unnecessary members in the structure was avoided. This would otherwise increase the weight of the vehicle, which is not desirable.
- Creation of unnecessary complicated joints in the structure was avoided. This could otherwise increase the fabrication cost of the frame.
- Drilling any holes in the loaded members was avoided. This could otherwise decrease the strength of the loaded members around the holes, leading to a possible premature failure.
- Creation of any air pockets inside/between members was avoided. Any air pocket could otherwise act as a pressure vessel and might cause immature failure of the structure, especially for deep ocean applications.
- Attachments were designed to install the components onto the frame. The attachments were welded to the frame and components will be bolted or riveted to the attachments.

5.4. Candidate Materials/Materials Selection

Aluminum, steel, and titanium were three candidate materials for the frame. Table MAF-17 gives the mechanical properties of the candidate materials. To select the appropriate material, the following issues were considered (Ashby80):

- Price and availability of the material. The material has to be cost effective and available in the market. It is economical to design the members of the frame using standards or stock sizes.
- Strength, stiffness, and density of the material. The material properties of the frame depend on the choice, heat treatment, and processing of the material. Choosing a proper

material can reduce the weight and increase the strength of the underwater vehicle structure.

- Weldment strength of the material. Welding is structurally sound joining technique for fabrication of the frame. It is especially important to know the strength of the welded region for the selected material. For example, the strength of the Aluminum reduces approximately 30-40% around the welded region (Pickering97).
- Corrosion. The material to be selected for the frame should have a good corrosion resistance since the frame operates in a highly corrosive environment, i.e., seawater. The underwater frame can be subjected to different types of corrosions, e.g., crevice corrosion, galvanic corrosion, pitting corrosion, stress corrosion, cracking corrosion, etc. (Jones92).

Aluminum 6061-T6 was the selected material for the frame for the following reasons. This material is available in the market in different sizes and is less expensive than steel and titanium. Fabrication cost of the aluminum frame is much less than titanium frame. Aluminum is lighter than titanium and steel. It has relatively good corrosion resistance. However, after each deployment, vehicle has to be washed with tap water. The main weakness of this material is its low-weldment strength.

5.5. Finite Element Analysis (FEA)

Finite element analysis is a powerful tool for the frame design because it involves all the factors influencing the behavior of the frame, such as geometry, material properties, loads, and boundary conditions (Huebner95). Thus, it leads to an excellent design in terms of strength, stiffness, and economic efficiency. The most efficient method to analyze the frame using finite element method is using 3-D space frame employing 1-D beam element with appropriate cross-sections and material properties. This method saves tremendous computational time and memory requirements, and gives sufficient information for the reliable design of the frame. Finite element analysis was performed to analyze the frame using I-DEAS finite element software. In the pre-processing step, two nodded beam elements with different cross-sectional dimensions were used. The material properties of aluminum were given to the software (Table MAF-17). The model of the frame was created according to the final design (see Figure MAF-74).

In the solution step, the load and boundary conditions were applied to the model and the solution was initiated. As mentioned before, the frame of the underwater vehicle carries the load of the vehicle components. The magnitudes of the loads have to be known by the designer. These loads can be static loads, which act as concentrated or distributed loads, buoyancy forces, which appear when the vehicle is placed in water, and dynamic loads such as thruster loads. Close interaction exists between the applied loads, the frame, and its supports. The loads on the frame produce stresses on the supports, which lead to the deformation of the members. Therefore, locations and the number of the supports can dictate the stress distributions on the frame and play critical roles for the serviceability and survivability of the frame. Four load and boundary condition cases were considered. Each case had two sub-cases, i.e., a) retracted robotic arms and b) extended robotic arms. First, it was assumed that the vehicle was supported on the ship or ground (dry condition). The major loads on the frame were the weight of the frame and the weight of the components, which were attached to the frame. These are all static loads. The best locations for the supports were found to be under each column of the frame (see Figure MAF-75). Second, it was assumed that the vehicle was lifted for deployment purpose. The loading conditions (lifting condition) were the same as previous case but the supports were located at the lifting points (see Figure MAF-76). As the vehicle was placed in the water and released form-lifting mechanism, the loads and boundary conditions of

the frame would change (wet condition). In this case, the loads applied on the vehicle were a combination of the weight of the frame and components as well as the buoyancy forces due to foams and buoy equipment. The net weight of the vehicle is zero or slightly greater than zero. The frame itself was under two equal but opposite loads, i.e., weights of the vehicle and buoyancy forces. The frame in reality was not supported. To avoid rigid body motions, it was assumed that the frame was supported at the four corners (see Figure MAF-77). The load conditions for the frame during operation were the same as previous case, but the maximum thruster forces were added to the load conditions (i.e., wet/dynamic condition).

The stress results were studied to modify the design by reinforcing the weak regions of the structure, eliminating unnecessary members, and changing the size and type of the beam members. It should be noted that the stress factor of safety was calculated based on the weldment strength of the aluminum (i.e., 12,000 psi). Due to the existence of different loads and boundary conditions, the frame was designed in such a way that it was sustained under different load and boundary conditions. The results of maximum stresses and displacements, and factor of safety of the frame are given in Table MAF-18. The minimum factor of safety occurred for wet/dynamic analysis with arms at rest position and was found to be 4.41. It should also be mentioned that to roughly a count for possible dynamic loading of the frame during lifting and deployment all loads on the frame were doubled prior to the analysis.

5.6. Fabrication of the Frame

The final step was the fabrication of the frame. All the members were drawn with all specifications and sent for fabrication by MED group. The designed frame was fabricated at the Hawaii Shipyard Machine Shop in Honolulu, HI. X-ray Radiography and penetration tests were performed on the welded regions to verify the quality of the weldment area by MED group.

6. Procedures for the Design, Manufacture, and Assembly of Composite Flooded Faring

A composite flooded fairing is designed for the SAUVIM vehicle to reduce the drag force during traveling in water and protect the internal equipment in case of a possible collision or impact. The design of the fairing is at its beginning stage. Figure MAF-78 shows the initial design of the fairing. The SAUVIM vehicle would travel on an average speed of 3 knots. The design of the fairing is peculiar, as the frontal part of the fairing should be made sacrificial. This is because under catastrophic crush situation, the frame and its containment should not be damaged at all. The frontal part should be able to sustain the force and absorb the energy during the impact, and be designed with the concept of disposable. The material system used for the fairing, supports, and joints should be indifferent to seawater environment with the capability to resist corrosion. It should be built using light-weighted materials in order to save energy and improve the ease of maneuvering. To manufacture the fairing, first, a foam model would be built according to the size and shape of the suggested fairing. Next, two sections of the female molds (left and right) would be built on top of the foam using wet composite lay-up and vacuum bagging method. Next, the woven composite male molds (i.e., the fairing) would be built on the inner surface of the female molds using similar technique. To keep the outer surface of the male mold (i.e., the fairing) smooth, the composite fabrics have to be wet-laid in the female molds since the inner surface of the female mold is very smooth. After the composite male molds (i.e., the fairing) are built, it is then cut into several desired segments. The joining mechanism between fairing segments will utilize a special locking mechanism.

Composite is chosen as the material system for the fairing and the joints (i.e. mounting points on the fairing for the supports on the frame). In comparison with metals such as steel or aluminum, polymeric composite materials have high strength and stiffness to weight ratio. They have good corrosion resistance, with low manufacturing costs, especially when the fairing is not of a straightforward shape. Graphite and Kevlar are chosen as the fiber materials in the form of the plain weave hybrid fabric for the fairing. Graphite is known as a material of lightweight, high strength and stiffness. Meanwhile, Kevlar is known for its toughness and good abrasion and impact resistance characteristics. For the matrix material, epoxy resin is chosen. The attachments between the fairing and the frame would utilize aluminum supports on the frame and Graphite/Epoxy plain weave woven composite wet-laid joints on the fairing. The reason for choosing aluminum as the material for the supporting bars as well as for the frame is because it is inexpensive, easy to modify, light, and corrosion resistant. The joint materials were chosen as woven Graphite composite since Kevlar is relatively weak under compression, and the joints are under bending stresses and not a direct impact. The manufacturing technique would also be different for the joints. They will be molded using the wet lay-up method. The 3-D effective orthotropic homogeneous composite properties of the Graphite-Kevlar/Epoxy hybrid woven as well as the Graphite/Epoxy plain weave plies are obtained given the material properties of the individual materials (see Table MAF-19) using 3-D Crimp model and (0/90) Cross-ply model (Ng00a). For the Graphite-Kevlar/Epoxy hybrid woven ply, two sets of lamina materials are needed to determine the 3-D effective material properties. The properties of each lamina are listed in Table MAF-19. The 3-D effective orthotropic properties of Graphite-Kevlar/Epoxy hybrid and Graphite/Epoxy plain-weave woven plies are obtained using 3-D Crimp model (Ng, et al., 2000a) and are given in Table MAF-20.

For the initial design, the thickness is determined as 0.2414 mm for each woven ply, and the composite fairing stacking sequence is proposed to be multiples of $[0_G/90_K/90_G/0_K/0_K/90_G/90_K/0_G]_n$. This orientation is prospective, yet meet all the criteria such as symmetric and balanced even for a satin weave. It should be mentioned that a $(0_G/90_K)$ represents a Graphite-Kevlar/Epoxy hybrid woven ply. The effective properties of Graphite-Kevlar/Epoxy plain weave material given in Table MAF-19 were used for this stacking sequence to obtain the overall effective properties of this static sequence to be used in the LS-DYNA crash simulation. The fairing is comprised of eight composite segments (see Figure MAF-79). The front and back is comprised of 3 pieces each, i.e., 1 piece on top and 2 pieces on the bottom. There will be 2 composite pieces covering the middle part of the submersible, as one on the left-hand side and the other on the right hand side. The fairing segments in Figure MAF-79 are numbered in the order of assembly. Based on this fairing configuration, the locations of joints and supports can be determined. As a preliminary decision, there will be 40 support bars and 40 joints equally distributed and held tight between the frame and the fairing (see Figure MAF-80). Figure MAF-80 also gives the order and assembly process of the fairing segments on the frame.

6.1. Utilization of DYNA-3D for Composite Flooded Fairing Crash Simulations

DYNA3D, an explicit transient three-dimensional non-linear finite element analysis package, has been utilized in the crash simulation of composite structures (Nejhad97). DYNA3D is used for analyzing large deformation dynamic response of inelastic solids and structures. A contact impact algorithm permits gaps and sliding with friction along material interfaces. Spatial discretization of the model is achieved by the use of 8-node brick or 4-node tetrahedral solid elements, 8-node solid shell elements, 4-node shell elements, 2-node beam elements, truss elements, membrane elements, and rigid bodies and discrete elements. The equations of motion are integrated in time by the central difference method.

For aluminum, MAT 24 was chosen to be the material of frame for the crash simulation. According to LS-DYNA (1999) keyword user's manual, it is an elasto-plastic material with an arbitrary stress versus strain curve, and arbitrary strain rate dependency can also be defined. Also, failure based on a plastic strain or a minimum time step size can be defined. For this material type, the values of the mass density for the material, Young's modulus, Poisson's ratio, Yield strength, and tangent modulus should be defined.

For the Carbon-Kevlar/Epoxy hybrid plain-weave woven composite, MAT 54 was chosen to be the material of fairing for the crash simulation. This model considers failure under compression. Chang-Chang (LS-DYNA99) failure theory is used during the crash simulation. Thus, it is only valid for thin shell elements. For this material type, the mass density of the material, Young's modulus in x, y and z direction, Poisson's ratio yx, zx, zy, shear modulus xy, yz, zx should be defined. Also, the tensile and compressive strengths in both longitudinal and transverse directions are to be defined. The in-plane shear strength should also be defined. According to the ICI publication, the tensile compressive, and shear strengths for Carbon/Epoxy plain weave composite are 75ksi, 65 ksi, and 7.7 ksi respectively. For Kevlar/Epoxy plain weave composite, the tensile, compressive, and shear strengths are 60 ksi, 25 ksi, and 5 ksi respectively. Those values are the more conservative one. Thus, based on those values, the tensile, compressive, and shear strengths for Carbon-Kevlar/Epoxy hybrid plain weave are 67.5 ksi, 45 ksi, and 6.35 ksi respectively given the stacking sequence of [0/90/90/0] using Rule of Mixture. For the Carbon/Epoxy plain weave composite, the tensile, compressive and shear strengths are 75 ksi, 65 ksi and 11 ksi respectively. The failure criterion was based on maximum principal stress criterion to obtain a factor of safety.

For the Carbon/Epoxy plain-weave composite, MAT 54 was chosen to be the material of fairing for the crash simulation. The same parameters apply to this model as mentioned before. The failure criterion was also based on maximum principal stress criterion to obtain a factor of safety.

The majority of the computational time for DYNA3D crash simulation is contributed to the momentum transfer that occurs with impacting bodies. For impact, a master and a slave surface are defined for the contact interface. They are made up of a list of nodes and element faces. With the contact type set to 13, the program automatically checks the nodes and elements that would participate in the simulation. It checks with complex algorithm, for penetration through the contact interface between the master and slave surfaces. Forces are placed at the nodes of the master and slave surfaces for momentum transfer upon penetration. After the contact interface process, the decelerations are updated and the kinematics boundary conditions are applied. Then, the velocities are updated and the finite element process loops back. The iteration speed is based on the time step, which in turn is based on the length of the smallest element in the whole model. During the initiation of the crash simulation, it will warn the user for the necessary time step size.

In this research, the frontal part of the fairing is meant to be sacrificial and replaceable. This is because the important equipment such as batteries, pressure vessels that house the electronic equipment and control systems are held within the frame. Therefore, the fairing has to be able to sustain the impact in the event of a crash, yet be able to absorb all the impact energies before the crash has any effects on the frame. In other words, the frame should be unharmed when the whole submersible attains the overall velocities of 0 m/s in the event of a crash. The submersible is considered as crashworthy if it fails in a controlled manner, has the ability to absorb the kinetic energy of the crash, and is able to maintain some "survival" space around the frame. Nevertheless, the main drawback of utilizing composites in the structural members of a vehicle is their inherent brittleness. Metals such as steel and aluminum are able to absorb high amounts of energy by plastic

deformation. Metals can undergo extensive slip without nucleation and propagation of cracks so that they are able to endure high strains before failure occurs. Unlike metals, composites fail in a brittle mode with no plastic deformation. Composites such as carbon can only endure strains between 1 to 3 percent before failing in a brittle mode (Hull83). As a result, Kevlar fibers are used to make up for the brittleness of carbon fibers, and in return, carbon fibers are used to make up for the low compressive properties of the Kevlar fibers. Therefore, the choice of Carbon-Kevlar/Epoxy hybrid woven composite is optimum given its mechanical and environmental properties compared with metals. Since the duration of the operation of the SAUVIM does not exceed eight hours the moisture absorption of the composite fairing and joint are less than 0.2% (Lundgren99; Shen81) and hence are negligible here.

Future Tasks (Phase II Tasks)

- Test the main thermoplastic composite pressure vessel and compare the strain results with analysis (FEA).
- Manufacture and test five more deep ocean thermoplastic composite pressure vessels.
- Finalized the design and analysis of the composite flooded fairing with its joints.
- Manufacture and test the composite flooded faring with its joints.

Table MAF-1. Mechanical Properties of Ti-6Al-4V

Property	Value	Property	Value
E (Msi)	16.5	S_y (Ksi)	120
G (Msi)	6.15	α $(10^{-6}/°F)$	4.80
ν	0.34	ρ (lb/in^3)	0.16

Table MAF-2. Unidirectional Mechanical Properties of the APC-2/AS4 and Graphite/Epoxy

Property	APC-2/AS4	Graphite/Epoxy	Property	APC-2/AS4	Graphite/Epoxy
E_1 (Msi)	20.0	20.6	E_2 (Msi)	1.48	1.50
G_{12} (Msi)	0.82	1.04	ν_{12}	0.28	0.27
$\alpha_{11}(10^{-6}/°F)$	-0.1	-0.50	$\alpha_{22}(10^{-6}/°F)$	13.3	15.0
β_{11}	0	0.01	β_{22}	0.3	0.2
S_{11T} (Ksi)	300	210	S_{11C} (Ksi)	175	170
S_{22T} (Ksi)	12.5	9.0	S_{22C} (Ksi)	28.4	29.0
S_{12} (Ksi)	27.3	8.7	ρ (lb/in^3)	0.057	0.057

Table MAF-3. Modified Coefficient of Thermal Expansion (MCTE) at 140°F and 32°F for Composite Systems

	140°F		32°F	
MCTE	APC-2/AS4	Graphite/Epoxy	APC-2/AS4	Graphite/Epoxy
$\alpha_{11}(1/°F)$	-1.00E-07	6.64E-06	-1.00E-07	-1.37E-05
$\alpha_{22}(1/°F)$	2.32E-05	1.58E-04	-4.86E-04	-2.48E-04

Table MAF-4. Thickness and 'd' Values for the Pressure Vessels

	Thickness (in)	d (in)
Ti-6Al-4V	1.35	0.0134
APC-2/AS4	1.68	0.0214
Graphite/Epoxy	1.68	0.0208

Table MAF-5. Radius of the End-cap Circular Taper, R, for Various Percentage of 'd' for Candidate Materials

d	d=0.0134" $R_{Ti-6Al-4V}$ (in)	d=0.0214" $R_{APC-2/AS4}$ (in)	d=0.0208" $R_{Graphite/Epoxy}$ (in)
100%	84	53	54
90%	93	58	60
80%	105	66	68
70%	120	75	77
60%	140	88	90
50%	168	105	108
40%	210	131	135
30%	280	175	180
20%	420	263	270
10%	841	526	541
0%	∞	∞	∞

Table MAF-6. Maximum Stress, Strain, and Deflection Results of the Ti-6Al-4V Pressure Vessel

Temperature	Stress (psi)	Strain (in/in)	Deflection (in)	Factor of Safety
32°F	64,742	0.0053	0.024	1.85
70°F	61,292	0.0050	0.022	1.96
140°F	58,149	0.0047	0.020	2.06

Table MAF-7. Maximum Stress, Strain, and Displacement Results of the APC-2/AS4 and
Graphite/Epoxy Pressure Vessels

	APC-2/AS4			Graphite/Epoxy		
	32°F	70°F	140°F	32°F	70°F	140°F
Radial Stress (psi)	-9,722	-9,723	-10,697	-13,130	-9,723	-14,289
Axial Stress (psi)	-11,950	-11,884	-13,078	-21,370	-11,903	-24,018
Hoop Stress (psi)	-75,406	-75,171	-77,302	-93,391	-77,067	-96,549
Radial Strain (in/in)	-0.0059	-0.0059	-0.0058	-0.0047	-0.0060	-0.0053
Axial Strain (in/in)	-0.0044	-0.0042	-0.0057	-0.0119	-0.0041	-0.0134
Hoop Strain (in/in)	-0.0037	-0.0037	-0.0037	-0.0046	-0.0037	-0.0048
Displacement (Axial) (in)	0.037	0.038	0.035	0.027	0.037	0.028
Factor of Safety	1.97	1.96	2.03	1.30	1.90	1.15

Table MAF-8. Bifurcation Pressure of the Pressure Vessels

Material	Bifurcation Buckling Pressure (psi)	Wall Thickness (in)
Ti-6Al-4V	100,422	1.35
APC-2/AS4	44,740	1.68
Graphite/Epoxy	47,426	1.68

Table MAF-9. Non-Linear Maximum Stress, Strain, and Displacement Results of the Ti-
6Al-4V Pressure Vessel

Temperature	Max. Stress (psi)	Max. Strain (in/in)	Max. Deflection (in)	Factor of Safety
32°F	64,246	0.0052	0.023	1.87
70°F	60,846	0.0049	0.022	1.97
140°F	57,951	0.0047	0.020	2.07

Table MAF-10. Non-Linear Maximum Stress, Strain, and Displacement Results of the APC-2/AS4 and Graphite/Epoxy Pressure Vessels

	APC-2/AS4			Graphite/Epoxy		
	32°F	70°F	140°F	32°F	70°F	140°F
Radial Stress (psi)	-9,727	-9,728	-10,652	-13,187	-9,729	-14,342
Axial Stress (psi)	-11,978	-11,869	-13,126	-21,366	-11,930	-24,013
Hoop Stress (psi)	-75,541	-75,306	-77,444	-93,543	-77,198	-96,712
Radial Strain (in/in)	-0.0059	-0.0059	-0.0059	-0.0048	-0.0060	-0.0054
Axial Strain (in/in)	-0.0044	-0.0042	-0.0057	-0.0119	-0.0041	-0.0134
Hoop Strain (in/in)	-0.0037	-0.0037	-0.0037	-0.0046	-0.0038	-0.0048
Displacement (Axial) (in)	0.037	0.038	0.035	0.027	0.037	0.028
Factor of Safety	1.96	1.95	2.03	1.29	1.89	1.15

Table MAF-11. Summary of the Analysis Results

Material	Ti-6Al-4V	APC-2/AS4	Graphite/Epoxy
Stress Factor of Safety	1.96	1.96	1.90
Minimum Buckling Factor of Safety	3.60	3.60	3.60
Wall Thickness (in)	1.35	1.68	1.68
Density (lb/in^3)	0.16	0.056	0.056
Weight (lbs)	204	91	91

Table MAF-12. Radius Circular Taper and Factor of Safety of SAUVIM Pressure Vessels

	APC-2/AS4-19" d=0.024 (in)		APC-2/AS4-21" d=0.024 (in)	
d	R (in)	Factor of Safety	R (in)	Factor of Safety
100%	46	0.78	46	0.78
90%	51	1.08	51	1.08
80%	58	1.57	58	1.57
70%	66	1.61	66	1.61
60%	77	1.64	77	1.64
50%	92	1.66	92	1.66
40%	115	1.67	115	1.67
30%	153	1.64	153	1.64
20%	230	1.45	230	1.45
10%	460	1.18	460	1.18
0%	∞	1.00	∞	1.00

Table MAF-13. Maximum Stress, Strain, and Displacement Results of the APC-2/AS4 Pressure Vessels with Optimum Tapered Radius for SAUVIM

	APC-2/AS4-19"			APC-2/AS4-21"		
	32°F	70°F	140°F	32°F	70°F	140°F
Radial Stress (psi)	-9,887	-9,655	-11,237	-9,887	-9,655	-11,237
Axial Stress (psi)	-12,276	-12,139	-13,710	-12,276	-12,139	-13,711
Hoop Stress (psi)	-88,735	-88,565	-90,112	-88,735	-88,565	-90,112
Radial Strain (in/in)	-0.0050	-0.0051	-0.0048	-0.0050	-0.0051	-0.0048
Axial Strain (in/in)	-0.0052	-0.0050	-0.0065	-0.0052	-0.0050	-0.0065
Hoop Strain (in/in)	-0.0043	-0.0043	-0.0044	-0.0043	-0.0043	-0.0044
Displacement (Axial) (in)	0.038	0.039	0.036	0.042	0.042	0.040
Factor of Safety	1.67	1.67	1.72	1.67	1.67	1.73

Table MAF-14. Bifurcation Pressure of the Pressure Vessels for SAUVIM

Material	Bifurcation Buckling Pressure (psi)	Wall Thickness (in)
APC-2/AS4-21"	32,911	1.188
APC-2/AS4-19"	34,504	1.188

Table MAF-15. Non-Linear Maximum Stress, Strain, and Displacement Results of the 19" and 21" APC-2/AS4 with Optimum Tapered Radius Pressure Vessels

	APC-2/AS4-19"			APC-2/AS4-21"		
	32°F	70°F	140°F	32°F	70°F	140°F
Radial Stress (psi)	-9,883	-9,648	-11,233	-9,883	-9,649	-11,233
Axial Stress (psi)	-12,370	-12,235	-13,754	-12,371	-12,235	-13,754
Hoop Stress (psi)	-89,001	-88,830	-90,386	-89,004	-88,834	-90,390
Radial Strain (in/in)	-0.0050	-0.0051	-0.0048	-0.0050	-0.0051	-0.0048
Axial Strain (in/in)	-0.0052	-0.0050	-0.0065	-0.0052	-0.0050	-0.0065
Hoop Strain (in/in)	-0.0043	-0.0043	-0.0044	-0.0043	-0.0043	-0.0044
Displacement (Axial) (in)	0.038	0.039	0.036	-0.042	0.042	0.040
Factor of Safety	1.67	1.66	1.72	1.67	1.66	1.72

Table MAF-16. List of Major Components of the SAUVIM Vehicle with various
Components Estimated Weight

Componets	Weight (lbs)
Cameras	109
Arms (two)	216
Batteries	1,459
Ballasts	1,260
Pressure Vessels	1,742
Thrusters	219
Fins	125
Foam	6,140
Fairing	929
Frame	1,200
Total Weigth	**13,400**

Table MAF-17. Mechanical Properties of the Candidate Materials for the Frame

	Tensile Strength (Ksi)	Yield Strength (Ksi)	Young's Modulus (Msi)	Density (lb/in^3)
Aluminum	35-45	31-40	10	0.10
Steel	56-72	41-55	30	0.26
Titanium	130-144	120-134	16.5	0.16

Table MAF-18. Results of Maximum Stresses, Displacements, and Factor of Safety for the
Frame

	Arms at the Extended Position			Arms at the Rest Position		
	δ_{max}(in)	σ_{max}(psi)	Factor of Safety	δ_{max}(in)	σ_{max}(psi)	Factor of Safety
Dry Analysis	0.007	1,270	9.45	0.007	1,840	6.52
Lifting Analysis	0.022	2,350	5.11	0.020	2,350	5.11
Wet Analysis	0.017	1,200	10.00	0.017	1,610	7.45
Wet/Dynamic Analysis	0.021	2,240	5.36	0.020	2,720	4.41
Note: The factor of safety is calculated based on the weldment strength of Aluminum (i.e., 12,000 psi)						

Table MAF-19. Unidirectional Lamina Properties of Kevlar-49/Epoxy and Graphite/Epoxy
(Mallick93)

Property	Kevlar-49/Epoxy	Graphite/Epoxy
E_1 (Pa)	7.59E+10	1.448E+11
E_2 (Pa)	5.52E+09	9.655E+09
E_3 (Pa)	5.52E+09	9.655E+09
G_{12} (Pa)	2.07E+09	5.862E+09
G_{13} (Pa)	2.07E+09	5.862E+09
G_{23} (Pa)	1.54E+09	3.462E+09
v_{12}	3.40E-01	2.50E-01
v_{13}	3.40E-01	2.50E-01
v_{23}	4.71E-01	4.07E-01
Density (g/m^{3})	1.38E+06	1.58E+06

Table MAF-20. 3-D Effective Orthotropic Properties of Graphite-Kevlar/Epoxy Hybrid and
Graphite/Epoxy Plain-Weave Woven Plies using 3-D Crimp Model (Ng00a)

3-D Effective Properties from Crimp Model	Graphite/Epoxy in Weft direction	Kevlar/Epoxy in Weft direction	Graphite-Kevlar/Epoxy lamina (Graphite in x-direction)	Graphite/Epoxy lamina
Ex (GPa)	27.16	18.74	27.16	31.22
Ey (GPa)	--	--	18.74	31.22
Ez (GPa)	7.82	6.98	7.40	9.29
vxy	0.02	0.04	0.02	0.02
vxz	0.44	0.53	0.44	0.45
vyz	--	--	0.53	0.45
Gxy (GPa)	3.37	2.77	3.07	5.08
Gxz (GPa)	3.78	2.48	3.78	4.46
Gyz (GPa)	--	--	2.48	4.46

```
                          ┌─────────┐
                          │  Start  │
                          └─────────┘
                               │
                               ▼
              ┌──────────────────────────────────┐
              │        Hygrothermal Effects        │
              └──────────────────────────────────┘
                    │                    │
                    ▼                    ▼
          ┌──────────────┐      ┌──────────────────┐
          │ Stress Analysis│    │ Buckling Analysis │
          └──────────────┘      └──────────────────┘
                    │                    │
                    ▼                    ▼
              ┌──────────────────────────────────┐
              │          Material Selection        │
              │  Ti-6Al-4V, Graphite/Epoxy, APC-2/AS4 │
              └──────────────────────────────────┘
                               │
                               ▼
                    ┌──────────────────┐
                    │ Design of End-cap │
                    └──────────────────┘
                               │
                               ▼
         ┌────────────────────────────────────────────┐
         │ Detailed Analyses of the Pressure Vessel and End-cap │
         └────────────────────────────────────────────┘
                               │
                               ▼
                ┌──────────────────────────┐
                │ Fabrication of Pressure Vessel │
                │       and the End-caps       │
                └──────────────────────────┘
                               │
                               ▼
                ┌──────────────────────────┐
                │    Pressure Vessel Test    │
                └──────────────────────────┘
                               │
                               ▼
                          ┌─────────┐
                          │   End   │
                          └─────────┘
```
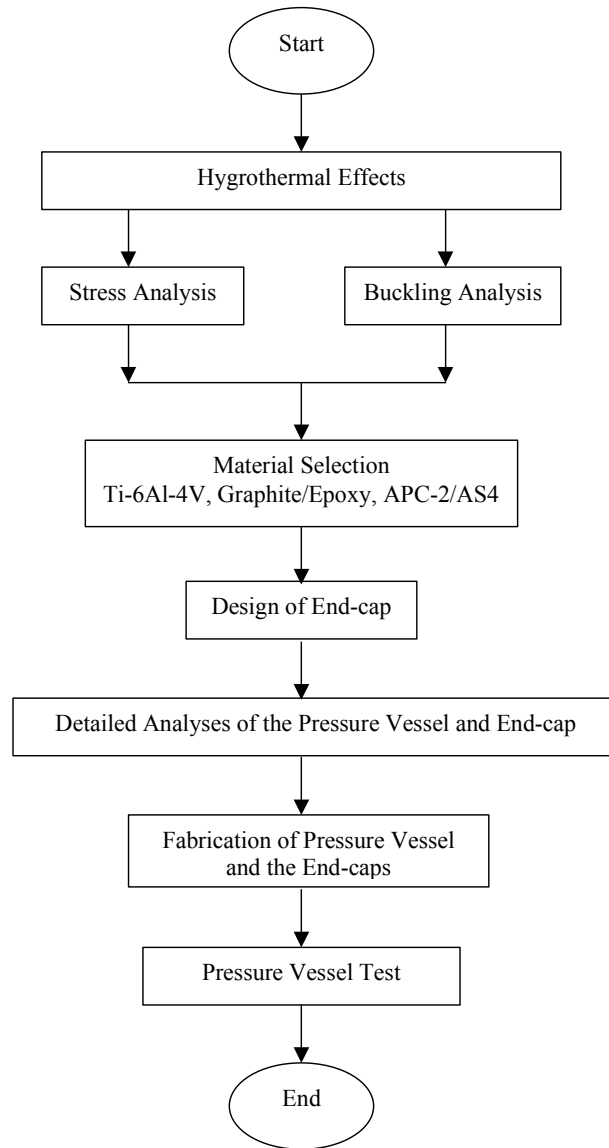
Figure MAF-1. Development Methodology of the Pressure Vessels
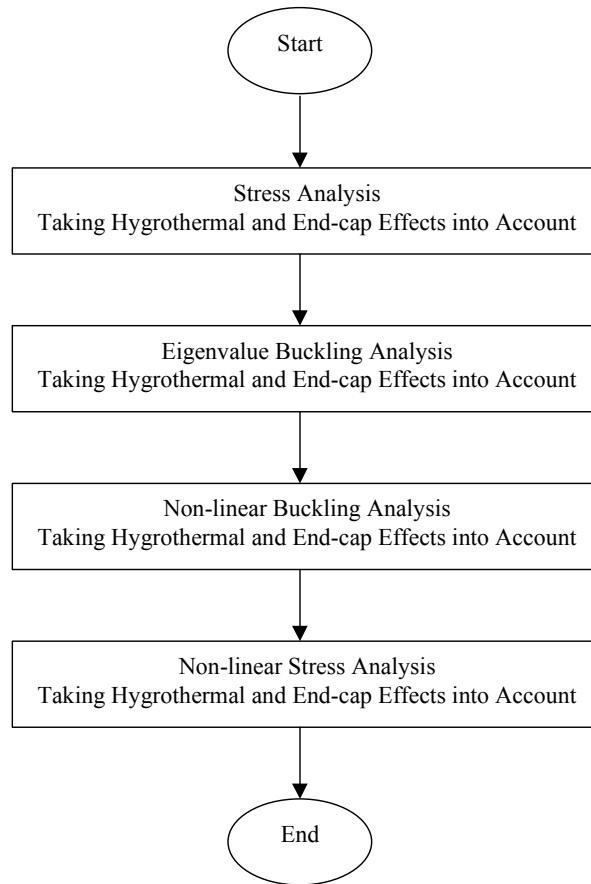
Figure MAF-2. Analysis Procedure for the Pressure Vessels
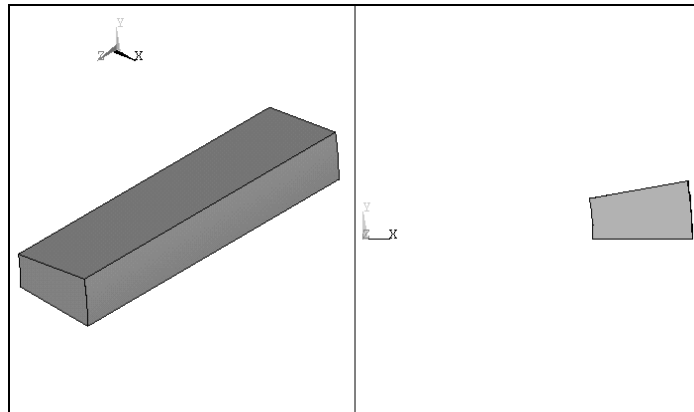
Figure MAF-3. Model of Ten Degrees Wedge of the Pressure Vessel in Stress Analysis
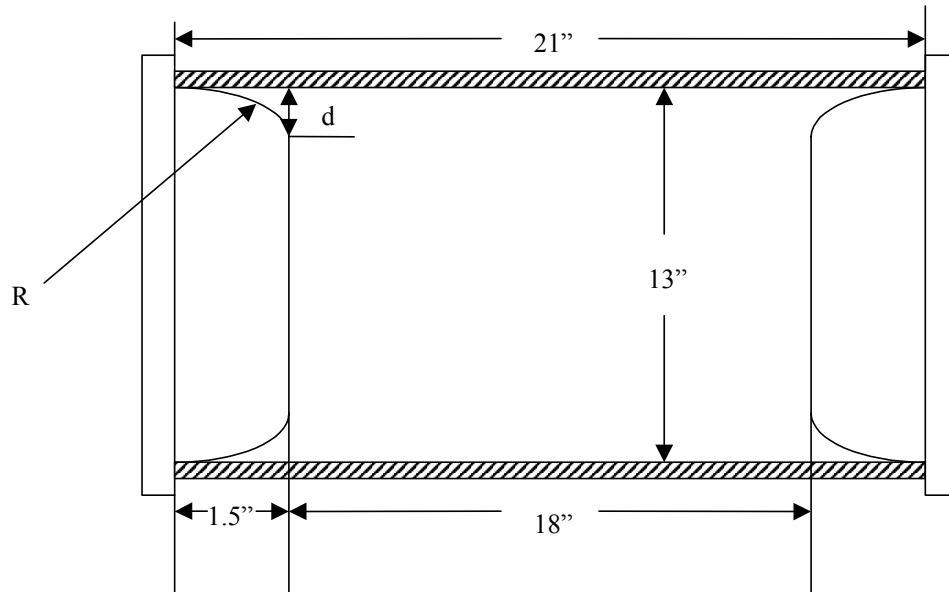
Figure MAF-4. Schematic of the Pressure Vessel with the Contoured-End Plug-supported

End-Cap
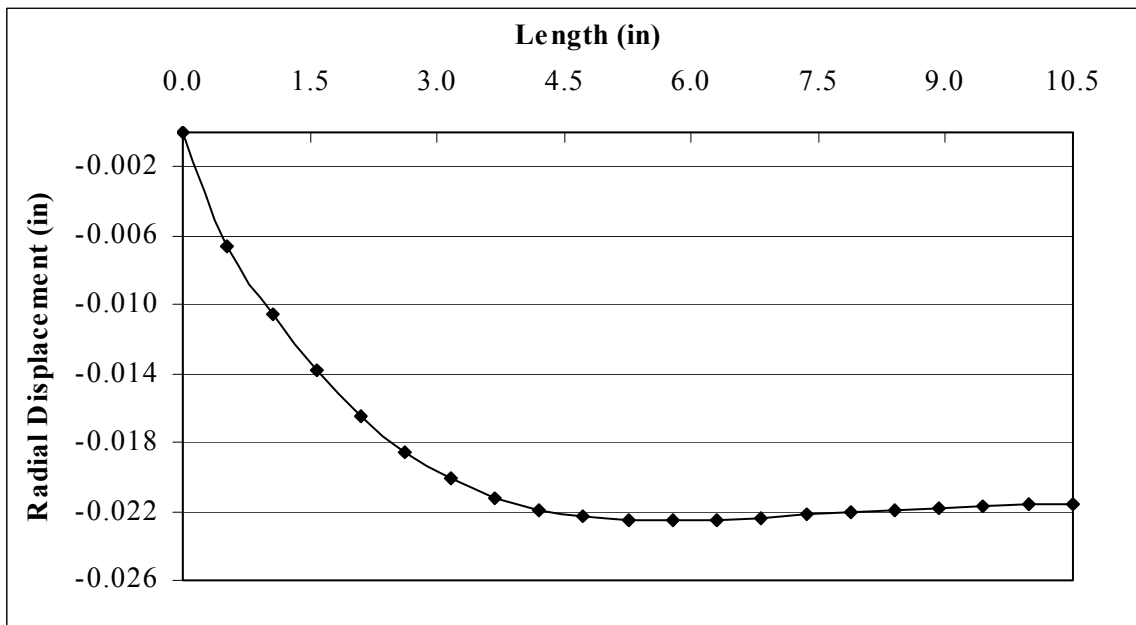
Figure MAF-5. Radial Displacement from the Cylinder End to the Mid-length of the Ti-6Al-
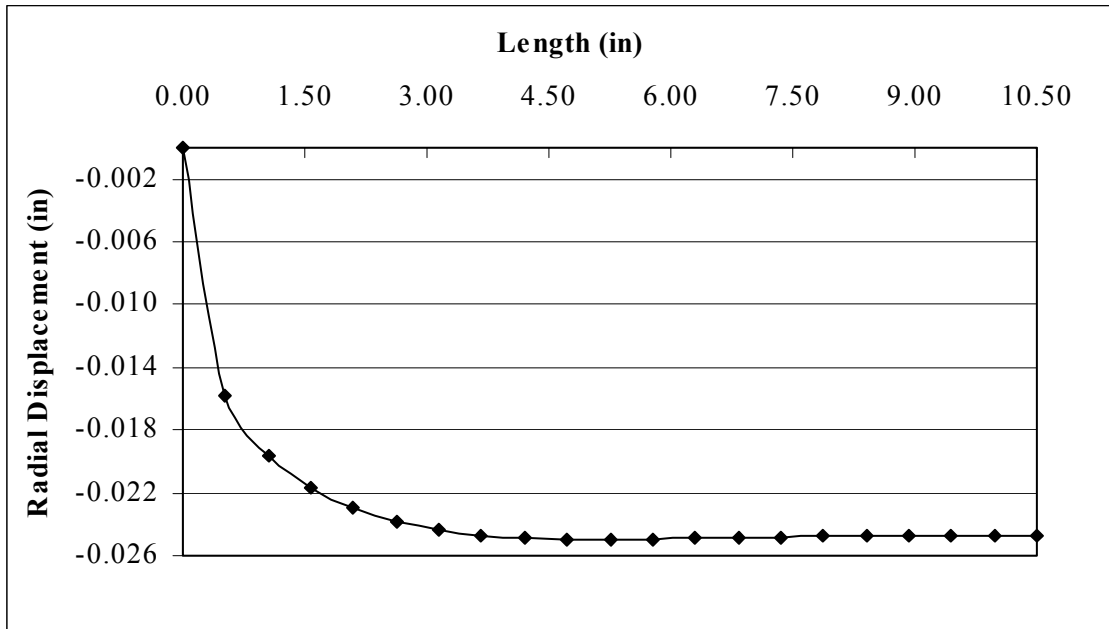
4V Pressure Vessel

Figure MAF-6. Radial Displacement from the Cylinder End to the Mid-length of the APC-

2/AS4 Pressure Vessel
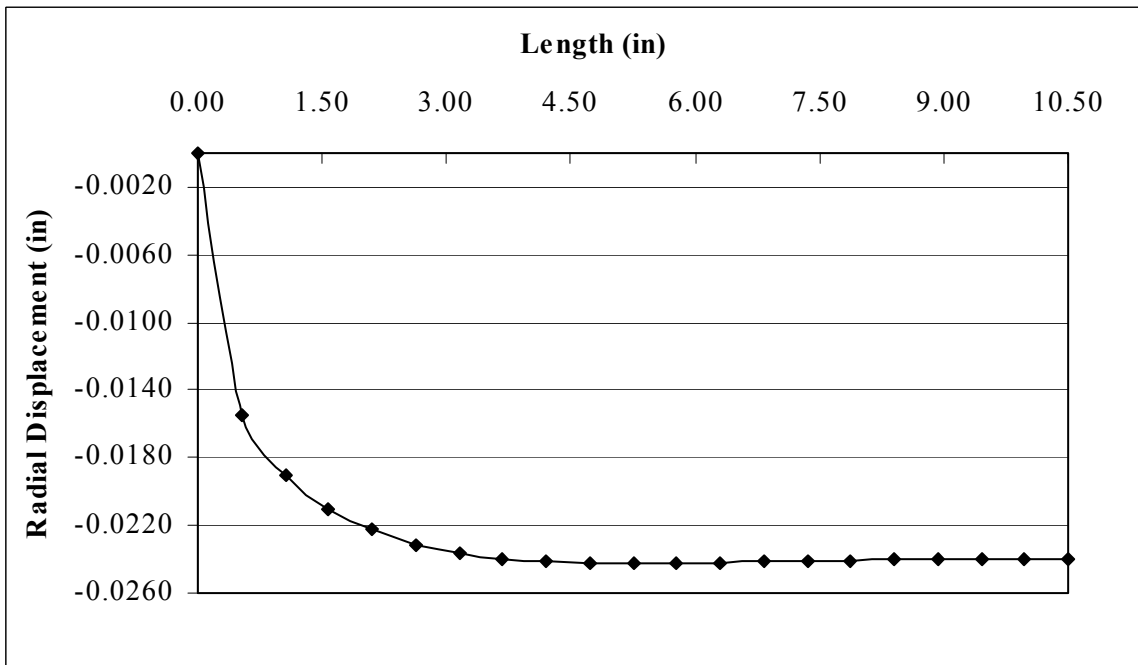
Figure MAF-7. Radial Displacement from the Cylinder End to the Mid-length of the

Graphite/Epoxy Pressure Vessel
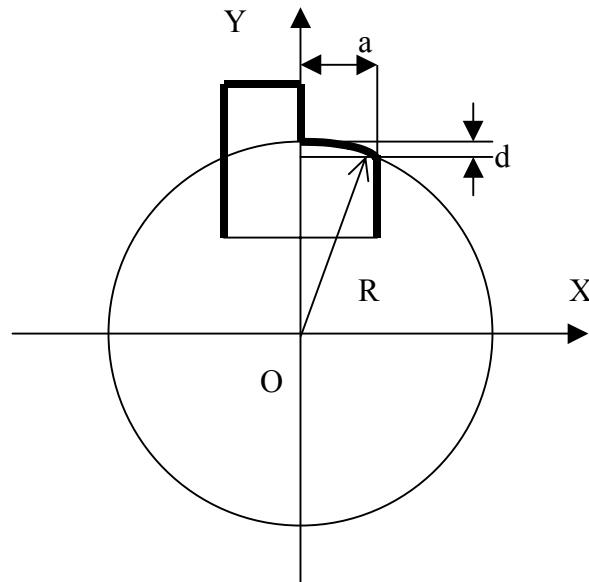
Figure MAF-8. End-cap and its Plug Circle with Radius R
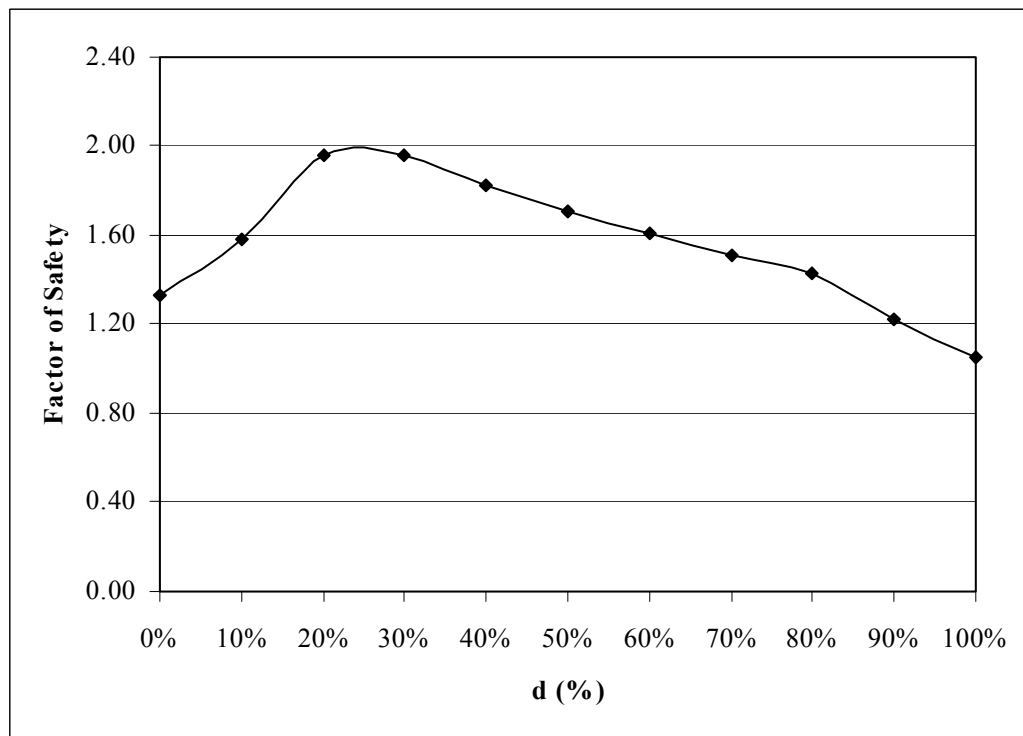
Figure MAF-9. Factor of Safety Based on different d% for the Ti-6Al-4V Pressure Vessel
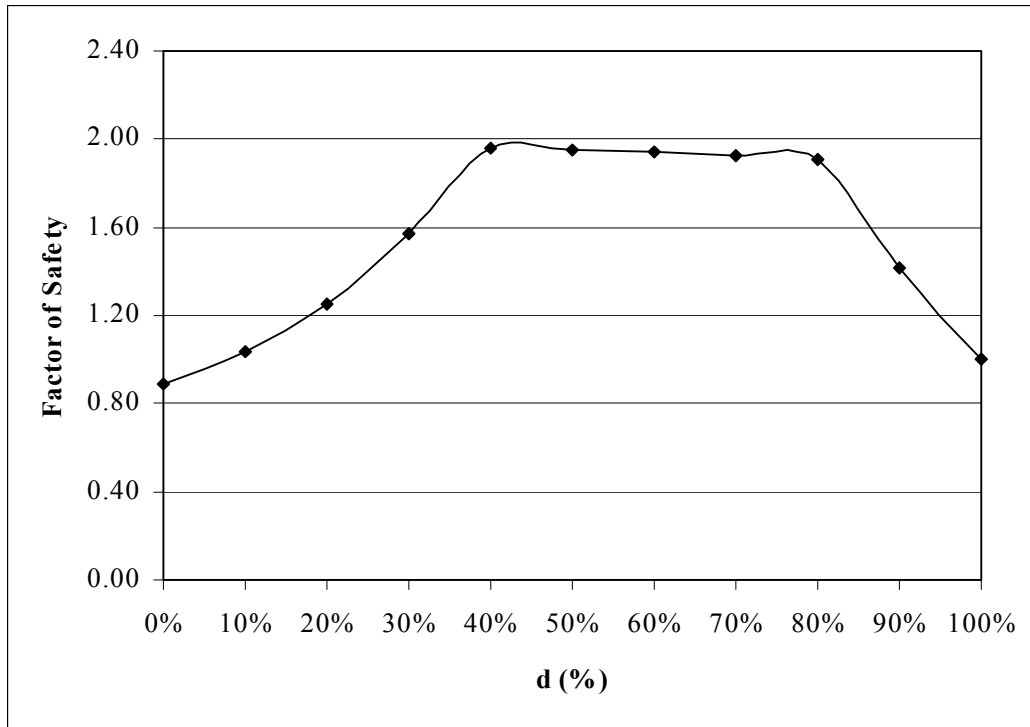
Figure MAF-10. Factor of Safety Based on different d% for the APC-2/AS4 Pressure Vessel
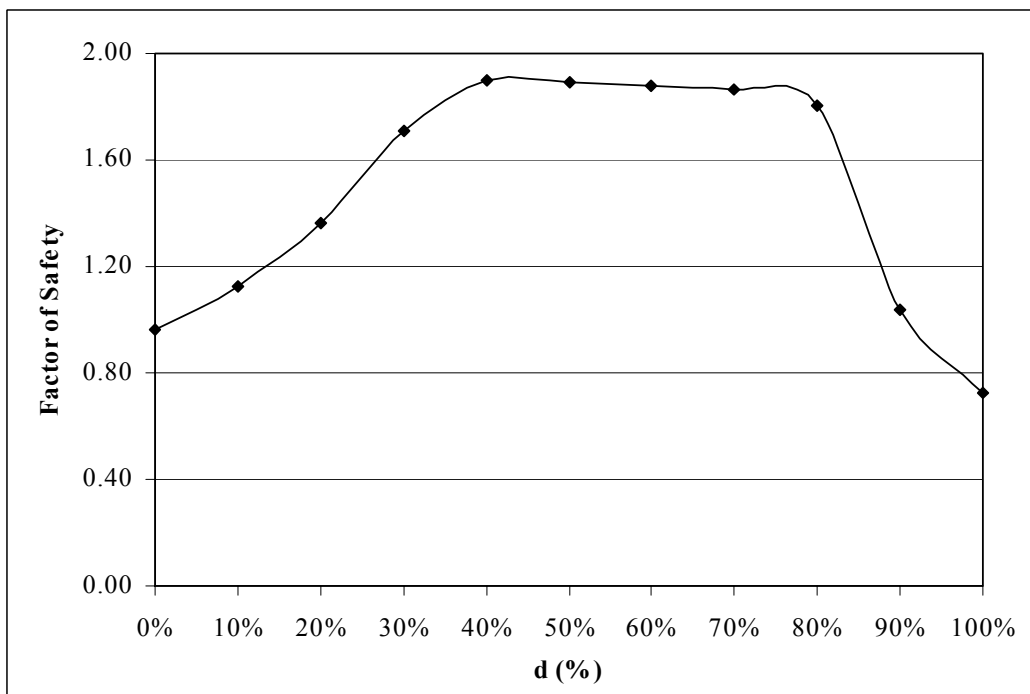
Figure MAF-11. Factor of Safety Based on different d% for the Graphite/Epoxy Pressure
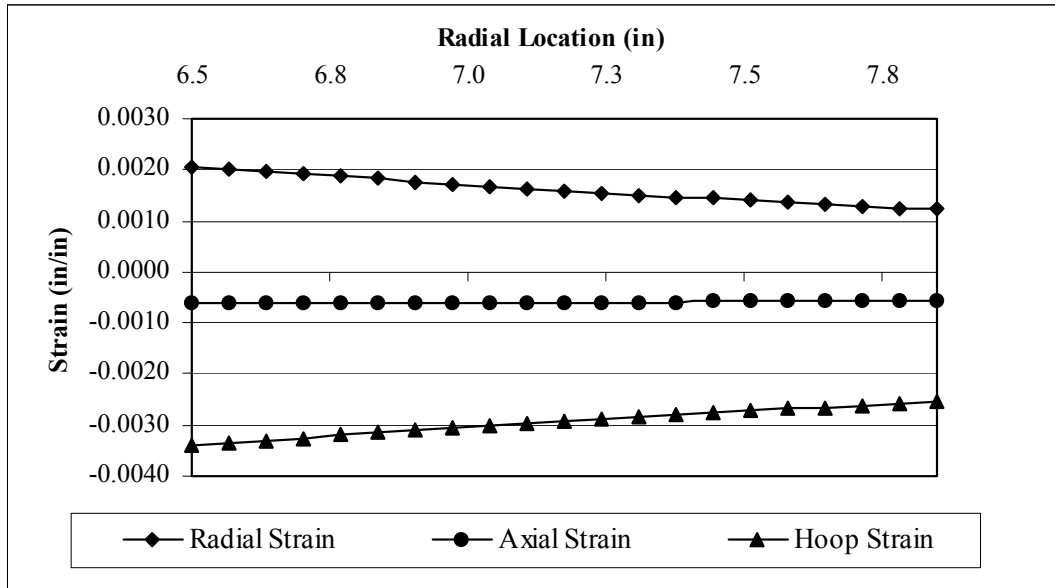
Vessel

Figure MAF-12. Strain Distributions through the Thickness at the Mid-length of the Ti-6Al-

4V Pressure Vessel at 70°F
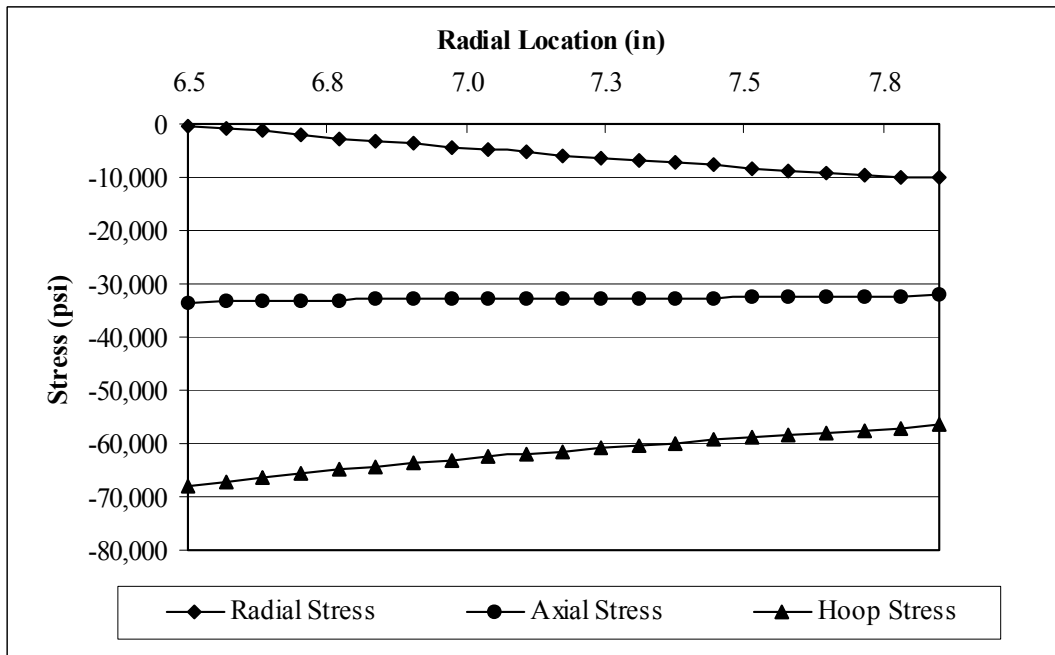
Figure MAF-13. Stress Distributions through the Thickness at the Mid-length of the Ti-6Al-

4V Pressure Vessel at 70°F
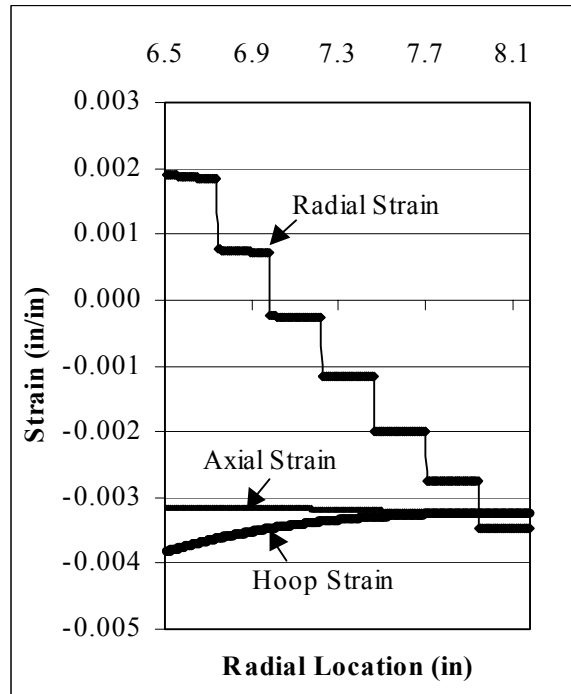
Figure MAF-14. Strain Distributions through the Thickness at the Mid-length of the APC-

2/AS4 Pressure Vessel at 70°F
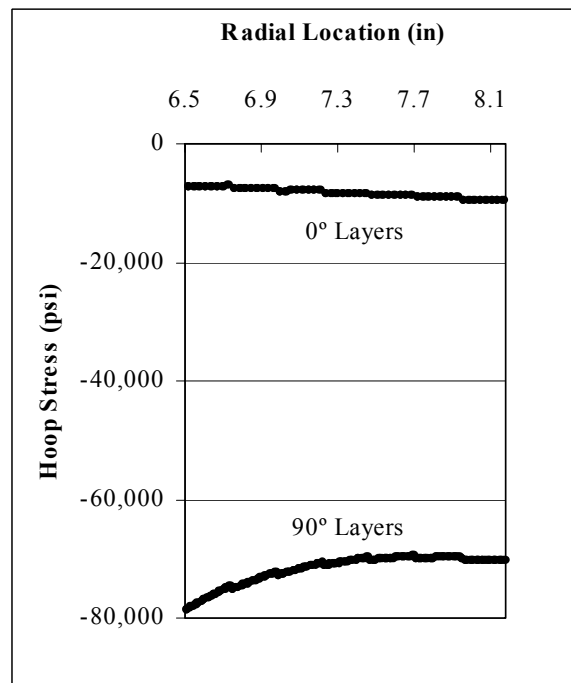
Figure MAF-15. Hoop Stress Distribution through the Thickness at the Mid-length of the

APC-2/AS4 Pressure Vessel at 70°F
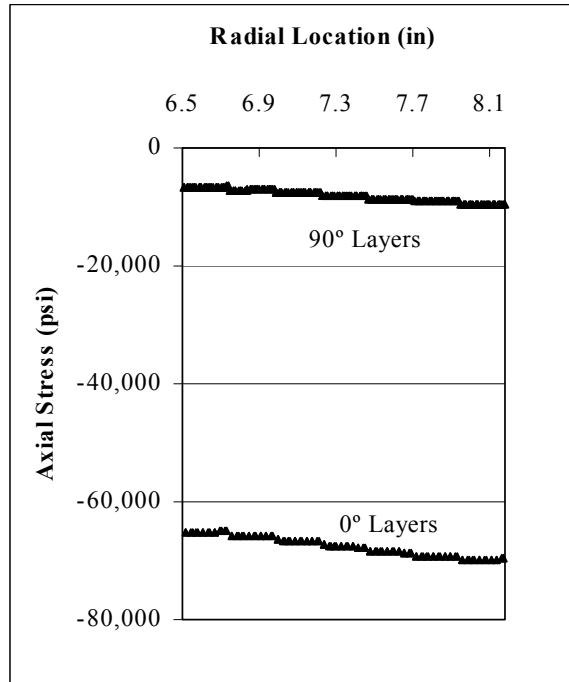
Figure MAF-16. Axial Stress Distribution through the Thickness at the Mid-length of the

APC-2/AS4 Pressure Vessel at 70°F
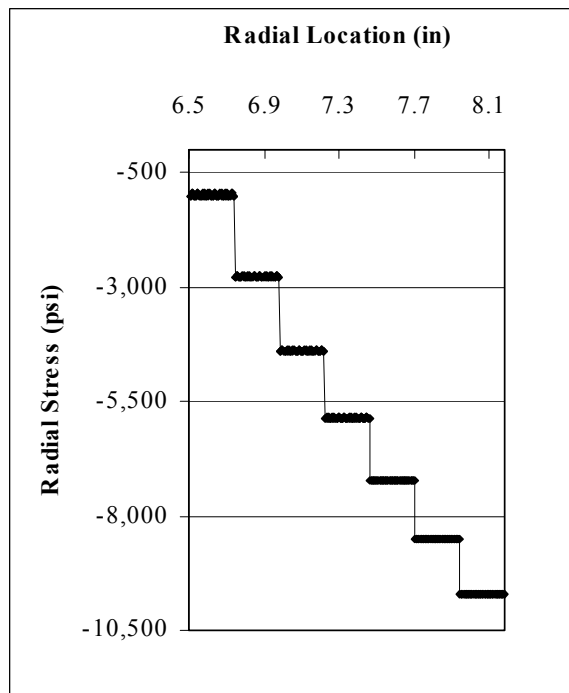
Figure MAF-17. Radial Stress Distribution through the Thickness at the Mid-length of the

APC-2/AS4 Pressure Vessel at 70°F
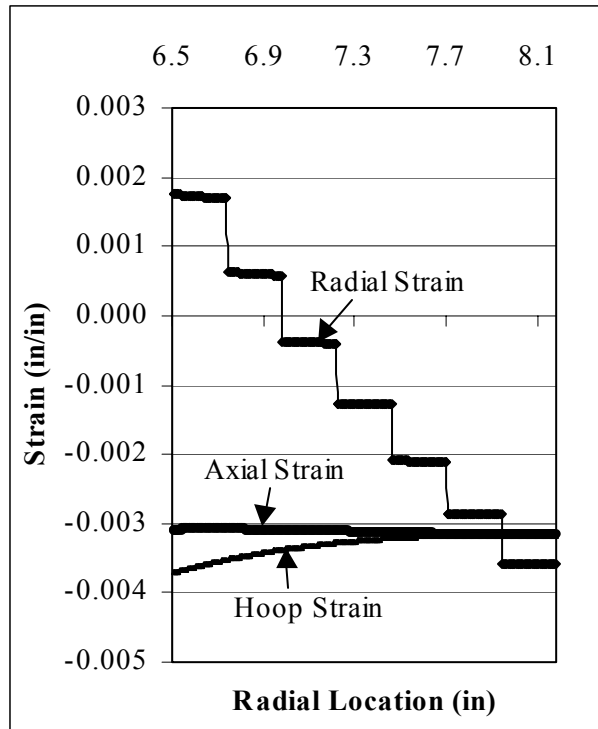
Figure MAF-18. Strain Distributions through the Thickness at the Mid-length of the Graphite/Epoxy Pressure Vessel at 70°F
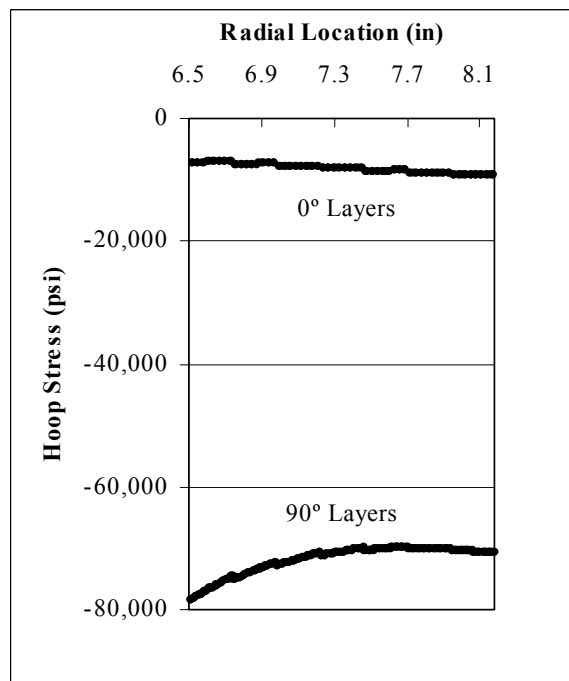
Figure MAF-19. Hoop Stress Distribution through the Thickness at the Mid-length of the Graphite/Epoxy Pressure Vessel at 70°F
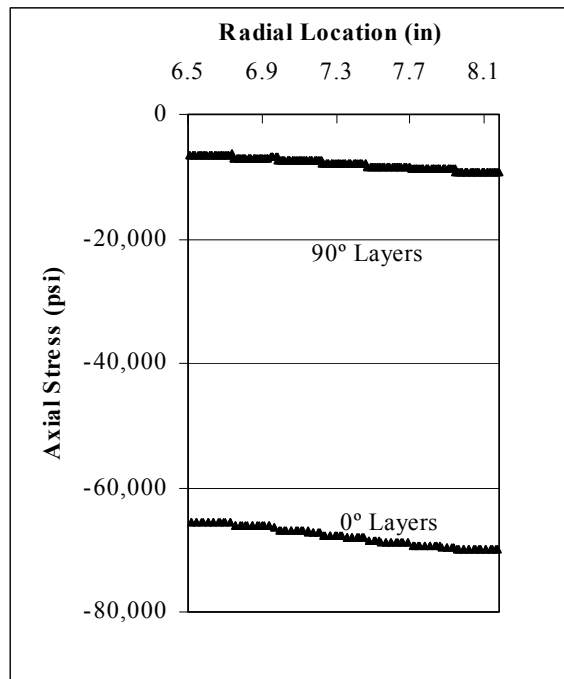
Figure MAF-20. Axial Stress Distribution through the Thickness at the Mid-length of the
Graphite/Epoxy Pressure Vessel at 70°F
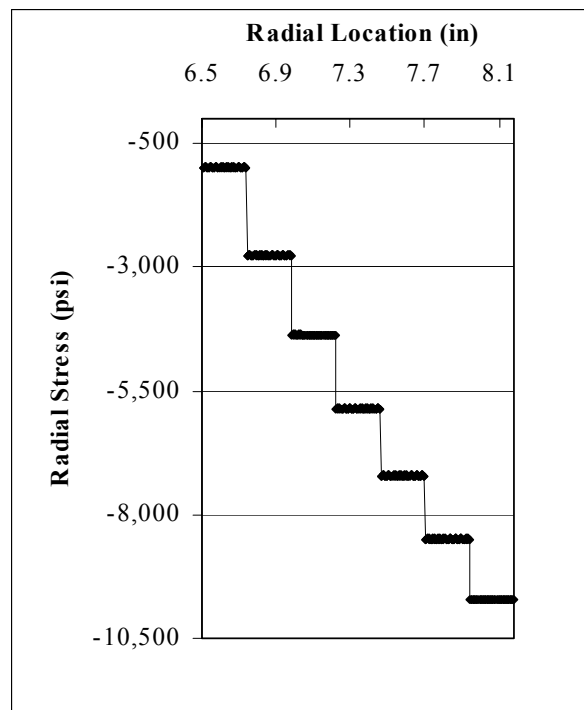
Figure MAF-21. Radial Stress Distribution through the Thickness at the Mid-length of the
Graphite/Epoxy Pressure Vessel at 70°F
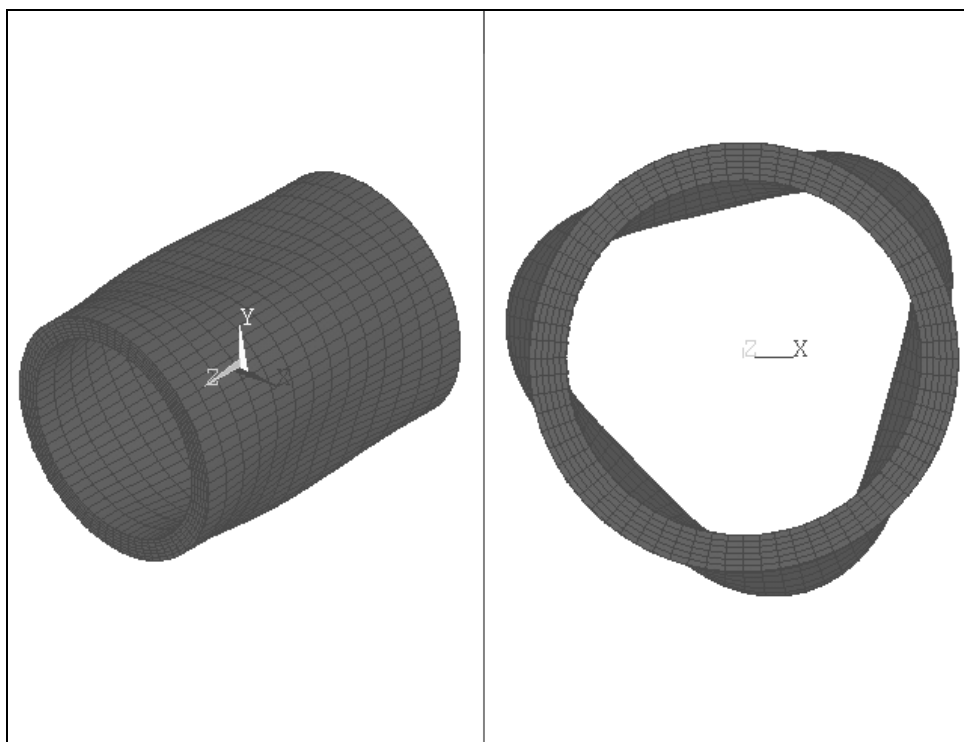
Figure MAF-22. Full Buckling Mode of the Ti-6Al-4V Pressure Vessel
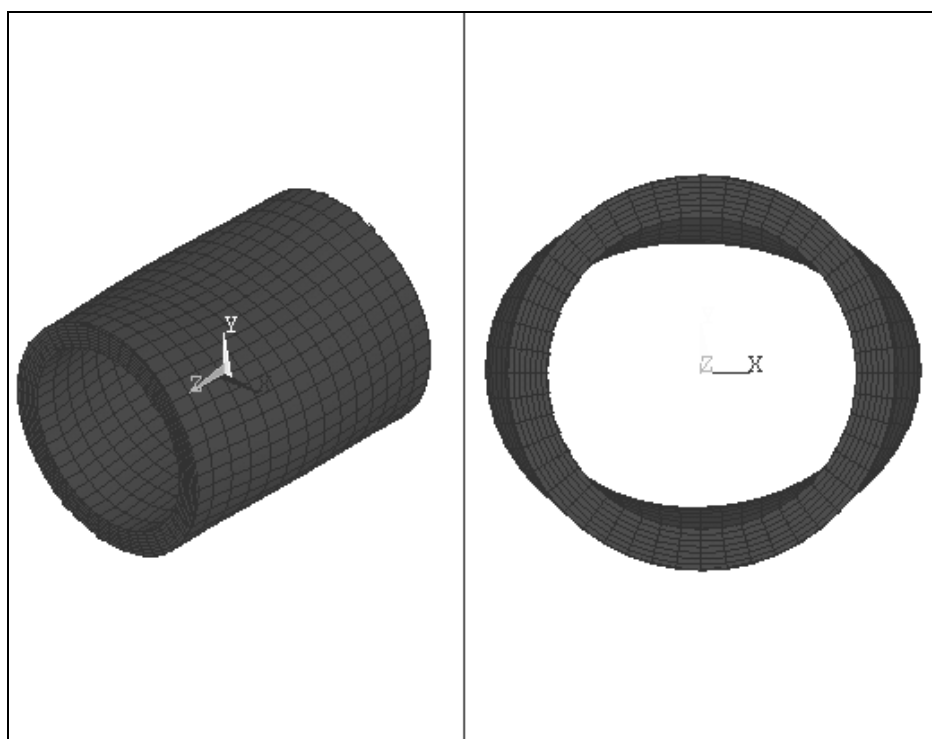
Figure MAF-23. Typical Full Buckling Mode of the Composite Pressure Vessels
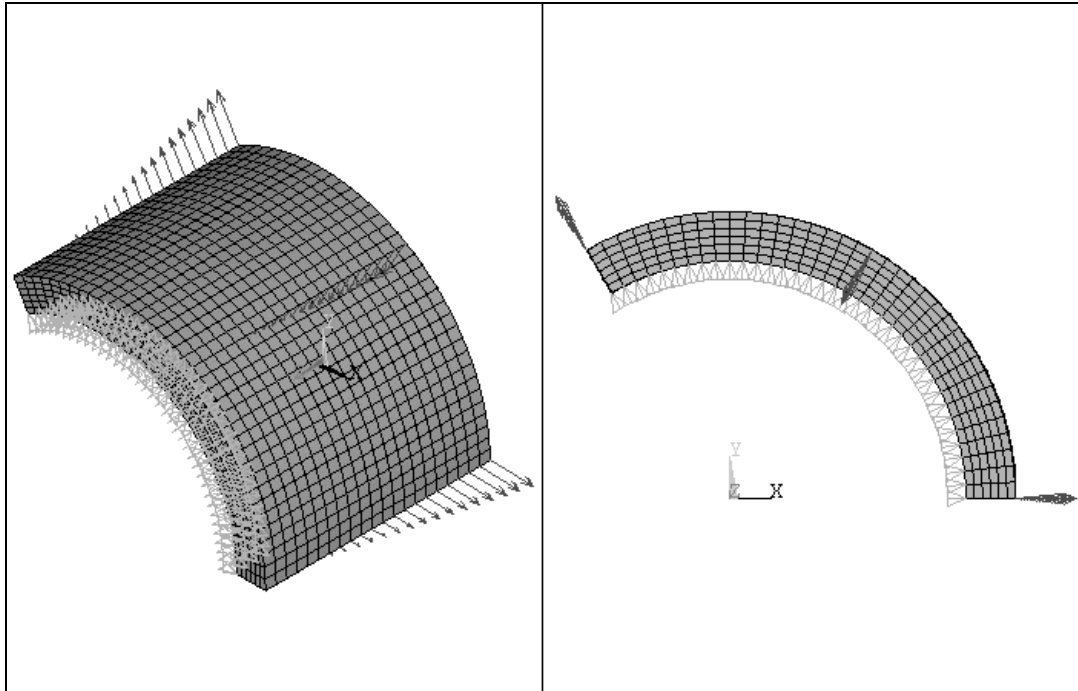
Figure MAF-24. One-Sixth of the Model of the Ti-6Al-4V Pressure Vessel
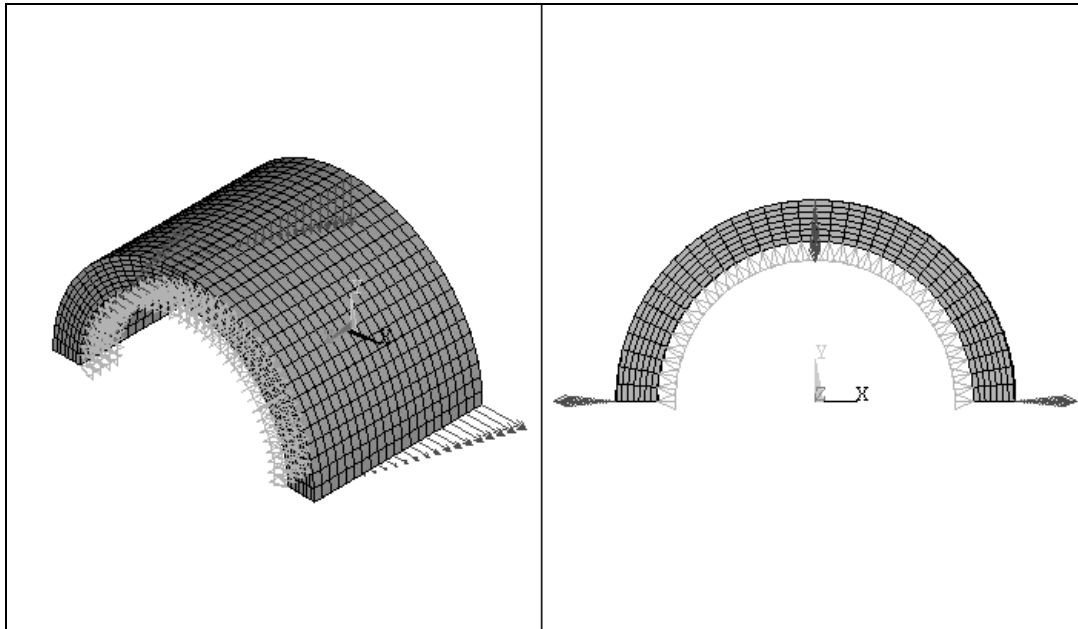
Figure MAF-25. One-fourth of the Model of the Composite Pressure Vessels
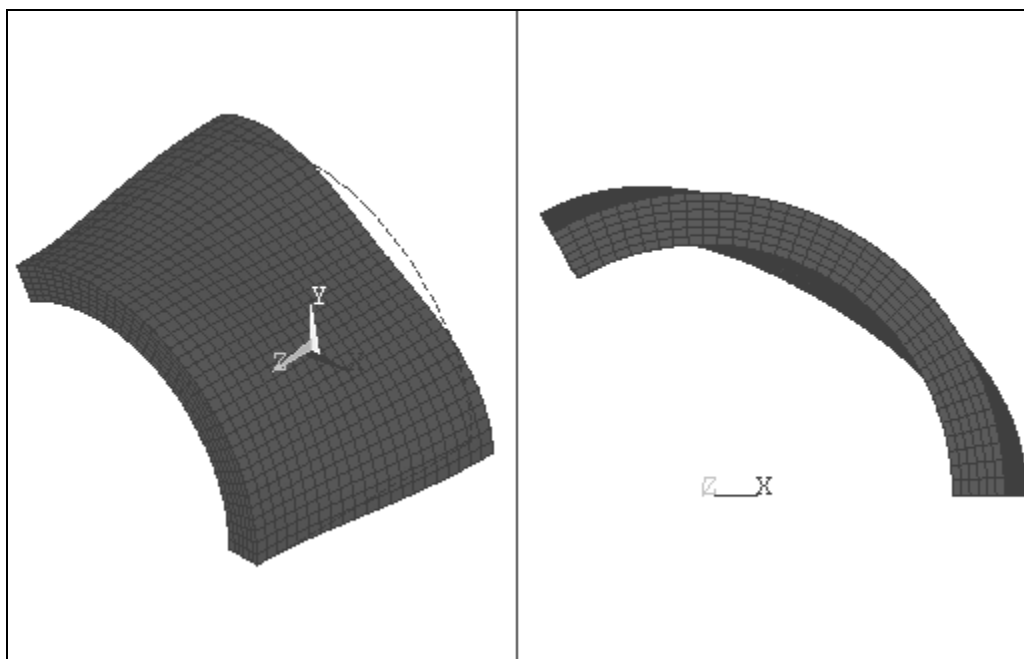
Figure MAF-26. Typical First Mode Shape of One-sixth of the Ti-6Al-4V Pressure Vessel
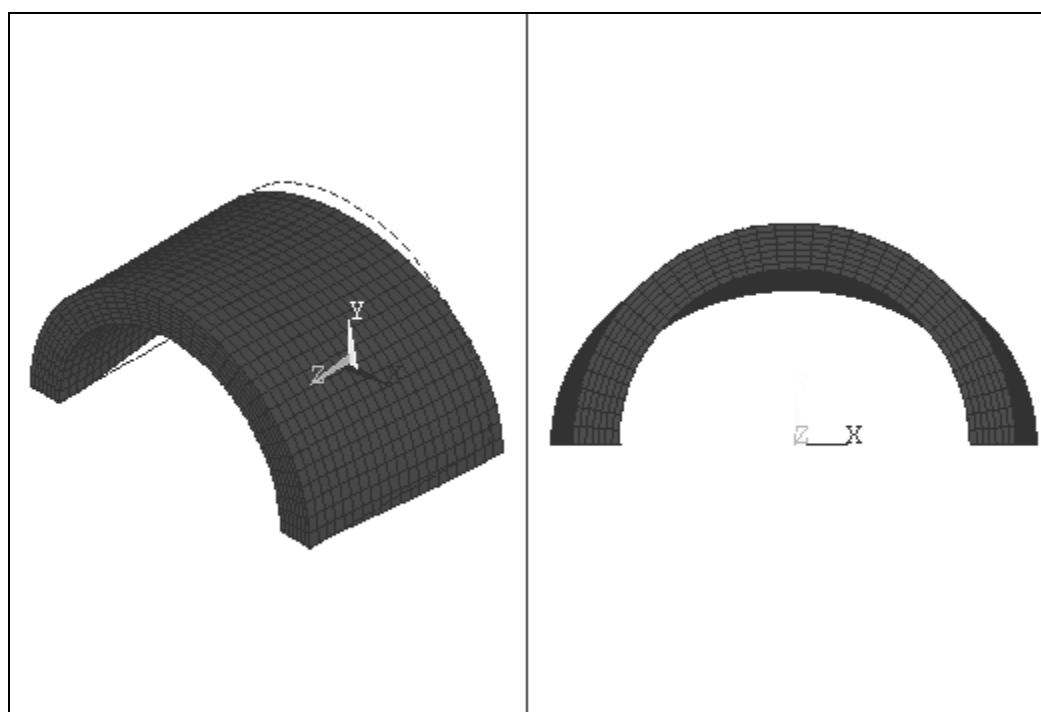
Figure MAF-27. Typical First Mode Shape of One-fourth of the Composite Pressure Vessels
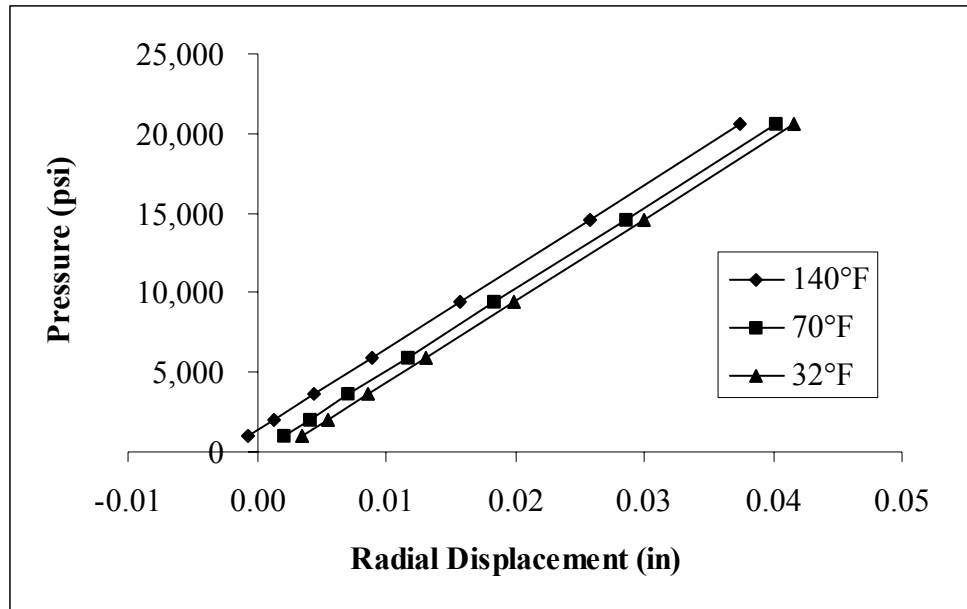
Figure MAF-28. Pressure-Displacement Curve of the Ti-6Al-4V Pressure Vessel

Considering Thermal Effects at Mid-length
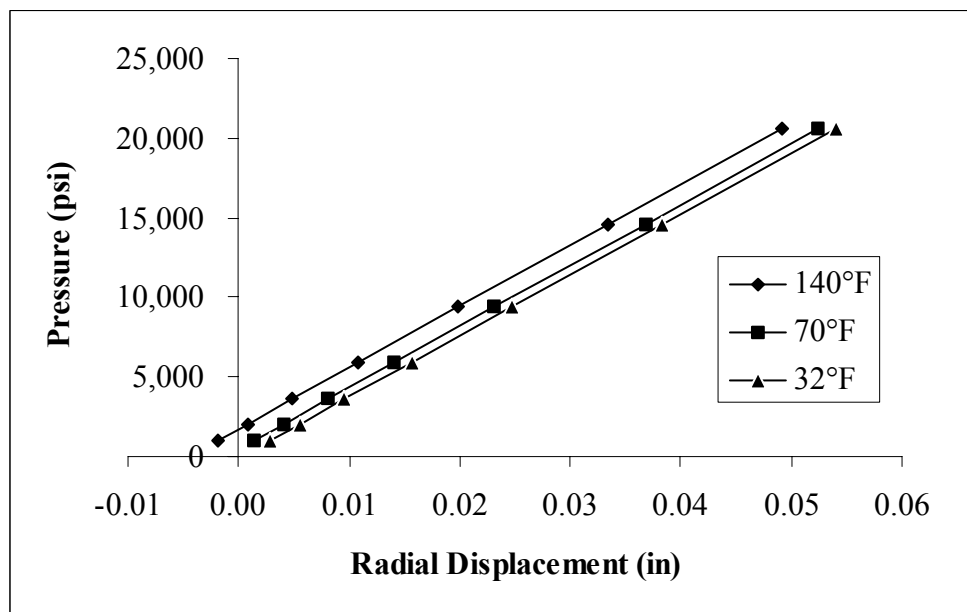
Figure MAF-29. Pressure-Displacement Curve of the APC-2/AS4 Pressure Vessel

Considering Hygrothermal Effects at Mid-length
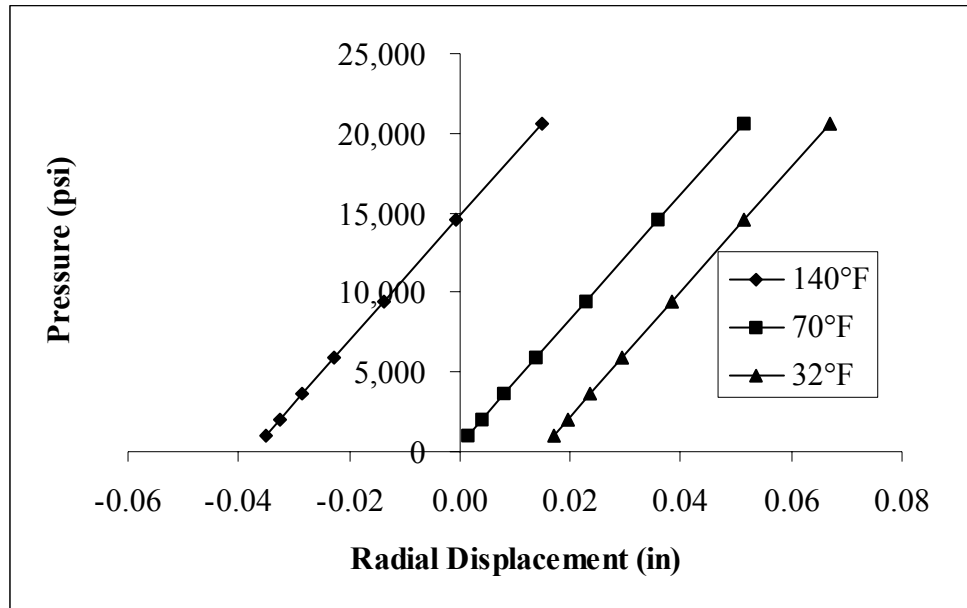
Figure MAF-30. Pressure-Displacement Curve of the Graphite/Epoxy Pressure Vessel

Considering Hygrothermal Effects at Mid-length
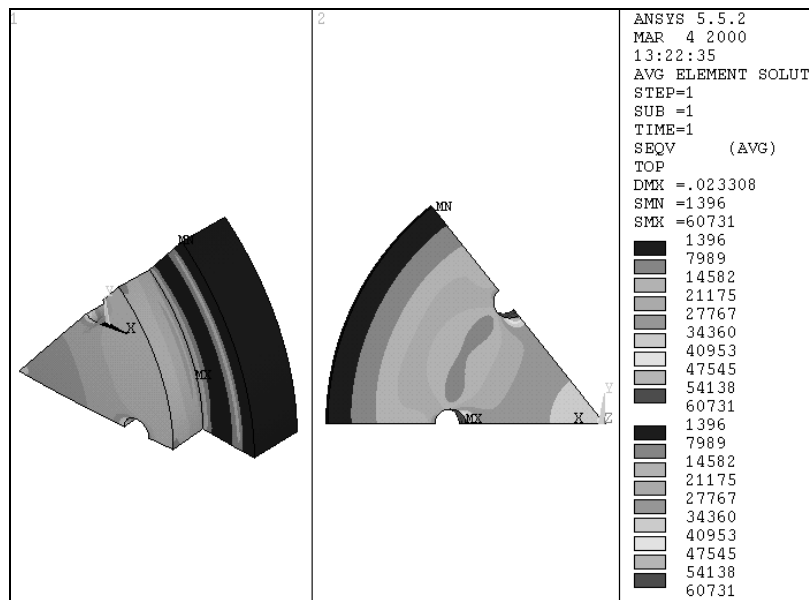
Figure MAF-31. Von Mises Stress Distribution of the End-cap
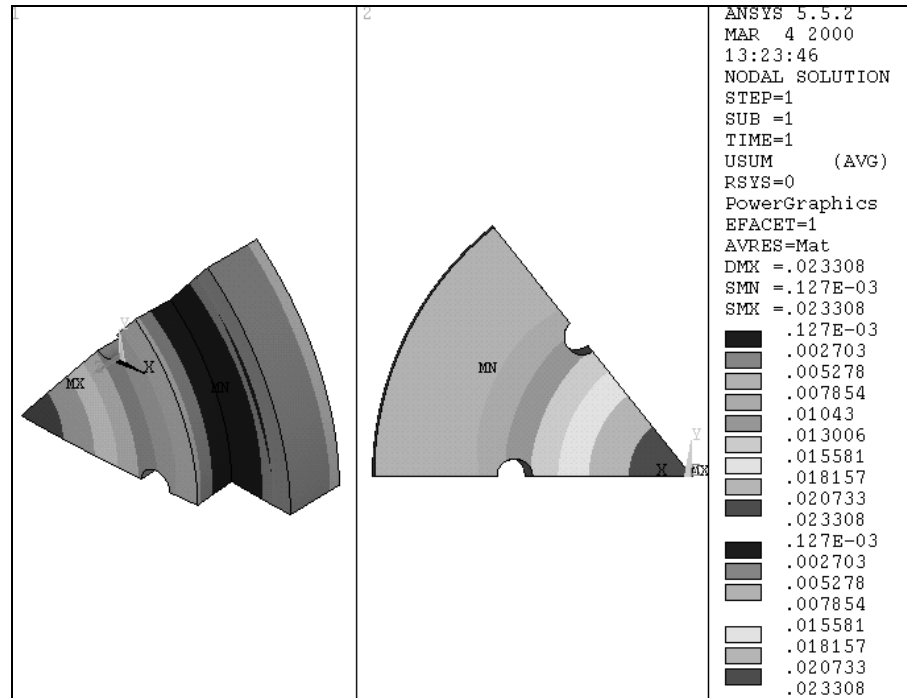
Figure MAF-32. Displacement of the End-cap
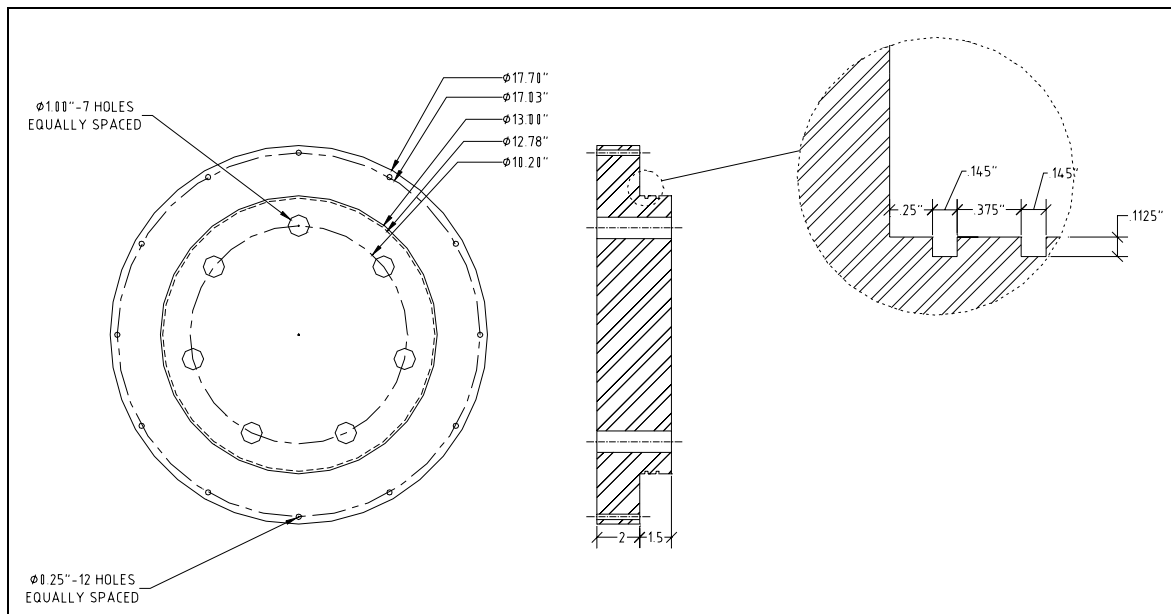
Figure MAF-33. End-Cap Dimensions
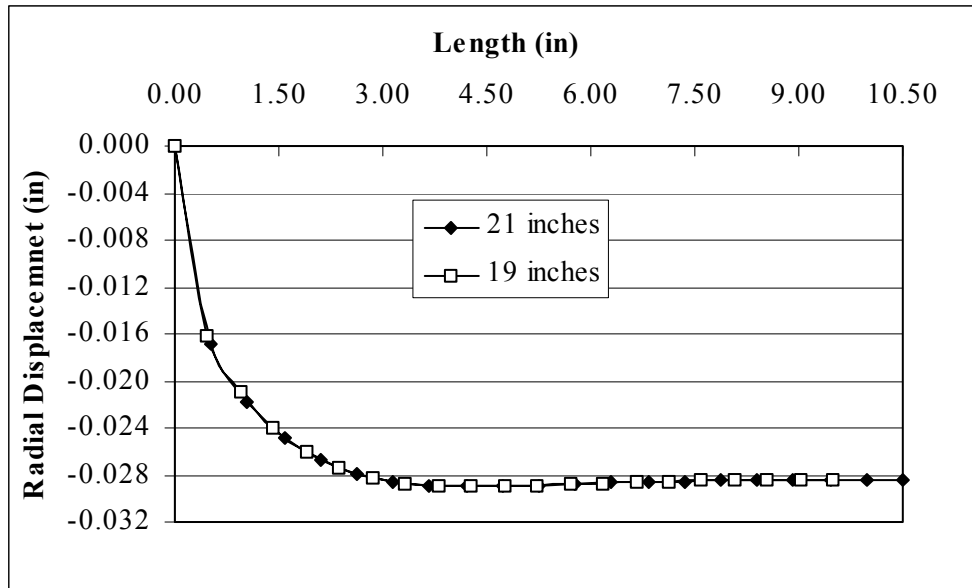
Figure MAF-34. Radial Displacement from the Cylinder End to the Mid-length of the 21"

and 19" Pressure Vessels with Edge Simply Supported for SAUVIM Pressure Vessel
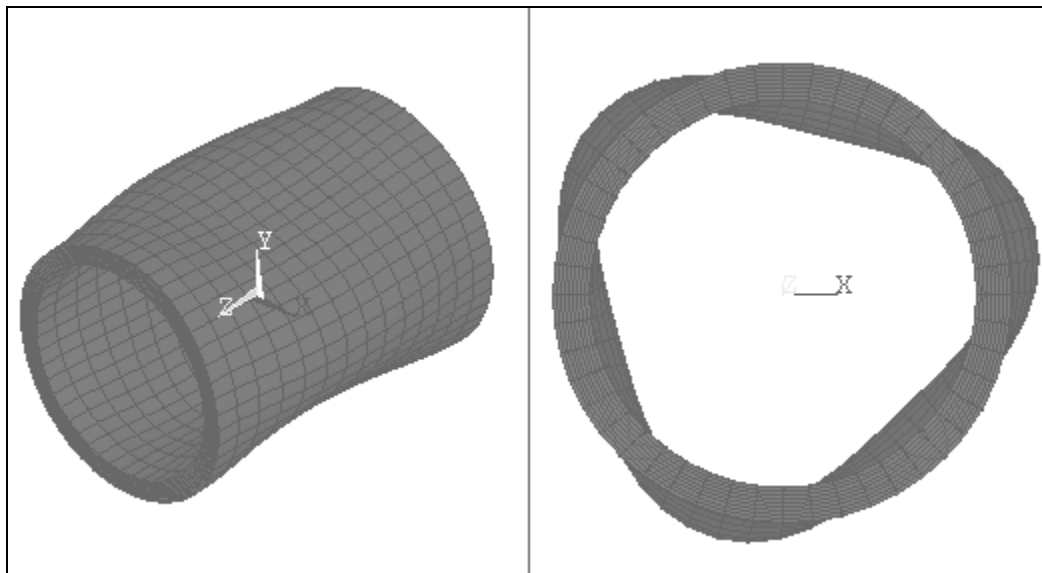
Figure MAF-35. Buckling Mode of the 21" APC-2/AS4 Pressure Vessel for SAUVIM
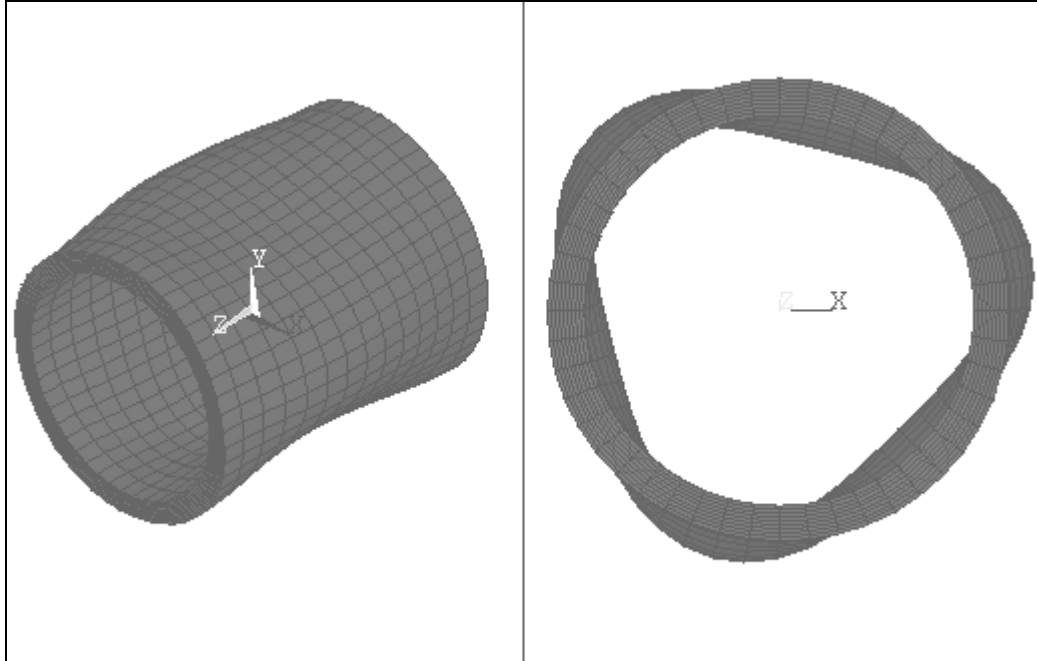
Figure MAF-36. Buckling Mode of the 19" APC-2/AS4 Pressure Vessel for SAUVIM
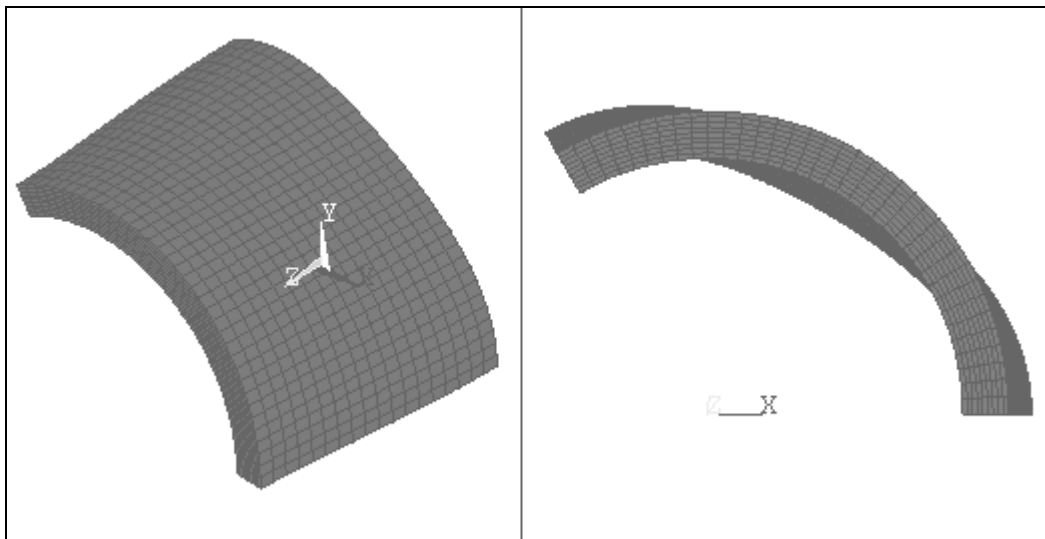
Figure MAF-37. First Mode Shape of the One-sixth of the 21" Pressure Vessel for SAUVIM
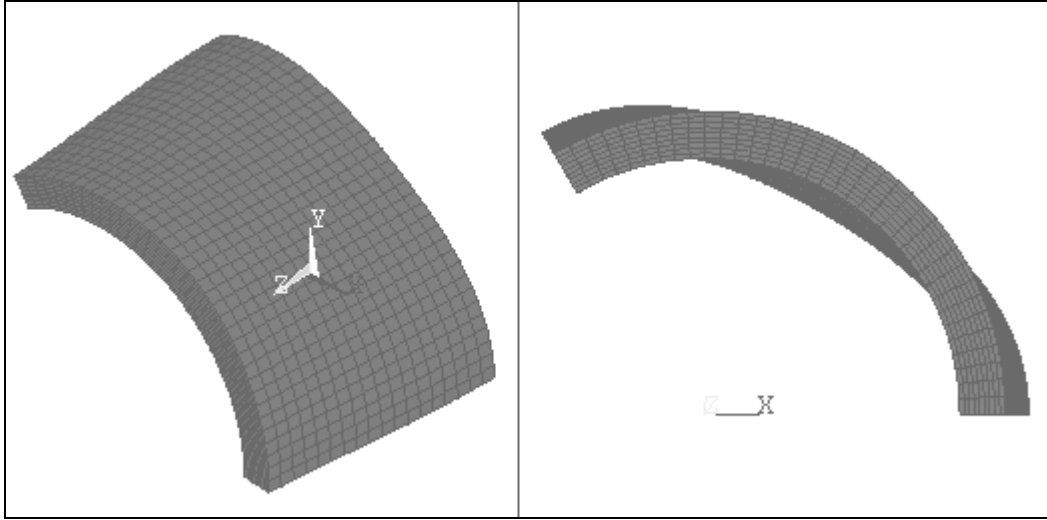
Figure MAF-38. First Mode Shape of the One-sixth of the 19" Pressure Vessel for SAUVIM
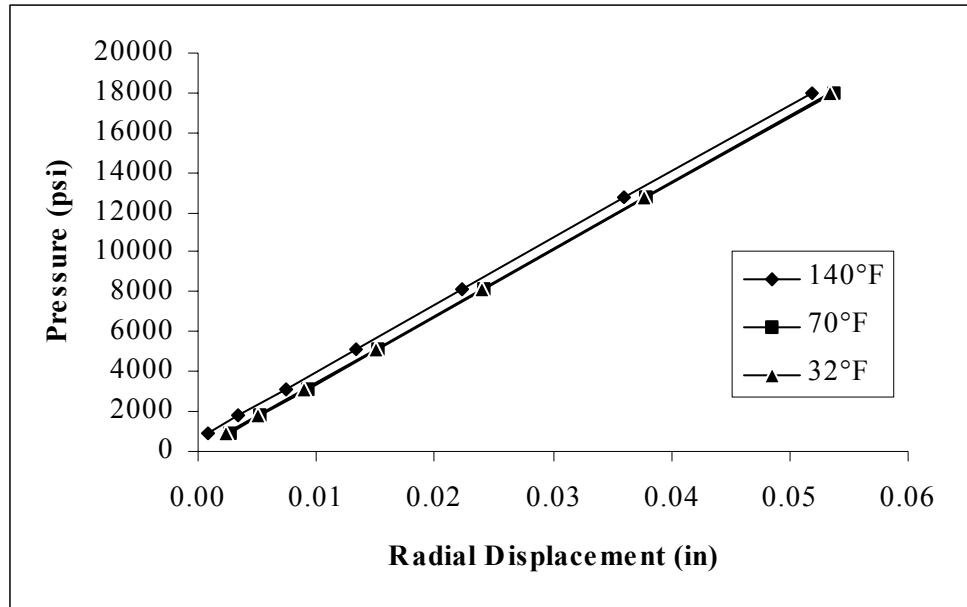
Figure MAF-39. Pressure-Displacement Curve of the 21" APC-2/AS4 Pressure Vessel with

Optimum Tapered Radius Considering Hygrothermal Effects for SAUVIM
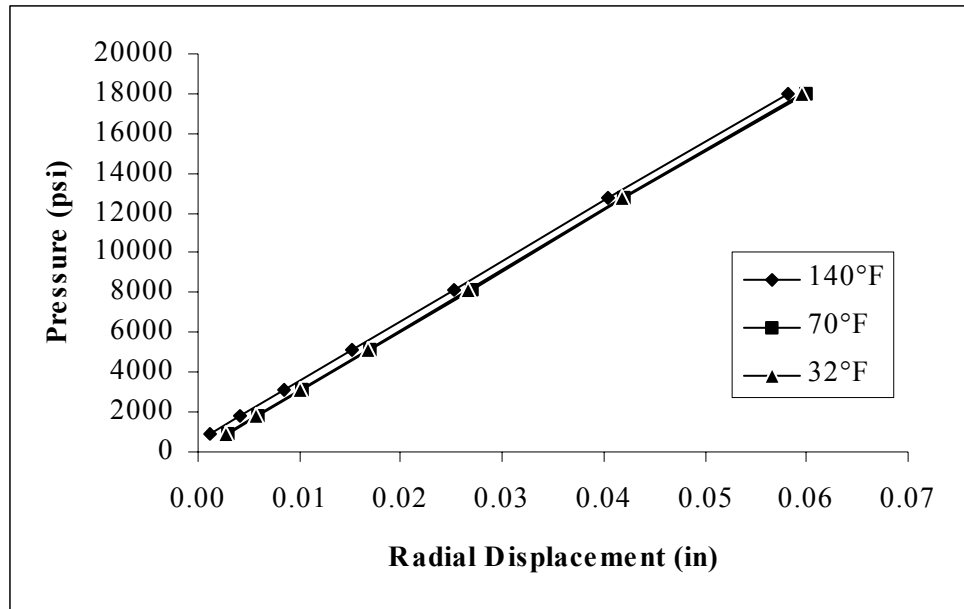
Figure MAF-40. Pressure-Displacement Curve of the 19" APC-2/AS4 Pressure Vessel with

Optimum Tapered Radius Considering Hygrothermal Effects for SAUVIM
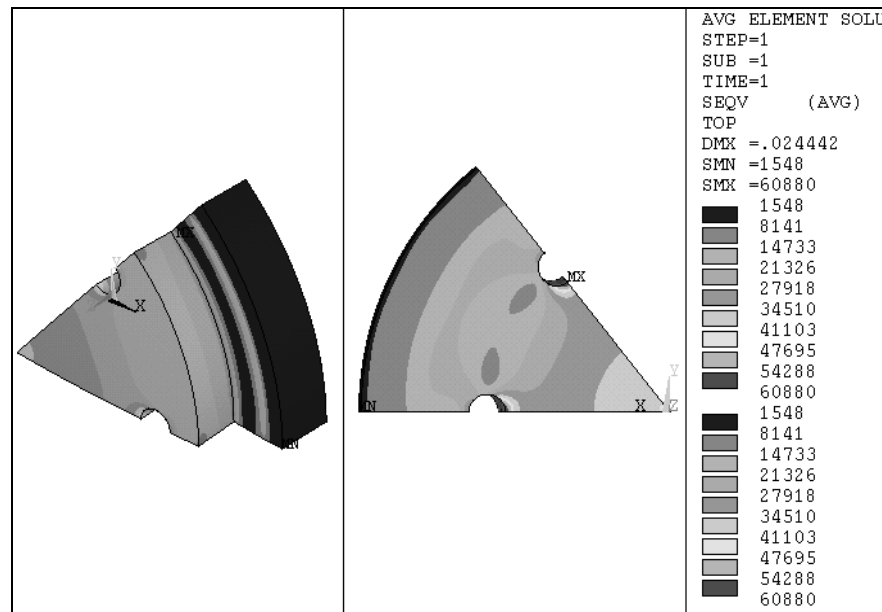
Figure MAF-41. Von Mises Stress Distribution of the End-cap for SAUVIM
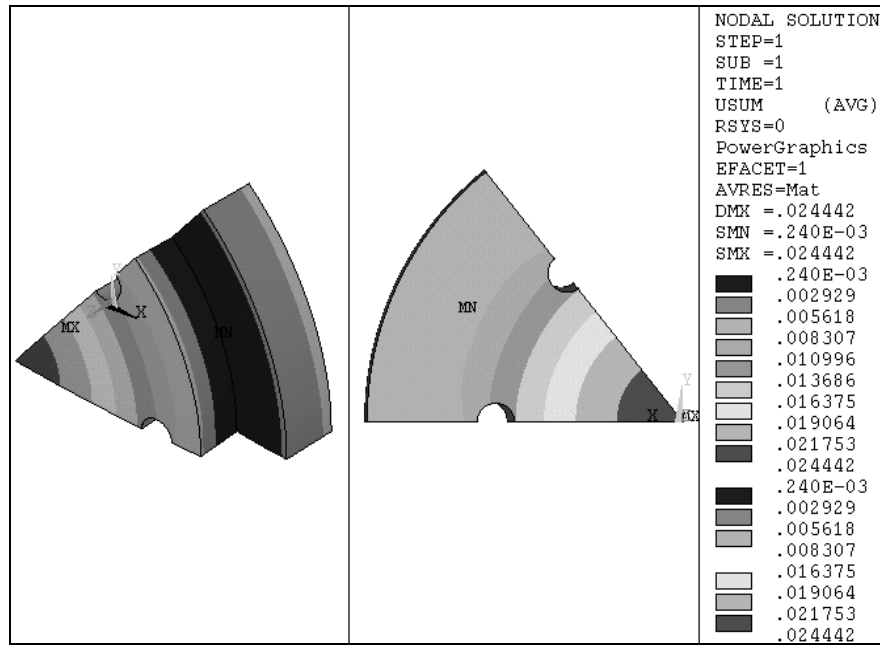
Figure MAF-42. Displacement of the End-cap for SAUVIM
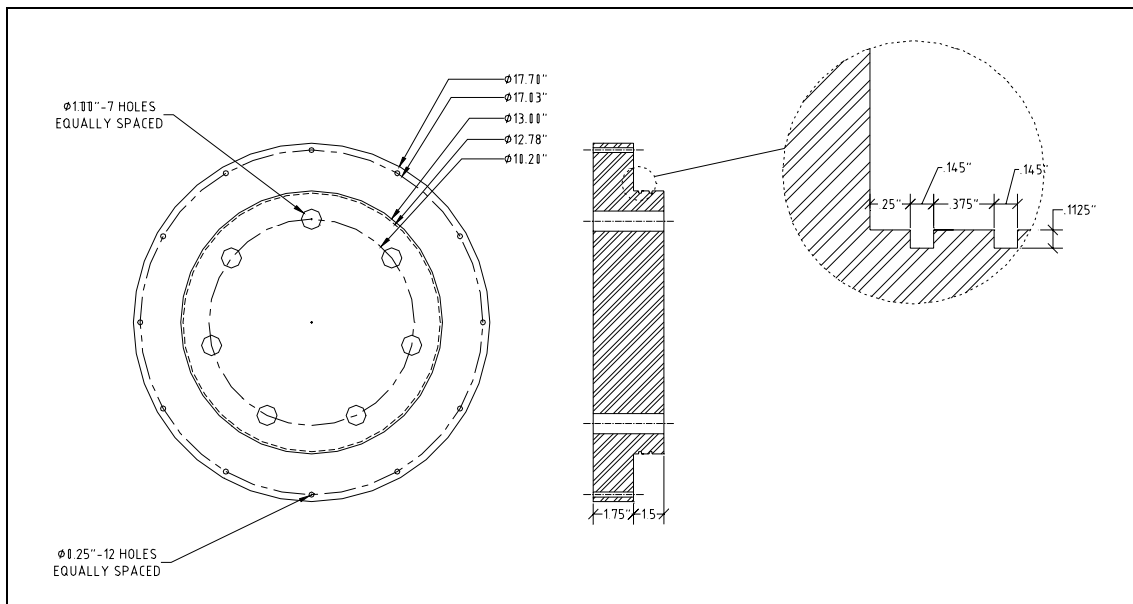
Figure MAF-43. End-Cap Dimensions for SAUVIM
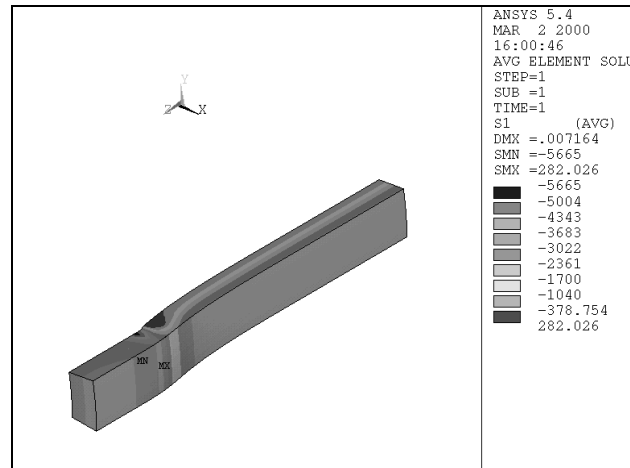
Figure MAF-44. Radial Stress of the Scaled Pressure Vessel
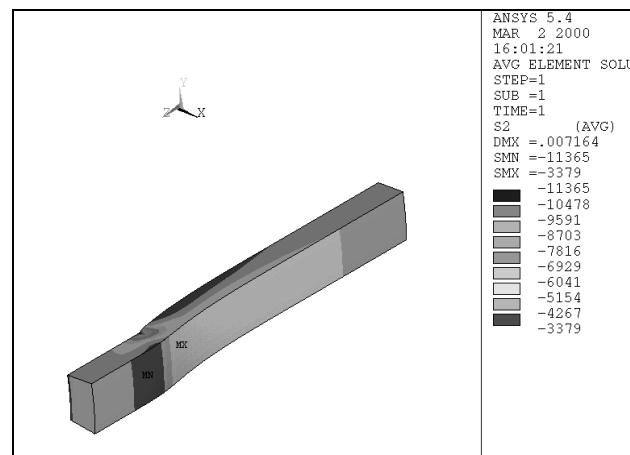
Figure MAF-45. Axial Stress of the Scaled Pressure Vessel
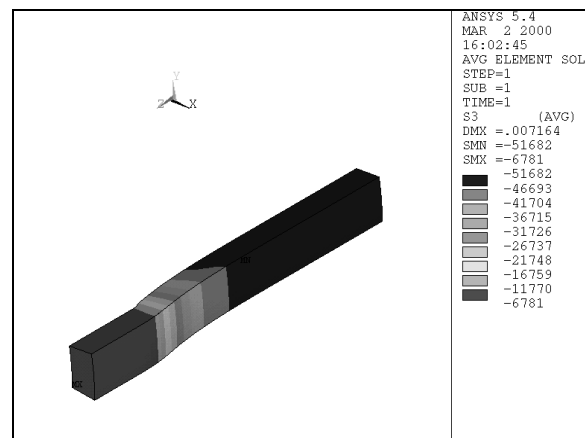
Figure MAF-46. Hoop Stress of the Scaled Pressure Vessel
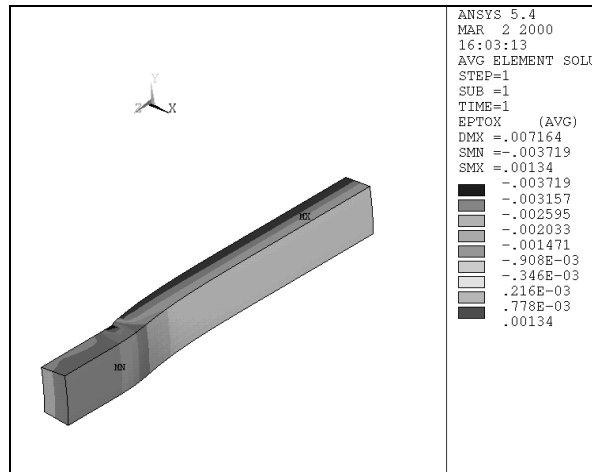
Figure MAF-47. Radial Strain of the Scaled Pressure Vessel
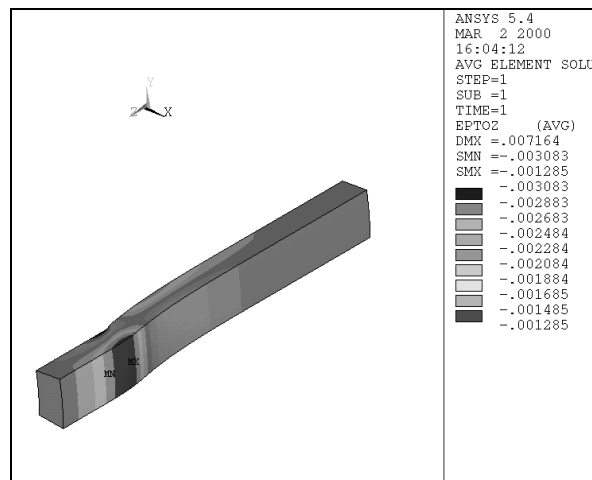
Figure MAF-48. Axial Strain of the Scaled Pressure Vessel
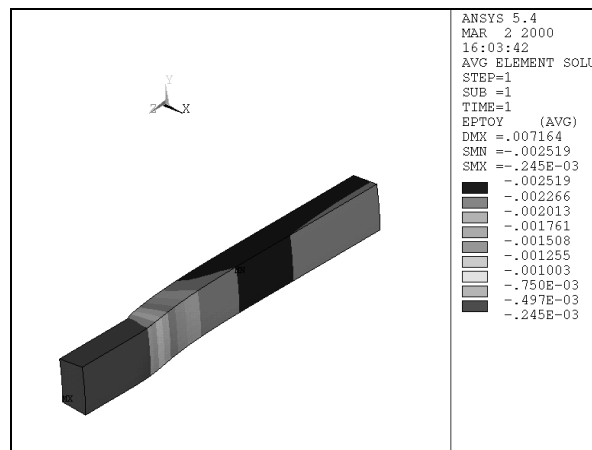
Figure MAF-49. Hoop Strain of the Scaled Pressure Vessel
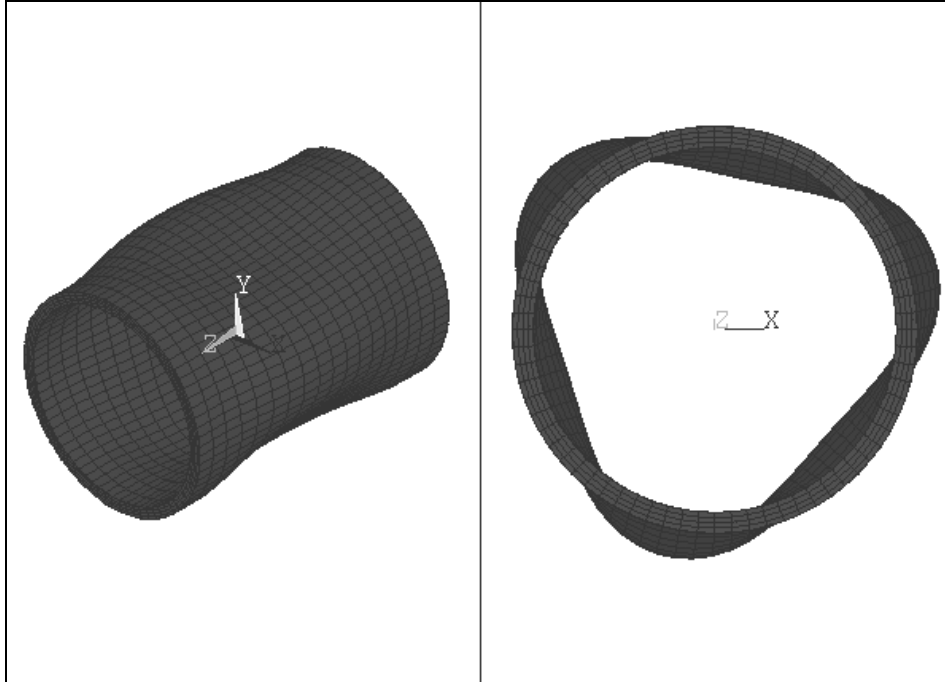
Figure MAF-50. Buckling Mode of the APC-2/AS4 Scaled Pressure Vessel
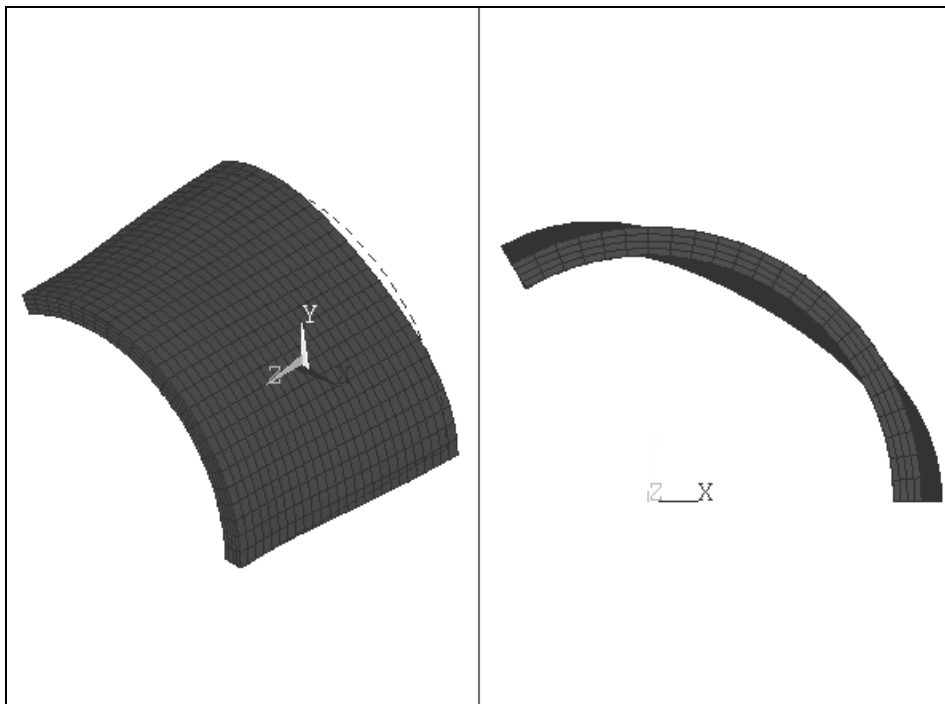
Figure MAF-51. First Mode Shape of the One-sixth of the Scaled Pressure Vessel
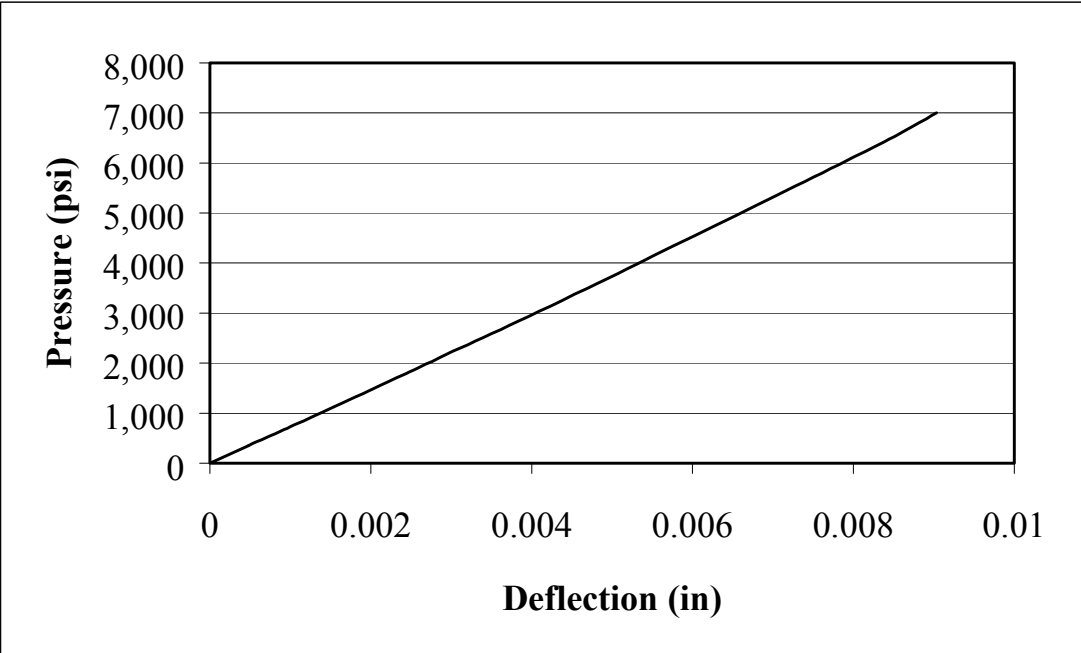
Figure MAF-52. Pressure-Deflection (Mid-length) Curve of Scaled Pressure Vessel
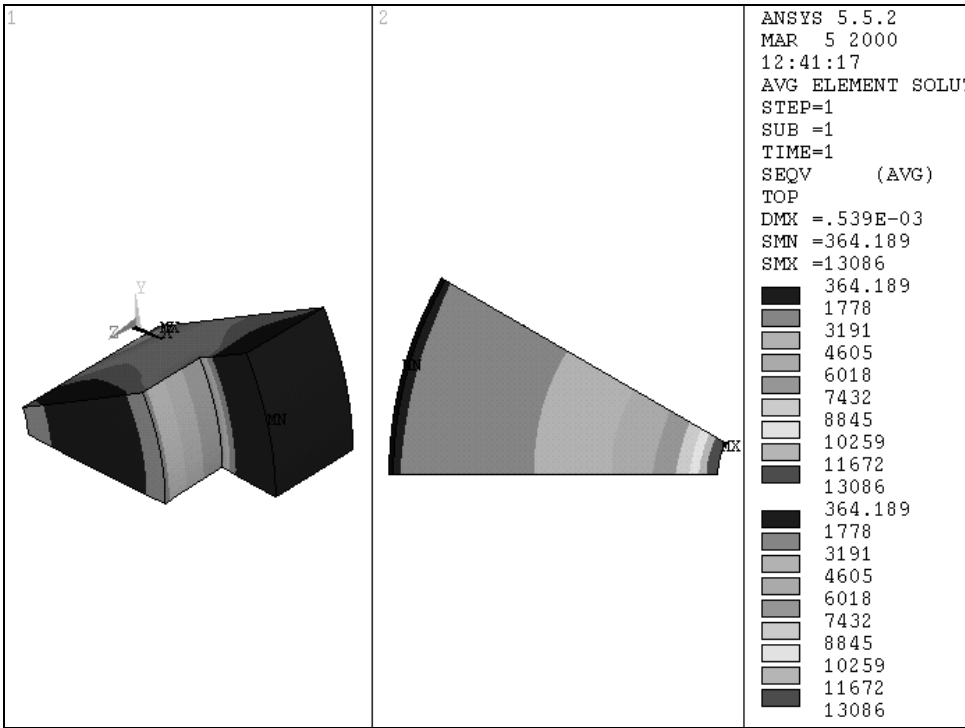
Figure MAF-53. Von Mises Stress Distribution of the Scaled End-cap

139
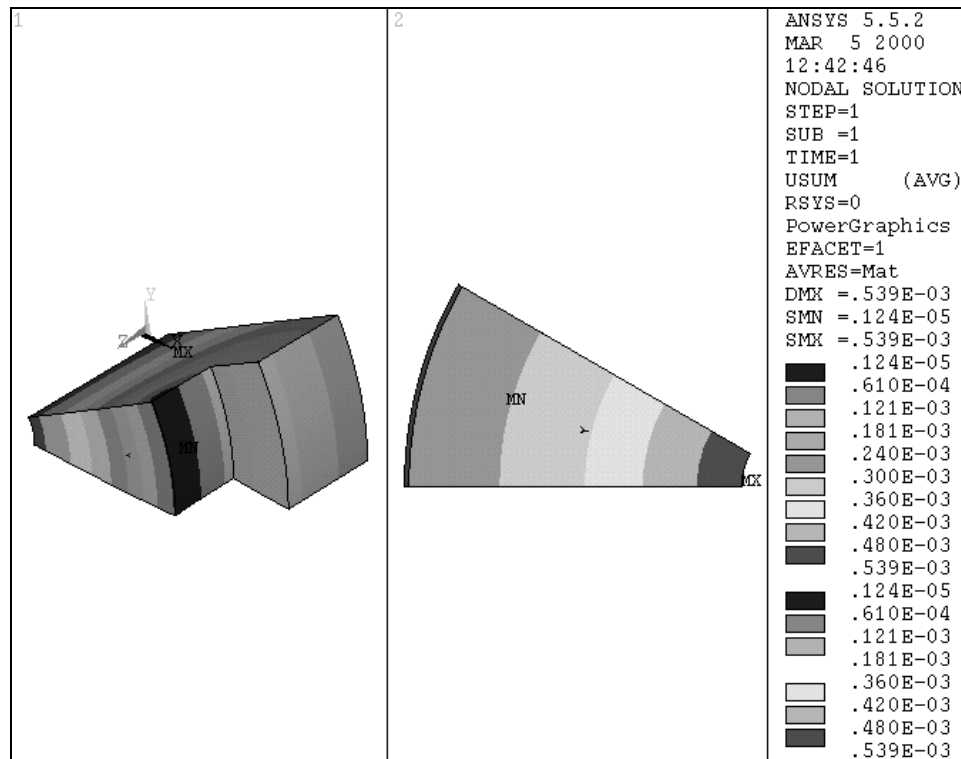
Figure MAF-54. Displacement of the Scaled End-cap
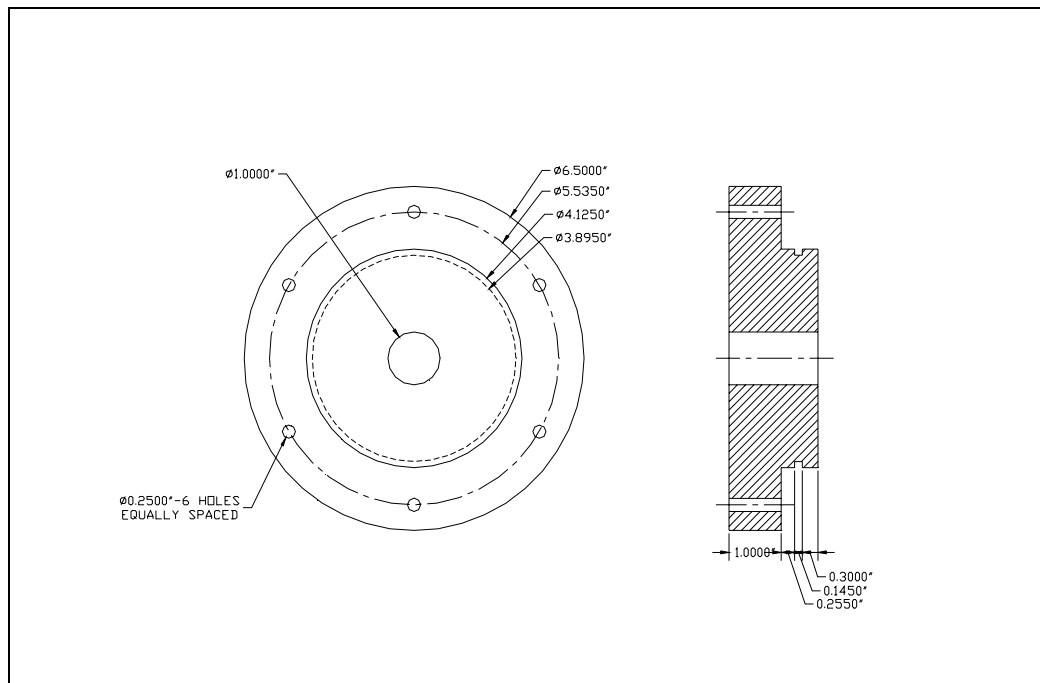
Figure MAF-55. End-Cap Dimensions for Scaled Pressure Vessel
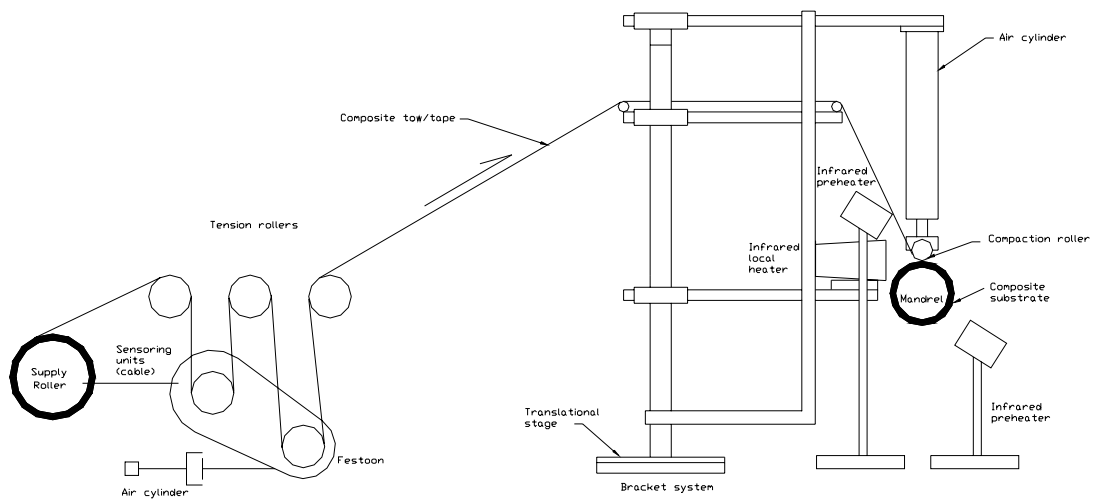
Figure MAF-56. Schematic of the In-situ Thermoplastic Filament Winding Set-up for the

Scaled Pressure Vessel
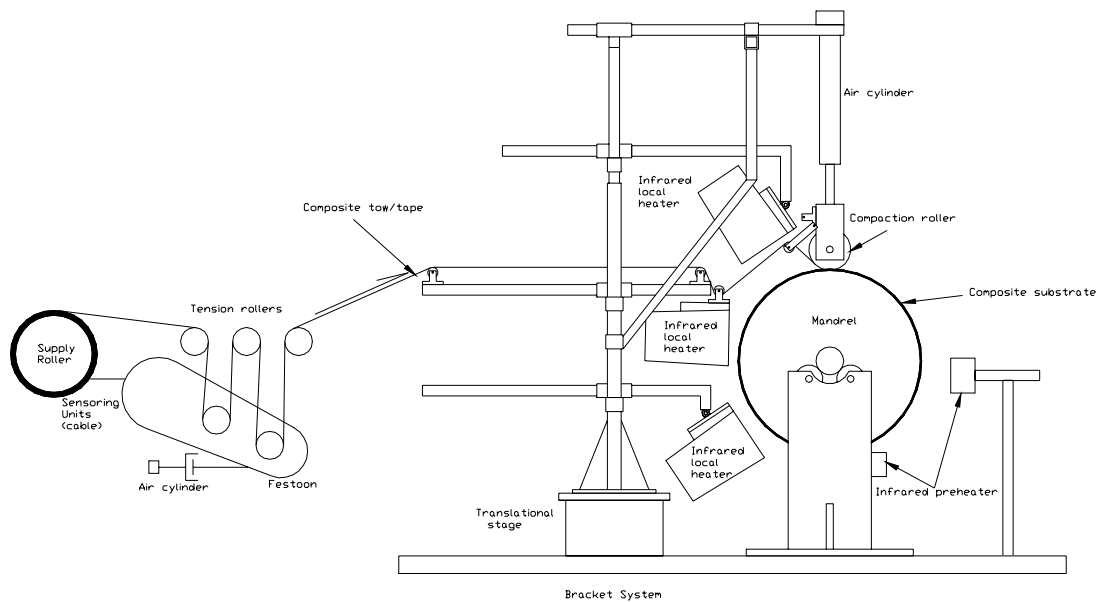
Figure MAF-57. Schematic of the In-situ Thermoplastic Filament Winding Set-up for the

Main Pressure Vessel

141
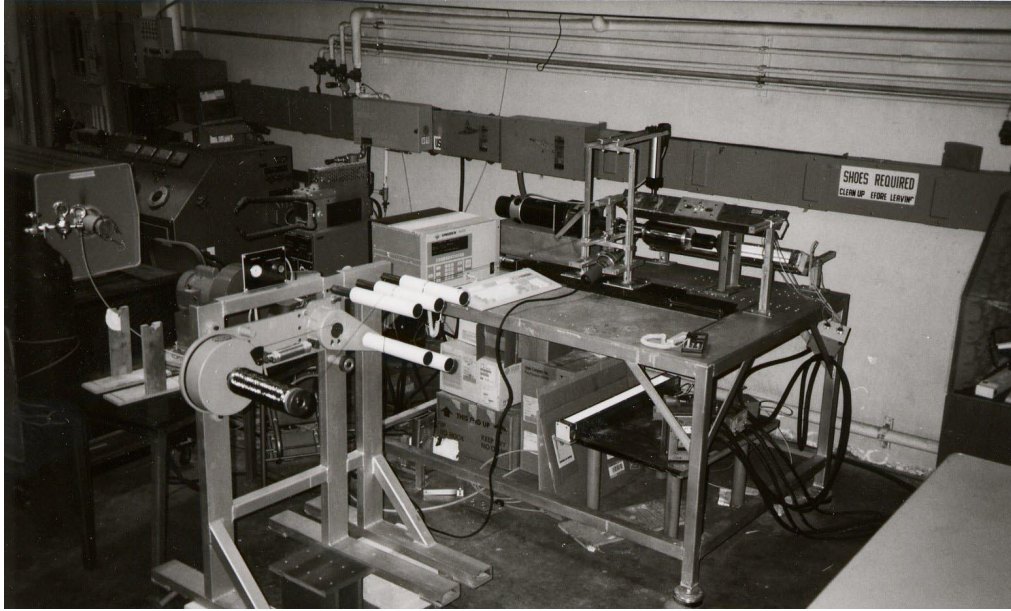
Figure MAF-58. Photograph of the Set-up for the Scaled Pressure Vessel
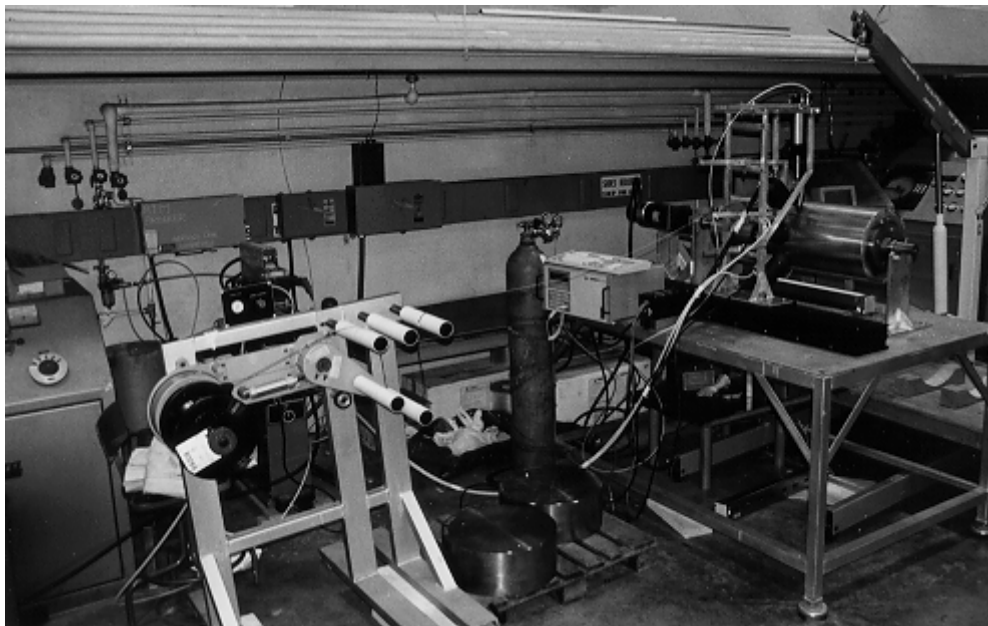
Figure MAF-59. Photograph of the Set-up for the Main Pressure Vessel
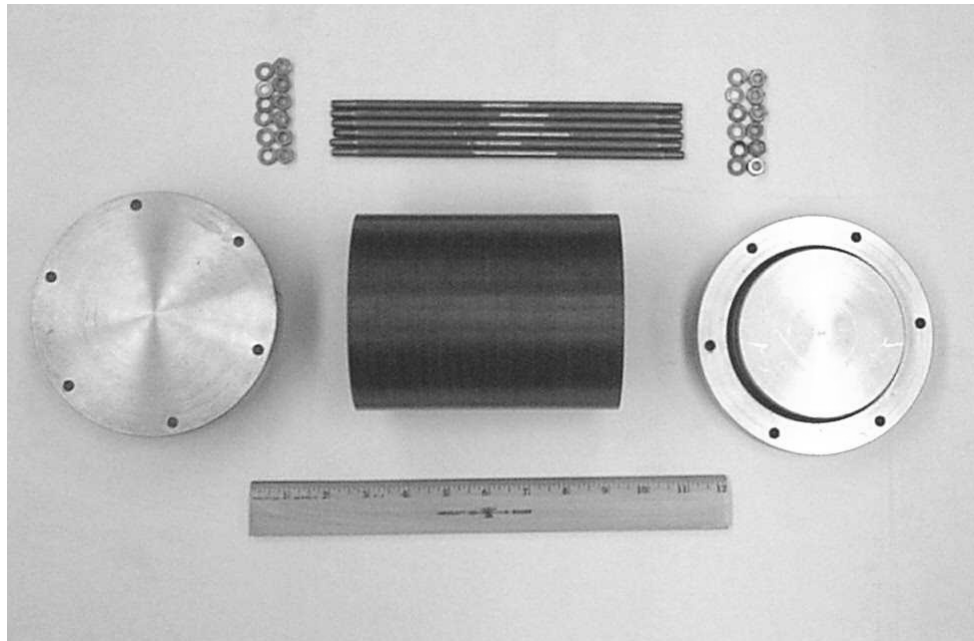
Figure MAF-60. Photograph of the Scaled Pressure Vessel with its End-caps and Tie Rods

a) Front View   b) Side View
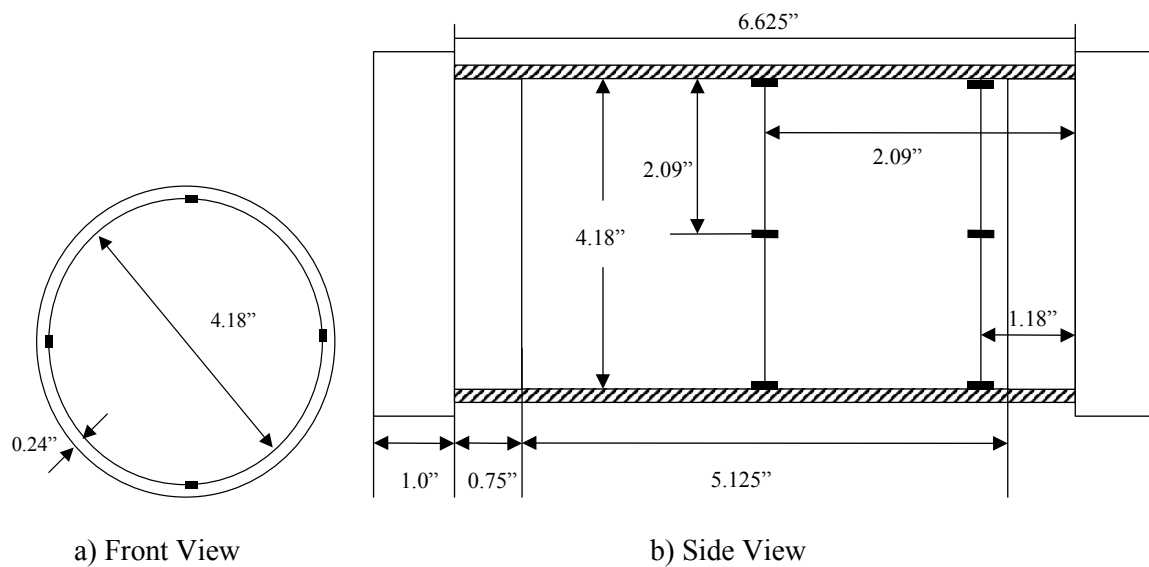
Figure MAF-61. Strain Gage Locations and Dimensions of the Scaled Pressure Vessel with End-caps in Place

Figure MAF-62. Photograph of the Scaled Pressure Vessel and the Connector

Figure MAF-63. Photograph of the Pressure Chamber End-cap and the Connector
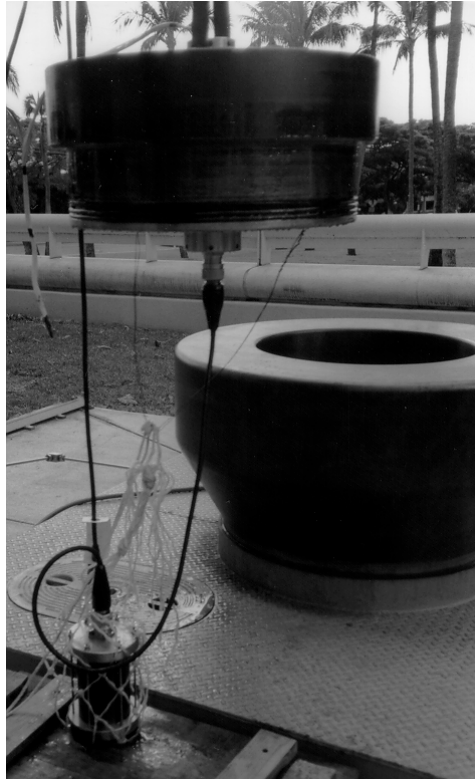
Figure MAF-64. Photograph of the Scaled Pressure Vessel, Pressure Chamber, and the Cable

Figure MAF-65. Photograph of the Scaled Pressure Vessel after the Test
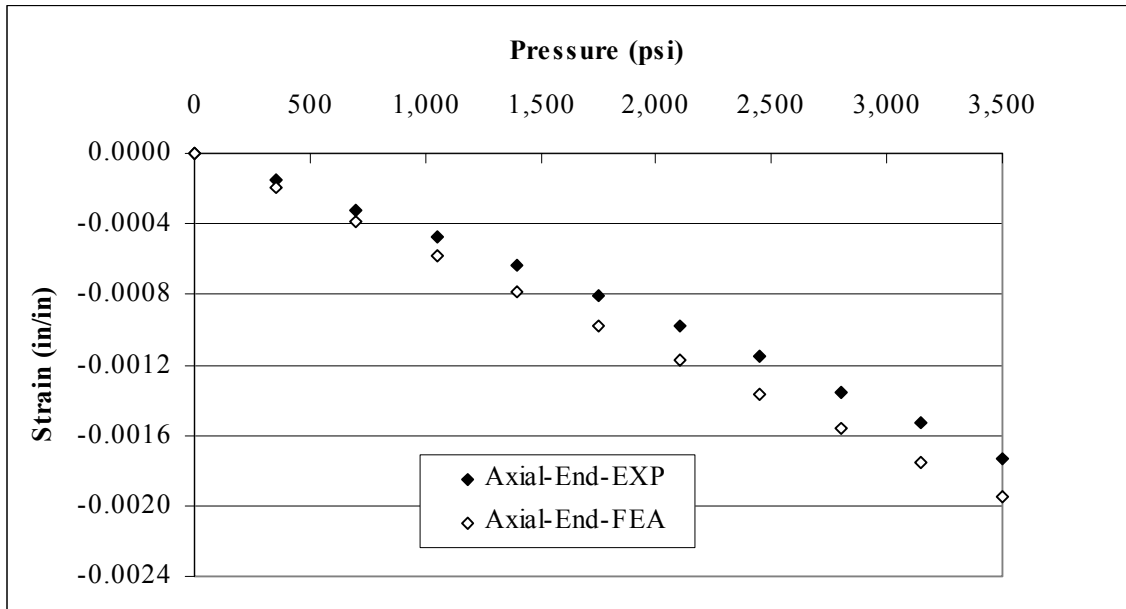
Figure MAF-66. Results of Axial Strain from Experiment and FEA Close to the End-cap
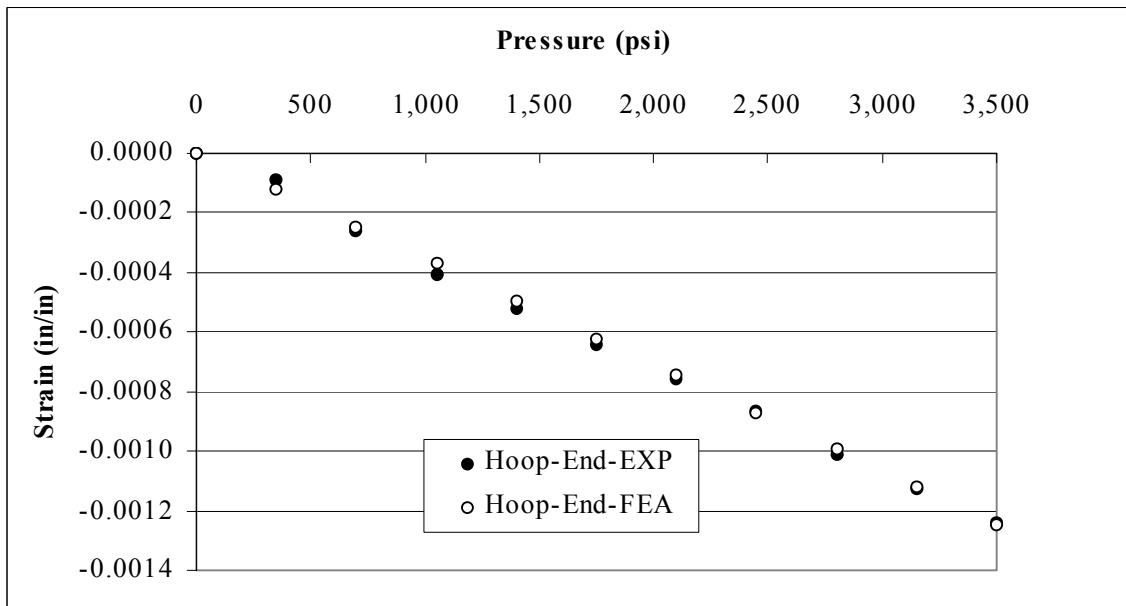
Figure MAF-67. Results of Hoop Strain from Experiment and FEA Close to the End-cap

146
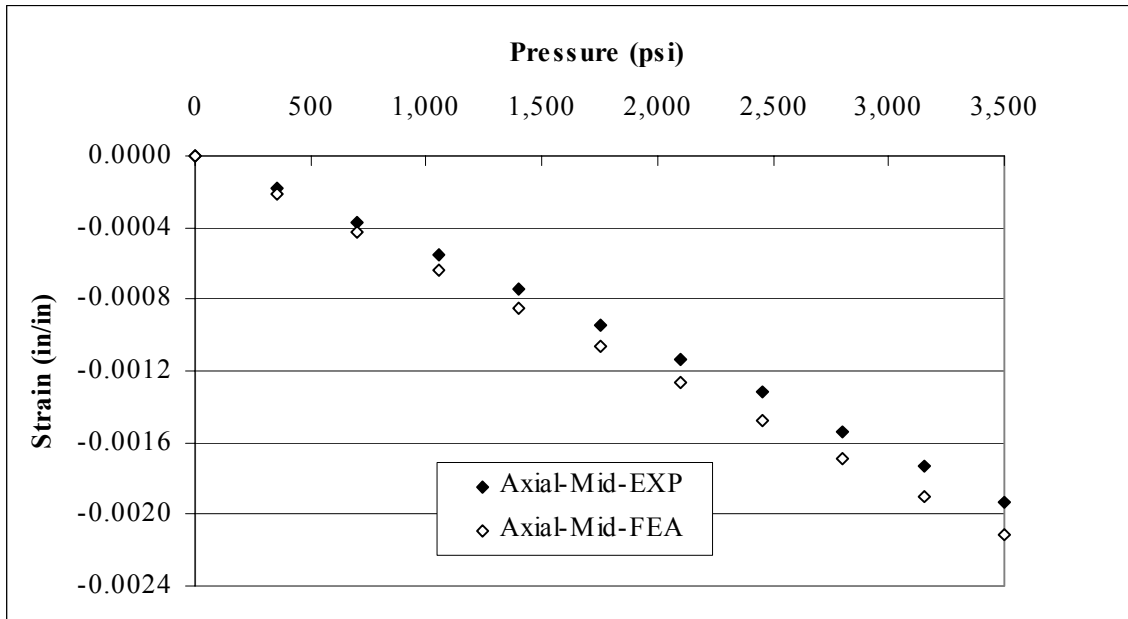
Figure MAF-68. Results of Axial Strain from Experiment and FEA at the Mid-length of the

Scaled Pressure Vessel
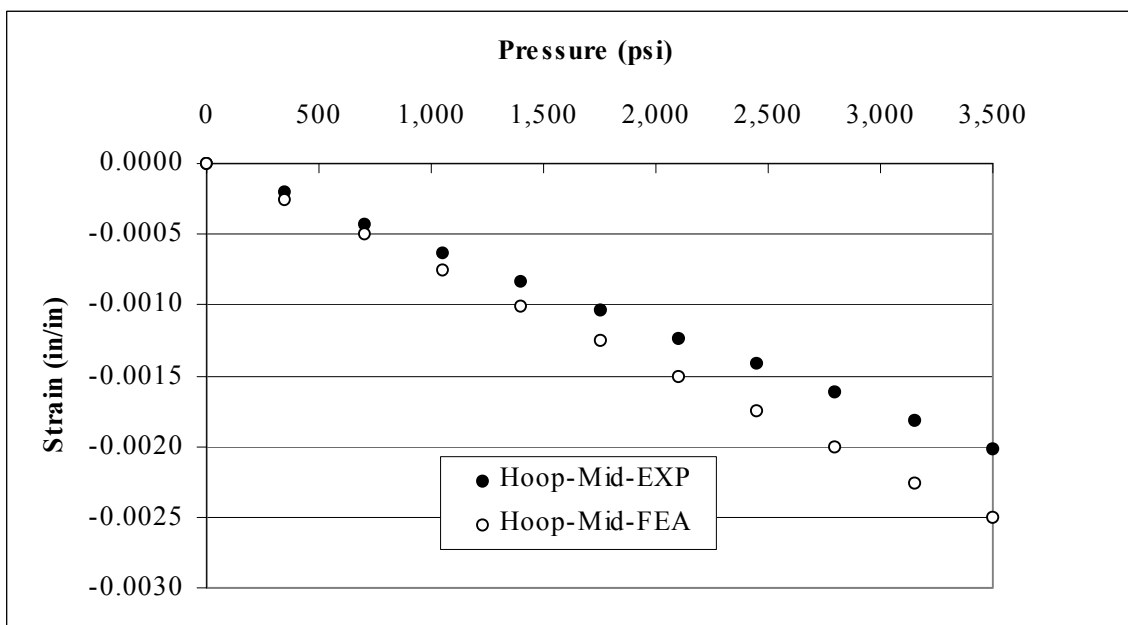
Figure MAF-69. Results of Hoop Strain from Experiment and FEA at the Mid-length of the

Scaled Pressure Vessel
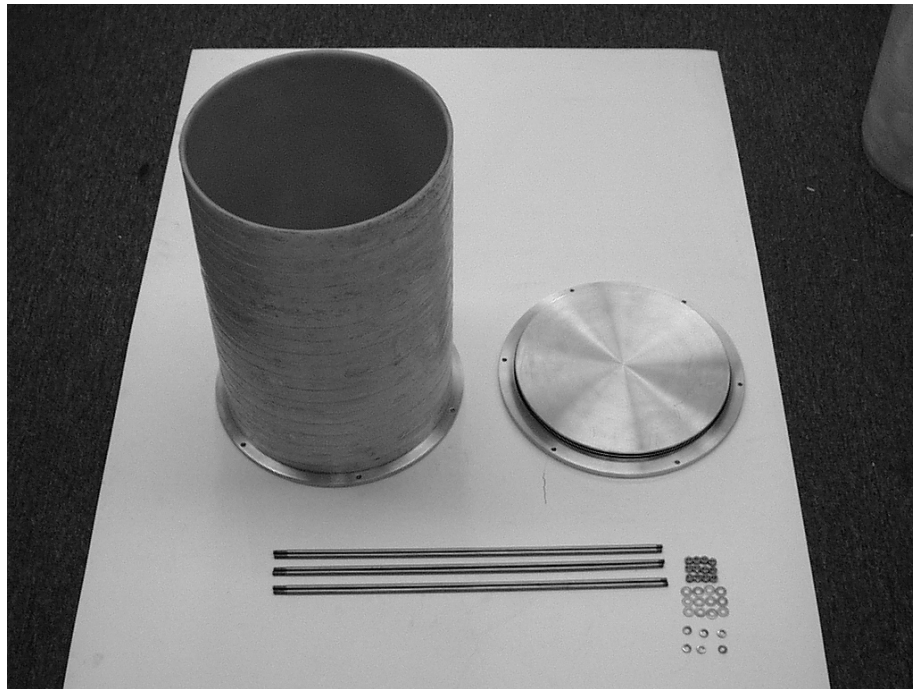
Figure MAF-70. Shallow Water Pressure Vessel with its End-caps and Tie Rods (Ng00a)
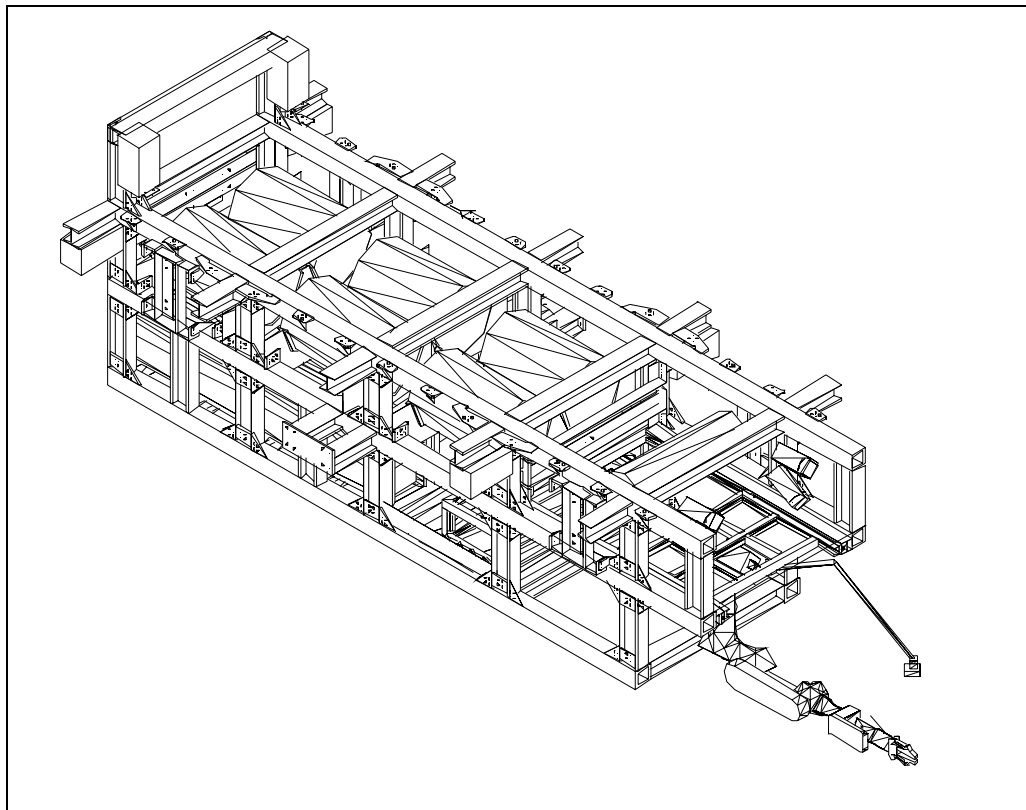
Figure MAF-71. Typical Component Layout of the Vehicle
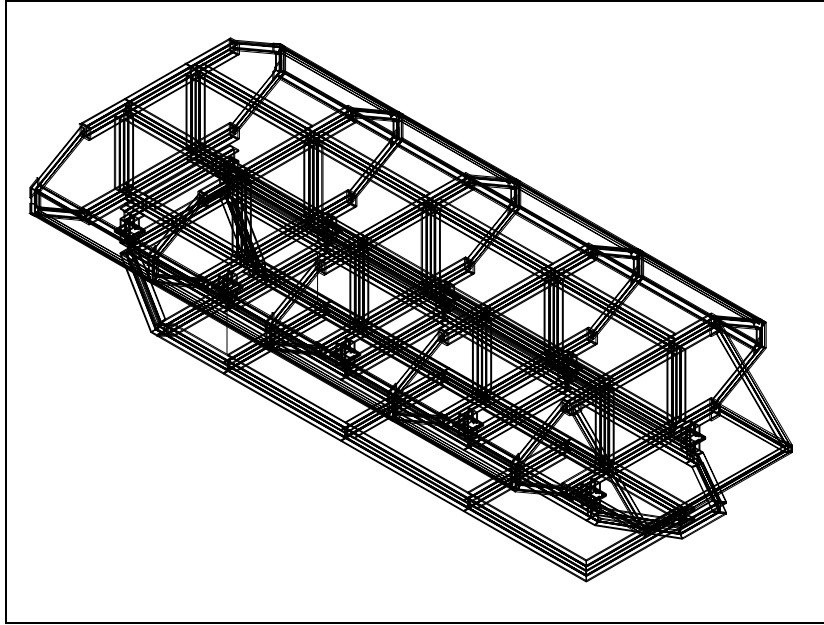
Figure MAF-72. Preliminary Design of the Frame
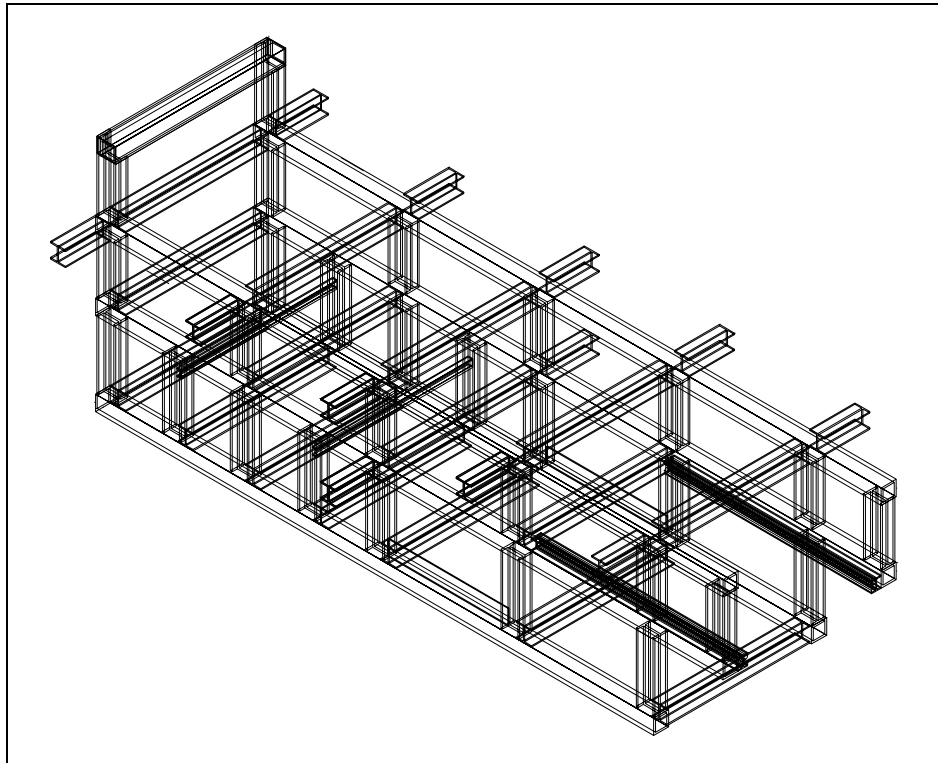
Figure MAF-73. Final Design of the Frame
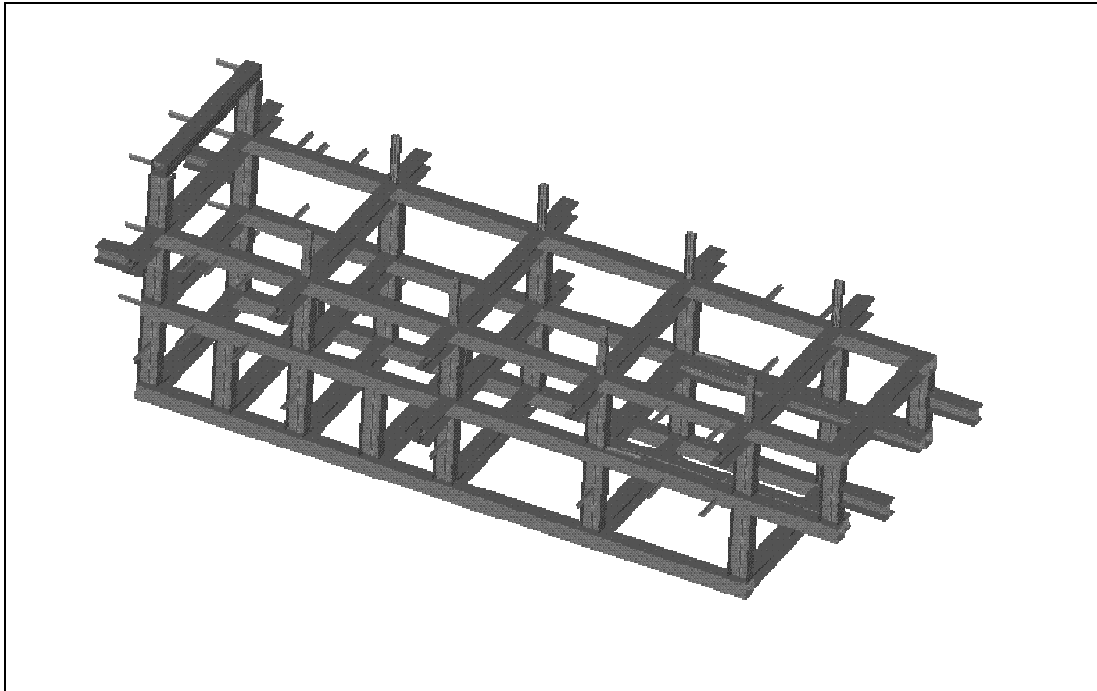
Figure MAF-74. Solid Model of the frame
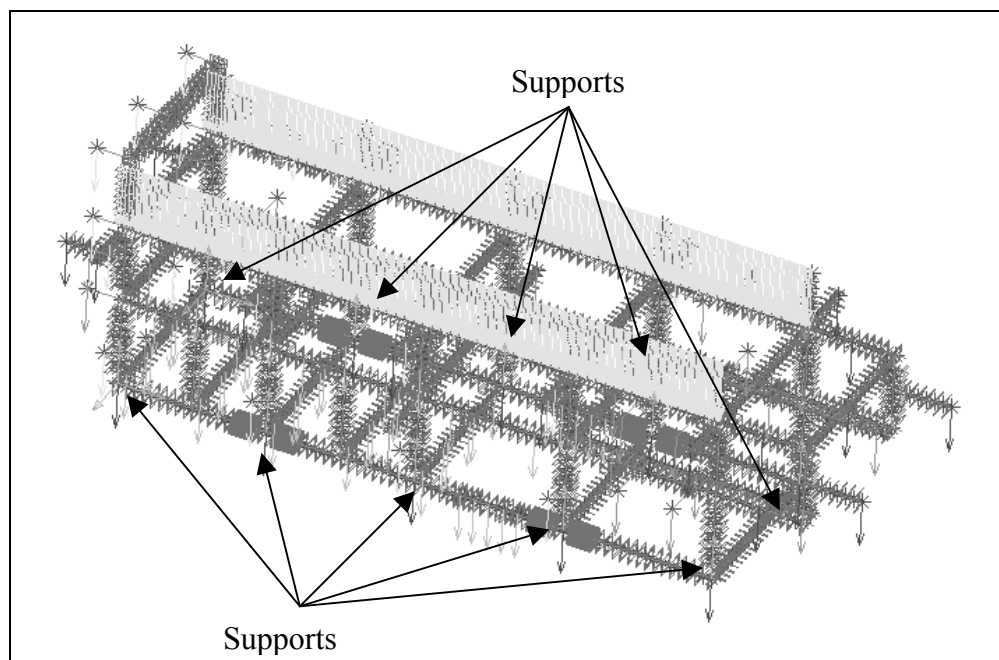
Figure MAF-75. Dry Boundary and Load Conditions with Arms Extended
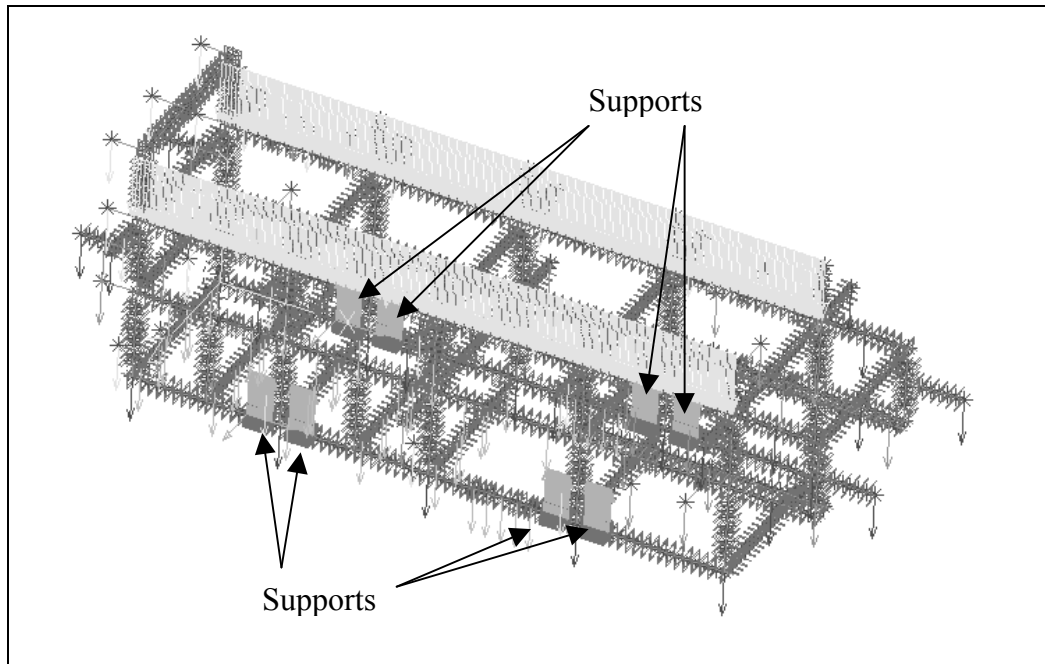
Figure MAF-76. Lifting Boundary and Load Conditions with Arms Extended
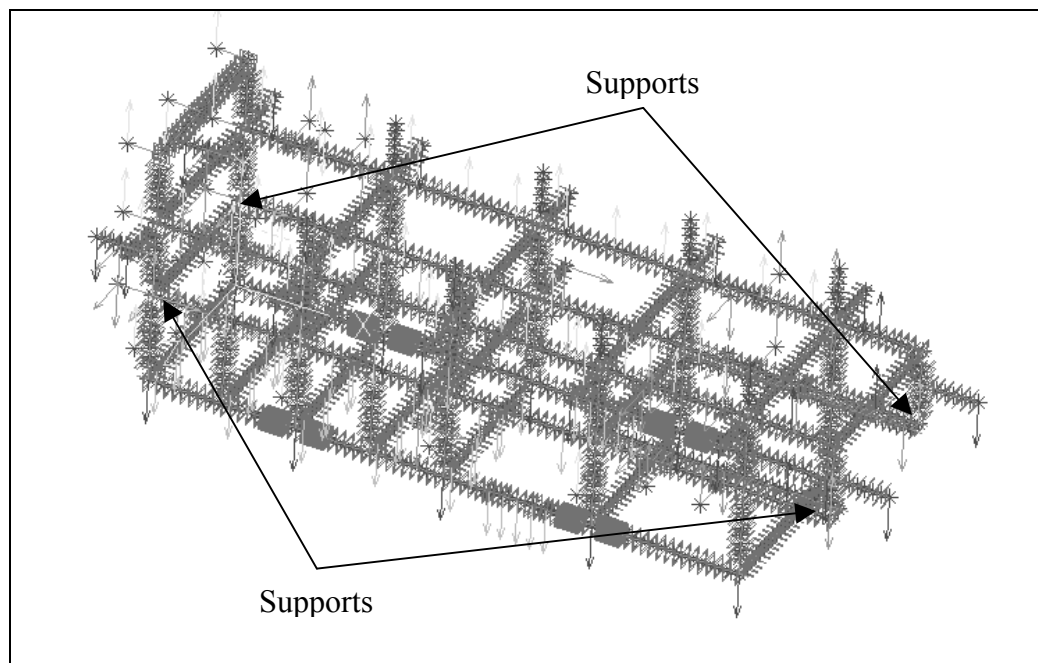
Figure MAF-77. Wet Boundary and Load Conditions with Arms Extended
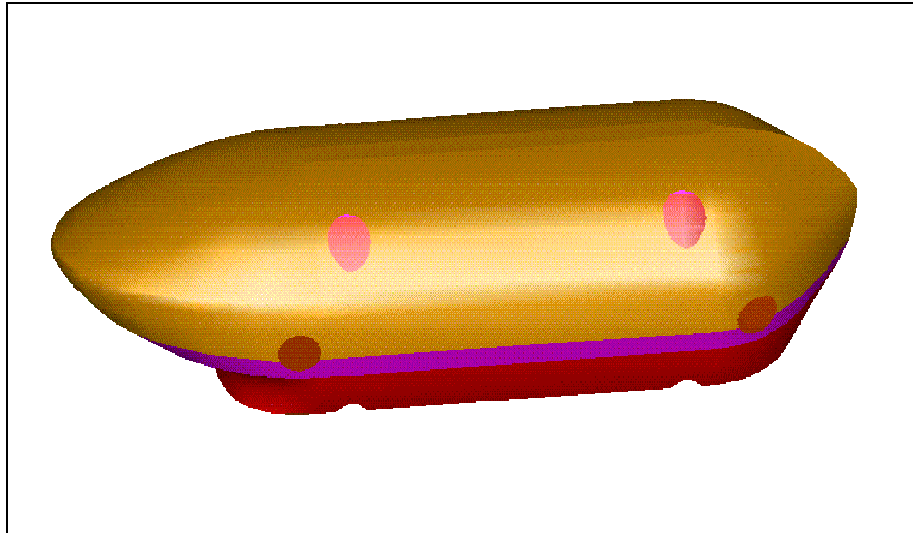
Figure MAF-78. Composite Flooded Fairing (Side/Isometric View)
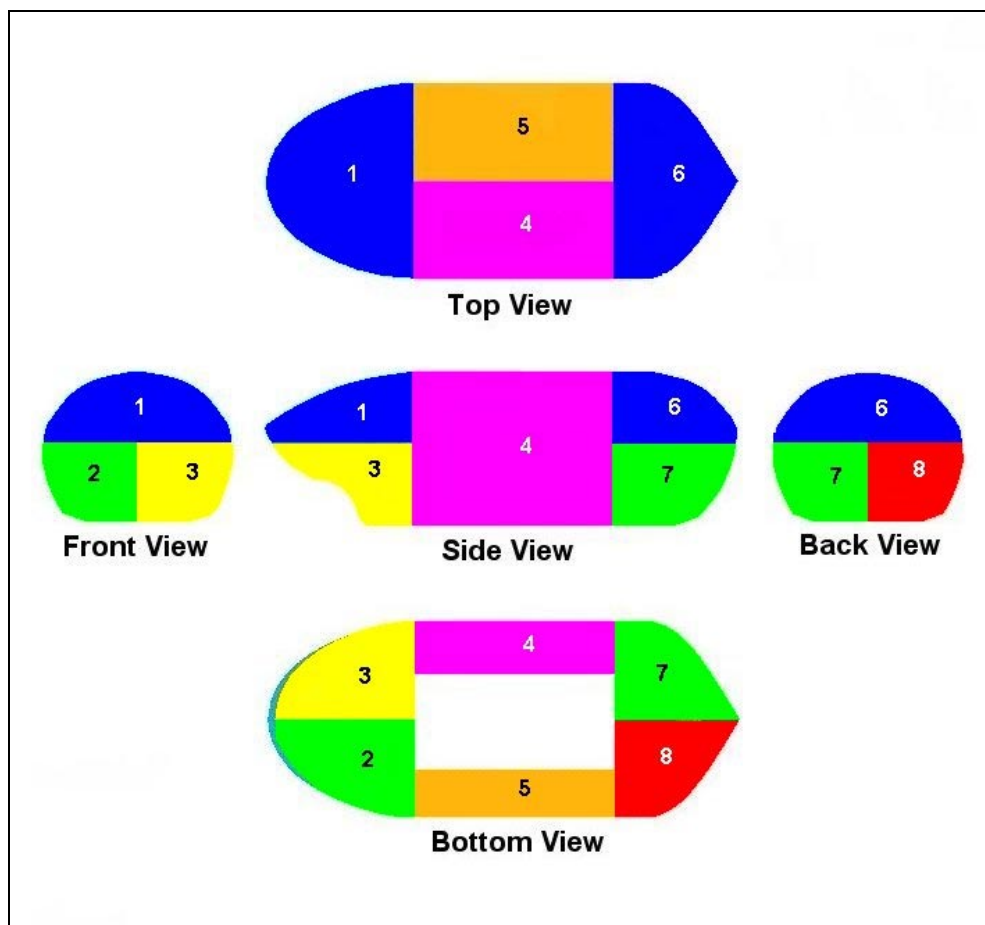
Figure MAF-79. Schematic of 8-Segmented Composite Flooded Fairing
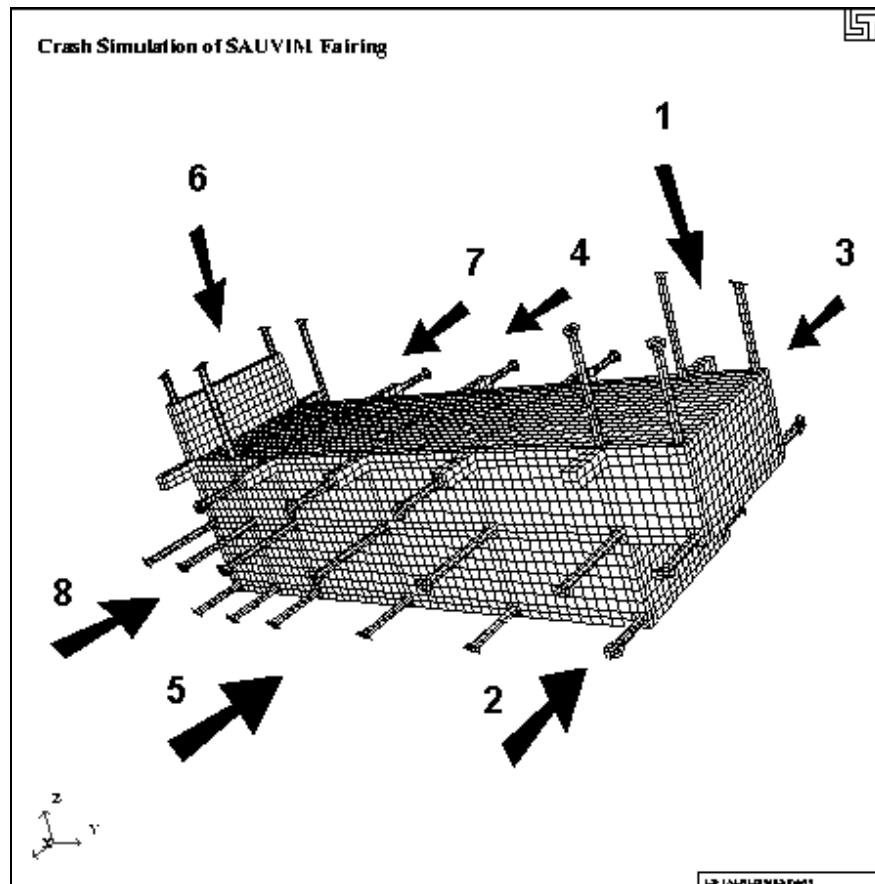
Figure MAF-80. Assembly Order of the Segmented Composite Flooded Fairing on the Meshed
Block, Supports, Joints, and Disks used in LS-DYNA3D for the Crash Simulation

Mechanical-Electrical Design (MED)

Project Leaders: Dr. Song K. Choi, Mr. Oliver Easterday & Mr. Gus Coutsourakis
Personnel: Mr. Kaikala Rosa, Mr. Mike Hall, Mr. Tai Blechta, Mr. Scott Sufak, Mr. Keith Sunderlin, Mr. Dante Julian, Mr. Stacy Hansen & Mr. Clyde Campos

Objectives

Integrate mechanical and electrical components of the SAUVIM vehicle and provide vehicle infrastructure in terms of structure and power to support research aspects of SAUVIM AUV.

Current Status (Tasks Completed During 8/1/97 – 10/30/00):

MED Group General Systems Status Overview - Mechanical/Electrical:

The SAUVIM vehicle design and construction development has been significant. A general overview of the vehicle systems development - both mechanical and electrical - will proceed to breakdown of progress/design/and technical specifications organized by sub-systems. Sub-systems will generally proceed in the following order: integration complete, fabrication complete, in-fabrication, entering fabrication/detailed design, design, conceptual design, problem specified/identified.

These requirements evolved out of the following vehicle objectives as set down in the SAUVIM Vehicle Proposal, ONR Grant Application. Some of these requirements have had a major impact on the evolution of the vehicular systems supporting them and therefore in the evolution of the SAUVIM; these are highlighted underneath each requirement below:

- A vehicle capable of bottom intervention for 95% of seabed floors (20,000 ft depth rating). Deep Submergence Vehicles (DSV=s) and Remotely Operated Vehicle (ROV) floatation and pressure sustaining bulkheads get correspondingly heavier in a very predictable fashion as depth rating increases. For SAUVIM syntactic floatation and pressure vessels are two main sources of vehicular mass.

- SAUVIM will incorporate intervention capability via a manipulator. The Ansaldo/Maris electric manipulator of the vehicle sets a bound on vehicle size due to need to have a storage bay area for vehicular cruise as well as the ability to have an unrestricted workspace during intervention tasks. Additional batteries, computational plant, control electronics and vehicle mass to provide a stable robotic platform drive vehicle size to a value somewhat larger than a flyby/wide-area survey AUV designed for similar depth.

- SAUVIM serve as a test-bed for full-ocean depth composite pressure vessels. One key aspect of research for the SAUVIM proposal is the employment of composite pressure vessels in the deep-ocean environment as manufactured by the Mechanical Analysis and Fabrication (MAF) group. Due to current manufacturing limitations in regards to size and geometry in the prototype vessels as well as projected size uncertainties in early in the project, the SAUVIM frame was oversized by a certain margin (around 20-25% over predicted minimal space from FEA analysis prediction by the MAF group). One aspect of

154

composite vessels that requires attention is that the thermal resistance of the vessel material is much higher than standard metallic vessels, hence high heat load devices must be either be conductively-sunk or moved into separate bottles.

- SAUVIM will test command/control using compression and command primitives over a bandwidth-limited link (acoustic modem). This requirement stipulates Autonomous Undersea Vehicle (AUV) cruise and navigation capabilities, which sets bounds on sensor placement, thruster configuration and ballast management. The MED Group has striven to keep systems that have proven operationally successful on the predecessor vehicle, the ODIN II, similar in form on the SAUVIM. Such examples include: an octet thruster configuration, an array of six first return sonar units are aligned in the principle directions, VME-based computer architecture, and the maintenance of power and signal ground isolation throughout the vehicle.

- SAUVIM will evaluate experimental proximity navigation sensors (AORD) for Automatic Object Ranging and Dimensioning. The three AORD systems will require space on the vehicle as well as accommodation for operative conditions. For example, the passive arm requires a space to be folded into, much like the active manipulator. Meanwhile, the laser array requires a certain amount of frontal area to project out into as well as control and power supply provisioning.

- SAUVIM will host on-line and off-line genetic algorithm (GA) based path planning.

- SAUVIM will host an independently functioning science package. This mission sensor package (MSP) will be typical of a standalone research instrument payload that the vehicle would be capable of hosting.

- The MSP though largely electrically and command independent of the SAUVIM vehicle will, nonetheless, require a space reserved within the vehicle for it and any outboard sensors. Also, the ability to poll the SAUVIM computers and trickle charge off of the main batteries will be provided.

- SAUVIM will serve as a test-bed for a real-time distributed control system (RDC) incorporation of 6U based VME computer architecture spread across multiple buses will be researched and tested in the prototype vehicle. The SAUVIM computers will be on twin VME bus/multiple CPU system. This was implemented due to three objective/constraint motivations: the first being the desire to test the feasibility of distributed architecture on the vehicle for control purposes. The second was the ability to assign robotic arm control to a separate computer of its own and off-load computational burden from the main navigation CPU. Third was the desire to add some measure of fault tolerance to the vehicle - should the main navigation computer fail, sufficient functionality and vehicle control is routed from the arm CPU to allow initiation and supervision of vehicle self-recovery attempts.

Since the initiation of the SAUVIM ONR project the prototype research vehicle has evolved into the following specifications given on the chart below. The shallow water vehicle, known as the Phase-I design, will be launched, tested and debugged in Ke'ehi Lagoon near Honolulu harbor, meanwhile, deep-water hardware development will continue in parallel, hence, two columns of specifications exist. This was done for several reasons, the primary being that the foam and lighter vessels would

result in a vehicle that is easier to launch and handle while developing the SAUVIM system software, integrating the advanced sensors, and running test missions.

The SAUVIM will have the following performance specifications:

Specification:	Phase-I design	Phase-II design
Vehicle Class:	Mid-Depth Intervention AUV	Deep Intervention AUV
Size:	192"L x 95"W x 74"H un-faired 251"L x 95"W x 74"H faired	192"L x 95"W x 74"H un-faired 251"L x 95"W x 74"H faired
Form:	Free-flooded vehicle with fiberglass frame, with six cylindrical vessels	A fairing, aluminum 6061 structural
Weight:	8,500 lbs (dry), -5 lbs (wet)	13,500 lbs (dry), -5 lbs (wet)
Power:	Lead acid batteries banked at 48, 72, and 144VDC on six buses. 12 batteries overall.	Lead acid batteries banked at 48, 72, and 144VDC on six buses. Approx.70 batteries overall within two fiberglass PBOF enclosures.
Mission duration:	5-6 hours all systems active 24 hours with power rationing	15-18 hours all systems active 1 week or more with advanced power management added.
Command Control	RS-232 and RJ-45 Ethernet tether with wireless LAN & RF modem link. Simulated degradation for deep water mission simulation.	Acoustic modem link. Location transponder, pinger and acoustic ballast release under review.
Floatation:	Twelve pieces of foam, six top and six side pieces. Rigid urethane foam. About 25% of foam space occupied. Density is 18 lbs/ft^3.	Syntactic foam blocks of same shape as shallow water foam. Foam space is fully occupied. ~40 lbs/ft^3 density.
Pressure vessels:	Six E-glass thermo set composite epoxy thermoplastic composite cylindrical, 13"ID x 18" cavity bottles with aluminum lids	Six carbon filament/PEEK bottles with titanium lids 13"ID x 18" cavity
Powered Cruise Range:	2.7 nautical miles powered Un-powered glide slope range varies with depth.	8.1 nautical miles powered
Speed:	1 knot cruise, 2-1/2 knots maximum speed	
Ballasting:	Hard ballast: 1 main/emergency weight - 600lbs, two descent weights - 150 lbs/each, 1 ascent weight - 300 lbs, two metering weight canisters - 60 lbs each. Ballast is scrap iron plate bolted together, metering weights are iron/lead shot	
Soft Ballast:	two 36 gallon tanks (300 lbs buoyancy each)	
Vehicle Control:	Six Technodyne Model 1020 thrusters, two Technodyne Model 2010 thrusters. Three articulating fins of about 3ft^2 apiece. Main ballast is on a tray with 18.0" stroke allowing trim from 8° nose up to 12° nose down.	
Deployment:	One standard (20') shipping container for vehicle, support equipment and control consoles.	
Robotic Arms:	One 7 joint (dof.) Electrical oil-filled manipulator capable of 21 lbs payload at full extension. One 7 dof. passive arm used for position sensing. Arms are on a deployable platform tray.	
Computer/Control:	Twin-VME back planes with twin Motorola 68060CPUs linked via RJ-45.	
System Software:	VxWorks RTOS. C-code drivers. Custom high-level interpreted language used for mission planning and reporting.	

Early in the project the operating scenarios that the SAUVIM vehicle would experience in a typical deep ocean mission were identified. Table MED-1 identifies these scenarios that the vehicle will proceed through in the course of a typical mission. The systems that are needed to support the mission objectives identified above are depicted in the graphic shown in Figure MED-1. As can been

seen the integration of all the research systems onto the prototype vehicle involves floatation, ballast, thrust/fins, trim, sensors, cabling, structural frame, and numerous other systems.

To obtain a visual overview of the matured vehicle design, the reader can examine Figure MED-2, which is a conceptual drawing of the complete Phase-II, deep-ocean SAUVIM vehicle complete with fairing. Photograph MED-1 shows a 1:12 scale model plug made of the vehicle fairing that was made for tow tank testing. Figure MED-3 shows the vehicle in an oblique view with all the main components labeled, save the fairing and floatation foam. Photograph MED-2 depicts the vehicle in a recent state with some of the major assemblies mounted onto the vehicle frame for fitting and testing purposes.

Mechanically, the vehicle is reaching the stage of advanced integration, where many of the major assemblies are being mounted onto and fit as part of the larger vehicle, among the systems at a more advanced stage of completion are: dorsal foam, pressure vessels, and battery systems. Entering the stage of being integrated at the present are the thrusters and sensors systems.

Meanwhile, the overall electrical system is maturing at this point. Based on the control hierarchy developed by the RDC group, the subsequent breakdown and assignment of functions into the various pressure vessels onboard the SAUVIM resulted in the electrical system depicted in Figure MED-4. The cabling interconnects between all the pressure vessels and the sensors, actuators and other outboard components are detailed in Figures MED-5 and MED-6. Many of these cables have been ordered - these include the main data interconnect, switching/control and power feed cables. The SAUVIM presently is in various stages of electrical fabrication, depending on the system. There are custom-built as well as off-the-shelf components being utilized used on the vehicle. Electrical design and layout is performed using PC-based CAD software.

SAUVIM Sub-system Breakdown - Mechanical:

Frame - The vehicle frame fabrication was completed in 1998 and is a free-flooded aluminum 6061 alloy structural frame welded with 4043 filler rod. Design of the frame was done in-house by the MED group, while analysis for structural strength was performed by the MAF group. Analysis criteria are detailed in that section of this report. The contractor that was involved with the fabrication of the frame was Honolulu Shipyard International (HSI), a subsidiary of Pacific Marine Company.

Photograph MED-3 shows the actual frame, while Figure MED-7 is a 3-view and isometric depiction of the frame. Al-6061 alloy and 4043 filler combination was chosen for reasons of good corrosion resistance, ease of revision work, economy, strength and relative ease of use. The bare frame weight is around 1200lbs dry and it measures 167" long by 63" high by 71" wide. The floatation foam is clamped to the top and side surfaces of the frame while the pressure vessels ride in the center level of the frame. Batteries, ballast and arm stowage space occupy the lower section of the frame as one proceeds from aft to the bow, respectively.

Comprised of six longitudinal box and inter-connecting vertical and horizontal I-beams, the entire structure free-floods upon immersion into water. Attention was given to avoiding voids in either the form of closed, hollow members, or weld beads in the pattern of closed curves.

Remaining tasks dealing with the frame include: 1) passive anodic protection, 2) protective barrier coating, 3) spray wash-down system fitting, and 4) mount-point revision work.

Passive zinc anodes have been specified and ordered for the frame and a determination of location of these prone to the following issues is currently underway. Electrical integrity of anode sites, ease of cursory visual inspection, mounting sites that do not compromise member strength, and sufficient distance from MSP package CTD sensor to not locally contaminate sampled water are being considered in the placement of these. From two to four anodes of 4"x8"x1" in size will be mounted. These have already been ordered.

The barrier coating work will be done after relocation of the frame down to the UH Snug Harbor facility and currently hand-brushed epoxy and polyurethane systems are being considered for use. The main function will be to cut the amount of surface area exposed to the seawater and to seal-in corrosion prone regions, notably the welds and joints where the structural members come together. As SAUVIM is a prototype vehicle, field applicable paint will be used, as much revision work is anticipated on the frame; this will necessitate re-coating small sections around the revision work performed.

Garden style soaker hoses and hardware fittings have been acquired for the project to allow wash-down of the frame and vehicle contents following recovery. A single-point attachment is going to be provided to allow for hookup to the recovery vessels water supply. This system will serve two purposes, first it will allow all of the vehicle electronics to be run while on desk without worry of overheating and secondly it will assist in the wash-down of saltwater off the vehicle hardware following post-mission recovery.

Addition of tab points will be performed for mounting many assemblies onto the frame including; sensors, instruments, the mission sensor package, ballast tray translation hardware, etc.

Floatation - After an initial survey and state-of-the-art review of floatation systems, two general techniques presented themselves as commonly in use for floatation on deep-diving AUV, ROV and DSV systems. Glass macro-spheres and syntactic foam were the two systems that proved capable of surviving to the SAUVIM=s design depth. In a trade-off design call of weight versus volumetric efficiency, syntactic foam was chosen for the SAUVIM.

Floatation foam for the SAUVIM is being acquired in two stages. The first set of foam which is rigid polyurethane foam manufactured (R-3315) by General Plastics Manufacturing Co. of Tacoma WA, is a 300psi rated polyurethane foam with a density of $15.0 lb/ft^3$. This foam will undergo a 5% volumetric compression at 300psi, and will undergo about a 5% weight gain if exposed to 250psi water for a period of 40-50 days, which is a logarithmic absorption limit. SAUVIM will carry enough foam to overcome this effect, however, it is planned that the foam will be barrier coated with a thin layer of brush on polyester or 2-part marine epoxy resin. Both the top (dorsal) foam and side foam have been shaped; the top foam has been mounted onto the frame as can be seen from Photograph MED-4. Inspection of Figures MED-8 and MED-9 will reveal that both the top and side foam pieces are of a constant cross-section, this serves multiple purposes: first, this will allow for use of the extra shallow water foam as a set of male molds for the vendors who fabricate the syntactic foam, second, during shallow water trials vehicle trim can not only adjusted by shifting ballast fore and aft but also sections of the floatation foam. As can be seen from Photograph 4, much void space remains between the foam spaces - this is due to two reasons: 1) the shallow water foam has about 2.2 times as much buoyancy as the deep water on a volumetric basis. 2) The pressure vessel hardware for the deepwater vehicle will be heavier due to the upgraded bottle walls and lids. These void spaces that are currently

visible will be filled when the deep-ocean foam blocks are widened. The placement of all the shallow water foam on the vehicle from can be seen in an isometric view as seen by Figure MED-10.

The second set of foam will be syntactic foam comprised of glass micro-spheres with an epoxy binder these will have a density of around 40 lbs/ft^3. Figure MED-11 depicts the deepwater foam as it will be mounted onto the frame. A series of likely vendors has been identified for these foam blocks. Extra shallow water foam blocks will be sent to the vendors after completion of the initial shallow water trials and these will serve as male molds for the chosen vendor to form the syntactic block out of. Nearly all of the foam space volume will be occupied by the syntactic floatation.

Attention was given to the location and sizing of the floatation pieces to ensure vehicle stability and the proper range of pitch and roll sensitivity/stability. The method by which this was tracked is covered under the Vehicle Static's sections.

Vehicle Statics - Though this is not vehicular hardware system per se, it is an area of the SAUVIM design that has required constant attention since the initial concept designs of the frame and major component placements were being considered throughout the first 12 months of the project. About three major iterations in the vehicular design at the advanced conceptual level were proceeded through and this factor was considered through each.

For purposes of keeping account of the vehicle statics, a coordinate system was defined on the vehicle as detailed in Figures MED-12 and MED-13. The origin point is located at the lowermost, rearmost point of the lowermost, rearmost lateral I-beam member of the SAUVIM vehicle. From here the +x-axis runs forward along the ventral line of the SAUVIM belly, meanwhile +y-axis proceeds out to the right side of the vehicle, therefore by right-hand screw rule the +z-axis proceeds vertically out of the top of the vehicle. This is not in keeping with the standard convention of coordinates systems for AUV control but this one was set up by MED staff for in-house measurement and component tracking and was deemed a more logical one for the task at hand here.

A database in spreadsheet form has been kept of all the larger masses and volumes on the vehicle and the coordinates as to their respective individual center of mass (COM) and centroid of volume (COV). A table of the over one hundred major components (i.e., floatation=21, frame=46, components=40) on the vehicle was complied and their exact coordinates along with their associated mass and volume were determined. Initially, these were comprised mainly of estimates, but as solid models and actual hardware have been developed over the last 18 months, more accurate estimates have been generated from the CAD software and also by means of direct measurement. The static moment contributions of each component were then computed using the classic mechanics equations.

Corrections in wet mass contribution were made to account for density loss upon immersion in seawater. Basically this was done by accounting for both mass and the volume of the various components together, from these data the effective specific gravity for the various components could be determined and therefore the wet weight determined by reducing the effective specific gravity (sg. is reduced by 1.0) for the immersed vehicle state. Meanwhile the dry mass state was also tracked as obviously vehicle stability and behavior during craning and launch/recovery operations is critical as well.

Table MED-2 is a condensed version of the spreadsheet database that is kept for tracking the static stability of the SAUVIM vehicle as design has progressed. As can be seen both mass and volume are tracked for each item on the vehicle including: frame members, foam pieces, pressure vessels,

sensors, brackets, etc. Some items will be added as the respective detailed designs get refined, among these items will be major fastening hardware, interconnecting cables and soft ballast tanks.

The estimate position of these points using data updated in the autumn of 1999 locate the center of mass (immersed SAUVIM) and the center of volume in the locations of the vehicle as summarized in Table MED-3. This places the COM at the following coordinates on the vehicle: x=69.39,in, y=-0.88in, and z=32.65in while the COV is at x=69.39in, y=-1.20in and z=37.28in. Therefore the relative positional difference between the two is 0.0in, 0.32in, and 4.63in with the COV being located above, of course. The restorative pitch couple on the submerged vehicle is around 2,815lbf working on these two points. This figure is the effective weight of the vehicle components in the immersed state, minus the floatation elements (e.g. foam); consequently it is also the amount of buoyancy the foam is providing in the neutral trim configuration. As can be seen from inspection of Figures MED-12 and MED-13, these points are located in the middle of the volume of the rectangular region defined by the upper section of the frame. It should be noted that upon pulling the vehicle out of the water the effective COM point shifts upward and slightly aft as the major masses of the foam and batteries exert their un-buoyed weight on the structure. It should be noted that this point is between the four sling points.

These points will shift around in the course of a typical mission as ballast is jettisoned (the manner in which will be detailed in the section immediately following), so tracking them and the attitudes that the SAUVIM assumes is of utmost importance to establish vehicle performance and controllability. Table MED-4 tracks these changes in location of the COM and COV during the various scenarios in a SAUVIM mission.

During cruise mode on the bottom, the SAUVIM will perform interventive tasks. This is when the arms will be deployed and external reactive forces will be imposed on the vehicle from them. To quantify the degree of vehicle reaction due to this a sensitivity analysis based on the design of the arm tray was performed. The results, summarized in Table MED-5, show that the vehicles range of motion.

As can be seen from the table the SAUVIM has some minor sensitivity to arm deployment and action as the SAUVIM pitch various from nearly-zero to 11° nose-down attitude with the arm loading case at the worst-case geometry and loading. As we can see mass shifting the main ballast allows us to compensate for most of the worst-case arm loading and geometry, reducing nose-down pitching to about 3°. For roll-motion the baseline SAUVIM needs trimming as it currently stands, however, roll motion of the vehicle is at most 2-3 from the initial attitude. Nonetheless, it will be worth investigating some manner in which the ascent weights could be articulated in a starboard-port manner in an area below and rearward of the stowed arms in the forward area of the frame.

Ballast - Like other deep diving vehicles with a limited power budget, namely DSVs and flyby AUVs the SAUVIM will use a hard ballasting system. Battery capacity would be quickly exhausted and range compromised by thrusting down through up to four vertical miles of water. So, in keeping with conventional practice, the SAUVIM will carry six major ballast masses known as: main/emergency ballast weight (one 600 lb weight, dry), descent weights (two 150 lb weights, dry), ascent weight (one 300lb weight, dry) and the metering ballast (two weights 60 lb weights, dry). This hard ballasting will be supplemented by two free-flooding lateral tanks, each of 30 gallons volume. These soft tanks will provide about 503lbs of buoyancy on the surface during launch checkout operations.

The employment of these masses throughout the course of a mission is detailed in Table MED-6. The table documents the SAUVIM ballast budget and expenditure during a typical mission. The initial phase of SAUVIM operations is launch and systems checkout on the surface, prior to proceeding with the mission. The vehicle will initially be around 500 pounds positively buoyant - this will be provided by a pair of twin 30.0-gallon fiberglass soft-ballast (e.g. air-filled) tanks that will be mounted down among the side- region of the vehicle. This initial positive buoyancy is to aid in vehicle release and surface checkout. Upon a go confirmation for mission the soft ballast tanks are flooded and the vehicle becomes 300 pounds negatively buoyant. The vehicle will now become nose-heavy as planned and tend to pitch forward to a 15 -20 nose down attitude. The vehicle will enter the un-powered descent phase now that will take it to the bottom. Occasional course correction and trim can be handled primarily by the fins, meanwhile, the negative buoyancy of the vehicle provides propulsion. For extreme course corrections thrusters can be used, but use of them should not be necessary as a matter of routine. Upon approach to the bottom the SAUVIM will release the twin 150lb (300lbs total) decent weights. These consist of scrap iron plates bolted into a stack with through bolts.

These and the associated release mounts are located in a nose forward configuration and their release will result in the vehicle assuming a near-neutral buoyancy with a near-level trim. Note that near- is a common prefix here as achieving completely level trim and buoyancy in operation is quite tricky even with a well-thought out trim plan and flexibly configure-able vehicle as many factors can perturb the system and are difficult to predict and adjust for pre-launch. Some of these possible factors include: salinity, presence of up- or downdraft currents, the adherence of mud to skids, differential compression of buoyancy elements, etc. Hence the ability to meter ballast and trim the vehicle by means of mass shifting will be provided. For SAUVIM it intended that mass shifting for pitch trim (the most critical and sensitive) will be accomplished by translation the main (emergency ballast) massing around 600lbs fore and aft on a 9" stroke to each side of center. For neutral trim (normal bottom cruising operations) it will be residing near the halfway point on its stroke, with the arm stowed.

For fine tuning to a slight negative buoyancy we are investigating various options - the leading concept consists of twin hopper units with around 60lbs of oil soaked or corrosion treated steel pellets, each of these will be equipped with a solenoid-operated release valve. The ability to dump these out as a pair or singly is deemed valuable as it affects some measure of corrective roll trim. The detailed design of these units remains to be performed at this time.

Upon dropping of the descent weights and completion of buoyancy and attitude trim the vehicle is now ready to enter the bottom powered cruise (or mid-depth as it may be) mode. Buoyancy at this point should be nearly neutral and trim is near neutral. Any slope following or extended climbing/descending during powered cruise can be accommodated by appropriate pitch attitude adjustment via the main ballast and vertical thruster action. This will allow the thrust of the main longitudinal thrusters to be vectored in the desired direction. Alternately, the vehicle can remain trim neutral and translational correction can be provided by vectoring the appropriate combination of thrusters, though analysis indicates that this is more power intensive.

During the intervention stage of the mission the main ballast can also be shifted rearward to balance the trim changes that will occur upon arm tray deployment.

Commencement of return to the surface is initiated by dropping the ascent weight off of the main ballast carriage. This is, like the descent weights, a mass comprised of bolted scrap iron plates.

Dropping it will result in a nose-up attitude of 10°-15° and buoyancy that is around 300lbs positive. Again the vehicle trim and maneuvering will be mainly via the fins during this un-powered cruise mode.

Finally, there is the main ballast mass (also referred to as the emergency ballast), which is 600lbs of plate steel (or iron) bolted together. Dropping of this will not be necessary during normal SAUVIM operations but should unusual events occur (e.g. flooded pressure vessel, compromised floatation, excessive mud load, etc.) this will provide, when dropped with the ascent weight 900 pounds of positive buoyancy thus providing a comfortable extra margin of positive buoyancy.

Based on the most recent drag and parameters available it is anticipated, the SAUVIM will cruise, with about a 12° nose down attitude and at 300lbs negative buoyancy, down a 43° glide slope and make 1.2-1.5 knots effective along this path. This means that time to bottom to a 20,000 ft range will take around 2 hours and 10 minutes.

During the shallow water trial operations the vehicle will simply be launched without descent weights and be powered to the bottom using vertical thrusters. There is a twofold reason for this; first Ke'ehi lagoon is less the 40' deep on average so power drain to accomplish powered descent will be minimal and, second, doing this will allow the conservation of ballast mass.

The detailed design of the main ballast tray, displayed in Figure MED-14, of which within are both the Main/Emergency ballast weight as well as the ascent weight are housed, is that of an aluminum 6061 structure that sits on six polymer wheels that runs in a captive track area of the main SAUVIM frame. The track length gives the ballast tray an 18" stroke with the normal rest spot at the midpoint of this. A L-channel bolts against this rail, this is to hold captive the tray to the track should the vehicle shift. The whole assembly is bolted together to allow installation and removal onto the frame.

The front and rear plates are removable to facilitate loading of the ballast masses into the frame, typically ballast will be moved into the frame area and jacked into position. The ballast dropping mechanism is based on the design employed on some DSV vehicles. The ballast blocks are scrap iron plates that are bolted together with tie rods. One or two of these rods will be run into a cam-lever release assembly which will allow a underwater solenoid (Pelagic Systems: DH-1) to trip the release. The adaptation of this design from a highly successful DSV is underway.

Photograph MED-5 shows the carriage resting within the SAUVIM frame upon its wheels. This is in the lower section of the frame just forward of the longitudinal mid-plane. The ballast mechanism translates fore and aft on the wheels while atop the unit will be located the Pelagic Systems underwater release solenoids and the release cam assemblies. There are two bays within the ballast tray, the larger bay is where the main ballast mount is suspended, whereas the smaller bay is for the ascent weight.

Issues of concern in the design of the ballast tray carriage unit included: serviceability, seawater corrosion resistance, static stability of the tray assembly through various vehicle attitudes, protection of release mechanisms from jamming/entanglement, ballast load that can be carried..

The articulation mechanism for the ballast tray is under conceptual design at this point; the reviews of a couple of designs for the trays are due in the next month. Competing designs at this point involve the following: twin ACME screw drive, chain gear drive systems, twin spur gear and rack designs. The design eventually chosen must deal with stirred up grit and sand, extensive seawater exposure, as

well as vehicle tilting and motion. This combination of constraints tends to eliminate a lot of commodity solutions as literature research has shown for this design solution as well as that for the arm tray.

The solenoid dropping mechanism is entering detailed design - implementation of this feature is not critical to after shallow water testing as the SAUVIM will thrust to the bottom during initial trials in Ke'ehi Lagoon. A solid model of the release cam assembly is shown in Figure MED-15.

The two forward ballast mounts, which house the descent weights, are mounted against the most forward set of vertical I-beams on the lower portion of the frame. These mounts depicted in Figure MED-16 are currently in fabrication as of this writing. These are basically four sided boxes that house the ballast weights, which are scrap iron plates held together in a single piece by means of tie-rods. The box prevents the weights from swinging about freely from the single point cam release mechanisms that hold them to the vehicle. The bottom of each box is open, thus allowing the released mass freedom to drop away upon release. These units are fabricated from Al-6061. The units are about 20 lbs in weight and are approximately 24" x 12" x 12' in size. Figure MED-17 shows the location of the major ballast masses on the SAUVIM Frame.

The ascent weight is, like the others, a series of stacked scrap iron plates that are bolted together. As indicated earlier the ascent weight rides in the tray along with the main or emergency ballast mass. A separate release mechanism will be designed for these.

Soft blow tanks are in the conceptual design phase at this point. They will consist of 30- or 15-gallons apiece with a either one or a pair located on each side of the vehicle, respectively. These will be contour matched to the floatation foam on the side of the vehicle. These tanks will be formed from male molds and will consist of fiberglass lay-up over a male mold. Photo MED-6 depicts a mold shape that will be used for the lay-up of the tanks. No foam or balsa core, though desirable for stiffness and preventing oil-canning of the walls, will be used due to the extreme hydrostatic pressure loading the tanks will have to withstand.

Batteries/Power - Power for the SAUVIM for proof testing trials, as well as initial deep-water trials, will be provided by a brand of commodity battery in fairly standard use within the oceanographic community. Physical placement of the batteries will be covered, electrical aspects will be detailed under the electrical systems section. The SAUVIM is using six Deepsea Power and Light model SB-24/38 and six model SB-48/19 units. From a mechanical standpoint these batteries are of identical mass, around 108 lbs (dry) with dimensions of approximately 18.1A long x 12.4" wide x 12.2" high. These batteries offer a fairly reliable, commodity power source for the deep ocean environment but at the tradeoff of a fairly low volumetric plate (energy) density. This was deemed an acceptable tradeoff for the vehicle development portion of the mission.

The twelve batteries will be located low and rearward on the vehicle frame in four rows of three batteries apiece. Each set of three batteries is strapped into a frame equipped with high density polyethylene (HDPE) skids to facilitate rapid removal and access from the rear, should a quick mission turnaround be desired with a spare set of batteries awaiting reloading. Photograph MED-7 displays the entire bank of batteries on the vehicle frame and Photograph MED-8 shows the empty trays on the vehicle. These trays, which have HDPE skid pads mounted on the bottom, are locked down to two rails that are also lined with HDPE (to facilitate slide loading from the rear, via bolts and tabs. Construction of the trays was performed by Moo=s Fabricate and Design Machine Works

of Honolulu with modification work being done at the University. Photograph MED-9, a view of one of the battery trays and the rails as seen from the rear demonstrates this idea.

The batteries themselves are strapped into the frames with a pair of polypropylene A seat belt strap that are cinched tight with twin non-metallic (to preclude corrosion) buckles. These straps are yet to be fabricated beyond the initial test pair. Taut securing of the batteries is deemed critical due to wave action when the SAUVIM is initially launched and recovered.

At the conceptual level, currently, is an anticipated upgrade of battery capacity of the SAUVIM vehicle should initial deep-diving tests prove successful. The use of twin oil filled battery boxes using coal mine cart lead-acid batteries should result in a anticipated three-fold increase in energy storage density in the same volume. At this point then additional maintenance of the power system will be well worth the trade-off in longevity.

Electrical aspects of the battery system will be discussed in the electrical sub-systems area of this report.

Pressure Vessels - Design, theoretical and finite-element analysis as well as manufacturing of these for both the shallow water as well as deep water SAUVIM vehicle was, or is being, handled by the MAF group and these aspects are detailed in that section of this report. However, some additional work is required for integration of the pressure vessels into the SAUVIM vehicle.

The first area consists of physically mounting the bottles to the frame of the SAUVIM vehicle. The following factors were among those deemed important in the design of the mounting system: stress of clamping is nearly uniform around circumference, mounting systems provides some compliance between bottles and rest of vehicle to allow compliance take-up for thermal expansion/contraction and hydrostatic as well as vehicle load stress settling, clamping system allows removal of individual bottles for servicing contents, system can withstand immersion within a marine environment, system provides some middle and high frequency shock/vibration and shock isolation. What has emerged for the Phase-I vehicle is a set of saddle units made of off 1" HDPE plastic that are in matched pairs that clamp and bolt together. These are lined with about 3/16" of neoprene rubber where the contact patches with the pressure bottle walls occur. Clamped via two SS-316 bolts that run from the top saddle half into SS-316 threaded inserts embedded in the lower half these provide a positive locking action onto the pressure vessel bottle. The neoprene pads give and provide positive compliance in the system while also allowing for slack take-up and some measure of high frequency noise dampening. Each pressure vessel has two saddles and each saddle unit clamps onto two longitudinal rails that run the length of the pressure vessel space. The HDPE plastic structure, having some inherent elasticity allows for flexure of the structure thus helping with isolating the pressure vessel contents from the rest of the vehicle. As can be seen from Figure MED-18, the saddles run in sets of six on each of the two sets of rails, which are comprised of Al-6061 L-channel, two of the saddles are for each bottle. The bottom half of the saddle units are shown installed onto the support rails and SAUVIM frame in Photo MED-10.

Figure MED-19 shows the geometric sizing of the shallow and deep-ocean vessels together with their lids. The interior volume space, which was established as a design constraint for the MAF group by the MED and RDC groups together, is 13.0" in diameter by 18" in length; this is the same for both pressure vessel assemblies. This size was arrived at based on an estimate of how much volume would be needed to house a 6-U based VME computer system along with support equipment. The shallow

water pressure vessels, shown in Photo MED-11 have been successfully mounted onto the frame as shown by Photo MED-12.

The vessels, being comprised of composite materials, have heat rejection that is somewhat inferior to that of metallic bottles of the same geometry.

Similarly, the watertight integrity of the shallow is critical to the vehicle systems stability so a series testing the shallow water pressure vessels was done upon their turnover to the MED group. The bottles were repeatedly tested in a series of integrity tests. These are also over-viewed under

Conditioning of the air within electronics bottles that are sealed is a standard practice, it was decided by the MED group after a literature review and researching the state of the art to incorporate a vacuum purging system on the SAUVIM pressure vessels. However, the 10,000psi hydrostatic environment that this hardware must survive in precludes use of any of the commodity valves we looked at. Based on some preliminary pressure testing in our pressure tester it was decided to modify some stainless steel bolts in to a valve system. Fortunately encountered during a review of commodity solutions, the UNC-2" bolt available from Zago Corporation was revealed to be a perfect solution. Shown in Figure MED-20, it is a conventional hex head stainless steel series-alloy 316 bolt equipped with an O-ring glad. The vendor was willing to add a purge channel into the bolts for us for pulling air into and out of the bottles. Shown in PhotoMED-13, the bolts have a center drilled air channel about 1/8" in diameter that meets a cross-drilled channel. When the bolt is fully screwed down the cross channel is covered up and the O-ring seal engages. Likewise, loosening of the bolt exposes this channel and allows for a sealing chuck wrench, depicted at the top of Photograph MED-13, to be placed over the bolt. Vacuum and controlled atmosphere can be applied to the bolt area via hoses connected to this chuck. This functionality gives the following useful features: 1) It allows the lids to be pulled onto the bottles with a minimum of shock applied. 2) It allows for detection of leaks, prior to vehicle launch, by monitoring a specified bottle over-pressure or under-pressure that can be added. This is accomplished by means of pressure sensors included in each bottle. This gives a very good diagnostic check on the vehicle seal integrity. 3) This feature also allows for replacement of moisture laden marine air with dry nitrogen or another filtered source, precluding any moisture condensation from forming in the bottles which could be exacerbated by the extreme temperature drop the SAUVIM would undergo from the ocean surface to any moderately deep task site.

The hole penetrations through the lids were assigned based on the equipment functions housed within the various bottles based on the RDC group design in consultation with the MAF group. Analysis by the MAF group set the MED group with the design constraint of only seven holes per a end-cap lid of no more than 1.0" in diameter. On the shallow bottle these will take the form of six electrical connector holes on a bolt circle pattern of about 8.0 inches in diameter with a 2" diameter vacuum bolt hole in the center of the lid. For the Phase-II lids, which are comprised of 3" of titanium, the holes, including the 2" diameter bolt hole, will move out onto a 8.0" diameter bolt circle. Photograph MED-14 displays the various underwater electrical hardware that is awaiting installation onto the SAUVIM vehicle upon completion of machining in the appropriate holes in the lids.

Thrusters/Fins - Eight thrusters will provide propulsion for the SAUVIM. These consist of six Technodyne model 1020 and two model 2010 thrusters. The larger 2010 thrusters are rated at around 130/80 lbf (forward/aft) of thrust static each while the smaller 1020 yield around 47/32 lbf static in the forward direction. Actually testing in the pool has confirmed that these values are about 20-25% under the actual output.

Four 2010 thrusters are oriented vertically, these are located roughly at each corner of the vehicle, and two are mounted in a lateral direction, these allow for thrusting to the port or starboard. The pair of larger model 2010 units is out on pylons approximately 2 back on the length of the vehicle, these are for fore and aft cruising thrust.

The Technodyne thrusters use DC brush-less motors, so commutation and power modulation are provided by Advanced Motion Controls (AMC) Model B60A40 and Model B40A20 controllers for the 2010 and 1020 units, respectively.

An initial literature search was performed in the attempt to find vendor-based solutions that provided symmetric thrust, this being identified as a highly desirable trait based on ODIN-II operational experience as a very useful feature for an AUV based thruster system, proved fruitless. Nothing was found among the dozen of so vendors contacted that fit our needs, so an in-house thruster was designed around stand C-face NEMA brushless drive motors and shaft seal components. This unit is shown here in Figure MED-21. Vendor quotes that came back for this unit were more than commodity thrusters of equivalent size and power and that did not factor development and debugging costs, so a second vendor search was conducted with the idea of modifying the thruster system to allow for symmetric thrust.

Unlike the ODIN-II vehicle, it was found to be cost effective to adopt a commodity thruster to use for the SAUVIM vehicle after fabrication, assembly, component and debugging/testing costs were worked out. Tabulation of machining costs alone (without accounting for debugging/development costs) proved that it was cheaper to go with a commodity product and later retro-fit it to provide symmetric thrust. Upon researching the vendors, again the Technodyne was the most economical thruster among those that meet all our other operational criteria. All of the thrusters have been ordered and half of the set the set have arrived in. Meanwhile symmetric thrust propeller blades that are sized to the SAUVIM ducts have been fabricated and hub material has been ordered. These propellers, which are similar to those depicted in Figure MED-21, are 3 bladed, bi-directional thrusters with tunable but constant pitch. It should be noted that these are optimized for bi-directionality of thrust and not for forward advance ratio (cruising speed).

The clamping and ducting of the thrusters is done by means of aluminum pipes, these are in turn bolted to the frame via a set of welded brackets. Within the tubes a set of split-collar clamps grip the thrusters and these are bolted within the tube via a set of four radial struts. Photograph MED-15 is a view of the thruster clamps which are comprised of 6061 Aluminum with SS-316 wrenching screws to hold them together.

A view of one of the eight ducts, in this case one of the longitudinal thruster tubes, is shown by Photograph MED-16, these ducts are sized about 12-1/8" across the interior diameter and 21@ down the length of the tube. Four of the thrusters will be mounted vertically, while the remaining two will span the vehicle in a lateral fashion. The mounts for these are being designed and fabricated, currently. Table MED-7 gives a summary as to the location of the vehicle thrusters, and the thrust vector direction (centered in the middle of the propeller hubs), using the static vehicle balance coordinate system.

Photograph MED-17 is a view of the smaller Technodyne 1020 thruster units along with both models of the Advanced Motion Controls brushless controllers that will be paired of with the thrusters and housed in the rear two pressure vessels. The machining work for all of the clamping hardware has been done in-house either by MED staff or by the College of Engineering machine shop.

While a appropriate vendor-based solution was found for the thrusters, the search for a direct drive, high torque low speed stepper motor based underwater drive was unsuccessful. So an in-house version has been designed out to the detail level. Based on the bi-polar stepper motor, gear-head and controller shown here in Photograph MED-18, this power canister will be used for the three fins as well as the ballast and arm tray deployment mechanisms. The motor is an AMP 4034-336 stepper motor that develops 450 oz-in of torque in direct drive and is bi-polar stepped while the gear head is a CMI 34EP010 planetary gear head that has a 10:1 ratio. The controller is an Intelligent Motion Systems (IMS) IB-463 model that runs at 12VDC and features input isolation from the motor winding feed terminals and power supply.

Figure MED-22 is a 3-view and isometric of the power canister unit that is nearing the shop-ready stage for fabrication. Basically the motor and gear-head are mounted within a thin-walled, oil-filled aluminum 6061 canister with a beefy for piece that serves for structural mounting as well as housing for the shaft seal. The shaft seals for these units are standard O-rings as the rotary shaft speeds are slow and intermittent in nature and the pressure difference is small across the seal.

Figure MED-23 shows the fin placements that are planned for the SAUVIM. At this stage of advanced conceptual planning the fins will be moderate aspect ratio surfaces (1.5:1) of approximately 3-4ft^2 that will be fabricated out of fiberglass and epoxy in a free-flooding surface-lay over an aluminum shaft. These shafts will be routed back into the vehicle and mated the power canister shafts. Figure MED-23 shows that the proposed layout of the fins on the SAUVIM vehicle includes one dorsal fin mounted the rear of the vehicle and two forward mounted side plane style fins. These locations were arrived at based on some vehicle static calculations though addition/relocation of fins may occur during shallow water trails.

Bottle interior structures -

These structures are needed to provide several functions for the contents within the main pressure vessels, among these are the following: provide a firm mount point for the components, maintain air gap space and air flow routing for component cooling, provide interconnect points for circuitry debugging/installation/removal.

The nature of these structures will vary from bottle to bottle. For the forward four bottles they consist of an assembly resembling a cable spool. Figure MED-24 shows a typical example that is going to be used in the Main CPU bottle, which is the bottle that is in the middle row on the vehicle port side. The two endplates are fiberglass plate and serve as end bulkheads to which the interface board connectors are brought out. Bus strips for the main power supply break out and switching relays will be mounted to these as well, hence the decision to use a insulating material. One cooling fan is mounted in the center of each plate and re-circulation holes for cooling air will be cut on the outer perimeter of the plates. Between the two bulkhead plates is an aluminum box, made of 1/8th-inch-thick welded aluminum plates that serve as both a structural unit to which various components can be screwed into but also as a heat-dissipating surface to help alleviate localized hotspots that active components may generate. Inside in the middle of this structure will sit the VME computer and bus back plane, this unit is the source of most heat in the bottle. The front side of this structure will be open to allow for installation of the VME unit as well as interfacing to its IO boards and ports. Meanwhile, on the backside will be mounted the DC-DC power units that will be needed to provide conditioned power within the pressure vessel. These units will be Autronic units distributed by Schafer systems. At each end of the structure are two brake shoe-like assemblies that can spread and grip the inner walls of the pressure vessel in a even and distributed fashion. This was seen as a viable

solution as to how to securely mount the bottle contents to the slick pressure vessel walls. These units are being fabricated and assembled in-house at the University by the MED staff.

Mounted to the plate below the VME computer will be the IB-463 stepper motor controllers, vehicle health monitoring circuitry (Please see the section labeled a "Vehicle Health Monitoring Circuitry" for more information on this), and an 8-port RJ-45 Ethernet hub. On a separate lower shelf, mounted on standoffs from the main aluminum box, will be up to three PC-104 computers. Mounted above the shelf will be up to six plug in boards (Vector Plug-in boards series 3677-2) of about 6.5" by 4.5" in size that host conditioning and switching circuitry for the VME computer Matrix IO boards. Up to six of these boards can be installed in two bays of three apiece. For the Phase-I vehicle only three will be populated. Behind these boards run a piece of aluminum U-shaped channel, this is used as a mount and heat sink for the larger interface switching transistors, which are typically TP-220 package MOSFETS.

This placement was arrived at based on the size that various anticipated vendor devices would consume by be hosted in the bottle. After determining the size and orientation specifications, for most of these devices a 1:1 actual scale mock-up was constructed and the spacing a fitting of the devices was figured from this, as shown in Photograph MED-19. The actual working bottle structures are in fabrication now as can be seen from Photograph MED-20.

The rear two bottles will house relatively few components; basically just the thruster motor controllers and some bottle health monitoring circuitry will be inside these two bottles. The reason for this is that the AMC controllers that drive the SAUVIM thrusters can dissipate a significant amount of heat and these may be under continuous duty at times resulting in a high heat load. Being that the bottles are poor conductors of heat these controllers will require lid real estate so they can be directly conducted to the outside of the bottles. The left side bottle, known as PV#5, will carry two AMC B60A40 and two AMC B40A20 units, while PV#6 will be carrying four of the smaller B40A20 units within.

Pressure Housings - Some SAUVIM hardware will be outboard of the main pressure vessel set. These items therefore require their own pressure vessels and/or compensated enclosures. Vendor solutions were researched. Each system that requires these is detailed below.

Switchboxes - Assigned one to each respective pressure vessel, these six boxes serve a two-fold purpose. The primary one is to house vehicle mode switching circuitry that sets the bottle power state to as needed by the vehicle operation. These states are: 1) bottle contents on, 2) bottle contents off, 3) system charging, and 4) system off and hot rails isolated (used for connector plug-in operations - a safe mode). The secondary function of these are to serve as recharging ports for each pressure vessel power bank to facilitate underwater charging of the vehicle, should it be necessary during Phase-I testing operations. These boxes will be located in an accessible but protected location. Likely they will be located somewhere in the vicinity of the arm/instrumentation frame-space.

Inside the box are the following contents: a machined detents and collar (to lock the shaft in the selected mode), twin micro-switches (to set vehicle mode) and penetrator wire splices (to enable charging pass-thru).

These switch boxes, diagramed in Figure MED-25, are standard O-ring equipped aluminum pressure housings with a 316-stainless steel switch shaft. Two UNC 2"-20 with spot face ports are cut into the bottom; these are the for the two connectors which enter the switch box. One proceeds to a

underwater-mate able Impulse IL-4-FC connector to which a charging cable can be mated, while the second is the tie in to the respective bottle that is switched. Photograph MED-21 shows the switch-box, cables and typical contents in assembled and disassembled fashion.

Review is underway as to whether to pre-fill these with oil before closure as a leakage damage-limiting measure. These units also wait proof testing to 10,000psi.

Junction boxes - Since the number of ports in the main pressure vessel lids for underwater cable connectors and penetrators is limited due to a stress-based design constraint set by the MAF group, a need was identified to be able to break out multiple SAUVIM functions of off individual lid ports. Three solutions were examined: the first involved custom-molded octopus-style dry-molded connectors, the second involved using PBOF tubing converging on a multiple plug-in through lid connector, and the third was using a dry patch-in/junction box. After review, it was determined that the third option was most economical, allowed the most after-installation reconfiguration of the vehicle sensor suite, and was the most field serviceable of the options.

Basically, as can be seen from Figure MED-26 the junction box is a aluminum 6061 canister with a lid and base canister. The dimensions of the lid are 7" in diameter by 1.5" thick, while the canister has an outer diameter of 7" and a height of 10". The interior cavity size is 4" in diameter by 7" in depth. The lid has one penetration in the lid for a high-density data connector to enter to the box, a SeaCon-Brantner MIN-M-37-FCR; this in turn ties back to the main pressure vessel bottles. On the bottom of the canister are typically four UNC1/2-20 threaded holes, into which the penetrator connectors of various vendors can be screwed into. Unoccupied holes can be sealed off by placing a vacuum bolt, the same as is used on the lids, in the spare holes. Within the cavity is mounted bus a strip for running patch panel interconnects into and out of the pressure vessel. The location of the junction boxes will be where a lot of the sensor signals need to be broken out; this is the area in the frame immediately behind the arm stowage space as can be seen from Photograph MED-22.

Review is underway as to whether to pre-fill these with oil before closure as a leakage damage limiting factor, as the contents should be capable of sustaining hydrostatic pressure and this could potentially limit sea-water intrusion to perhaps 10-15% by volume (depending on depth of course) should a leak occur. These units wait testing to 10,000psi hydrostatic.

Camera housing - Optical grade camera housings were an item that was identified as needed early in the vehicle development. After a review of vendor solutions, it was decided that manufacturing the housings in-house at the University of Hawaii (UH) would offer significant cost advantage as well as permit greater flexibility in the camera systems and contents selected. This ability to evaluate and miniaturize the cameras was considered a distinct advantage for a system that may be employed in automatic vision processing and scanning.

Fabrication of a flat-faced housing was performed at UH, the camera housing is a 6061 one-piece aluminum cylinder as seen from Figure MED-27 that measures 6.0" in length by 2-7/8" in diameter. The cavity is 1-9/16" in diameter by 4-3/4" deep. The front optical face is a cylindrical piece of ground boro-silicate glass that is 1.0" thick by 3.0" in diameter. Electrical penetration is via an Impulse IE-SS-1206-BCR connector that is threaded into the rear of the housing. The glass and cylinder body was designed to withstand hydrostatic pressures to 10,000psi while the glass was rated to 4,000psi. For full-ocean depth an upgrade to 1-3/4" to 2" glass or replacement with acrylic will occur. As can be seen from Photograph MED-23, these units have a pair of retaining rings with 8 tie-rods to pull the housings closed and maintain the seal at low pressures.

Six of these units have been fabricated and one of these units was successfully proof-tested to 4,000psi hydrostatic within the lab.

Both a smaller and larger version of this basic design have been fabricated as well; the smaller is housing the AORD Manipulator Homing Sensor (MHS) located outboard on the Ansaldo arm near the end effector, the other unit was designed for a larger camera for the AORD laser ranging sensor (LRS).

<u>Laser</u> <u>housings</u> - Two other pieces of SAUVIM hardware in development also need optical housings to be enclosed within. These are the laser diodes for the AORD LRA and the fluorescent light tubes that will be used for general low power illumination around the SAUVIM vehicle. As Figure MED-28 and Photograph MED-24 show these are all-acrylic housings with a bore tube and two end-cap pieces.

These units are designed to withstand pressures of up to 10,000psi, a sample unit awaits testing within the MED pressure test facility.

Arm-tray - The arm-tray has evolved as into a SAUVIM system as it was determined early in the vehicle conceptual design that a way to store the manipulation system out the way of harm during autonomous navigation scenarios was a critical need. Unlike a manned DSV, the SAUVIM, being a prototype AUV, will need to protect non-critical (from the standpoint of total system loss/failure), nonetheless, sensitive systems in protected areas of its structure as collisions are very likely during the debugging of system software.

The arm-tray, pictured here in Figure MED-29, accomplishes this task by having a 24" stroke that allows the tray, with the arms slung beneath it to emerge and gain access to the relatively unrestricted workspace in front of the frame. Upon completion of any interventive tasks the whole tray, along with the arms can retract to within the frame to provide a caged area to protect these systems, as well as cut their adverse effect of vehicle hydrodynamics down. The arm tray is a Al-6061 structure built up of 1.5" high C-channel and 1/4" thick plate stock. The tray runs along these rails with captive stainless 316 alloy polished shoes that slide between the shaped HDPE rails. Commodity solutions that featured the right combination of seawater immerse-ability, strength, anti-particulate jam resistance, lack of jitter, and geometric profile were deemed unavailable. The HDPE squeeze rail arrangement provides a fairly tight system to hold the tray without suffering the effects of corrosion, jamming from stirred up silt and wide temperature tolerance. Photograph MED-25 shows that the arm-tray is mounted well forward on the SAUVIM frame and show how both the active and passive arms mount to the tray. The bulk of the tray fabrication was done by Miller Welding and Supply of Honolulu, while the shaped stainless shoes were fabricated by the College of Engineering Machine shop.

The mechanisms to extend and retract the tray are under advanced conceptual design, currently two design solutions are seen as potentially promising. The first mechanism is a dual pinion and linear rack gear design, and the second is a dual captive ACME screw and drive collar design. The power to drive the tray in and out will come from the same power canister unit being designed for the fin units; it was deemed that the low-speed high, torque output of that motor as well as the simplicity of using open-loop control to place the tray in the positions suited that unit well. Also, this will help keep maintenance on the vehicle simpler by reusing the same design and parts. The outer and inner stroke limits of the tray will be signaled by means of frame mounted hall effect switches that are tripped by

171

tray mounted magnets. Figure MED-30 is a conceptual design view of what the gear and rack version of the mechanism may look like.

Fairing - A fairing was deemed an important system for the SAUVIM to have for deep-water missions early on in the conceptual design phase. The fairing design is still in conceptual design and its final form is still unclear. Analysis revealed that a fairing would be critical to a smooth and controlled glide-slope decent of the SAUVIM vehicle as well as extending the powered cruise range in a significant fashion. Figures MED-2 and MED-13 give a good indication as what shape the SAUVIM fairing takes.

This shape was configured by the MED group as a compromise between the following factors: reduction of cruise drag, ease of fabrication, and minimization of additional bulk and size to the vehicle. Basically, a shape that totally wrapped around the vehicle frame and floatation while providing some flow development around the nose and tail was sought. The main compromises were in keeping the tail-cone short to keep vehicle length down and the provision for a flat region forward for the arms to be deployed through and work in front of.

Analysis of the fairing shape for a frontal drag coefficient was performed by three parties - these included the HDCA group, Pacific Marine and the CHAM company. Frontal drag coefficients were all between 0.30 and 0.35 - eventually 0.32 was chosen as a representative value. Optimization was not a goal of these analyses. Meanwhile analysis of low-speed collision and strength was performed by the MAF group.

 The detail design of the mounting struts, fairing stiffeners, composite materials selection and orientation await the shallow water-testing portion of the vehicle development.

MSP - The Mission Sensor Package (MSP) is typical of a independent science payload that the SAUVIM could host in the course of a typical mission and is the demonstration system for such an arrangement.

The design and function of this system is covered in the appropriate section of this report, the main MED task for this unit and its outlying sensor head units it provide physical mounting onto the vehicle frame as well as power and communication support.

Figure MED-31 shows the location of the MSP main canister, CTD sensor, nephelometer and magnetometer onto the SAUVIM vehicle. The mounts for the main canister will be made out of HDPE machined into a clamp shape. The clamps will be lined with neoprene pads to provide compliance and cushion the MSP canister and its contents.

The cable interface to provide trickle-charging power and RS-232 communication for talking to the rest of SAUVIM has been ordered from Impulse Enterprises. Power and communication will route through the forward-most pressure vessel on the vehicle left.

Sensors - The SAUVIM is equipped with a full suite of sensors that have been specified and ordered by the AORD, MED and RDC groups. Table MED-8 presents a current summary of the SAUVIM sensors; included in there is where on the vehicle they will be mounted, interface type and cabling, and any special considerations in terms of mounting that these devices require.

It is considered most critical to mount the following devices onto the SAUVIM vehicle before Phase-I testing commencement in the spring of 2001: the Perry-Tritech ranging sonar, the Data Instruments DH-1 pressure sensors, the Watson INS and 1-2 of the video cameras. These are the minimal compliment of sensors that will give SAUVIM ranging and sensory abilities that are similar to the ODIN-II. Most of these sensors will be provided with mounts that have field adjustable azimuth and elevation settings for the sensor heads.

SAUVIM Sub-system Breakdown - Support:

The SAUVIM vehicle as it gets closer to becoming an operational system will need support facilities, equipment, and protocol documents to be set in place to ensure safe and efficient test mission operation. Also some functions that are performed by the MED group are not directly related to vehicle construction, but are critical to meeting the ONR Grant Proposal goals. The following section overviews many of these activities.

General - A member of the SAUVIM team with previous scientific ocean research cruise experience drafted the initial mission and range guide for SAUVIM launch practices. Right now this is merely a framework document but it will be expanded to cover all vehicle preparation, checkout and launch/recovery procedures along with abbreviated checklists. A good analogy would be the vehicle operation and field maintenance manual that comes with aircraft and automobiles.

Many of the operations goals of the SAUVIM vehicle were set in consultation with this member as well as after a review of the state-of-the-art in deep-sea vehicles via literature and consultation with other research groups. These goals included: a vehicle frame that was easily modified and added to, a vehicle that can be fit into a standard shipping container with minimal knockdown, modularity of design to allow for design configuration changes later in the lifecycle, initial mission duration of 8 hours, inclusion of infrastructure for research topics on vehicle (PVs, arm, ranging, sensor suite for software).

Launch/Recovery - SAUVIM will be launched and recovered for shallow water testing by means of a combination of spreader frame, cargo straps and crane. Photograph MED-26 is a view of the vehicle spreader bar. Two 6" wide polypropylene cargo straps, one forward and one rear, that are retained on the vehicle in a basket configuration run up the frame which serves as a spreader bar. The four eyelets of the straps are fit to large steel pins that insert right through the straps. From the spreader bar a four-point chain bridle connects to a crane hook allowing single point recovery from the water. The placement of the lifting/sling points was in consultation with the MAF group, who performed FEA analysis on the vehicle frame. This system will receive much in-use testing during shallow water operations at SNUG Harbor and modifications improvements for deep-sea operation will be expected.

Possible deep-ocean system launch recovery operations include the following conceptual ideas: modification to dorsal single-point recovery hook, refurbishment and use of a flooding pontoon catamaran launch platform at the SNUG facility, and hardening of the current system.

Operational Support facility (SNUG Harbor) - Shortly after the project commencement there was the realization that the SAUVIM would need a base of operations for the later integration and early testing trials for the vehicle. The MED group was charged with surveying a series of sites for the project to eventually move its testing and mechanical integration operations to. Four main candidates emerged, these were: 1) UH Marine Biology Laboratory Coconut Island, 2) UH Marine Center -

Snug Harbor Facility, 3) UH School of Ocean and Earth Sciences Makai Pier Facility, and 4) The Ocean Engineering Departments Look Lab Facility. The Look Lab facility and the Makai Pier facilities were eliminated early due to the substandard quality of the proving grounds close to these labs; Look Lab had murky water and a cluttered bottom, while Makai Pier had no protected water nor a sandy bottom for easy grounding available. Superior support facilities narrowed the choice to the UH Marine facility at SNUG harbor.

Renovation, electrical service additions, and the construction of a climate-controlled electronics shack has been underway for the past couple of months at the Snug harbor facility in preparation for relocating the SAUVIM down to this facility toward the end of this year.

Photograph MED-27 shows the UH Research Vessel at the SNUG Harbor facility that the SAUVIM will be located at and Figure MED-32 shows the laboratory facility floor plan for the SAUVIM project at Snug Harbor. Upon being properly equipped, this facility is expected to allow for accelerated pace of vehicle hardware development since it is a more applicable space to do welding, painting and other heavy industrial operations that the current space in Holmes140A, due to its public location limits somewhat.

Vehicle Dry-Harness Testing and Evaluation - An area has been set up in the ASL Robotic Labs for SAUVIM electrical vehicle systems integration. Large enough to eventually accommodate the pressure vessel bottle interior structures, underwater cabling/connector hardware, sensors, thrusters, and all other electrically actuated parts that comprise the vehicle, the set up of the central VME computers, outlying sensors and PC-104 hardware in this space is underway by the RDC group. The Navigation pressure vessel contents will be added and interfaced to the various external sensors, stepper motors, ballast release solenoids, junction boxes, switch boxes, and of course, batteries, as the wiring harnesses interior to the bottles are each completed. Thruster vessels contents will be added and interfaced to the thrusters as well as the VME computers.

Remaining vessels will be added, as they become ready along with external components they interface with such as the Mission Sensor Package and the Ansaldo robotic arm. Bench testing and evaluation will be performed by the MED and RDC groups to insure signal and electrical integrity before the vehicle is assembled with all the electrical systems active for the first powered testing mission..

Testing/Proofing - Literature reviews of engineering handbooks and/or vendor-supplied data often fail to establish whether a proposed design solution will work on the SAUVIM vehicle, especially due to the extreme environmental conditions that SAUVIM will be subjected to in the course of a normal mission. Healthy skepticism does not hurt and often data is also inconsistent or hard to extrapolate from for our needed purpose. As a result in-house studies have been undertaken. These are generally experimentally rigorous in design but, for purposes of expediency, are not designed to be full statistically sampled studies. Table MED-9 is a summary of what, why and how studies were performed in the course of establishing the in/appropriateness of certain design options for the SAUVIM vehicle. As can be seen from the chart these experiments, generally executed by University of Hawaii undergraduate students, cover topics ranging all over the place from establishing the corrosion resistance of Aluminum alloys in contact with other metals in a seawater environment to establishing operational compatibility between vendor supplied components.

One of the more important testing facilities set up has been a pressure tester that is for establishing the ability of various SAUVIM components to function/survive at pressure. A small high-pressure chamber capable of testing pressures to 10,000psi hydrostatic has been set up in Holmes 140A. Shown in Photograph MED-28, it is comprised of a hydraulic jack body with a modified lid. Two stout high-carbon steel plates with high-tension threaded rods hold the lid captive to allow pressurization of the unit by means of a hand-pump oil pump. Two Impulse Enterprises penetrators allow up to twelve testing lines to be run to electrically active components inside the test chamber. Many items have been proof tested in here ranging from camera housings, to oil samples under consideration for compensating fluid use. Table MED-10 covers pressure-tested items within it.

A brief overview of a couple of the proofing tests performed by the MED group will follow:

Cold Oil Motor Losses - Initial calculations of power requirements and cruising ranges for the SAUVIM during the conceptual design phase required estimates of power losses due to pressure-compensation in components including the in-house thruster, the fin motors, and accessories motors. Knowledge of cold oil constitutive properties as well as simulated tests was desired to get a bounds estimate. One of these tests established free-running motor power losses do to the presence of compensating oil within the motor. A hall-effect switch commutated brushless motor, the BEI Motion Systems DIH23-19-BBNA, which is about 2.2" in diameter by about 1.9" in length, was chosen for testing because most commodity thrusters had such a setup. White #9 mineral oil was chosen as the compensating medium for having been employed in previous ocean vehicles for compensation as well as having fairly typical viscosity and compressibility for most oils used for compensation.

The motor was operated in a tub of the oil in three states, 1) empty tub, in air, inverted, 2) tub full of oil up to 1/2 depth on motor axially, inverted, and 3) tub full of oil with motor totally submerged, inverted. The tub and motor were resting in a temperature bath and the tests were run at both 23C and 20C for controlled parameters. The motor was in a free speed condition. The current was feed into the motors from a standard 3-hall sensor brushless controller chip rated for about 50 Watts; this input current was monitored via an ammeter. Meanwhile one of the hall commutation sensor lines was tapped to a standard oscilloscope to allow tracking of the revolutions per a second (RPS), this enabled a measurement of the shaft speed. A plot of the input current, in amps, versus shaft speed, in RPS, was generated for the following operating parameters: temperature at 2C, 20C and in air, half in oil, fully in oil. The testing runs were terminated upon reaching 0.50Amps or 120 RPS of shaft speed.

The results are shown here in Figure MED-33. These graphs demonstrate that shaft and power losses to oil can be significant, even at lower shaft speeds. At a typical anticipated propeller speed of 20 rps it can bee seen that current consumption ranges from 0.24 amps in air to 0.51 amps when half submerged at room temperature to 1.55 amps for the fully submerged in 2C oil. So the efficiency losses at moderate speeds in oil can be quite large. From here loss results are up around 80% in the worst case test, however when subsequent analysis of a brake-torque loaded motor is performed it is found that the losses are more around 30-50%. This figure was employed in subsequent SAUVIM design and performance prediction calculations.

It is important to note however that the losses shown here are far worse than when the motors are operating under load for the following two-fold reasons, 1) under load the thrusters will spin at the lower range of the shown shaft speeds, even at a high speed of 3600rpm one would one approaching 60 rps and for large, slow speed bi-directional propellers this is certainly an over-speed condition, and 2) the motors were tested without brake torque loads, in any event these normally useful work losses are small in these tests and will be proportionately much larger in the loaded systems.

175

Nonetheless though, this test did yield some useful efficiency data that was utilized in conceptual design calculations and that had proven difficult to find in the literature.

Leakage Testing of Pressure Vessels - The pressure vessels when delivered to the MED group had no statistical testing to establish reliability of seal or refine preparation and closure procedures. A series of tests was undertaken to resolve both of these unknowns. The pressure vessels in were submitted to a battery of four simple immersion tests of about 24-72 hours in duration each. This was accomplished by submerging them in a 55-gallon oil drum with steel weights set on top. Paper towels marked with parallel sets of water-soluble dye marks were hung inside against the walls to provide a tracing medium if any leaks were to occur. A battery of four tests was run for each bottle; they were rotated through the tests one at a time.

While these tests were run, a review of the closure, vacuum sealing, purging, and preparation procedures was performed. Procedure modifications were tested and implemented when they were deemed to be improvements.

Some important observations and procedures were generated as a result of this testing include:
The superiority of using clearance specifications over torque specifications for ensuring closure of the vacuum bolts.

The importance of keeping dissimilar metals from contacting the lids is to avoid corrosion from forming (it is planned to add zinc anodes to each lid now). It was discovered that a light, powdery corrosion occurred on the lids formed until the practice of setting the steel weights on a sheet of wood was adopted.

The vacuum closure procedure was generally the method that passed shock to the bottle contents the least.
Which bottles sealed with the most ease as well as reliability. The most reliable bottles were assigned to house the VME computers while the thruster controllers were assigned the middle two bottles and the least reliable were reserved for the front two bottle locations.

Pressure Vessel Heating - Temperature rise within the individual pressure vessels when operational was identified early on as a major design concern, especially when the vehicle is not submerged in the water. This is due to the fact that the composite materials being used in the pressure vessels have poor thermal conductivity relative to the conventional metal pressure vessels in use in deep-ocean vehicle. Additionally, interviews with research teams using currently deployed vehicles indicated that is was normal practice to spray cool the electronics canisters in some fashion when being operated when the vehicles were out of water.

To address and quantify the severity of this problem a number of tests were run that tracked internal vessel temperatures as well as ambient temperatures over time with a simulated heat load. A setup using the pressure vessel structure from the scale model fitting was used as can be seen in Figure MED-34; simulated heat loads were setup inside the bottle as well as outside to represent the predicted heat loads that would be generated by the VME Computer, DC-DC converters and stepper motor controllers. Four thermistors were spread throughout the bottle interior as shown in Figure MED-34 and one was placed outside the system to monitor the room temperature. The tests were run and the data was recorded both manually as well as on a Mac computer equipped with a National Instruments NB-MIO-16 A/D board. The worst case was at an ambient air temperature of 20C, the resulting interior temperature of 60C to 85C, depending on the probe location, beyond the maximum that the VME CPU can sustain and well past where the DC-DC power supply loads have to be de-

rated do to over-temperature. This occurred after about ninety minutes with all of the heating elements turned on.

To alleviate this heating problem, further tests where conducted with the setup placed in a tank that could drip water over the bottle and end caps from a 12V bilge pump at a rate of around 1gpm. The bottle was placed on wooden stands that kept it out of the water. This acted to cool the vessel sufficiently for safe operation out of water. In conclusion, it is felt that there is no problem with overheating once the vessels are completely submerged in water. In addition, consideration was given to fabricating the interior so that no hot spots occurred, by using heat-sinks and two re-circulating fans to move air around the interior. Figure MED-35 illustrates a typical test run after these conditions were implemented. As can be seen even these moderate cooling features, which are planned on the SAUVIM, keep all of the interior temperatures under 60C except when a dual fan failure occurs, as shown by the spikes in the middle. It should be noted that the thermal environment of the vehicle in operation will be much more benign, especially in the near freezing conditions in the deep ocean. The conclusion is that thermal build-up even with only metallic end caps should be manageable as long as appropriate deck handling procedures are followed.

SAUVIM Sub-system Breakdown - Electrical:

SAUVIM electrical implementation has moved forward to the stage of detailed design and initial fabrication. This includes fabrication of all the circuits housed within all six pressure vessels, outboard junction boxes, thrusters, fins, trays, sensors, robotic arm, batteries, and interconnecting cables. Figure MED-3 shows the conceptual design layout for the signal and power routing for the SAUVIM vehicle as based on the RDC groups control hierarchy. As can be seen from Figure MED-3 a rough breakdown in bottle contents is summarized as follows:

- Left-front bottle (PV1) - MSP bottle. This bottle houses the following components: DC-DC power supplies, the primary INS unit, a camcorder for mission video- and data-logging, pass-thru for the MSP bottle power and communication support. Low power lights will be powered off this bottle. There is plenty of spare space in this bottle for additional expansion components to be mounted.

- Right-front bottle (PV2) - Arm Controller Bottle. This bottle houses the ELMO motion control servo amplifier bus and the boards that populate it. These are used to control and actuate the Ansaldo/Maris robotic arm. This bottle houses all of the boards used to drive the arm, some expansion space will be available to the sides of the servo-boards bus.

- Left- middle bottle (PV3) - Navigation CPU vessel. This bottle houses: DC-DC power supplies, one of the two VME bus computers, cooling fans, stepper controllers for the arm and ballast trays, interface circuitry to condition outgoing and incoming signals to the VME I/O boards, a RJ-45 Ethernet hub, three PC-104 computers (two with video boards), interface patch panels and accessories switching relays. This is the primary navigation and control CPU bottle. Most vehicular functions are coordinated by the VME computer in this bottle. About half of the connections for solenoids, powered accessories and sensors are routed through this bottle. The thrusters all originate from this bottle. The reason for splitting a lot of these functions and routing half from the Arm CPU bottle is to provide some system level redundancy for the vehicle to initiate self recovery efforts and continue to navigate should a bottle flood or loose power. A RJ-45 based Ethernet line will span from this bottle to PV4 along with a RS-232 serial line to provide for synching.

- Right-middle bottle (PV4) - Arm CPU bottle. Housed within this bottle are: DC-DC power supplies, one of the two VME bus computers, cooling fans, stepper controllers for the three fins, interface circuitry to condition outgoing and incoming signals to the VME I/O boards, a RJ-45 Ethernet hub, two PC-104 computers (one with a video board), interface patch panels and accessories switching relays. This bottle is primarily for running and coordinating arm motion and control tasks. This offloads these computationally intensive tasks off of the main navigation computer. The secondary function of this computer is to provide vehicle command and navigation control should something compromise PV3. To accommodate this roughly half of the sensors and actuators route through this bottle.

- Left-rear bottle (PV5) - Thruster Controller Bottle - This bottle houses the servo-amp controllers for four of the thrusters these being the two longitudinal ones as well as the forward vertical pair. These are far smaller than the bottle volume, but few components are housed within due to the severe anticipated heat loads that these controllers can generate. Due to this they will be directly mounted to the end lids to aid in establishing a low resistance path for thermal dissipation. Pending the actual severity of bottle heating from shallow water testing some expansion space may be available in this bottle as well as PV6.

- Right-rear bottle (PV6) - Thruster Controller Bottle. The remaining thruster servo-amp controllers are housed within this bottle.

- Common to all bottles will be the inclusion of health monitoring circuitry and sensors as well as relays and/or power contactors to perform bus tie-in and power switching.

Interconnecting cables from the pressure vessels to peripheral devices will span junction boxes, arms, cameras, sensors, lights, and solenoids. This underwater cabling is shown in Figure MED-5, while Figure MED-6 shows power and motor cabling for the vehicle. In this drawing, power cable routing between the batteries and their respective switch boxes for a given pressure vessel is shown. Shown also is routing from appropriate vessels to thrusters, trays and fins, all of which are motor driven. The ballast release solenoid cabling is also included in this drawing. Some of the general systems circuitry will be overviewed, after which a bottle-by-bottle breakdown will be presented.

Batteries/Power - The batteries are the origin of all power for the SAUVIM systems. For the phase-I vehicle a conventional lead-acid gel-cell battery has been chosen. Six Deep-Sea Power and Light SB-24/38 and six SB-48/18 batteries are in the vehicle. These models put out 24 volts with 38 amp-hours of capacity and 48volts with 18 amp-hours of capacity, respectively. The banking of these units is shown in Figure MED-36. As can be seen from this the breakdown of deepwater power is that bottles PV1, PV3, and PV4 will be feed by one SB-24/38 battery apiece. A set of three SB 24/38 will be banked together to supply PV2 for the arm operations at 72V while two banks of three SB48/18 will be each be feeding PV5 and PV6 for thruster power at 144V. Provision for bus tie-in and power sharing between bottles may be implemented through spare lines and capacity has been reserved for the vehicle on the interconnecting cables.

These batteries are in common use in the oceanographic community for underwater instrumentation systems. They were chosen for ease of use for the shallow water testing of the SAUVIM vehicle though the energy density is sub-optimal. As discussed earlier the battery banks may undergo modification after successful deep-ocean testing.

Power/Distribution Cabling - The power underwater cabling is shown in Figure MED-6 while the system is shown at a component level in Figure MED-37. Some features of this routing are worth noting. First, each pressure vessel is supplied by a separate battery and/or bank thereof. This was done to prevent a short on a power bus within one bottle from bringing down the others, which would be the case if shared power was one a common bus. Provision was made to add additional load sharing and bus tie-in, as enough spare conductors of sufficient current capacity exist between the bottles. Provisions for bus isolation will be retained though to protect against these types of failure. Second, it can be noted that charging can be applied to each bank through the switchboxes that are paired to each bottle. Third, all of the connectors in the cables are noted in by the double arrow signals.

The power cables in Figure MED-37 are for the full-deep water configuration. An additional pair of Y-cables has been obtained for shallow water testing of the SAUVIM. These bank two of the 24V in the arm battery bank and parallel them together with the battery feeding PV3 and this feeds the navigation CPU. Meanwhile the other Y-cable allows paralleling the PV1 battery, the PV4 battery and the remaining arm battery together to feed PV4. It is anticipated that this will allow for vastly extended debugging mission duration when the vehicle is running armless.

Photograph MED-29 shows the cables that will be used to route power from the batteries into each pressure vessel. There are three of the straight assemblies and three of the Y-cable assemblies for the full compliment. The stainless steel 316 connectors are flange mount Impulse Enterprises IE-55(V)2410-FCR that are mounted on a 1.00" diameter smooth bore hole and seal by means of an axial O-ring seal. These are rated to 10,000psi mated. The 10-line wires of the Impulse connectors are divided evenly between the positive and negative leads.

Data Cabling - Besides the low-density power and switching cables running to each pressure vessel the SAUVIM has some high-density lines that serve to interconnect control signals across the various bottles, including the distributed computing architecture (Ethernet). To accommodate this high pin-density cables were specified for the vehicle. There are 10, 36" long lines on the vehicle of two varieties. Most of these cables run between the main pressure vessels though some run out to the junction boxes for signal breakout. The first variety are 37-pin straight cables running between SeaCon/Brantner MIN-M-37 FCR flange mount connectors rated to 10,000psi mated. These titanium connectors fit into a 1" hole and have an axial and radial seal. Nine of these cable runs are of this variety. The other cable, the one that spans from bottle PV3 to PV4, consists of eighteen pairs of twisted shield pairs with the last pin on each end being a drain wire that is in conductive communication with the Mylar shielding wrapped around the pairs. This cable will be carrying Ethernet between these two bottles hence this layout. One spare of each variety was also ordered for the vehicle.

Photo MED-30 is a close-up of these cable connector assembly ends as well as the fitting that will accommodate these at the pressure vessel lids. More data line connectors remain to be obtained. A scan of Table MED-10 will give an overview of the cable connector assemblies that the SAUVIM will carry. The more complex assemblies have generally been obtained whereas the low complexity cables have yet to be specified and ordered.

Switching Control - Provision for energizing and cutting power to the bottles in a direct fashion was seen as an important vehicle feature early on for reasons of personnel safety as well as prolonging of battery charge. Four modes have been provided: 1) vehicle buses off, 2) vehicle buses on, 3) battery banks tied in to charging port (power off to buses), 4) isolate charging port (power off to buses). The

first state is a power off state for handling, the second state is for mission operations. The third state allows for charging of the vehicle with the power shut down, and the fourth allows for safe mate/de-mate of the charging connectors underwater. One cable and connector assembly, which are comprised of Impulse IE55(V)24-FCR connectors inboard and 1/2" diameter penetrators (Z020354-1/2-PNA) outboard, run out of each pressure vessel leads to the associated switchbox for that pressure vessel. Photograph MED-21, shows the cabling and lid connector assemblies that are associated with one of the switch boxes. The six boxes will be located in a protected area forward on the vehicle, yet within easy grasp of support personnel who are in the water.

The active switchbox contents are shown in Figure MED-38. Within each switchbox are two cam-operated micro switches that can send back a two-bit encoded state to set the vehicle operation back at the switching interface circuitry. The remaining two lines are led into another Impulse 1/2" penetrator on about 8' of cable that terminates in an Impulse IM-4-FS connector, the same as the batteries. This feature allows for the SAUVIM to be recharged underwater if need be, as well as receive operating power for computer functions while underwater. This is anticipated to be of great value while debugging and testing system software.

Sensors - SAUVIM will carry a full suite of sensors, both built in-house and commodity in nature. The performance specifications and nature of the data handling and utilization is covered in the RDC section of this report. The main concern for the MED is supplying the appropriate connections and power to the instruments. Consultation of Tables MED-8 and -10 while give the reader a good idea of what these requirements are. The interconnecting cables and their routing is best seen by examining Figure MED-5.
Some of the sensors are of in-house construction and development, these are covered as follows: the laser array ranger, passive arm, and mission homing sensor are in the AORD section, while the whisker velocimeter is under its own section.

Lights - Lights are planned for the SAUVIM vehicle. Currently, the plan is to include both a high-power and a low power set of lights. The high-power set of three lamps will be halogen lamps of 100-150 Watts in power; these will be vendor-supplied and a review of vendors is underway for these. Two will be mounted forward and one to the rear, and these will be switched off of the battery bank feeding bottle PV6. These lights will be mainly for the benefit of human operators in the Semi-Autonomous loop to see any video uploads. Other than at these times these lights will be off. The low power lights will consist of six to eight 5 Watt fluorescent tubes. Half of these will feed off of the battery supply for PV1 while the other half will feed off of PV2 and its supply. The ballast/driving circuitry needed will be located in these bottles. These electronics and tubes are very similar to those found in battery operated fluorescent camping lanterns. Each tube will be enclosed in a laser array tube and they will be mounted around the vehicle and connected together in a daisy chain fashion.

Data Com to Surface - The MED group will be providing the mechanical, power, and cabling infrastructure to this sub-system one the RDC group determines the complete needs of the SAUVIM system. Currently in advanced conceptual design for both the deep-ocean as well as shallow water variants the following is a quick summary.

For the shallow water communication link it is planned that a connection coming out of PV3 will be dedicated to a tether line that will carry a dual twisted pair RJ-45 link as well as a serial line and two fuse-linked power feed lines. Strain relief via a kelams grip will be provided at both ends. Topside, a towed buoy fabricated from the shallow water foam will house a wireless Ethernet transceiver and

well as a wireless radio modem. The high data rate will allow for real time monitoring of the vehicle during testing and development. As the vehicle nears the proposed software functionality the link can be degraded to simulate the slow bandwidth connections that the deep-ocean vehicle will face.

Towards the end of Phase-I testing the equipment from the connection will be replaced with an acoustic modem unit. Also the addition of a recovery strobe light, transponder and passive pinger is under consideration and vendors are being contacted for their literature.

Health Monitoring Circuitry - Two sets of circuitry are being developed by a NASA Space Grantee for allowing the SAUVIM vehicle to monitor its systems state and perform self-diagnosis. Development and design of these systems are covered under the appropriate section of "Vehicle Health Monitoring".

Interface Circuitry- Basically this topic area is an overview of the distribution and transformation of electrical power ranging from the batteries and ending at individual components located throughout the vehicle. At present, the design and choice of components are nearing completion. This includes design of interfacing vehicle for charging batteries and auxiliary power provision.

Figures MED-4, -5, and -6, show the cable routing throughout the vehicle. The batteries, B1 B B6, comprise the battery banks composed of one 72V bank (B1, B2, B3), three 24V banks (B4, B5, B6), and two 144V banks (B7 through B12). Part numbers note individual cables in the vehicle. Multiple conductors comprising a cable assembly are enclosed within ellipses that are near the part number. Each pressure vessel has its own dedicated battery or bank supplying it. There are six switch boxes shown on the right of the drawing, there is one for each pressure vessel, each which can interface with an off-board battery charger by means of a dongle cable with an Impulse IL-4-FS underwater-mate-able connector. Each vessel has auxiliary circuits with relays to route power between the batteries, charger inputs, and vessel load via a selector switch on the switch box. Auxiliary circuitry refers discrete component electrical/electronic component circuitry fabricated in-house that may include custom built boards, relays, converters, etc. The various functions on these boards are detailed in other sections to follow.

Individual Pressure Vessel Electronics -There are six composite pressure vessels that house the main bulk of electronics located onboard the SAUVIM. The description and status for each pressure vessel follows:

Mission Sensor Package Vessel, Pressure Vessel # 1 Figure MED-39 shows the contents and wiring into and out of this bottle. This vessel is mainly a spare bottle. Currently its chief functions are to serve as a pass-through for the Mission Sensor Package, house the primary INS unit and house a video and data logging camcorder to serve as a vehicular black box/mission data recorder. This bottle uses a mount structure much like PV3 and PV4 use. Liaison between this group and the RDC and MED groups has been established to work out interfacing of the Mission Sensor Package to the rest of the vehicle.

Ansaldo Arm Controller Vessel, Pressure Vessel # 2 - Figure MED-40 shows that the main contents of this bottle will be the ELMO Motion Controls stepper motor controller/resolver boards and their back-plane housing. This controller has been purchased some time ago and has been in continual bench use interfaced to the Ansaldo robotic arm for testing and software development by the DTDS group. Packaging of this unit and support electronics will await success during initial vehicle navigation testing in Ke'ehi lagoon.

Navigation CPU Vessel, Pressure Vessel # 3 - Fabrication of this vessel has been a major focus of this group for the last several months. At present, electrical/mechanical packaging detailed design is nearing completion with several cad-based drawings that document wiring to the various components within the vessel including CPU, PC104s, DC/DC Converters, power relays, electronic boards, heat-sunk power transistors, stepper motor drivers, and Ethernet hub being included. As can be seen from Figures MED-41 and -24 this bottle is quite densely populated with systems. A conceptual layout of the contents is revealed in Figure MED-41.

Interior packaging of the vessel, as shown in Figure MED-24, shows the physical locations of the VME-CPU, Interface Boards (disks), and fans. The CPU actually resides in a three-sided aluminum shelf. Ribbon cables (not shown) from the CPU issue out from the open side of the shelf and are plugged into either of the two Interface Disks. The vessel lids are not detailed on the drawing but are located on both ends of the 18" dimension, the length of the vessel cavity itself. Shown also are the various components, including Auxiliary Circuits, that will be mounted around the three sides of the shelf. In addition to holes housing connectors, the Interface Disks will have sufficient holes drilled out to allow for air passage of the re-circulating air produced by the fans.

To facilitate packaging configuration for this densely packed vessel, a mock-up of its interior, consisting of scale models of all of its components were fashioned out of wood and Styrofoam. These allowed for testing, visualizing and analyzing different packing configurations.

Figure MED-42 is a wiring diagram showing interfacing of the CPU ribbon cables to connectors on the Interface Disks, wiring from connectors on the Interface Discs to the lid connectors, and other wiring to Auxiliary circuits, PC104s, and the Ethernet hub. Commonly referred to as the >spaghetti diagram=, it can be seen that the Interface Discs serve as patch panels between all the connectors affixed to them. On the left side is a vertical column of IDE-header connectors that are mounted on the Interface Disks (both fore and aft). These connectors are receptacles for ribbon cables originating from the CPU headers (not shown). To better understand the physical location of the remaining connectors located on the Interface Discs and end lids, each one is noted as to its location by a suffixed number as noted on the drawing.

Figure MED-43 show how the Auxiliary circuits are interfaced to the Interface Discs via connectors P36AA (aft) and P36FF (fore). Of the many components shown, some are self-explanatory, but those that need clarification will be discussed below.

Fabrication of the Auxiliary Circuits is in various stages of completion. There are three electronic boards, two of which are completed and checked out (Mode and Power Up boards) with the third completed with respect for detailed design. The interior shelf to house the CPU and mount auxiliary components upon has been constructed. Delivery of DC/DC Converters and power relays for subsequent mounting and wiring is underway. Other components have been already purchased and are ready to be installed.

Electrical isolation between battery and signal voltages has been a feature maintained in the overall design of the vehicle. This has been a feature that has been implemented based on interviewing designers of similar vehicles as well as practical experience gained from the ODIN-II vehicle. Any interfacing of signals between them is done using opto-isolator chips as will be explained below for various circuits. Isolation is an important consideration in eliminating unwanted electrical interference in the signal wiring from battery voltage sources, which are subject to noise when powering high frequency switching circuitry such as DC/DC converters seen in Figure MED-43.

Also voltage drifts on the main bus due to battery draw down or the switching of heavy loads will not affect the supply voltages of signal ground paths. These converters have built in isolation between input and output, as they are magnetically coupled inside, thereby providing isolation between the battery bus and supplied voltages.

The importance of health monitoring of the vehicle cannot be ignored. This covers monitoring of the battery voltage and current, vessel interior temperature, and leakage detection. To insure secure monitoring, two independent health-monitoring circuits are incorporated in the design. The first is a self-contained modular unit shown at the top of Figure MED-43. It communicates with the CPU using a two-wire RS-485 interface. The second resides as part of the Mode Board, described below and is interfaced to the CPU with digital I/O lines. (These are covered under the section 'Vehicle Health Monitoring'). Both circuits are somewhat similar in their circuit configuration and the description under the Mode Board give an idea of how they function.

To get an idea of how signals are fed from/to the Navigation VME computer, Figure MED-43 also gives a good idea of how the signals route out. On the left margin of this drawing are the various I/O pins of the two Matrix-I/O boards as well as those of the MVC-16 and Force CPU boards. The other three margins include the outgoing connections that route to the bulkhead connectors that are on each bottle. These include lines that jump to the Arm control CPU in PV4, the thrusters in PV5, units located in PV1, the Imagenex scanning sonar unit, and some of the instrumentation junction boxes. This diagram is mainly for construction checkout and line continuity debugging.

A representative example of some accessories that will be wired within the Navigation CPU bottle is the two IB-463 stepper motors within PV3. Figure MED-44 shows how the two units for the ballast and arm tray motions are feed power as well as logic controlled and how the interconnects run.

MODE BOARD B Figure MED-45 includes health monitoring and Switch Box decoding circuitry. The selection of a mode on the Switch Box (see Figure MED-38) sends a DC voltage level to the voltage comparators, Z2; depending on the voltage level sent over the Mode line, a set number of the comparators are triggered, switching on applicable output transistors, Q5, Q6 and Q7 which in turn actuate relays, K1 through K6, seen in Figure MED-45. This voltage level method was chosen due to the limited number of available underwater cables conductors that connect the Switch Boxes to their appropriate vessels.

The CPU Enable circuit is used in a power up sequencing initiated by the Little Bd. P5I, part of the VME chassis seen in Figure MED-43. Its output, labeled "Enable CPU", turns on DC/DC Converters that only power the CPU. Electrical isolation using Z4 is necessary to isolate the signal input voltage from the output, which is referenced to battery voltage in the Converters.

The battery current and voltage sense circuits both employ analog optical isolation chips (Z5 and Z8) for the same reason mentioned above. The current sense circuit monitors the voltage drop across the .01ohm current sense resistor located next to the relays of Figure MED-43. This shunt resistor monitors battery current being feed to the entire load of the vessel when the system is turned on. Its terminals are routed to the differential inputs of Z5 by the lines labeled "DC/DC Converter Ground' and "0V Bat., Switched". The circuit output is fed back to the CPU, whereupon it is scaled at 0.1V for each 1 Amp of battery current draw.

The battery voltage sense circuit works in the same manner except that its input is derived from a voltage divider, R38 & R40, across "B+ 24V" and "0V Bat., Switched (B-)". Its output is scaled to

0.5V fed to the Matrix A/D board for each 1.0V of battery voltage change with 0V out corresponding to B+ minimum volts for safe operation of the vessel.

The temperature sense circuit employs a thermistor, R45, for monitoring. The circuit provides a constant current source of 1 milliamp for the thermistor, resulting in a scaled output of 1 millivolt/ohm. Its output, labeled "Temperature Sense", is fed to an A/D input of the CPU.

The Leakage Sensor circuit uses a sandwich like device for leak detection (not shown). It basically is constructed of two copper plates with paper material squeezed in-between and placed at the bottom of the vessel. If the paper gets wet from leakage, there is conduction through the plates, which triggers the digital output of Z11 to a high state. If a high state occurs, it is fed to the CPU to initiate emergency procedures for releasing ballast so the vehicle can surface.

A photograph of the completed mode board is shown in Photograph MED-31.

POWER UP BOARD B In order to conserve battery power, the vehicle has been designed to turn on only those electrical components needed at any given time during a mission. The Power-Up board serves this function by accepting power on signals from the VME-CPU (and PC104's for some subsystems like the Imegenex and laser ranging array), and conditioning them so that they can turn on/off gates on power mosfet transistors for individual components. Referring to Figure MED-46, these transistors are located to the right of the Power Up board and are labeled as to the functions they switch. Also shown are the details of this board, which mostly consists of redundant circuitry used to switch on the mosfets. A digital chip, Z1, is used to message digital turn on signals coming from the AORD PC104.

The completed board is shown here in Photograph MED-32.

STEPPER/BALLAST BOARD B Design circuitry for this board has been done but not incorporated into one unified drawing at the time of this writing. It will include the circuitry and boxed components drawn at the bottom of Figure MED-43. These include the ascent and main ballast release circuits, soft tank blow and flood, and the arm and ballast tray stepper motor controllers. The RDC group has designed a micro controller-based stepper circuit to offload synching tasks off of the main VME computer.

For reasons described before, digital optical-isolator chips are used in both ballast release circuits. These outputs trigger ballast release solenoids, which have already been tested satisfactorily with these circuits. One of the requirements for the ballast release solenoids used is that they only be activated for a few seconds to prevent their coils from overheating. For this requirement, the circuits include 555 timer chips used in a mono-stable mode (Z13 and Z15), which limit the turn on time to these few seconds.

Ansaldo Arm CPU, Pressure Vessel # 4 - Resident within PV4 will be the Arm Control Computer, a second VME bus-based computer. This structure and physical layout of this bottle will be very similar to PV3. Figure MED-47 shows the conceptual layout and signal routing of the items loaded into this bottle. It should be noted that about half of the sensor inputs and command-control outputs are routed through this bottle and originate from the Arm Control Computer. Though this makes system programming and real time task scheduling somewhat more tricky, both the MED and RDC groups agree this provides a essential layer of fault tolerance in the SAUVIM design.

Detailed design of some of the interface wiring in this bottle has been initiated. A good representative sample is the stepper interface circuits for the three fins as shown in Figure MED-48. As with the Ansaldo Arm Controller/ELMO back plane, this CPU has been in use by the DTDS group on the bench interfaced to the controller and arm for testing. It remains to be packaged in its pressure vessel as part of the vehicle.

Thruster Controllers, Pressure Vessels # 5 & 6

Figures MED-49, -50, -51, and -52 all reveal the contents of the rear two bottles, PV5 and PV6. Besides that power switching, health monitoring circuitry the main contents will be the thruster controllers. This is due to the very high thermal loads that these units are capable of emitting. Figures MED-49 and MED-51 are conceptual overviews for PV5 and PV6, while the remaining two drawings show how the units are tied in electrically to the SAUVIM systems.

As can be seen from the above figures, each pressure vessel contains four thruster controllers giving a total of eight for powering the eight thrusters of the vehicle. The controllers are Advanced Motion Controls, two model B60A30 and six model B40A20 units. Close examination of Photograph MED-17 reveals that the larger two controllers needed custom heat sinks fabricated and retrofit on. This was due to the fact they were shipped with extruded fin heat sinks that were of no use for being mounted directly to the pressure vessel end-lids. These retrofit sinks, fabricated in-house, will allow direct conductive communication of heat through the lids. The interior construction of each vessel is almost identical with the exception that one of them (PV5) has two motor controllers designed for greater power output for driving the longitudinal thrusters.

Five of the six Technodyne 1020 units have arrived in and the remaining units as well as the larger 2010 units are on order.

Battery Charging - The SAUVIM has three different battery bank voltage levels that require charging. These are 24, 72, and 144volts for the VME computer bottles, arm controller bottle and thruster bottles, respectively. Chargers to be used for battery replenishment are off-board and not an integral part of the vehicle. A two-fold approach has been taken to provide these chargers, one via a set of commodity units and the other via an in-house fabrication. Charger specifications for the vehicle batteries are somewhat stringent, thus literature reviews for choices available on the market has been somewhat sparse. The second approach, that of building an in-house charger, can naturally be tailored to the specifications called out.

Outside vendor purchase of these charger types have been investigated and after narrowing down to what is applicable under the specifications, request for quotes are being sent out for custom-built battery chargers from vendors capable of meeting these specifications. Once these chargers are purchased, they will be most likely used out in the field since they will be specified as portable.

Figure MED-53 is a view of the in-house charger circuitry while Photograph MED-33 shows the unit during assembly.

Component Wiring - This includes wiring between shelf mounted components and electronic circuit boards, wiring from interior components to the two interface boards, and wiring from the interface boards to the lid connectors. The CPU is interfaced to the disk shaped Interface Boards via ribbon cables. The above entails mechanical as well as electrical fabrication considering such items as the mounting of components, heat-sink fabrication, the mounting of cooling fans, and subsequent

mounting of the entire assembly inside the vessel. Upon completion of each phase of wiring, test and debug procedures will be done to insure correct wiring connections. Circuit drawings will be modified and updated during fabrication when necessary.

Future Tasks (Phase II Tasks)

- Send out detailed design of fin canisters to contractor for bid.
- Finish fabrication of bottle PV1-PV4 electronics racks.
- Mount side foam onto vehicle.
- Mount vertical and later thrusters onto vehicle.
- Commence fabrication of wiring interconnects for PV3 electronics. Mount electronics to bottle structure.
- Field test battery in-house battery system charger.
- Secure ballast to frame locations.
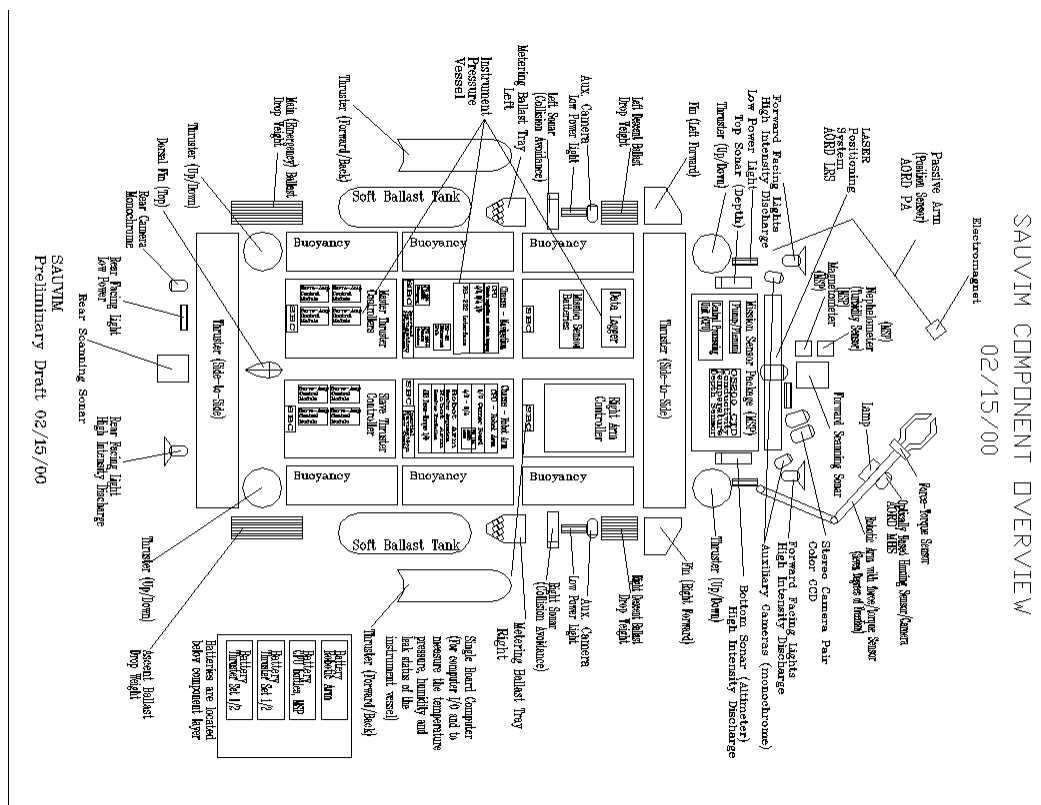
Figure MED-1: SAUVIM Components.
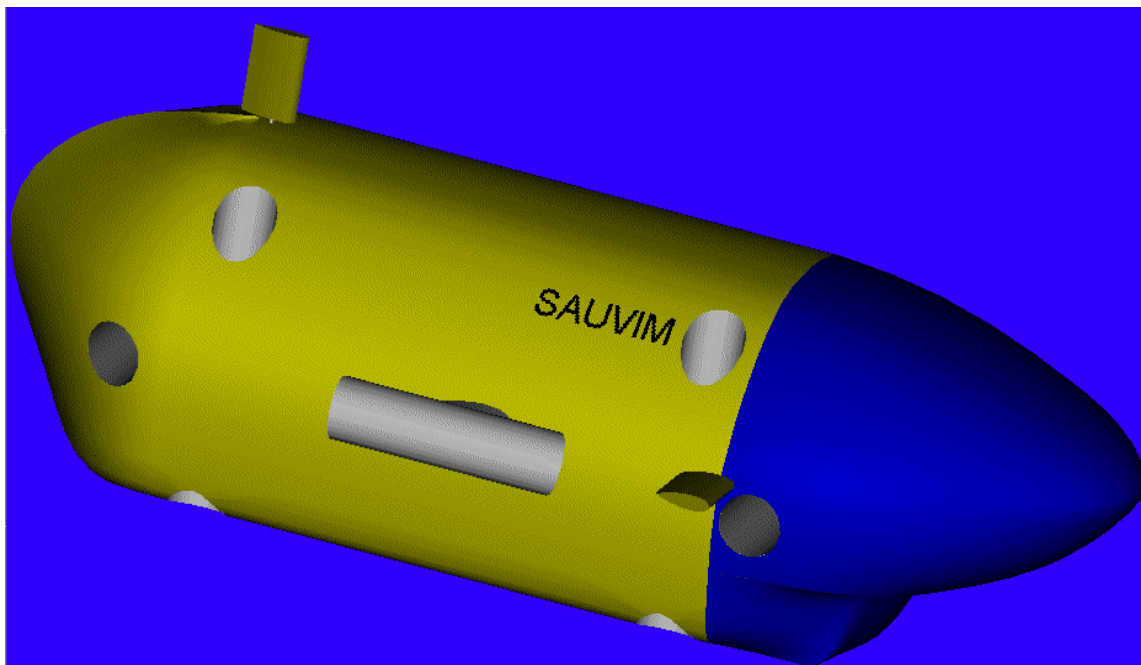
Figure MED-2: Concept View of Faired AUV.

Photograph MED-1: Scale Model (1:12) Tank Plug of Faired SAUVIM.
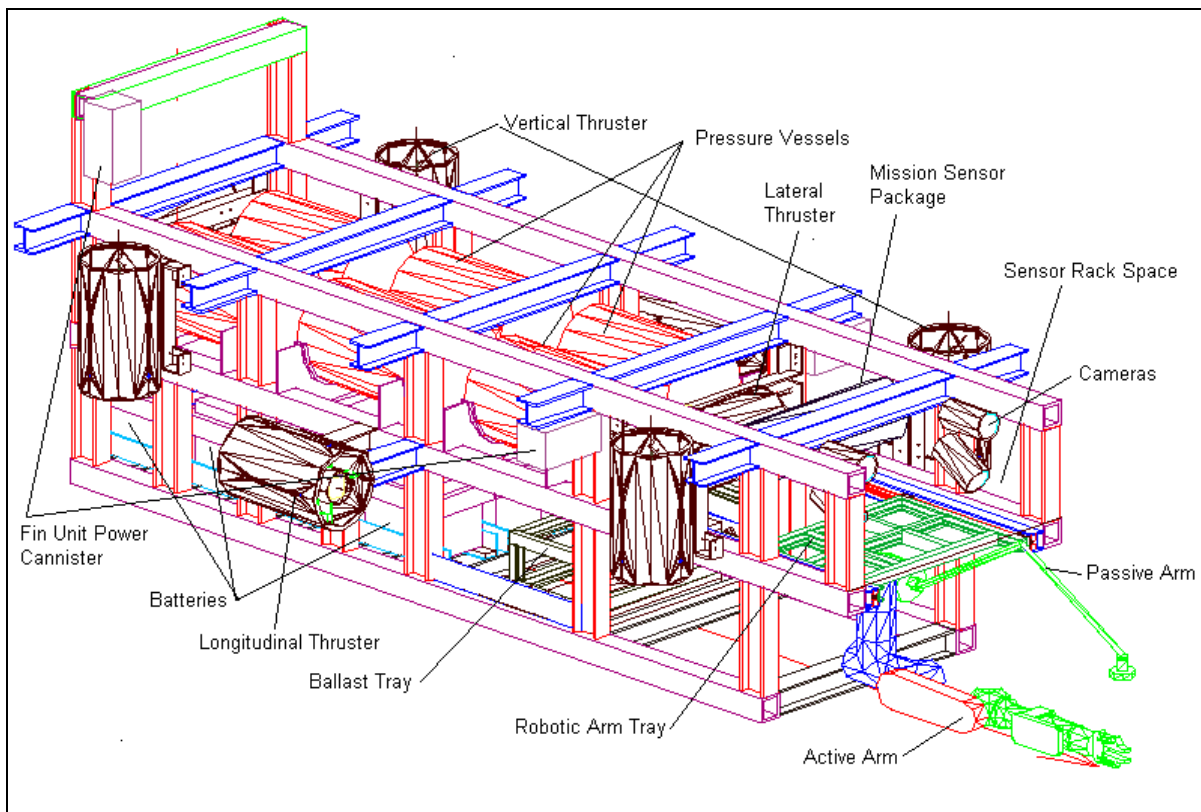
Figure MED-3: Major Components on SAUVIM Vehicle.

Photograph MED-2: SAUVIM Vehicle with Components Mounted.

Figure MED-4: SAUVIM System Level Wiring/Electrical Layout.
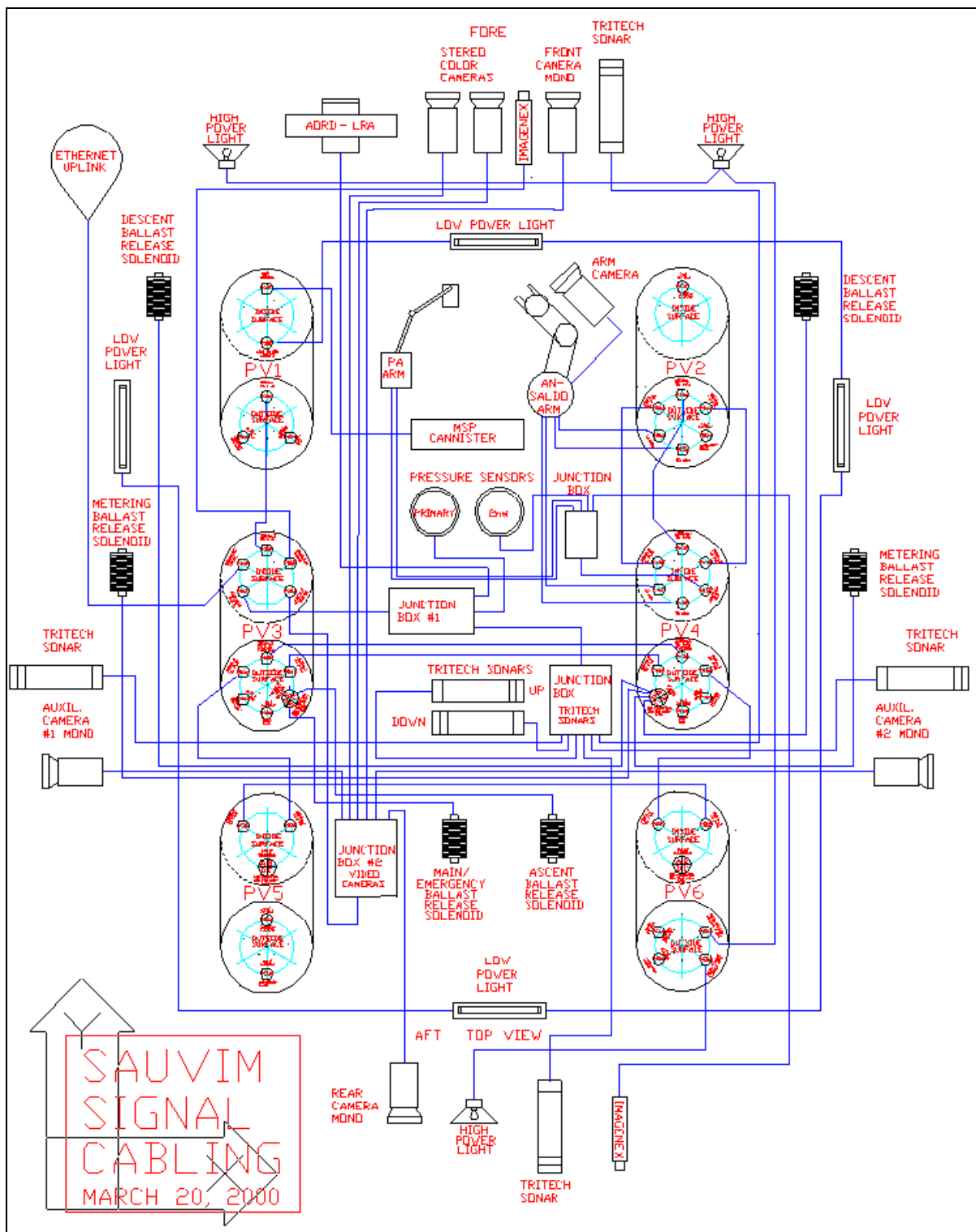
Figure MED-5: Pressure-Tolerant Underwater Wiring - Signals/Communications.
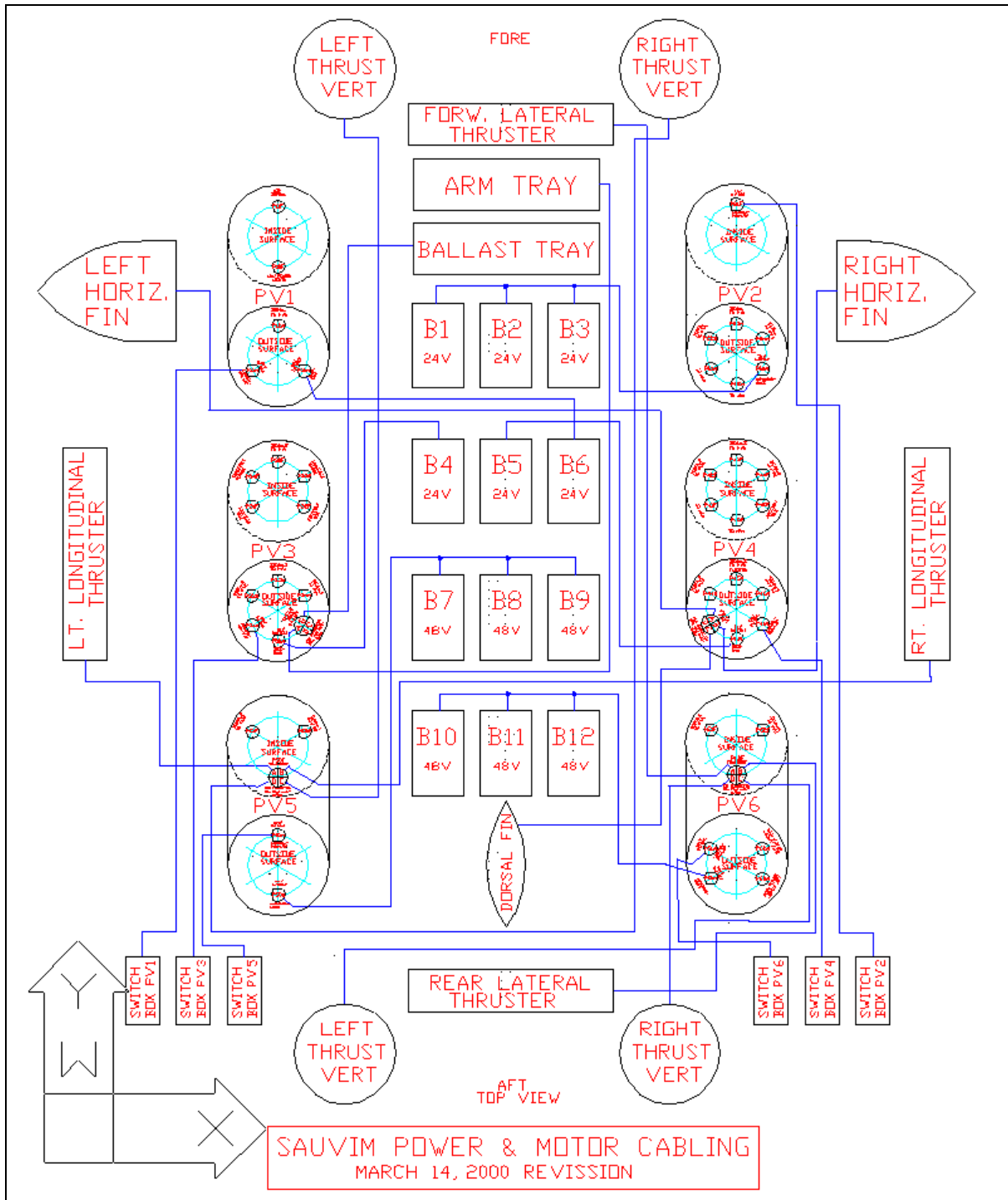
Figure MED-6: Pressure-Tolerant Underwater Wiring - Power/Actuation.
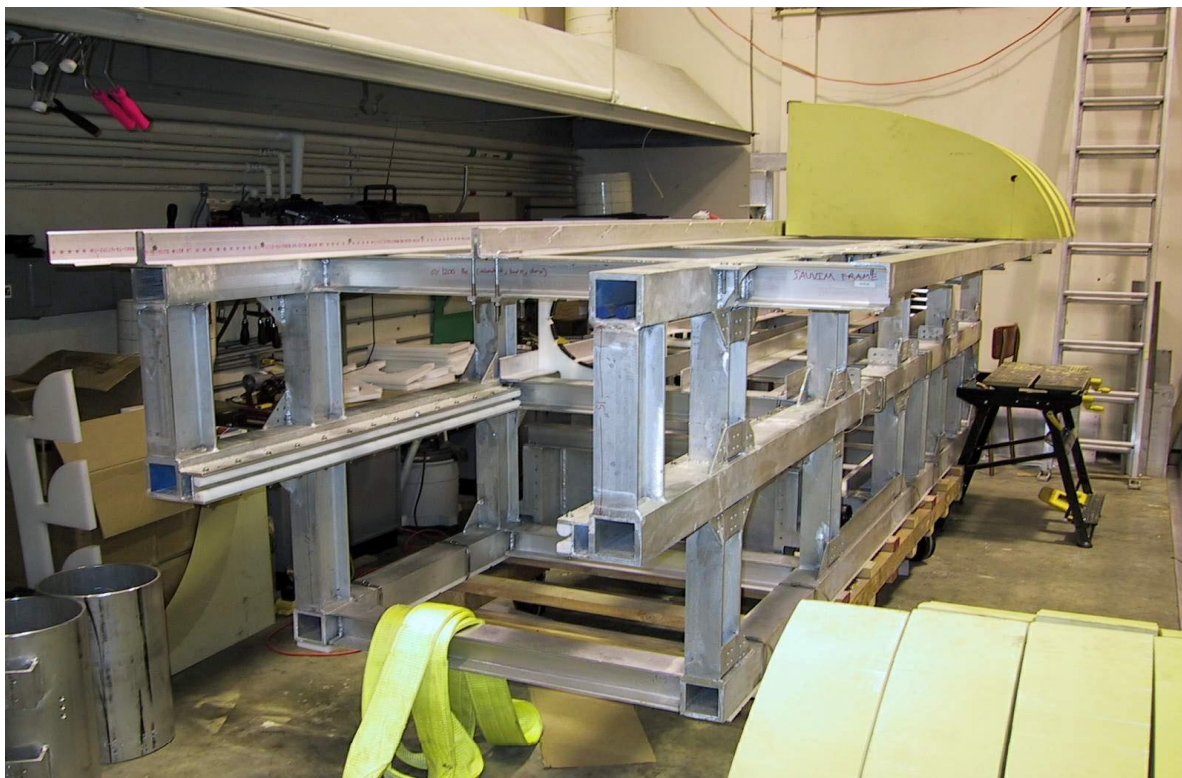
Photograph MED-3: SAUVIM Vehicle Structural Frame.
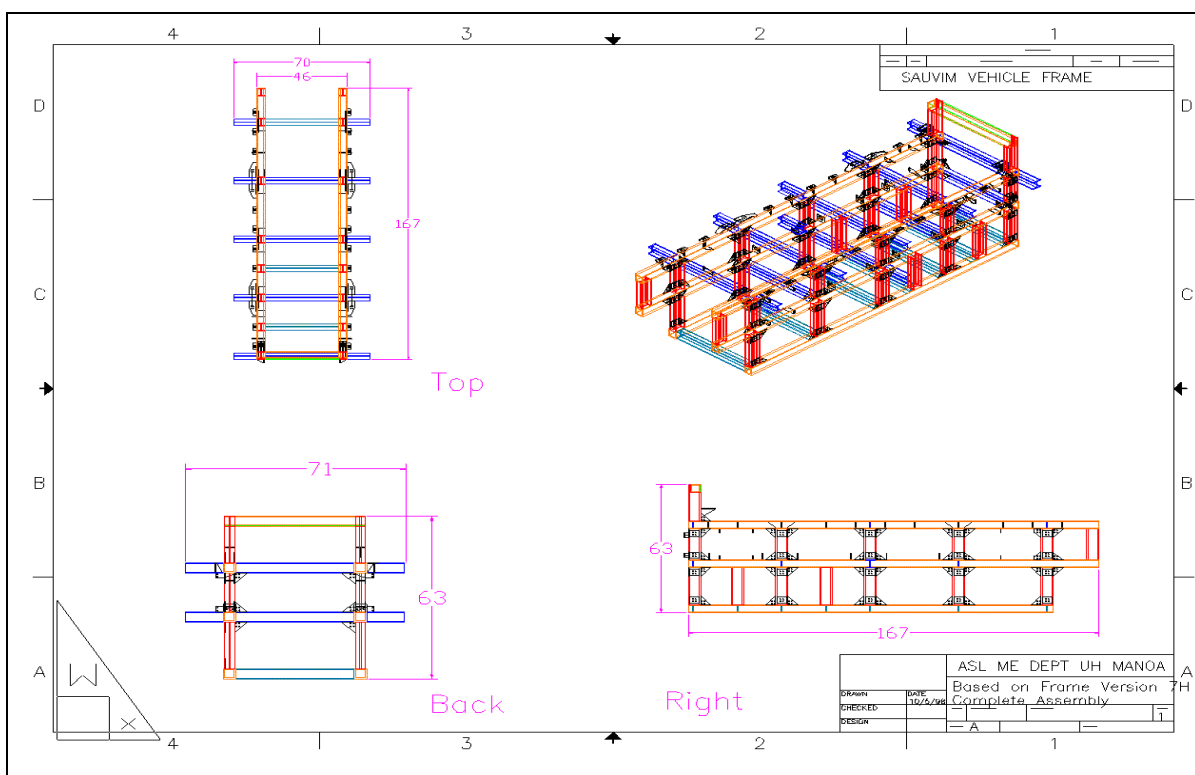
Figure MED-7: Three-View and Isometric Drawing of the SAUVIM Frame.

Photograph MED-4: Dorsal Foam.
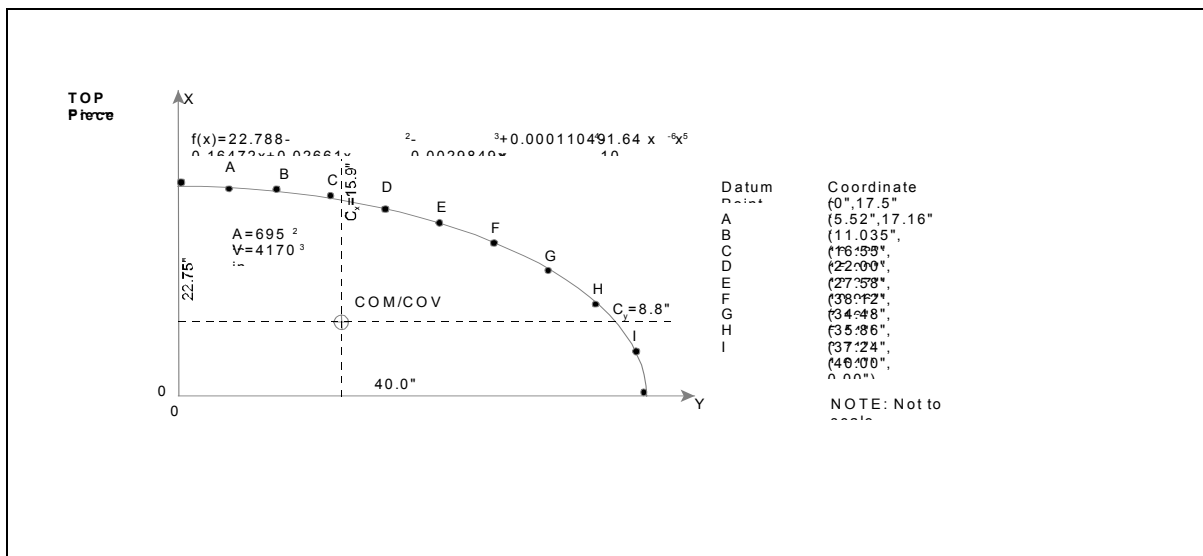
Figure MED-8: Top Foam, Geometry of Standard Block.
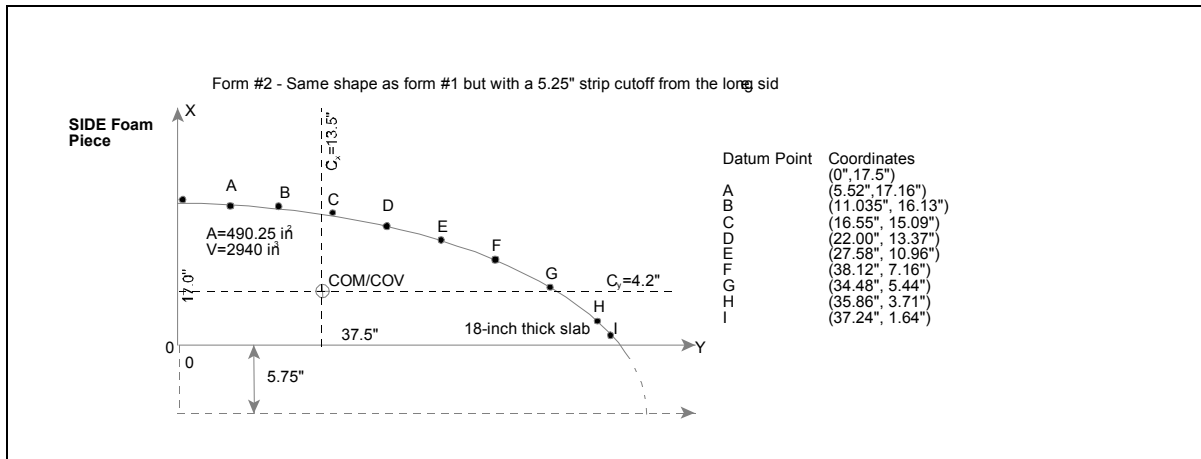
Figure MED-9: Side Foam, Geometry of Standard Block.
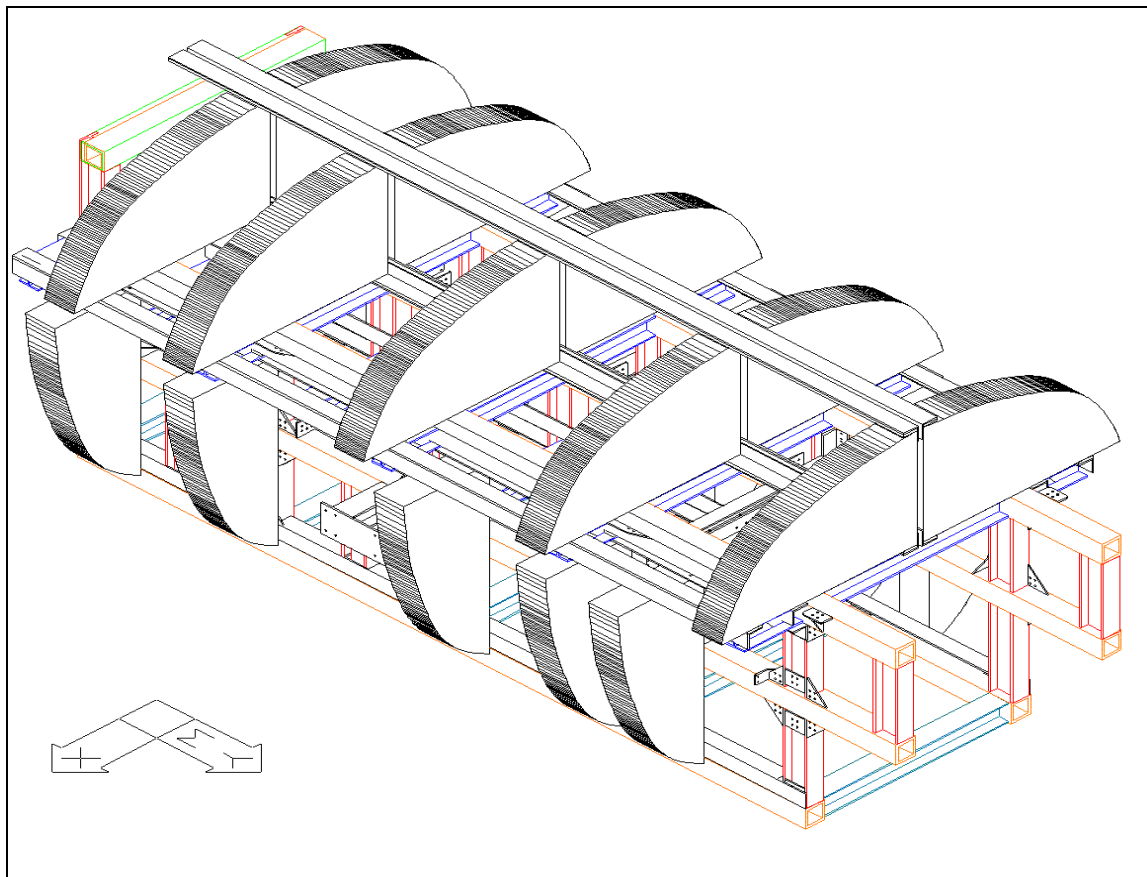
Figure MED-10: Shallow-Water Dorsal and Side Foam Installed on Frame.

195
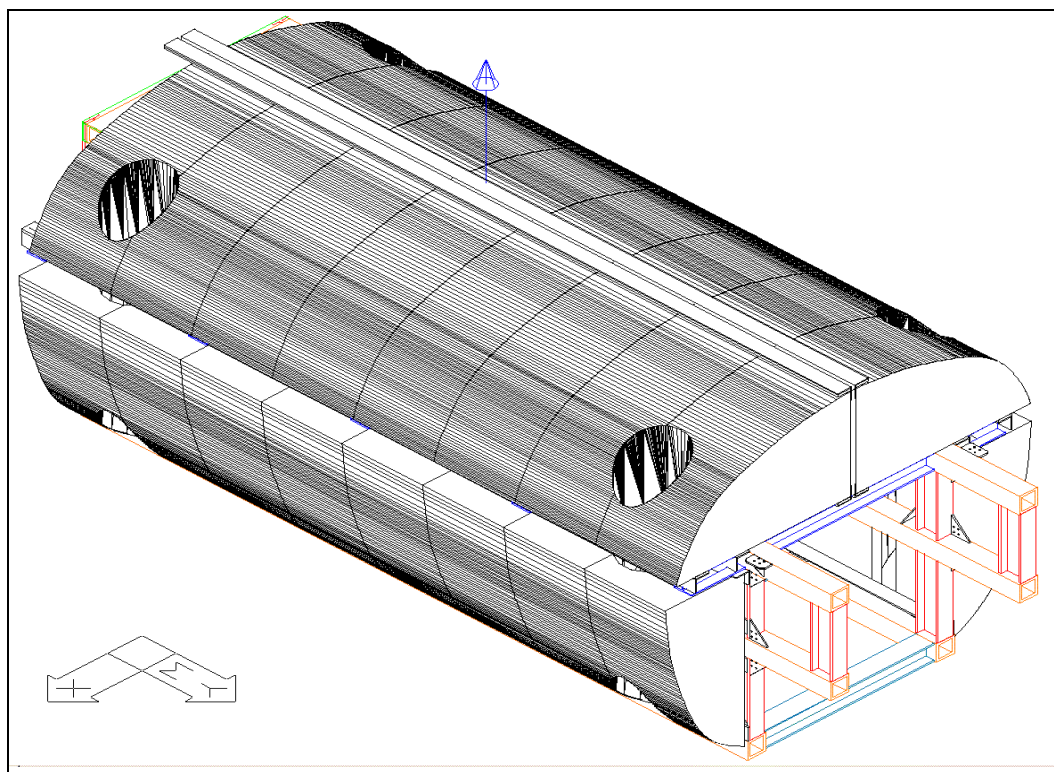
Figure MED-11: Deep-Water Syntactic Foam Installed on Frame.
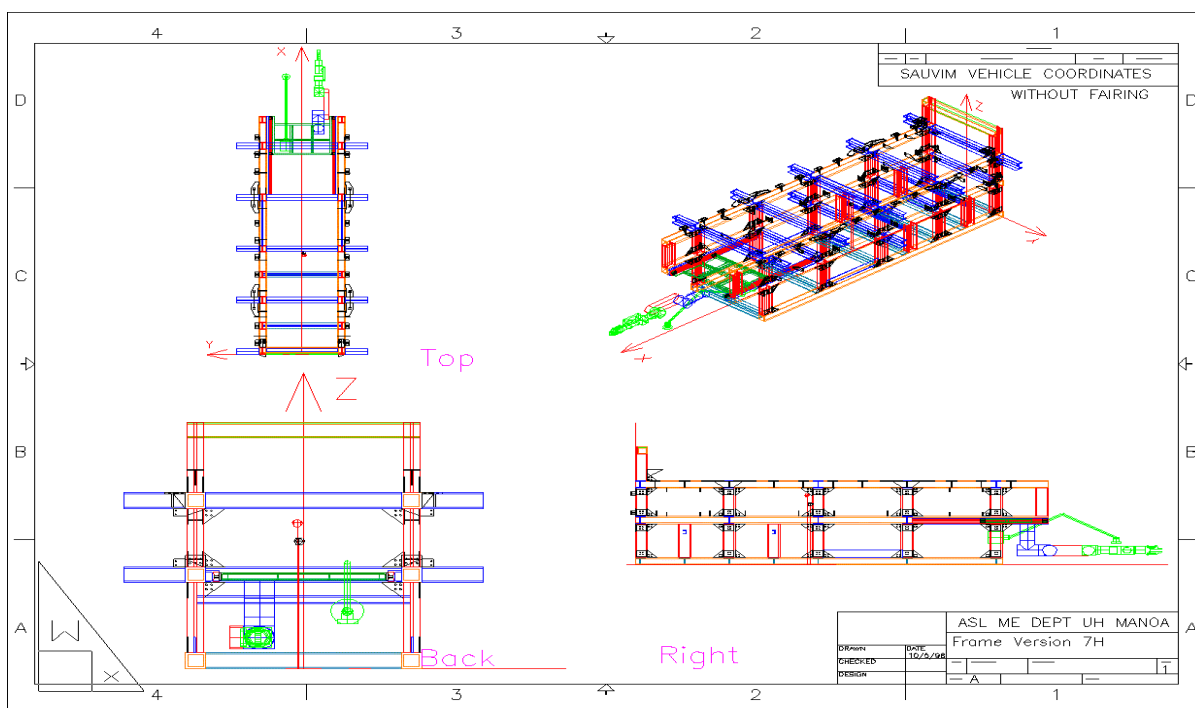
Figure MED-12: Location of Center-of-Mass Wet (Black) and Center-of-Volume (Red) on Frame.
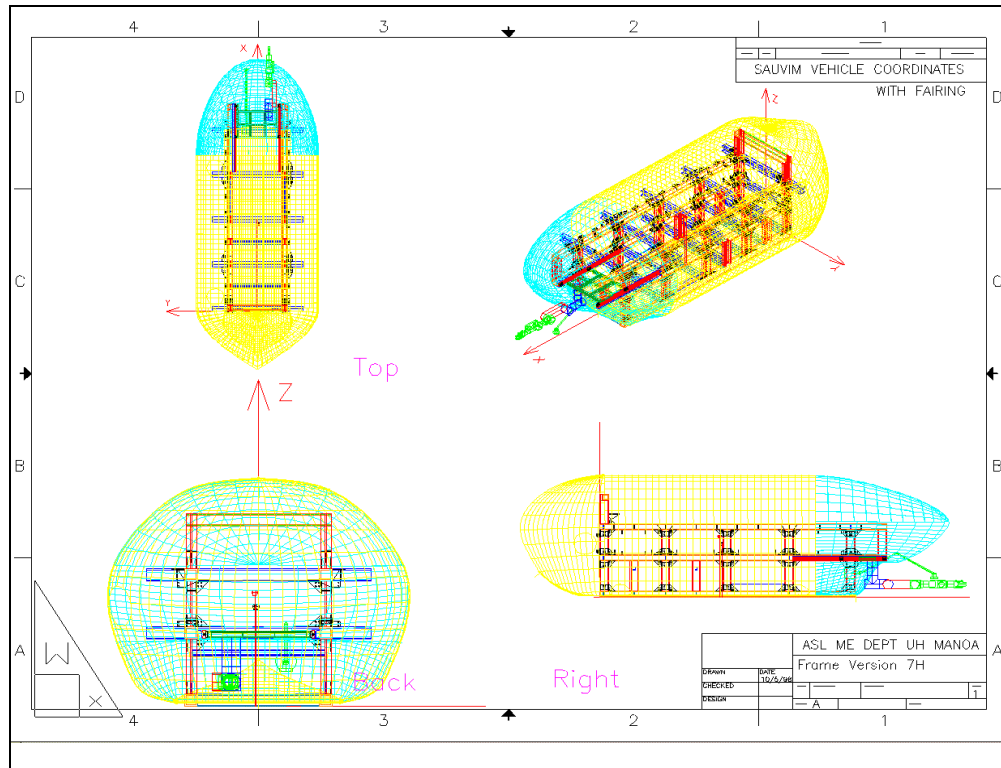
Figure MED-13: Location of Center-of-Mass Wet (Black) and Center-of-Volume (Red) on Faired AUV.
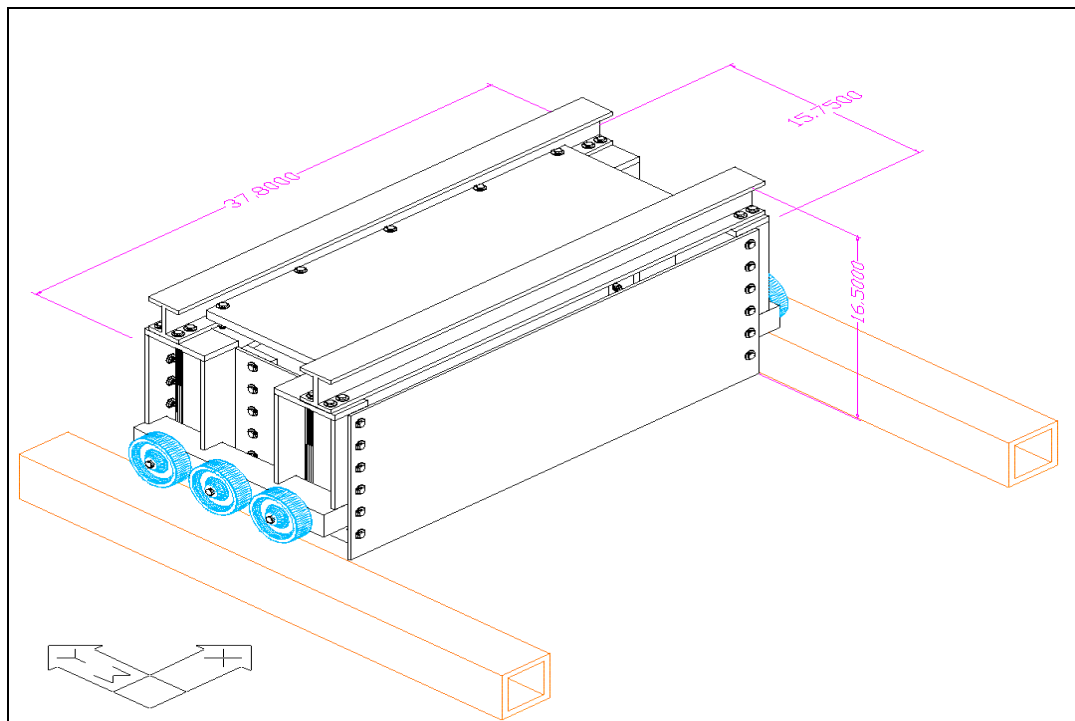
Figure MED-14: Main Ballast Tray Schematic View.
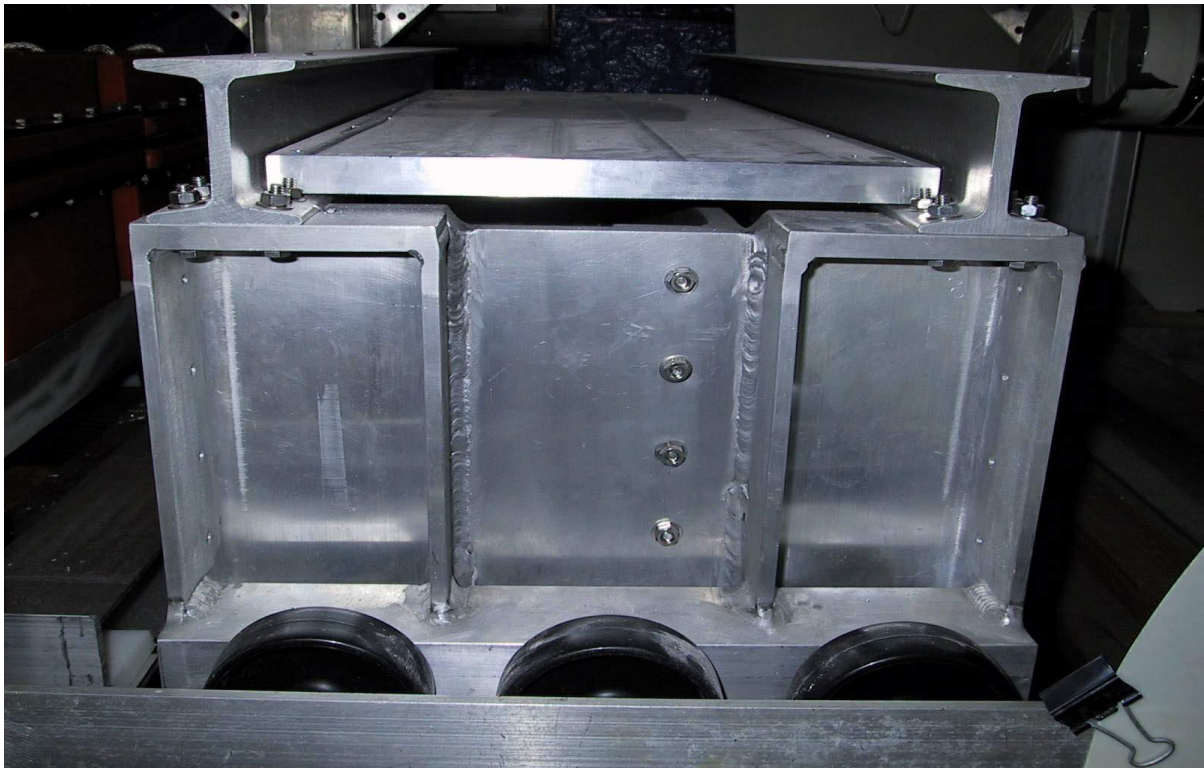
Photograph MED-5: Main Ballast Carriage Viewed from Side.
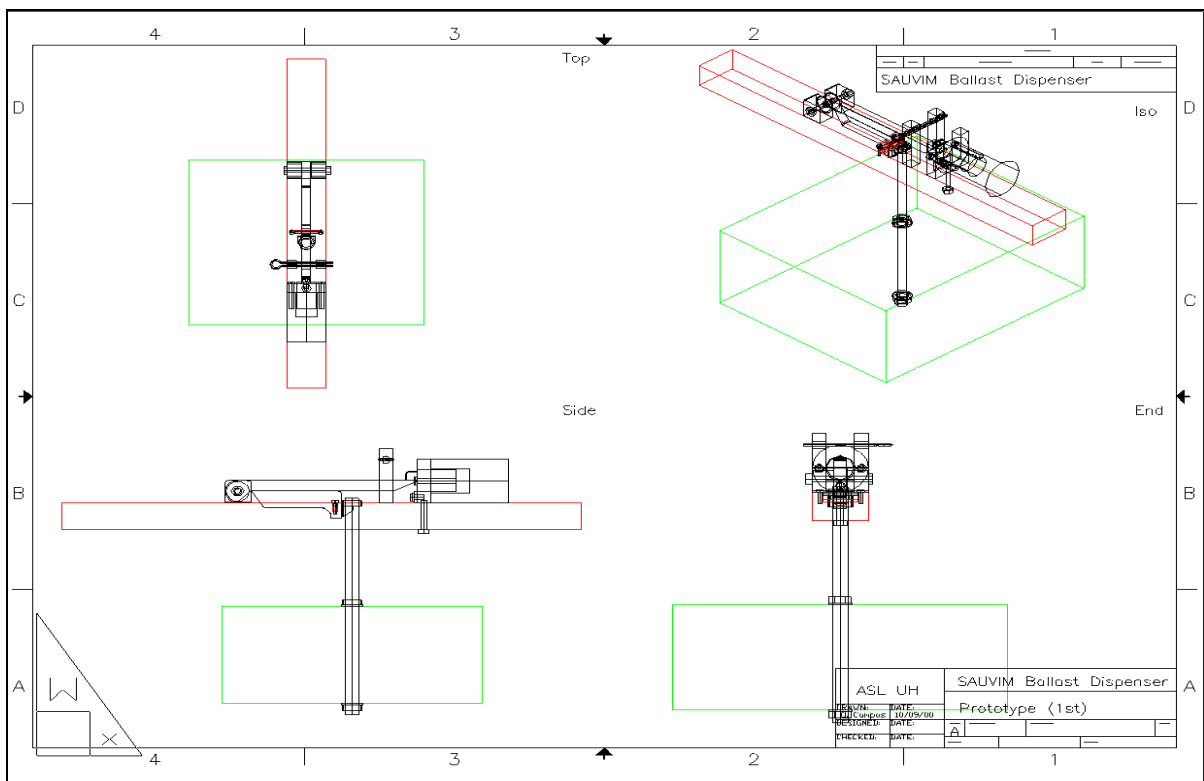
Figure MED-15: Ballast Release Cam Schematic.
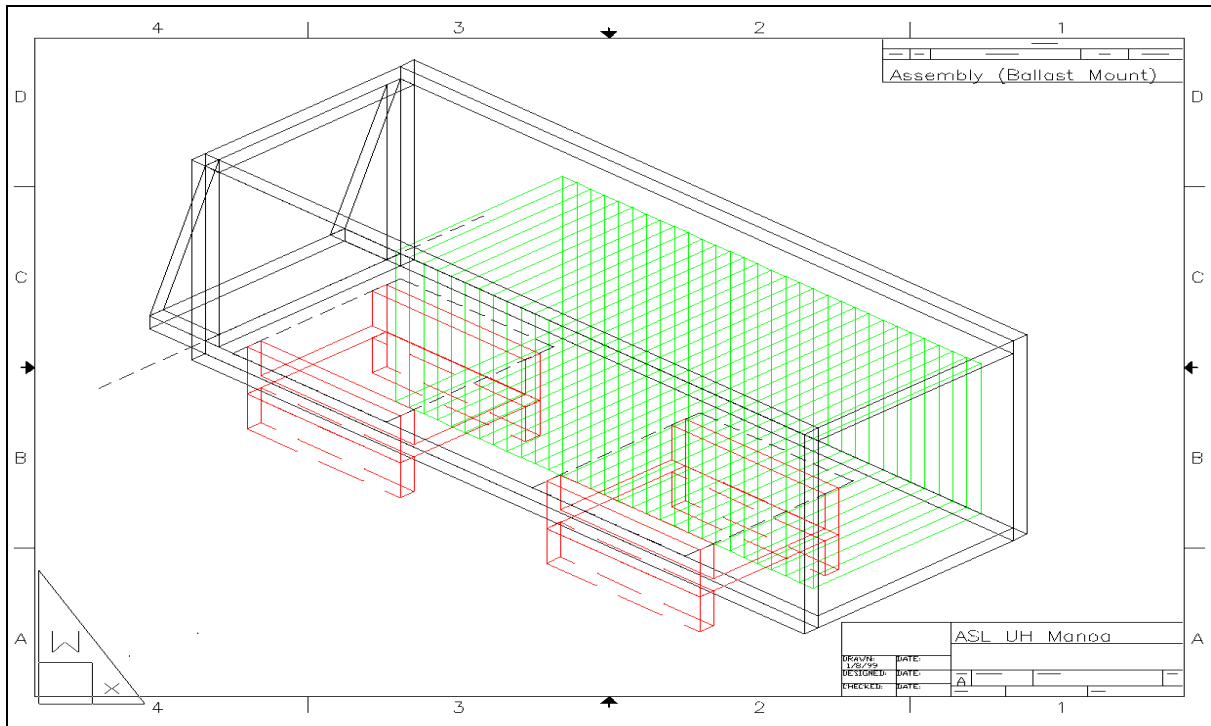
Figure MED-16: Descent Ballast Mount Assembly.

Main Ballast
Tray (Ascent
and Main
Ballast Masses)

Descent Ballast Mounts
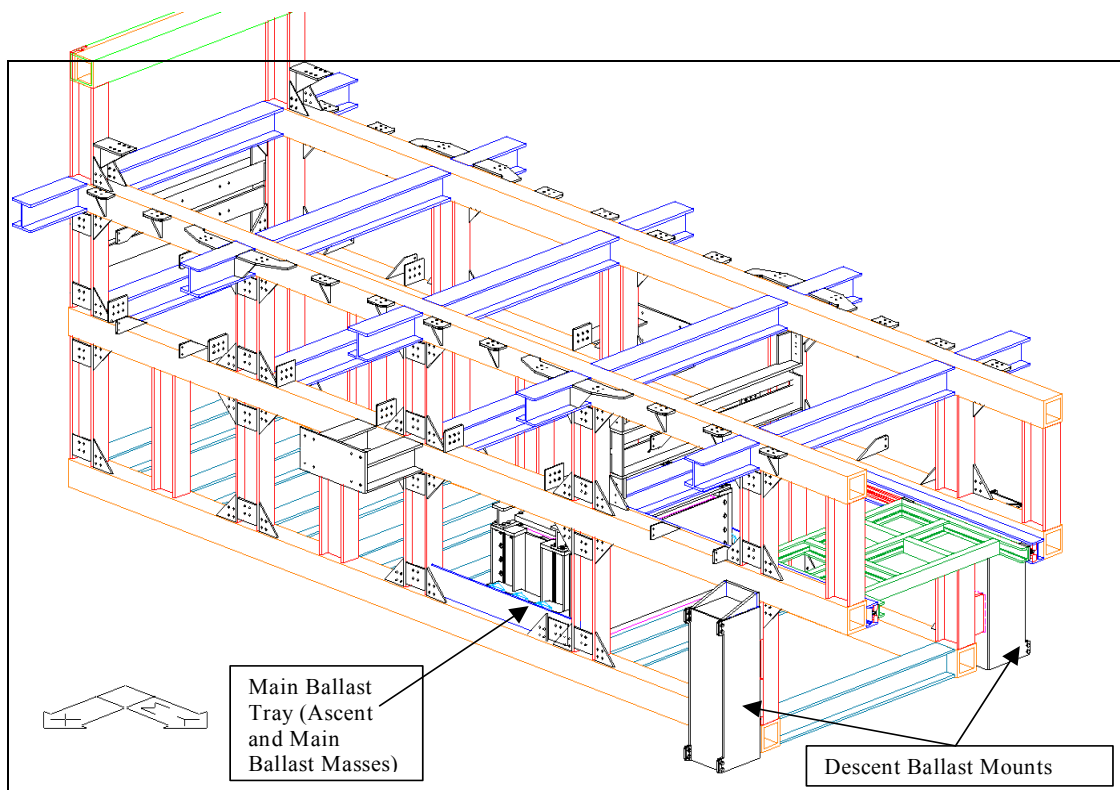
Figure MED-17 Ballast Mass Locations on SAUVIM.

Photograph MED-6: A Soft Ballast Tank Mold.
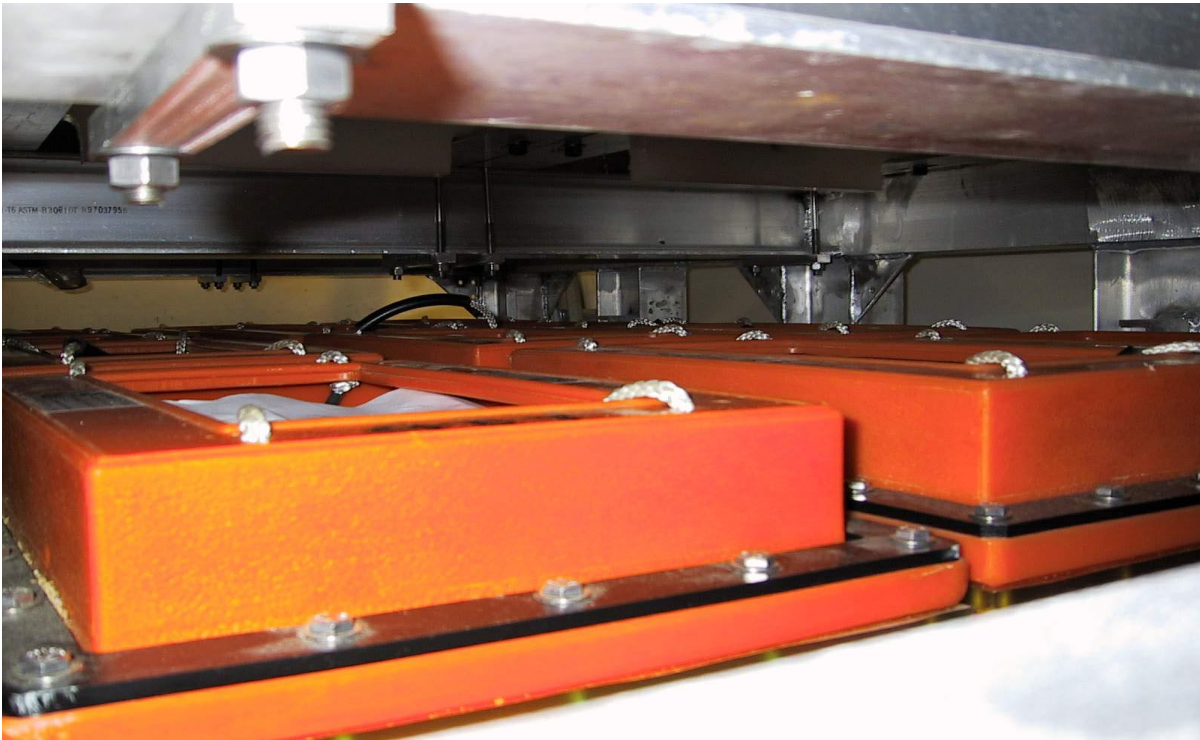
Photograph MED-7: Battery Banks in Place on Lower Tray of Frame.

Photograph MED-8: Battery Trays in Lower Portion of SAUVIM Vehicle.

Photograph MED-9: Battery Tray on the Loading Rails.
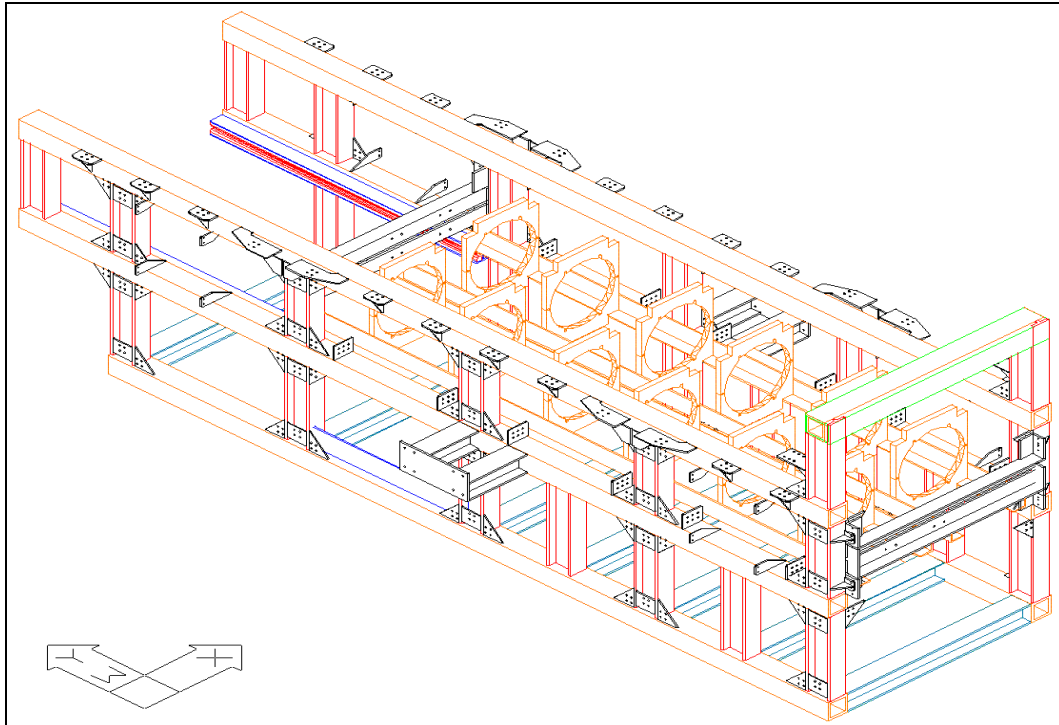
Figure MED- 18: Pressure Vessel Saddles on Frame.

Figure MED-10: Lower Half of Pressure Vessel Mount Saddles in Place on Frame.
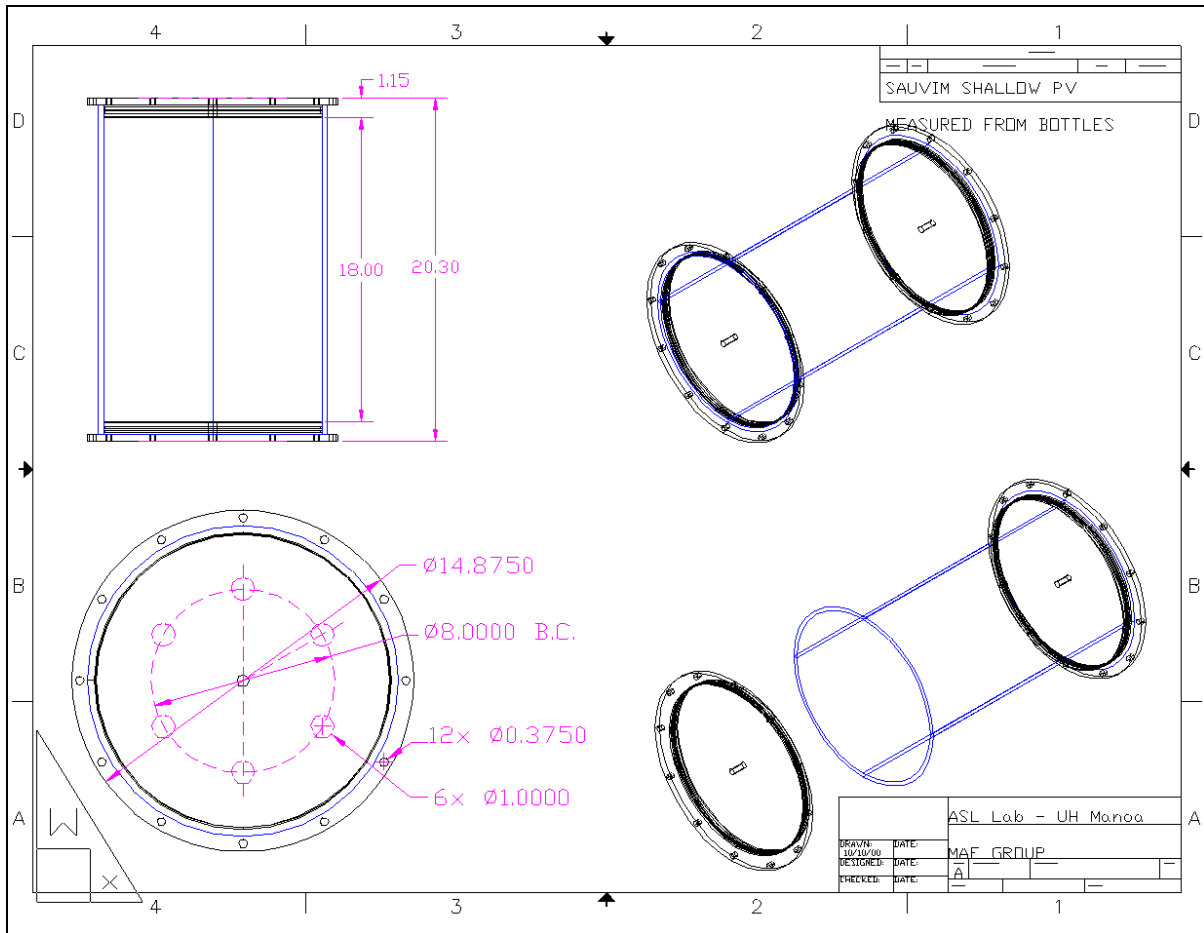
Figure MED-19: Shallow Water Vessels Diagram of Size.

Photograph MED-11: Shallow Water Pressure Vessel Set with Lids, Seal Sets and Purge Bolts.

Photograph MED-12: Shallow Water Pressure Vessels Mounted onto SAUVIM Vehicle.
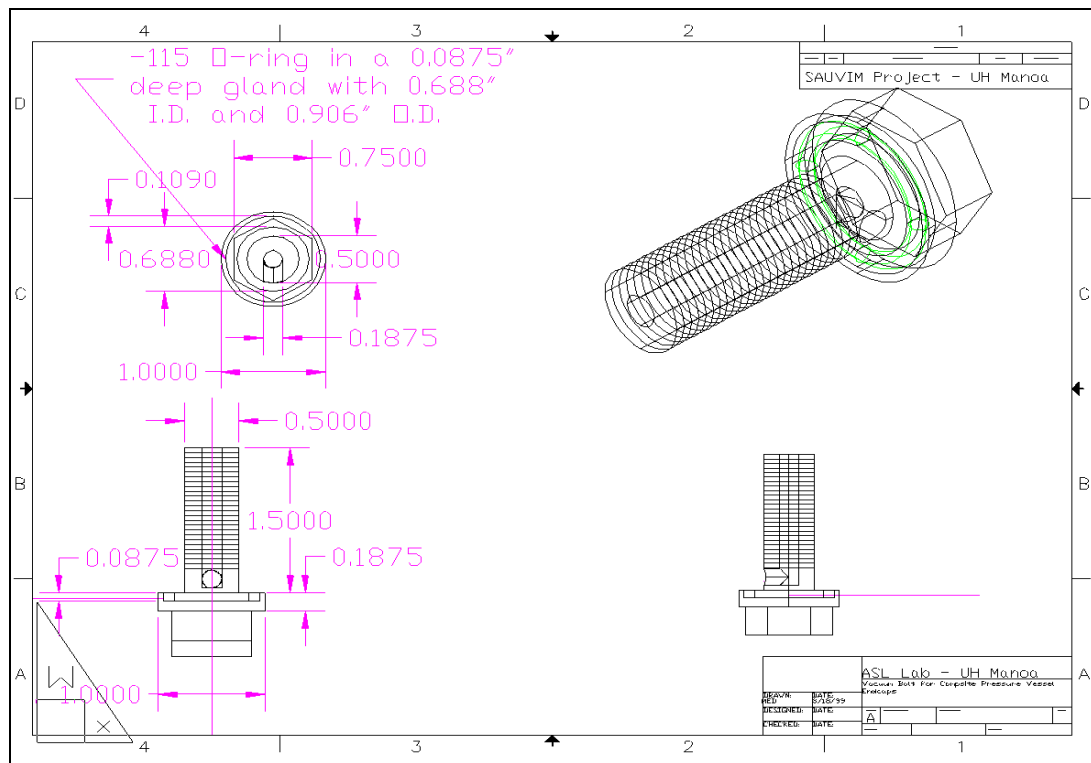
Figure MED-20: Three-view and Isometric of SAUVIM Vacuum/Purge Bolt.

Photograph MED-13: Vacuum Bolt and Chuck in Use for Sealing Shallow Water Pressure Vessel.

Photograph MED-14: Close-up of Vacuum Bolt and Chucks for SAUVIM Pressure Vessels.
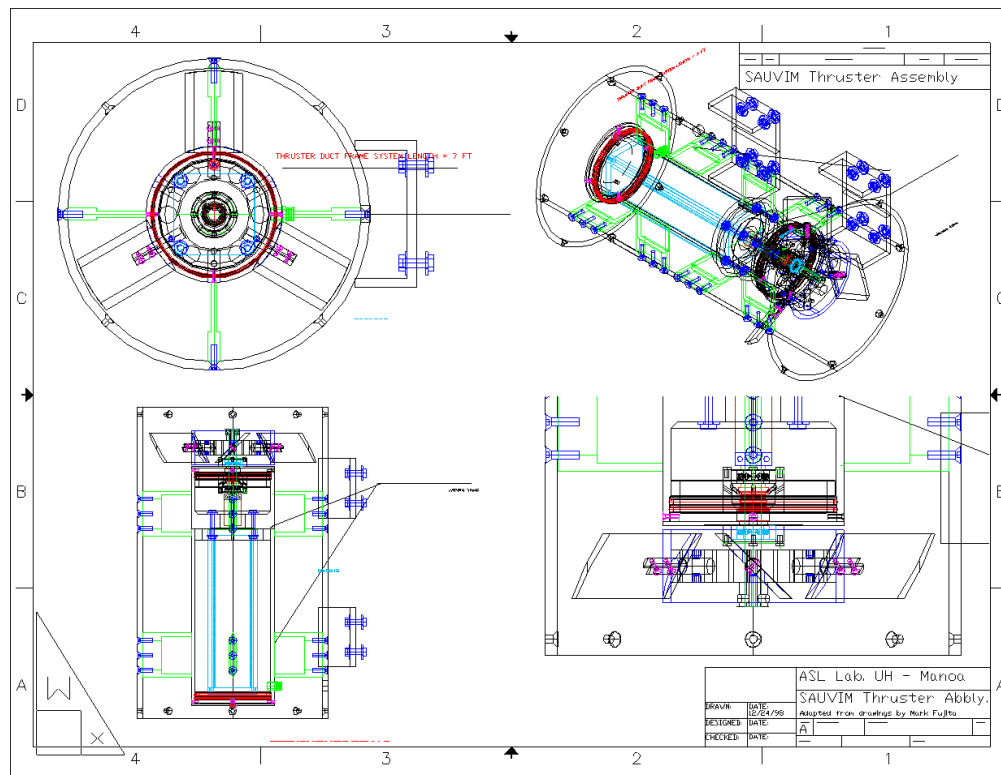
Figure MED-21: In-House Symmetric Thruster Designed for SAUVIM AUV.
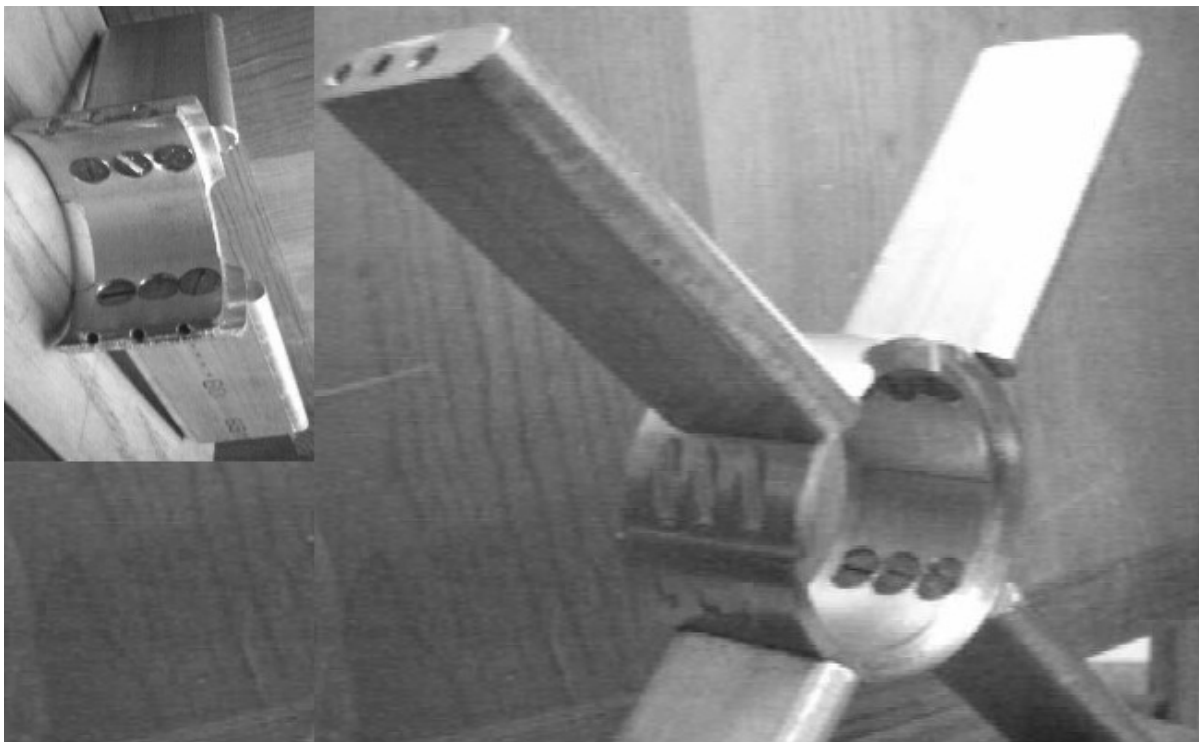
Photograph MED-15: Thruster Struts for SAUVIM Vehicle.

Photograph MED-16: View of Longitudinal Thruster Tube.
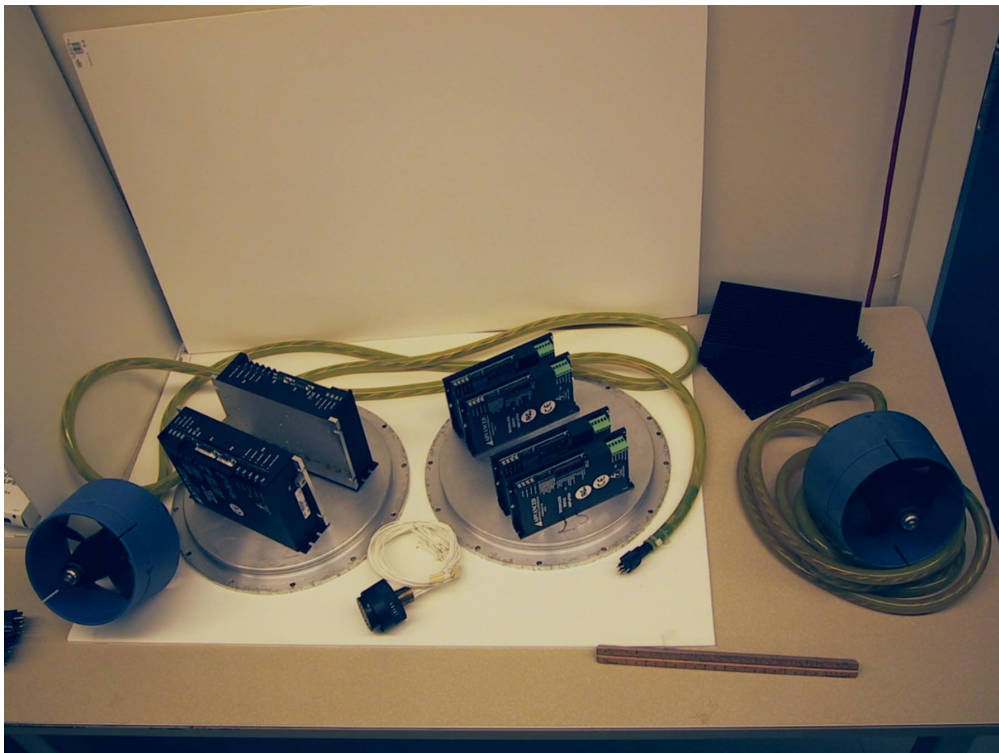
Photograph MED-17: Technodyne 1020 Thrusters with AMC B40A20 /B60A30 Controllers.
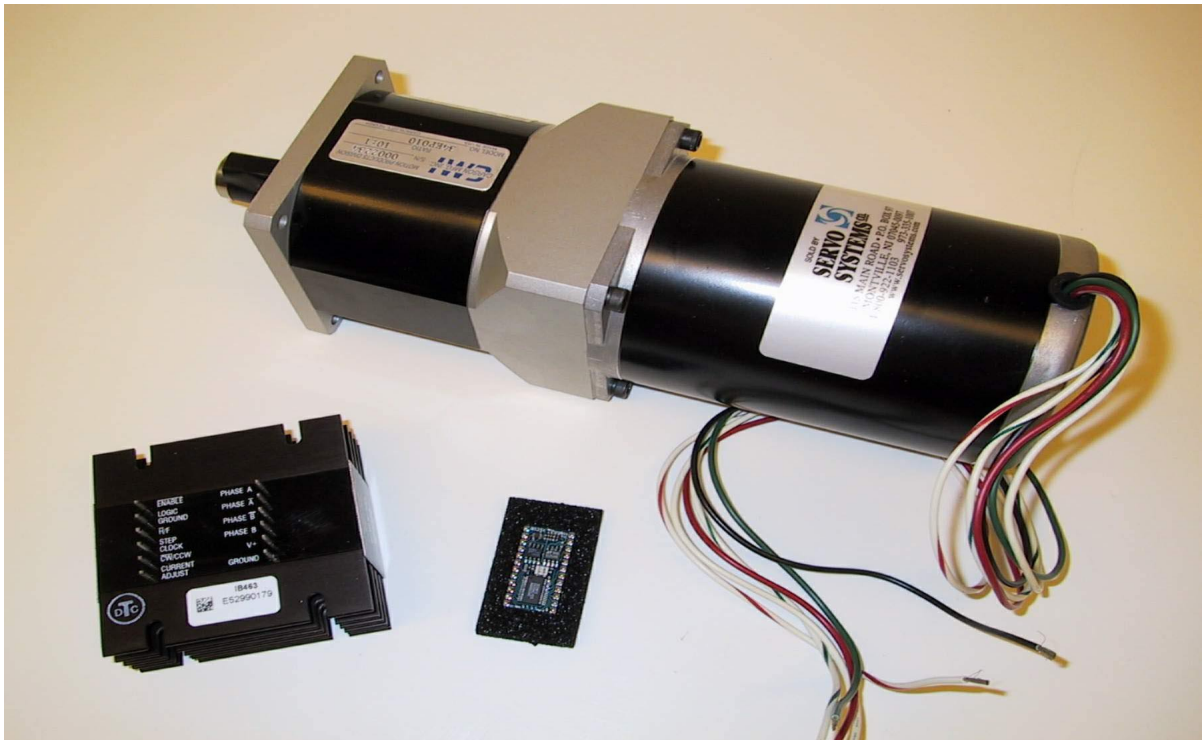
Photograph MED-18: IB-463 Stepper Controller, Motor, Gear-head and Micro controller Chip.
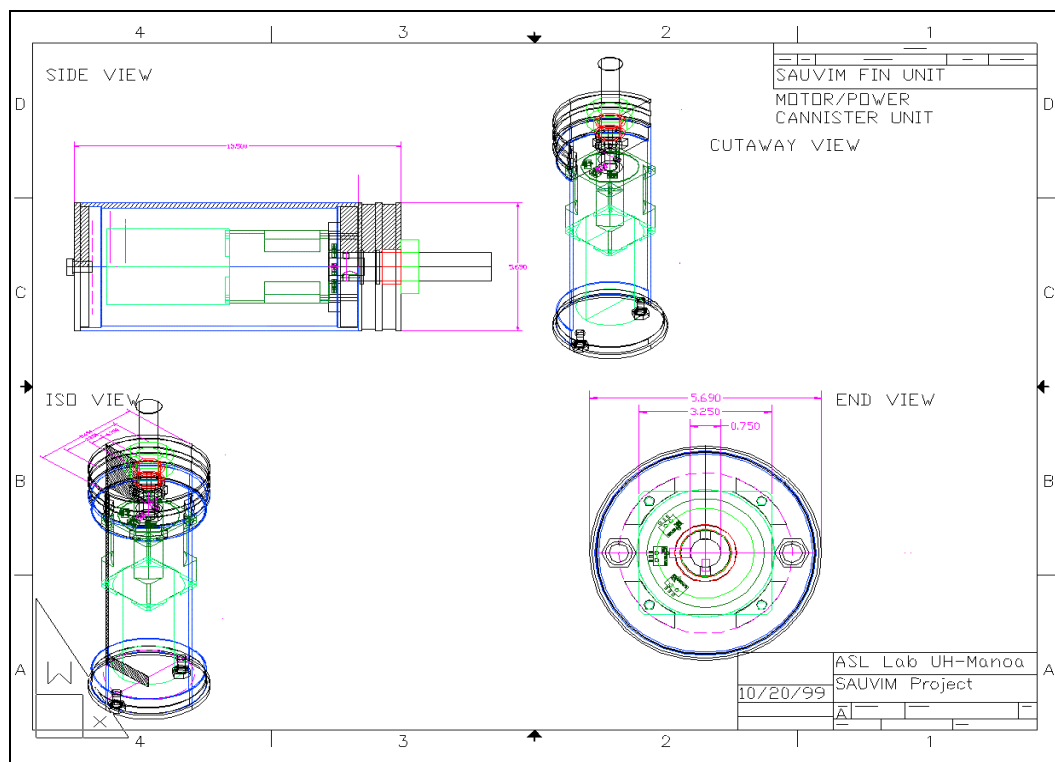
Figure MED-22: Fin, Ballast Tray and Arm Tray Power Canister.
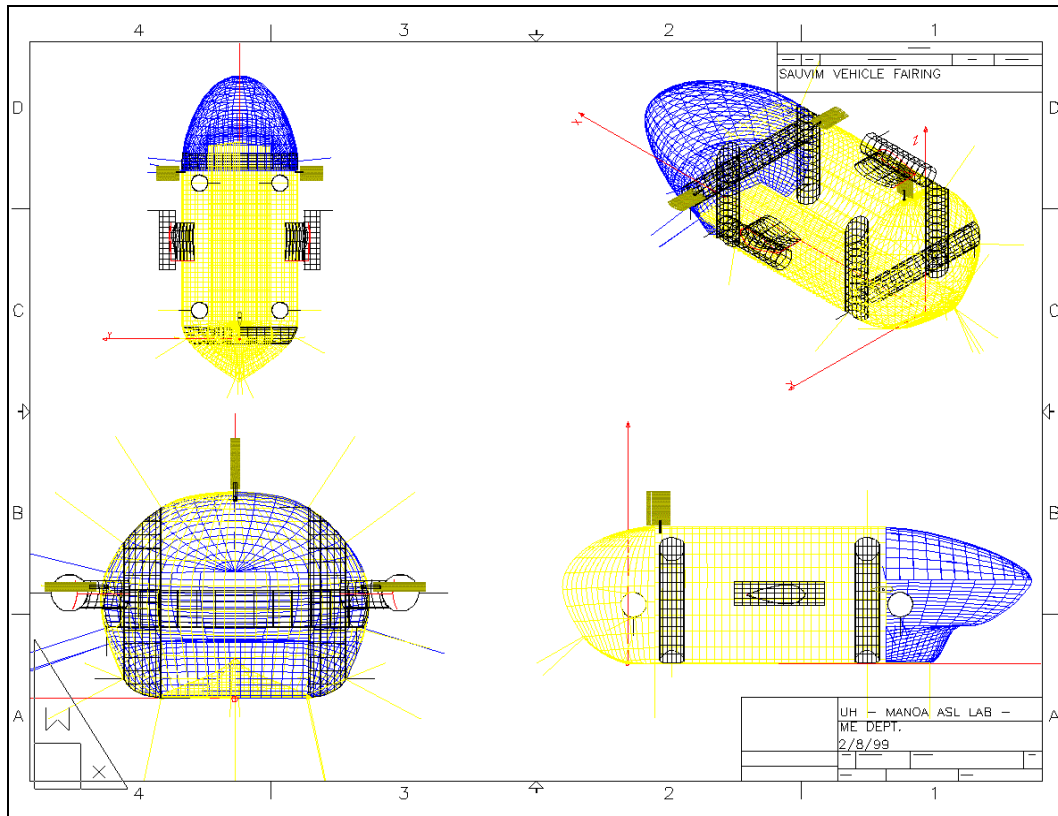
Figure MED-23: Placement of Fins Onto AUV Vehicle.
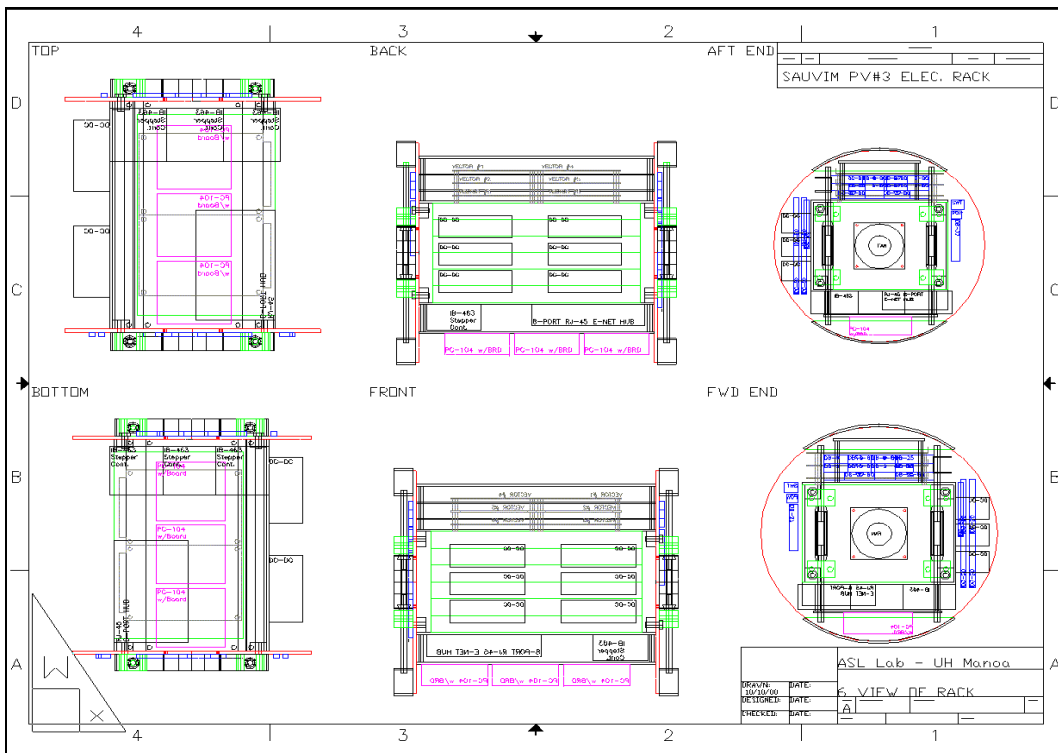
Figure MED-24: Pressure Vessel Electronics Rack Mount Structure. Shown is the one for the NavCPU.

Photograph MED-19: Pressure Vessel Electronics Rack Space Mockup.
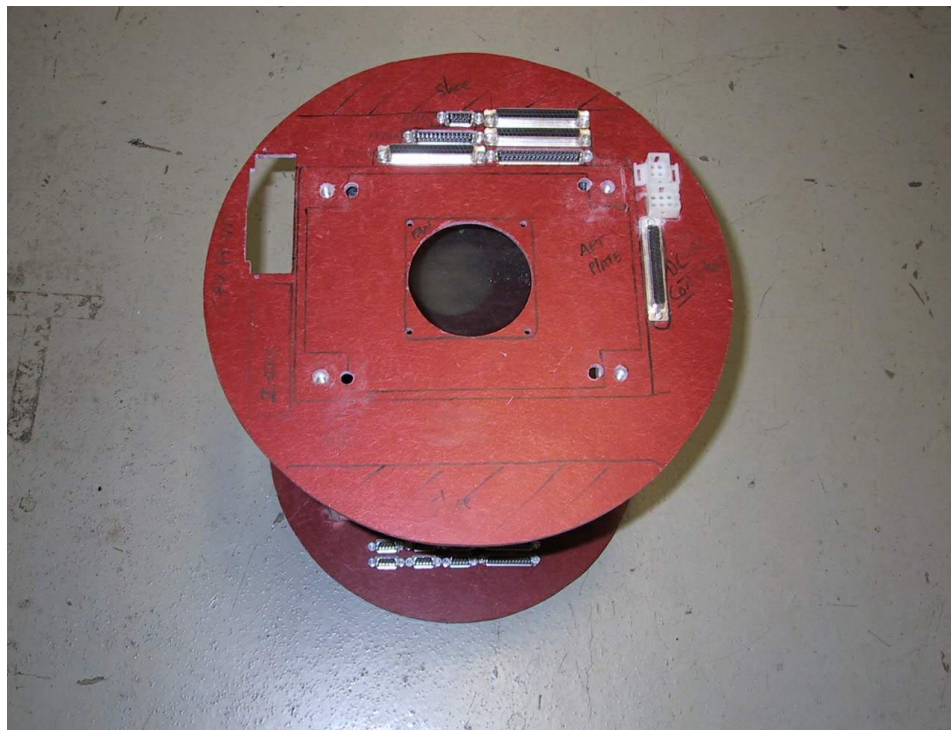
Photograph MED-20: End View of Bottle Structures in Construction.
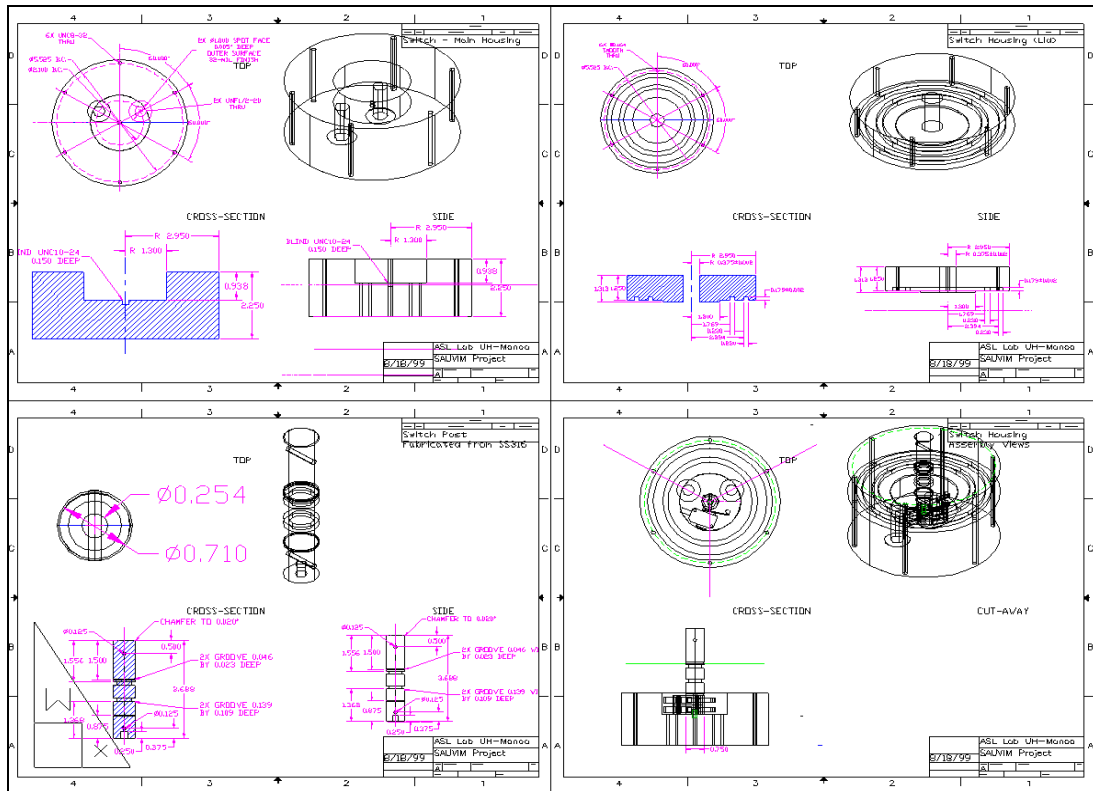
Figure MED-25: Switchboxes CAD

Photograph MED-21: Pressure Vessel Switch-Box, Underwater Cables and Contents.
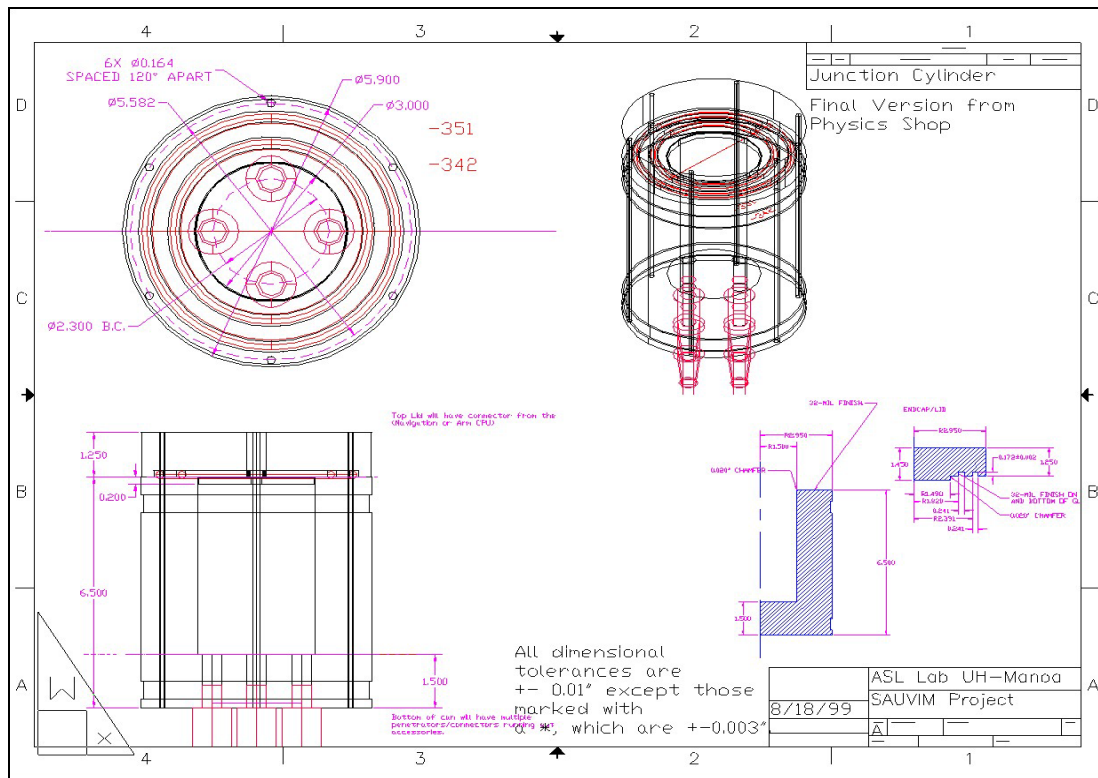
Figure MED-26: Junction Box Three-view and Isometric.

Photograph MED-22: Junction Boxes Installed onto SAUVIM Frame.

Figure MED-27: Camera Housing Three-view and Isometric.

Photograph MED-23: Camera Housings, with Contents, Glass Front, and Connector Hardware.
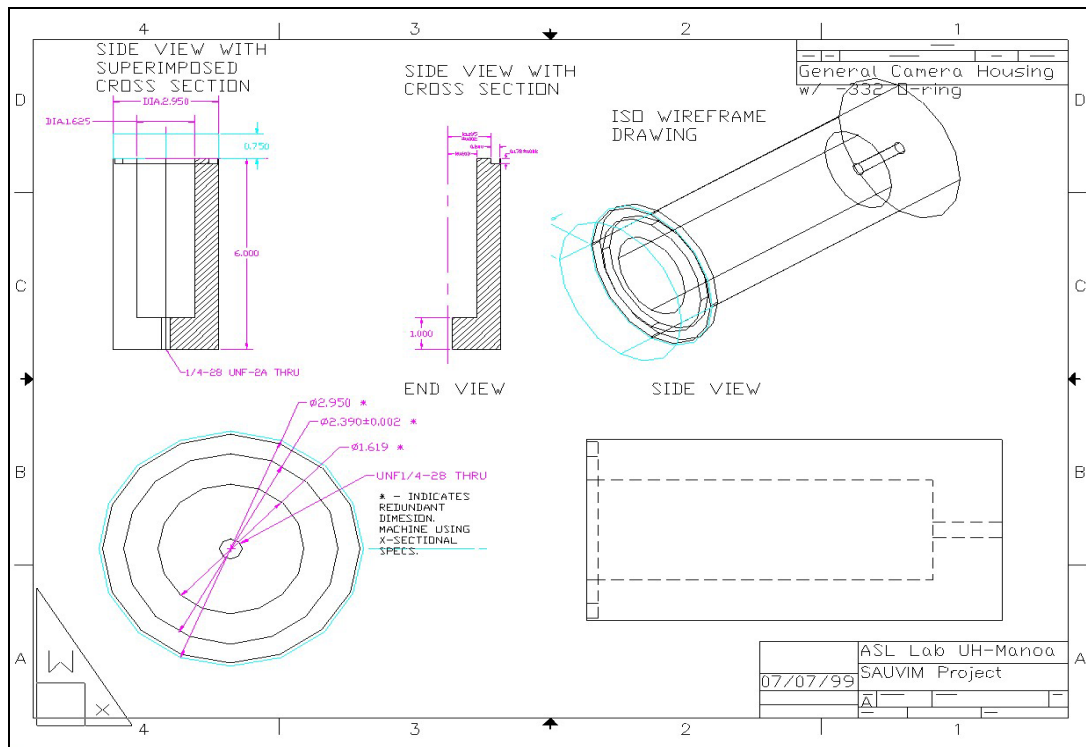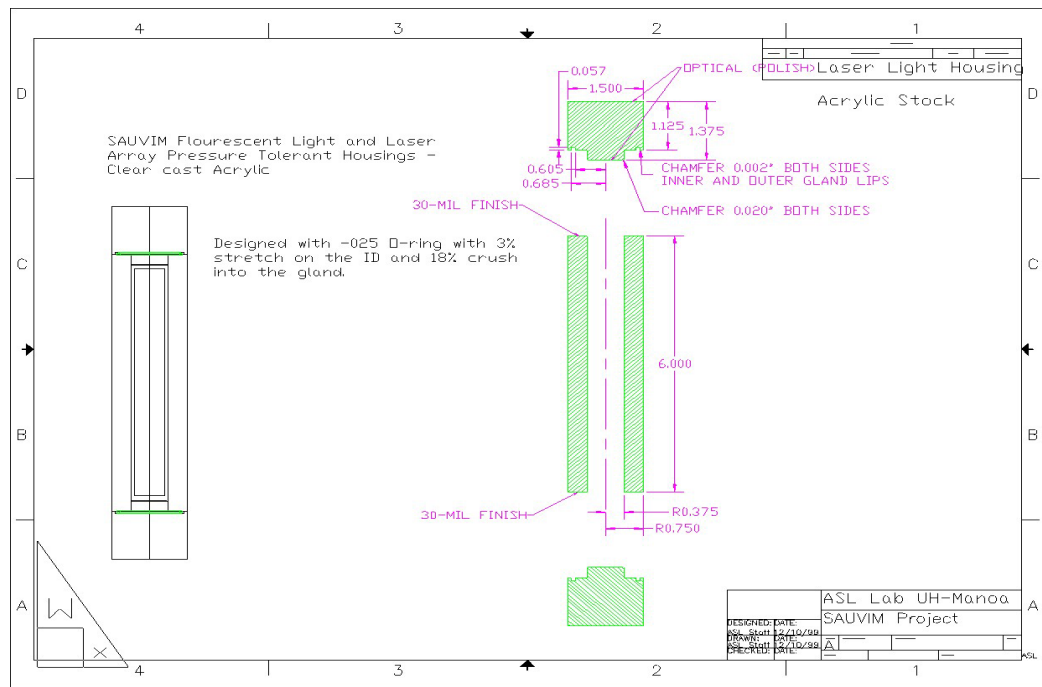
Figure MED-28: Design of Laser and Low-Power Light Ocean Tolerant Housing.

Photograph MED-24: Laser Array and Low Power Light Pressure Tolerant Housings.
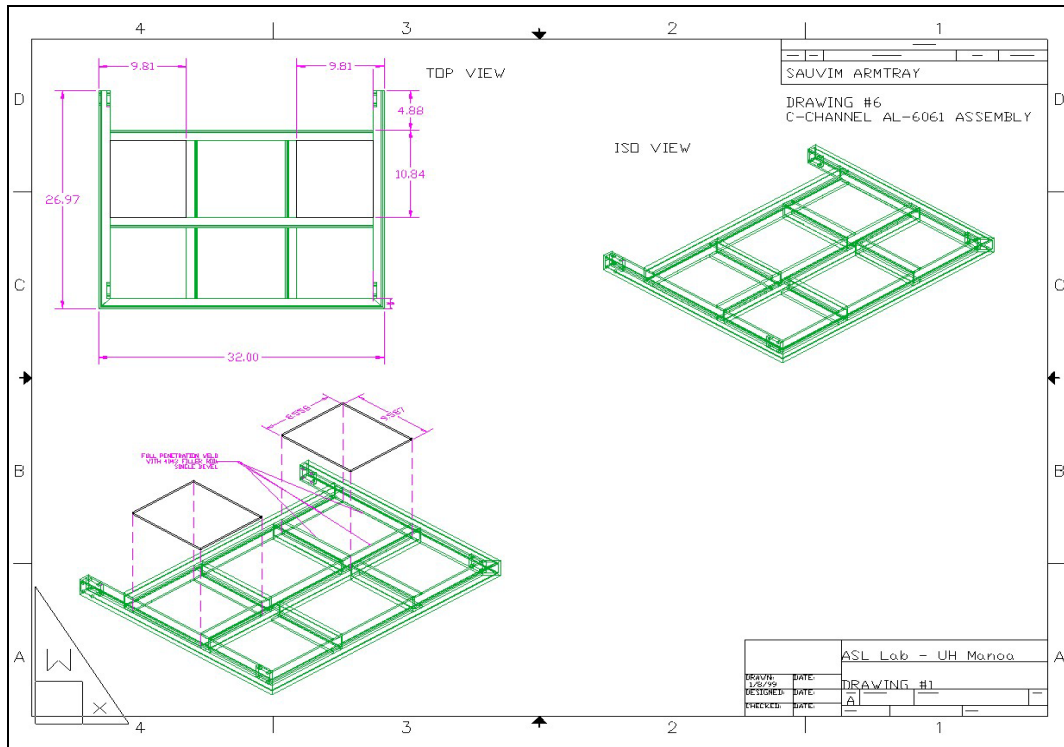
Figure MED-29: SAUVIM Arm Tray.
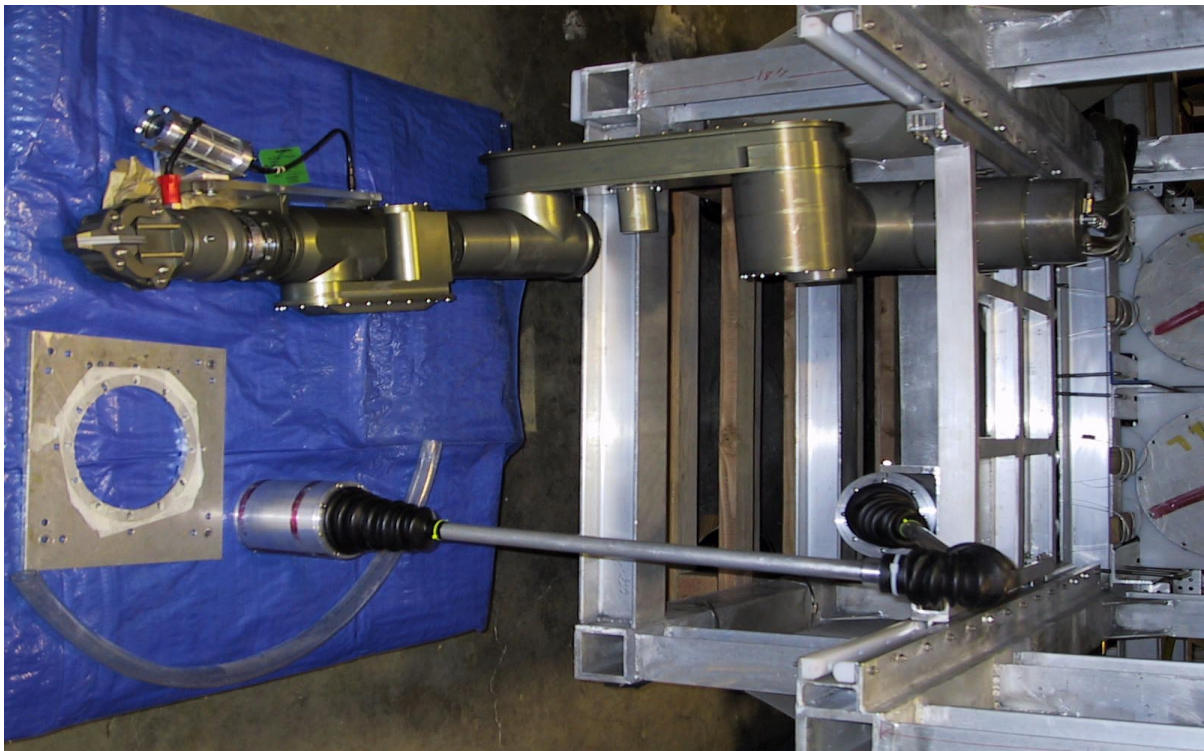
Photograph MED-25: Frontal View of SAUVIM Arm tray.
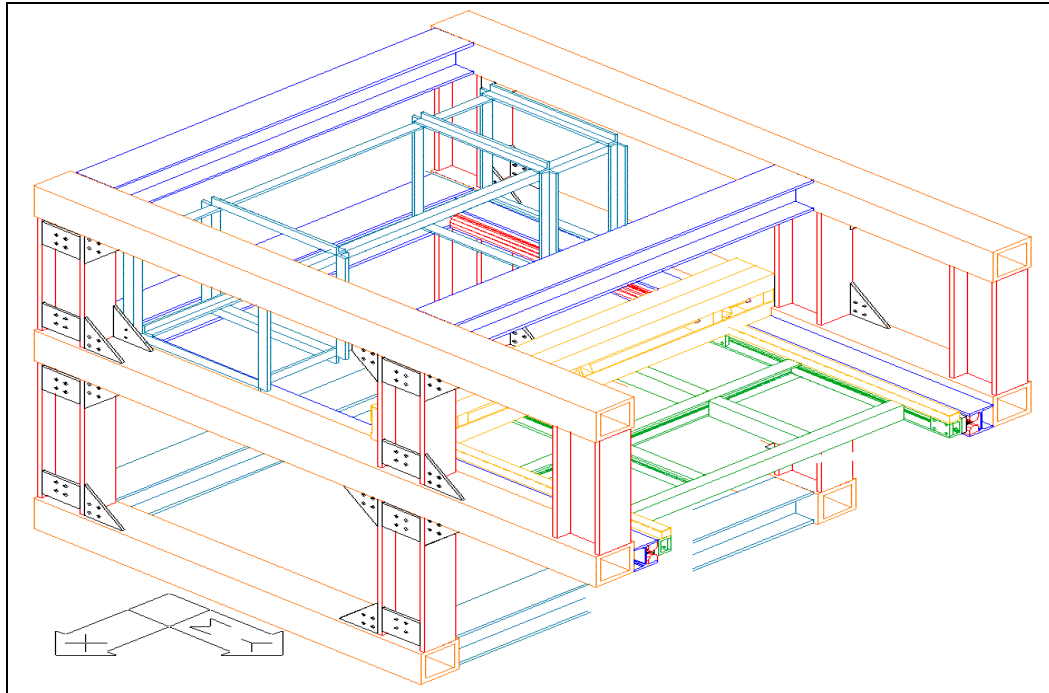
Figure MED-30 Arm tray Extension/Retraction Mechanism Concept Design.
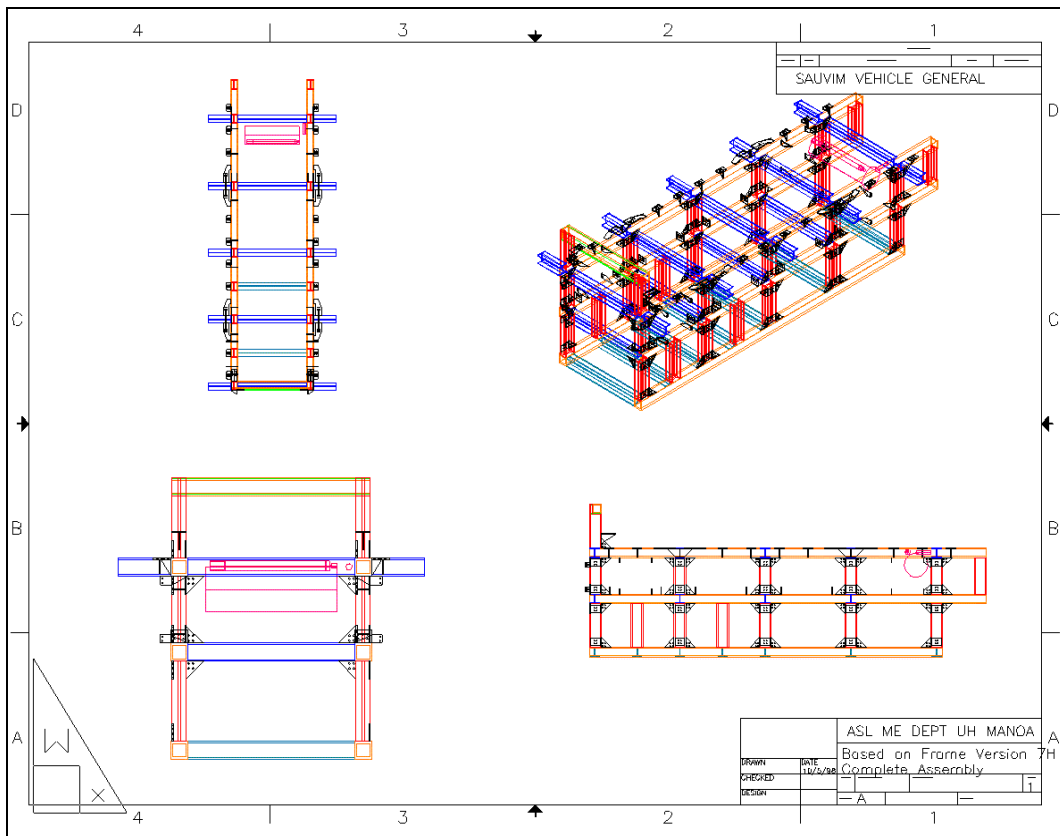
Figure MED-31: MSP Components Locations.
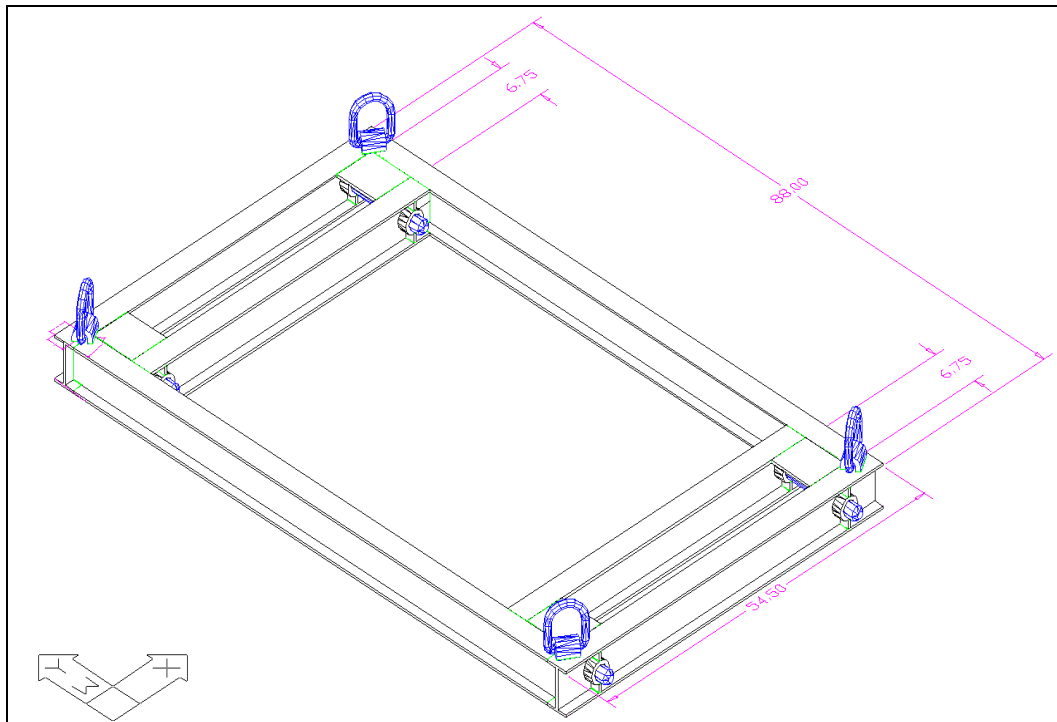
Photograph MED-26: SAUVIM Recovery/Launching Frame.

Photograph MED-27: View of the UH Research Vessel at Snug Harbor.
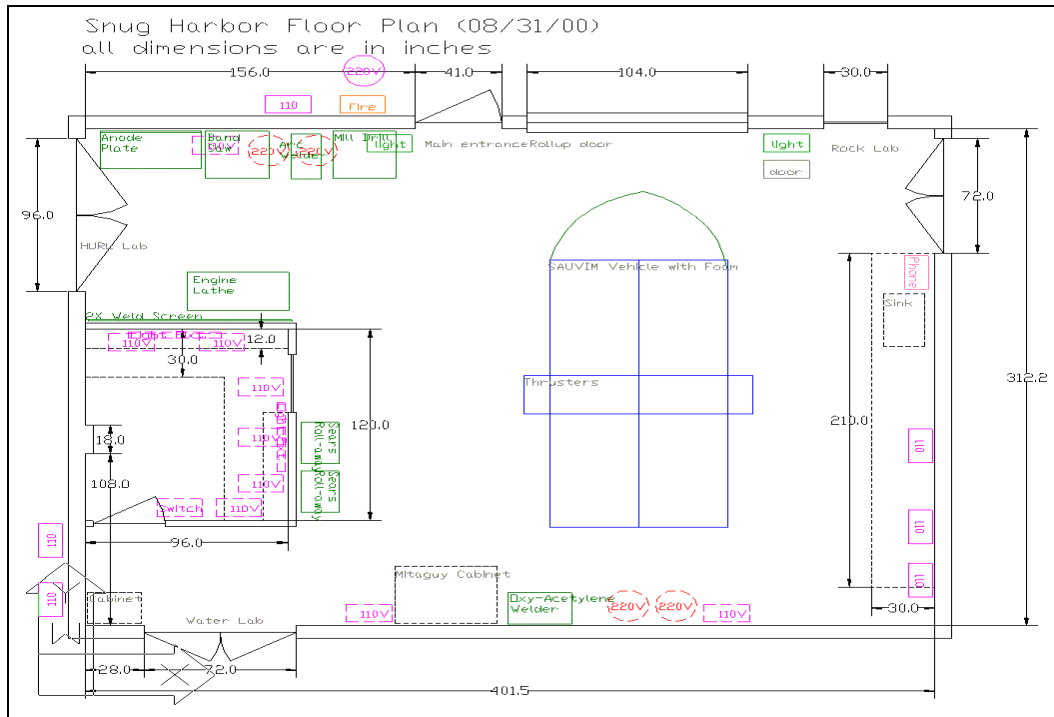
Figure MED-32: Floor-plan of SNUG Harbor Facility for SAUVIM Final Integration and Testing.

Photograph MED-28: Views of 10,000psi MED Pressure Test Facility.
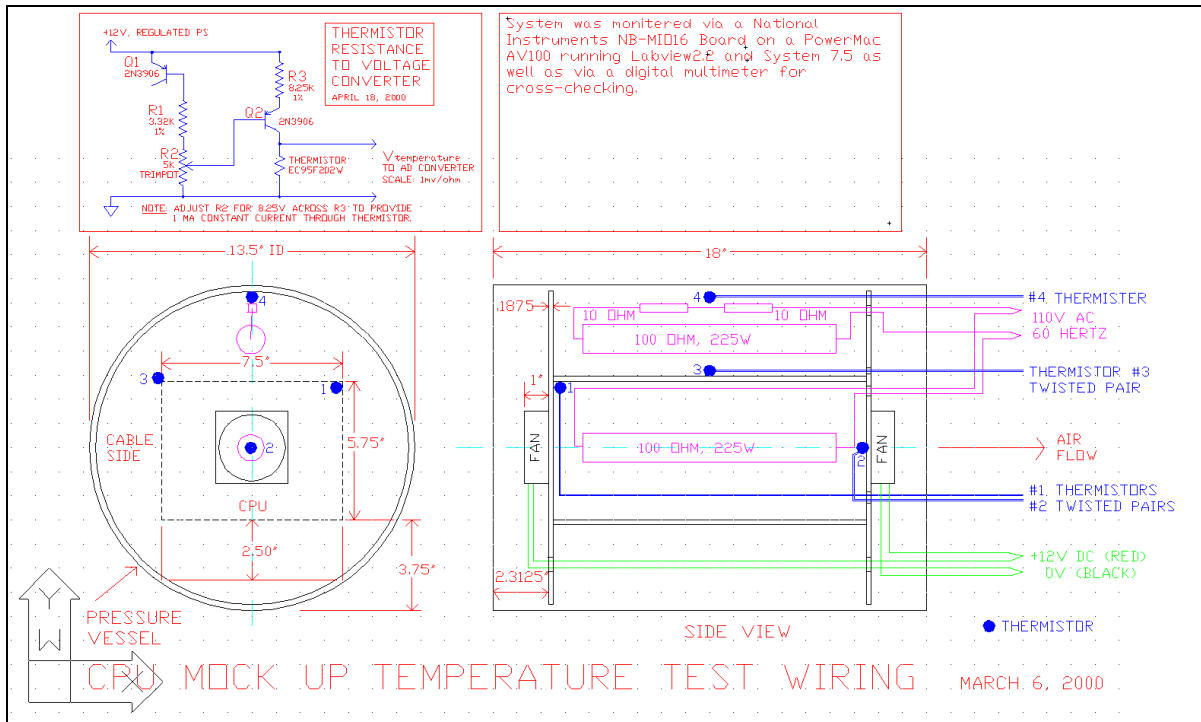
Figure MED-34: Thermal Test Setup Diagramming Locations of Heaters and Thermistor Probes.
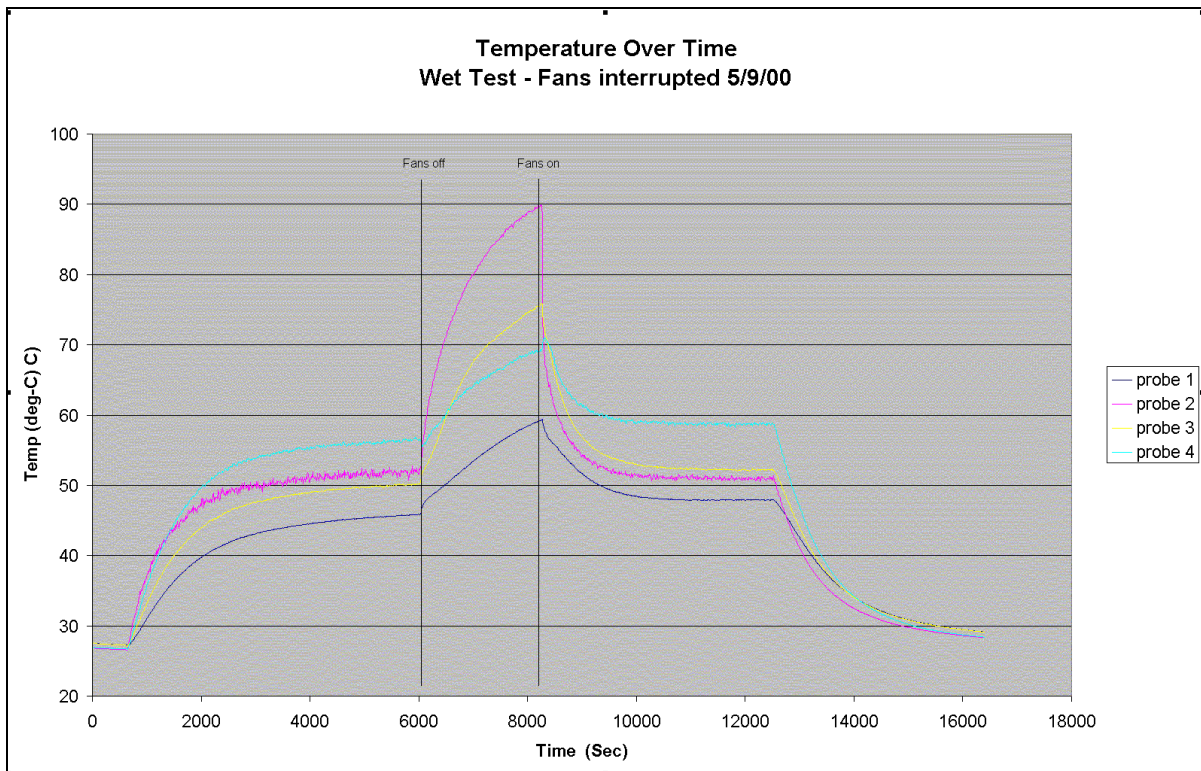
Figure MED-35: Thermal Test of Pressure Vessel in a Sprayed State. Temperature vs. Time.

219
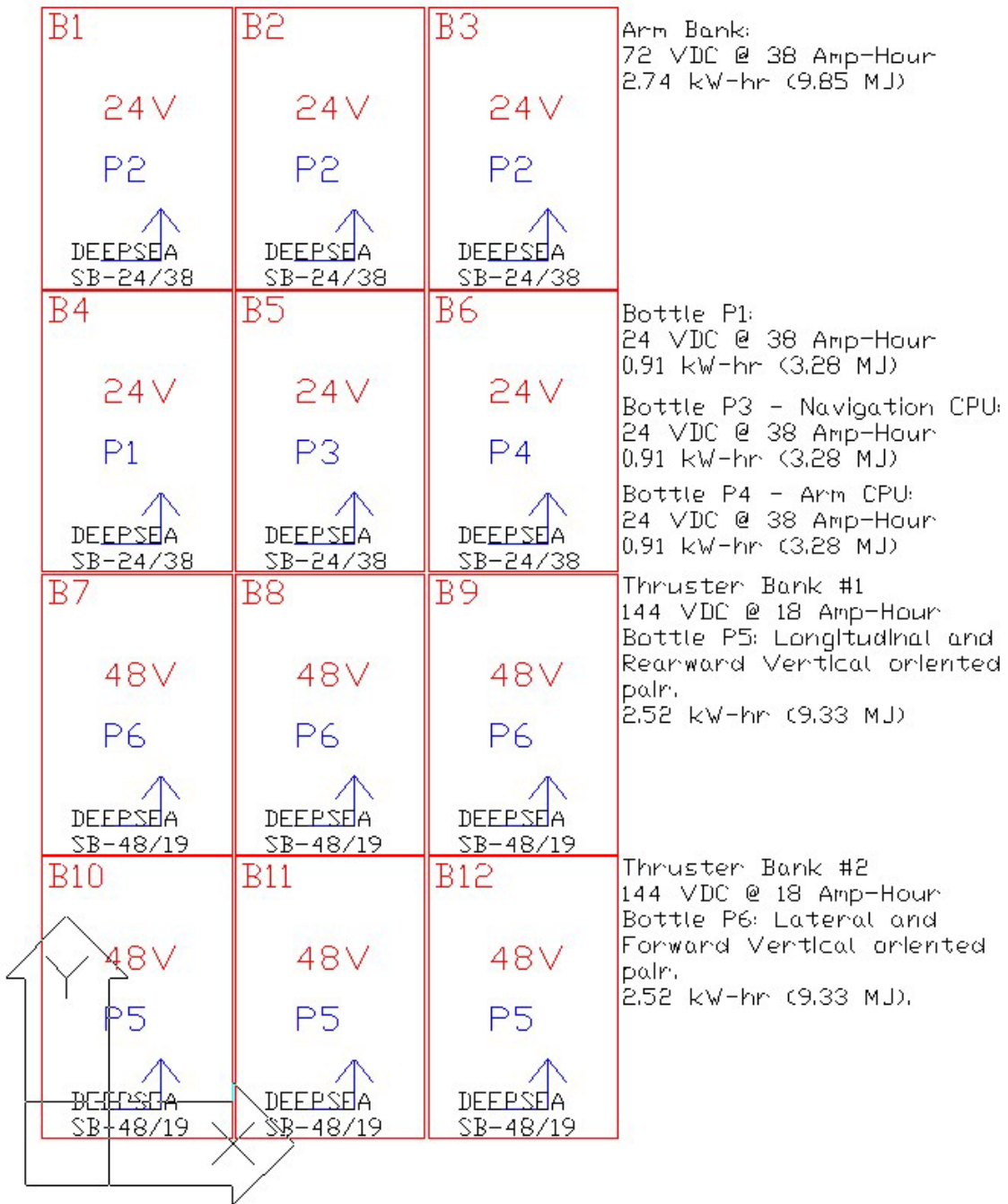
Figure MED-36: Battery Bank Layout for SAUVIM Vehicle.
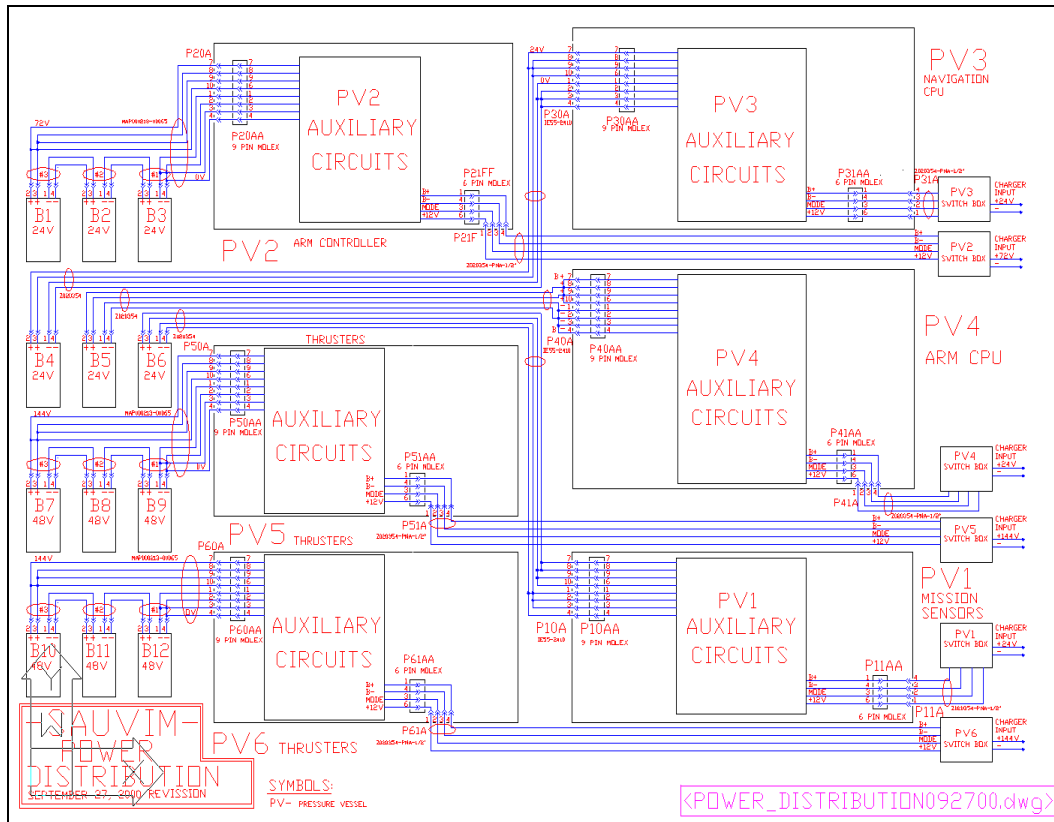
Figure MED-37: SAUVIM Power Distribution System Schematic.

Photograph MED-29: Deep-Ocean Power Supply Wiring Hardware for Battery to Pressure Vessels.

Photograph MED-30: High-Density Deep-Ocean Underwater Cabling and Pressure Vessel Fitting.
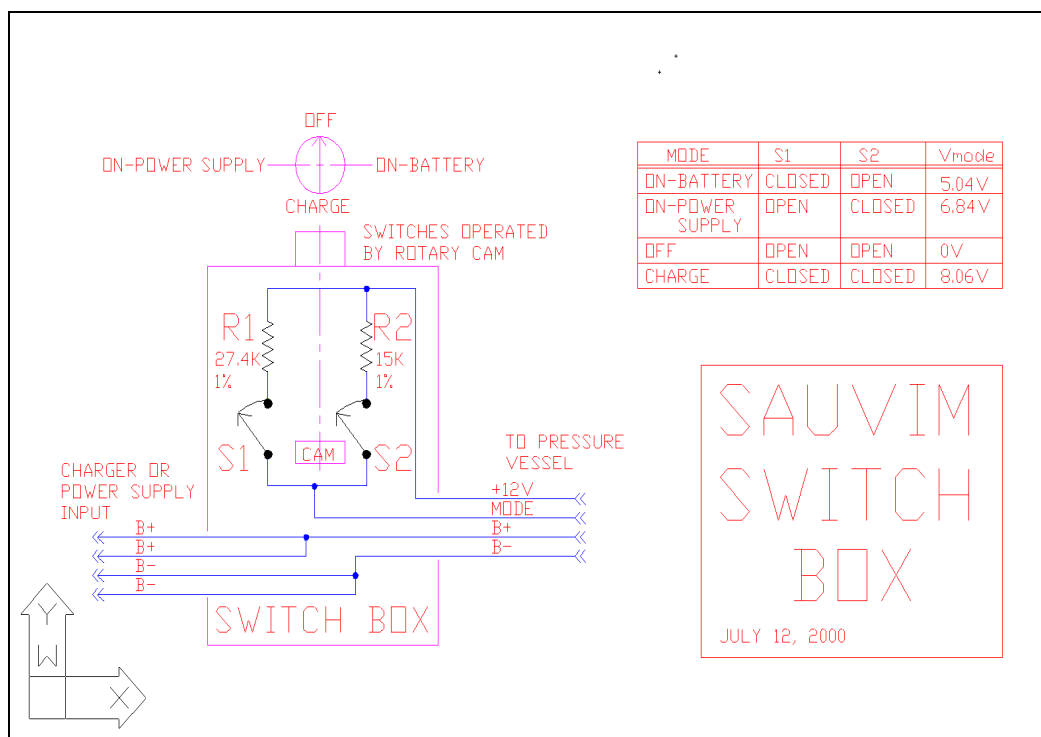
Figure MED-38: Switchbox Electrical Contents Schematic.
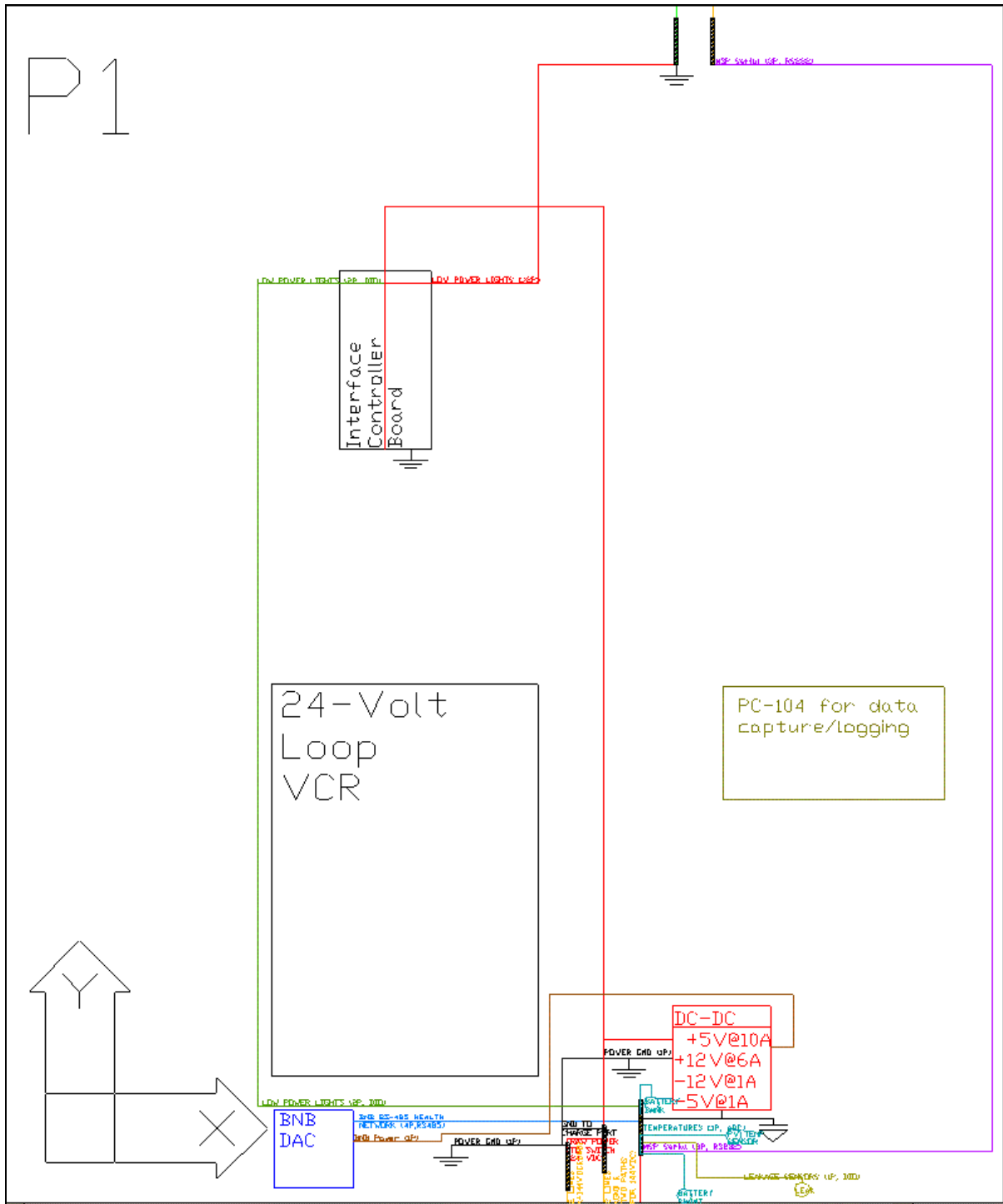
Figure MED-39: Pressure Vessel #1 Contents and Wiring Concept.
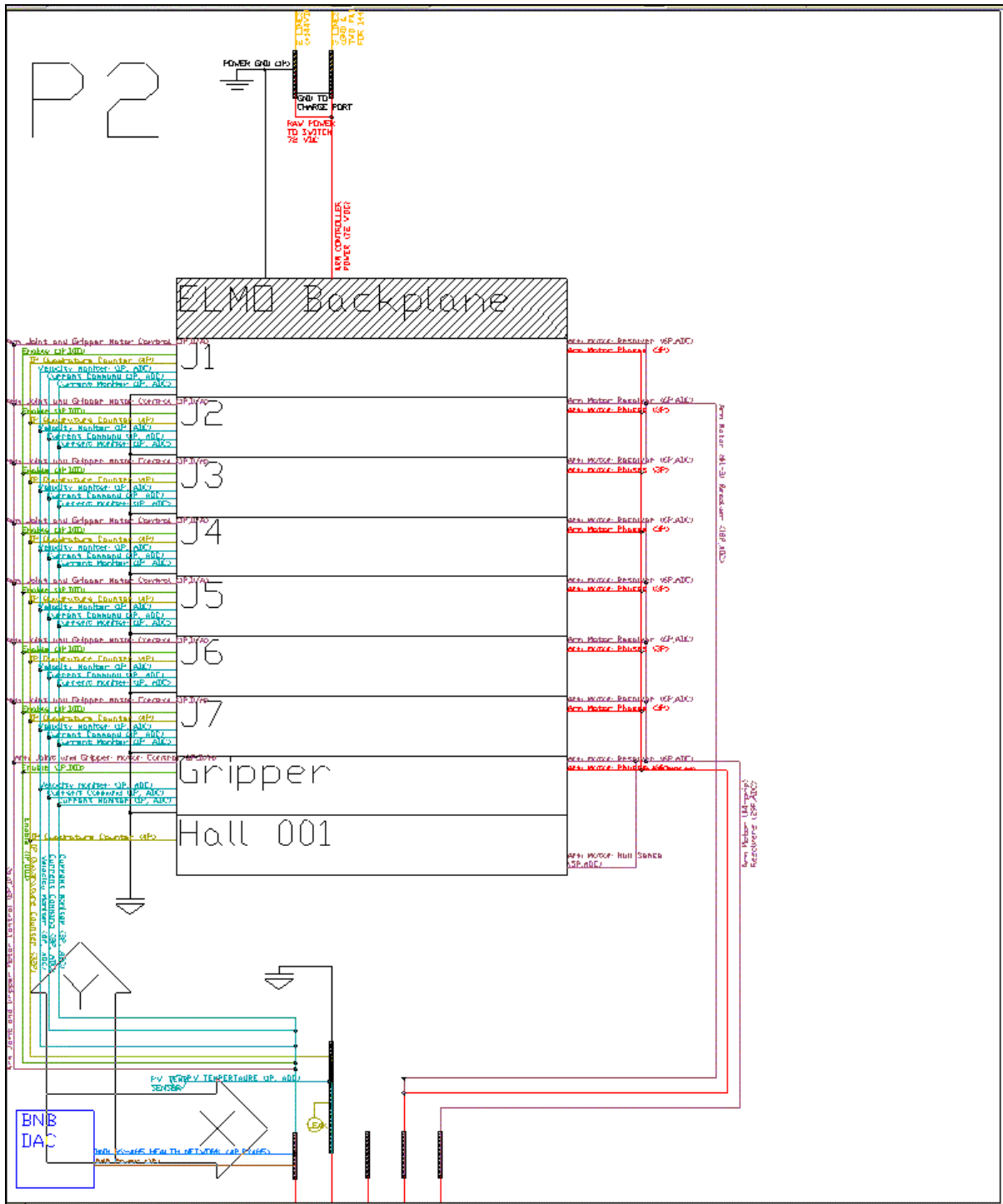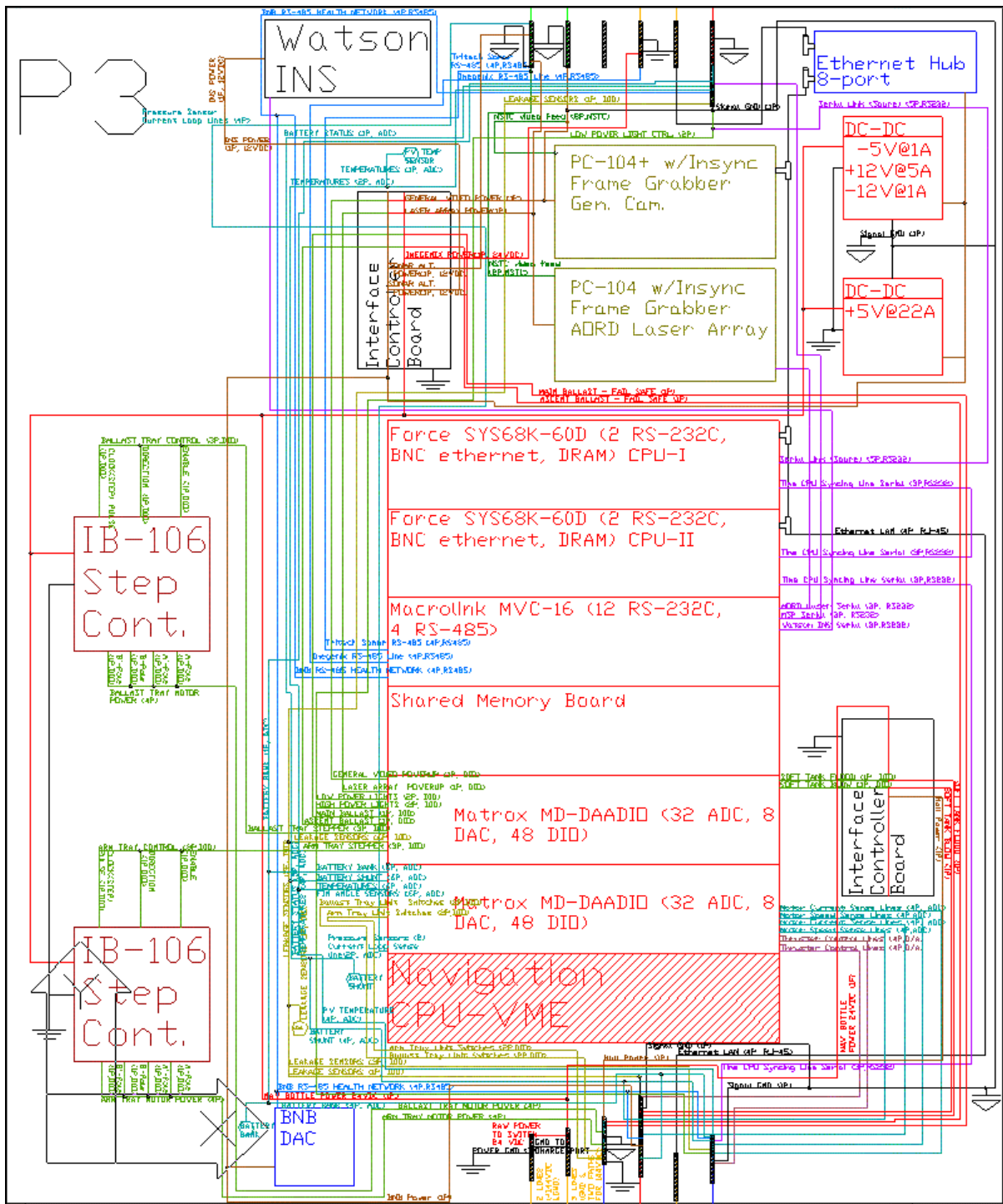
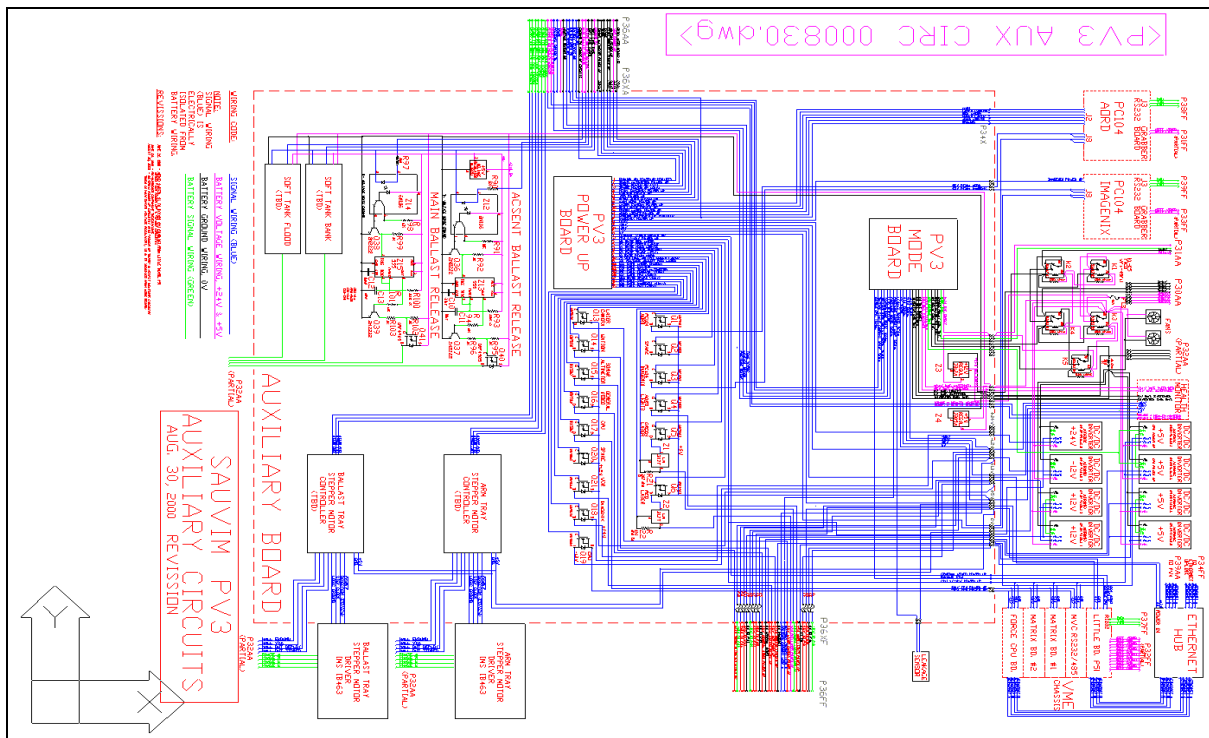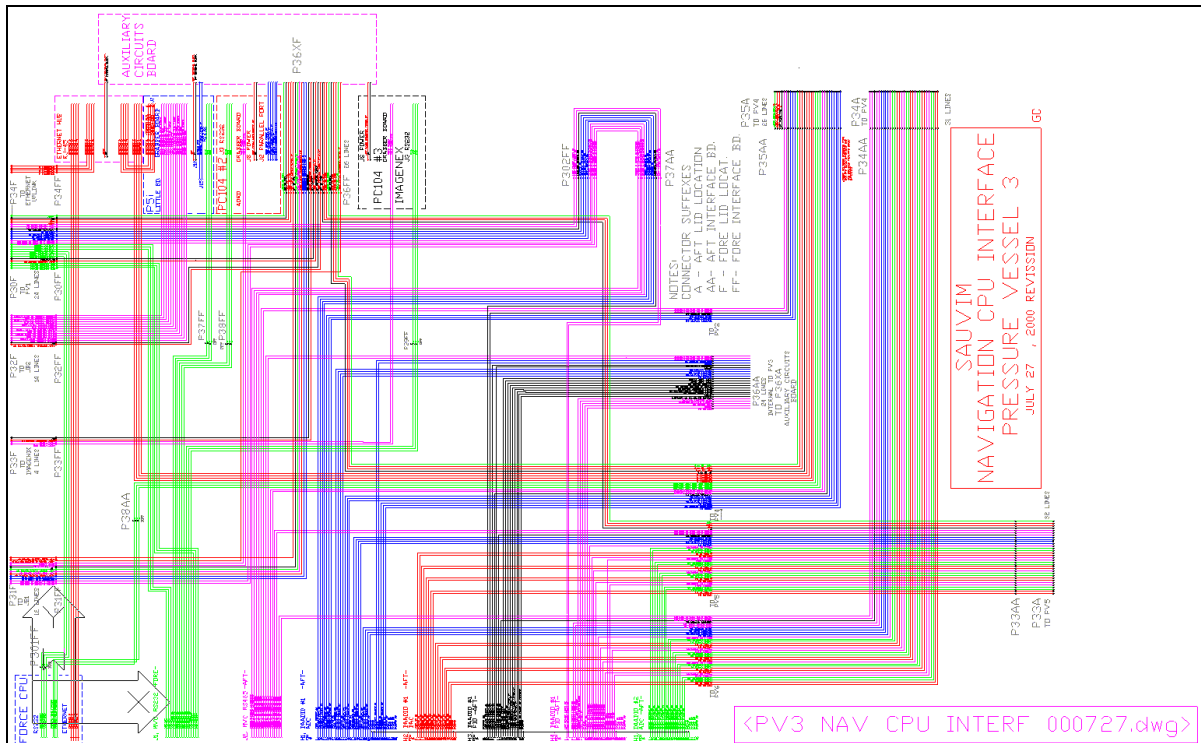Figure MED-40: Pressure Vessel #2 Contents and Wiring Concept.

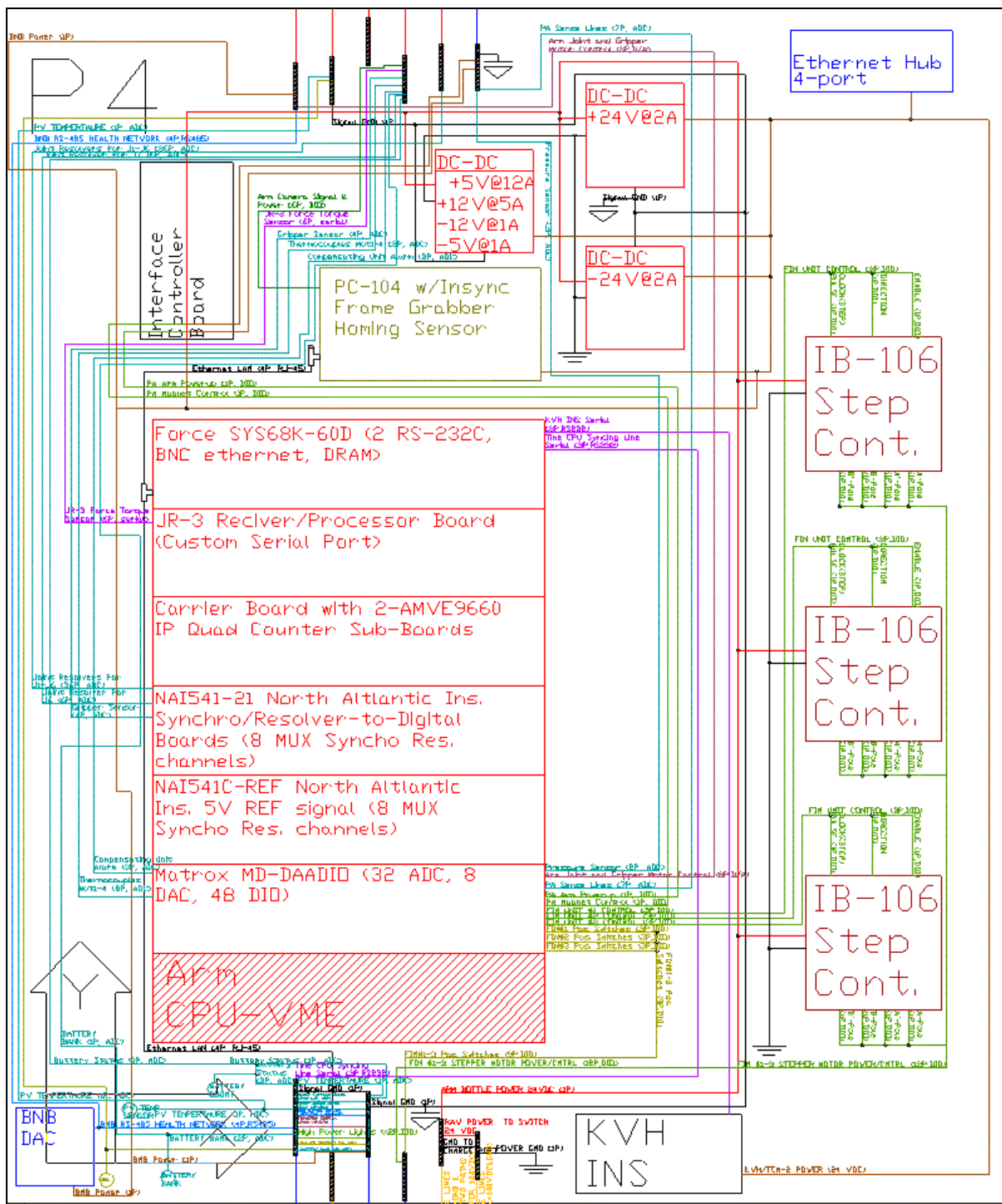Figure MED-41: Pressure Vessel #3 Contents and Wiring Concept.

Figure MED-42: Pressure Vessel #3 Wiring Patch Connection Schematic.

Figure MED-43: Pressure Vessel #3 Auxiliary Circuits Diagram.

226

Figure MED-44: Pressure Vessel #3 Stepper Motor Control Circuit Schematic.

Figure MED-45: Pressure Vessel #3 Mode Board Circuit Schematic.

Photograph MED-31: Pressure Vessel #3 Mode Board.

Figure MED-46: Pressure Vessel #3 Power-Up Board Circuit Schematic.

Photograph MED-32: Power-Up Board.

Figure MED47: Pressure Vessel #4 Contents and Wiring Concept.
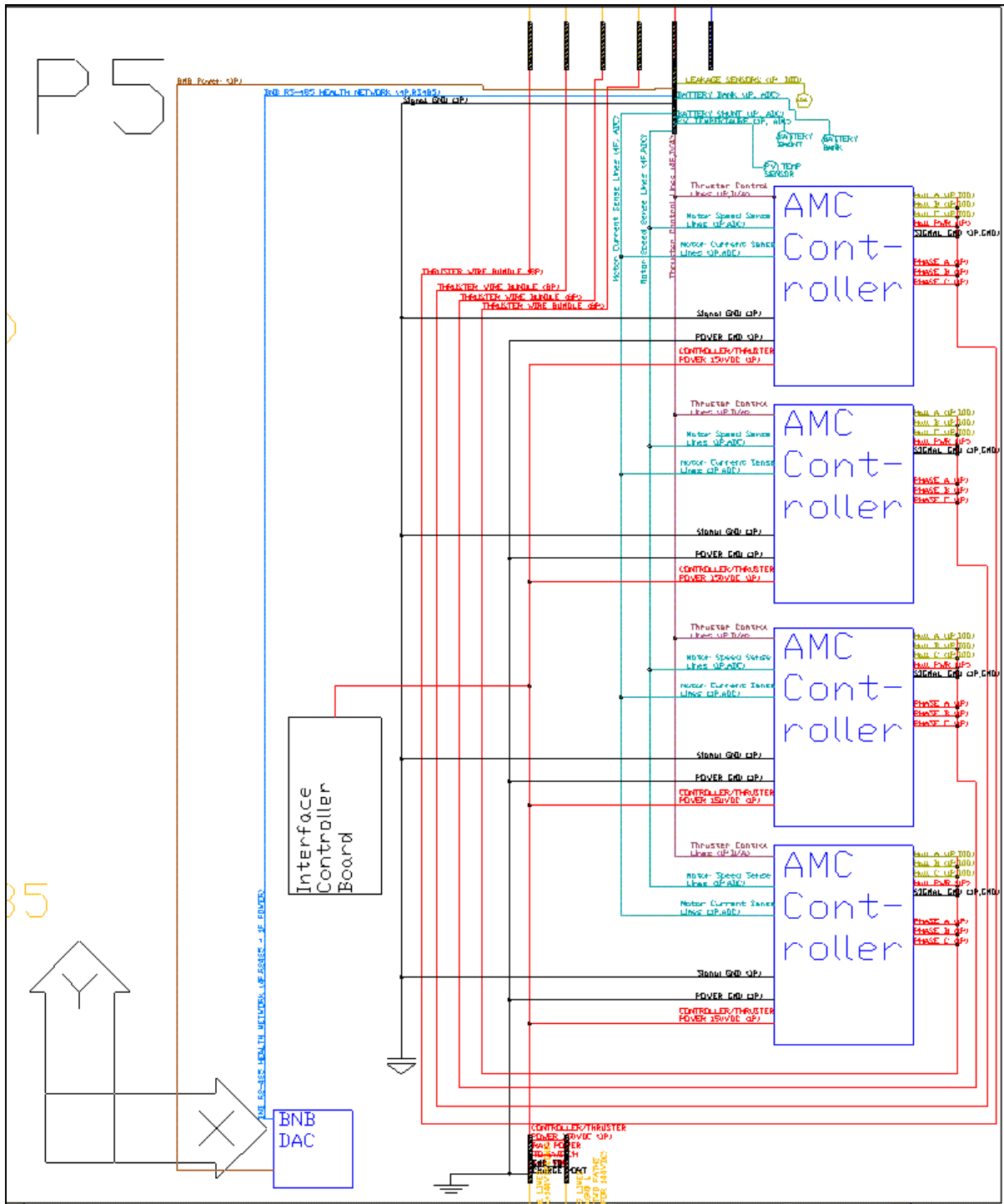
Figure MED-48:

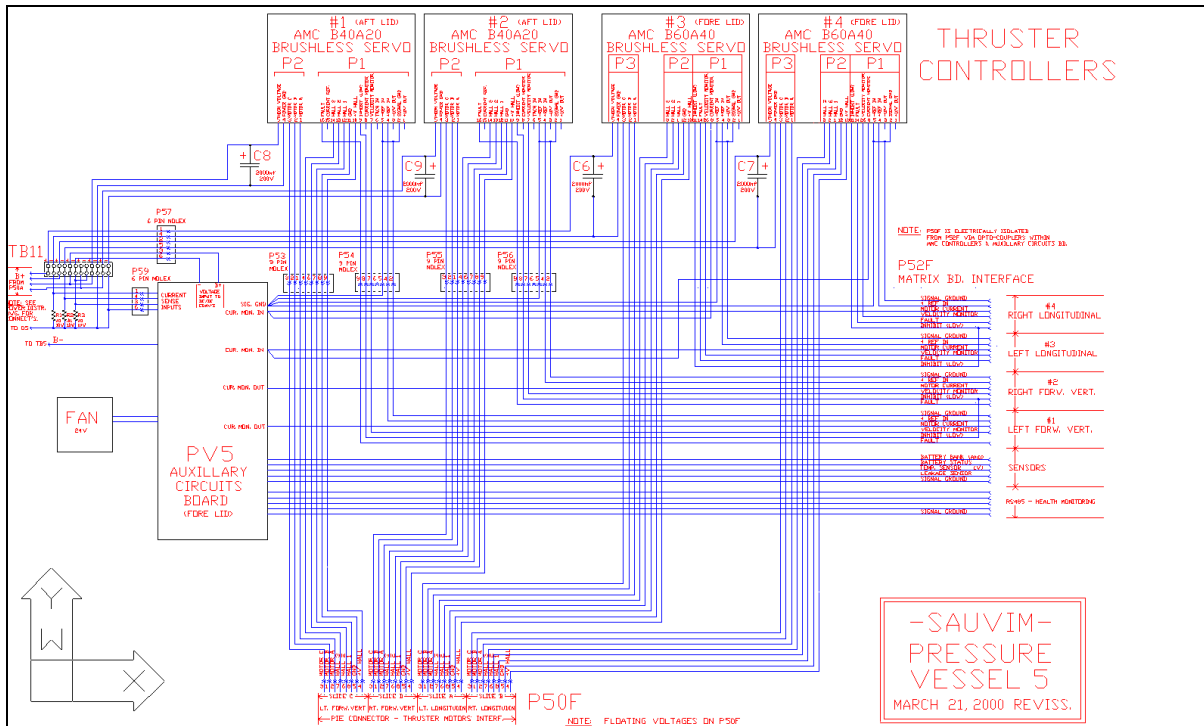Figure MED-49: Pressure Vessel #5 Contents and Wiring Concept.

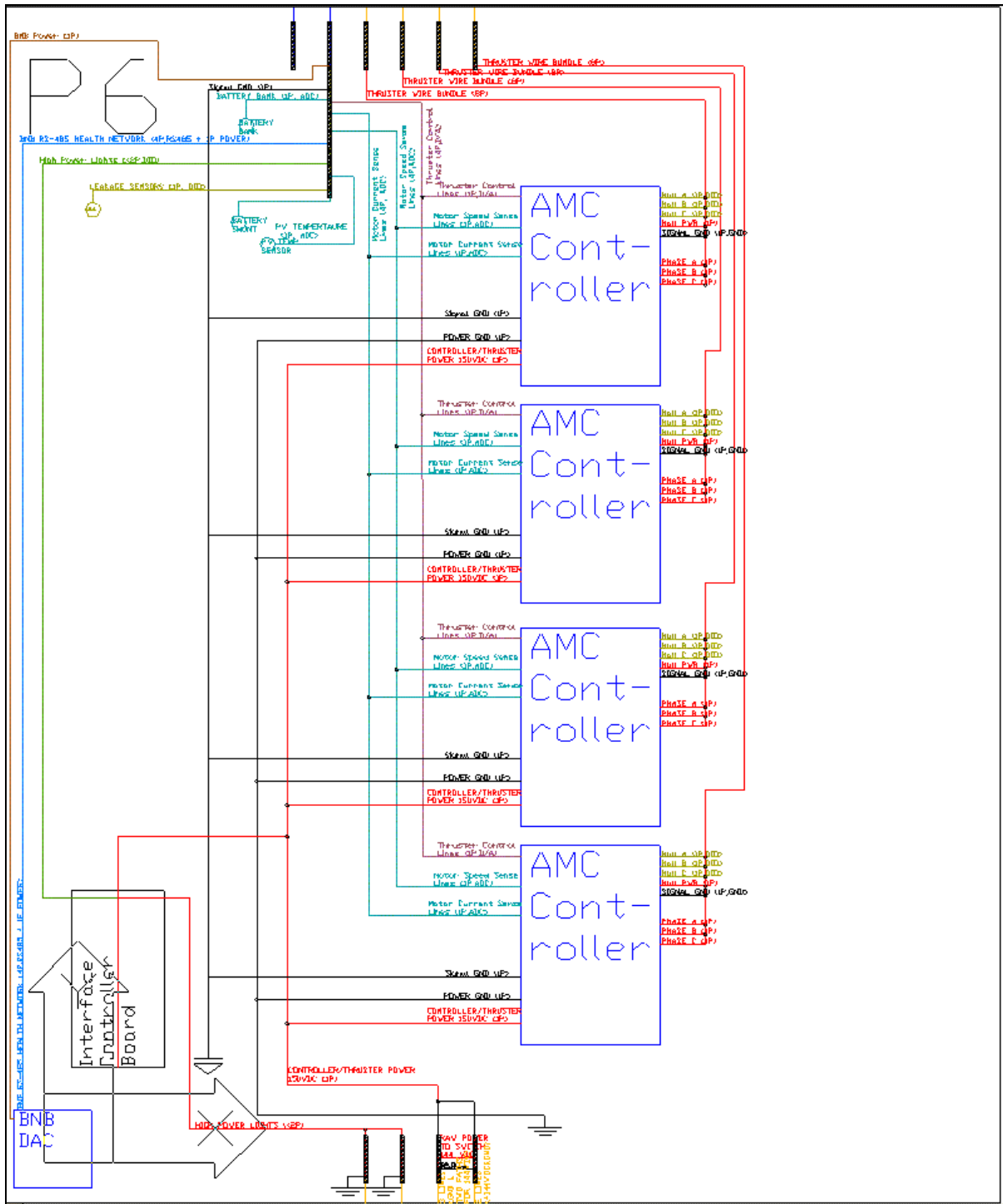Figure MED-50: Thruster Controller Circuit Schematic for Pressure Vessel #5.

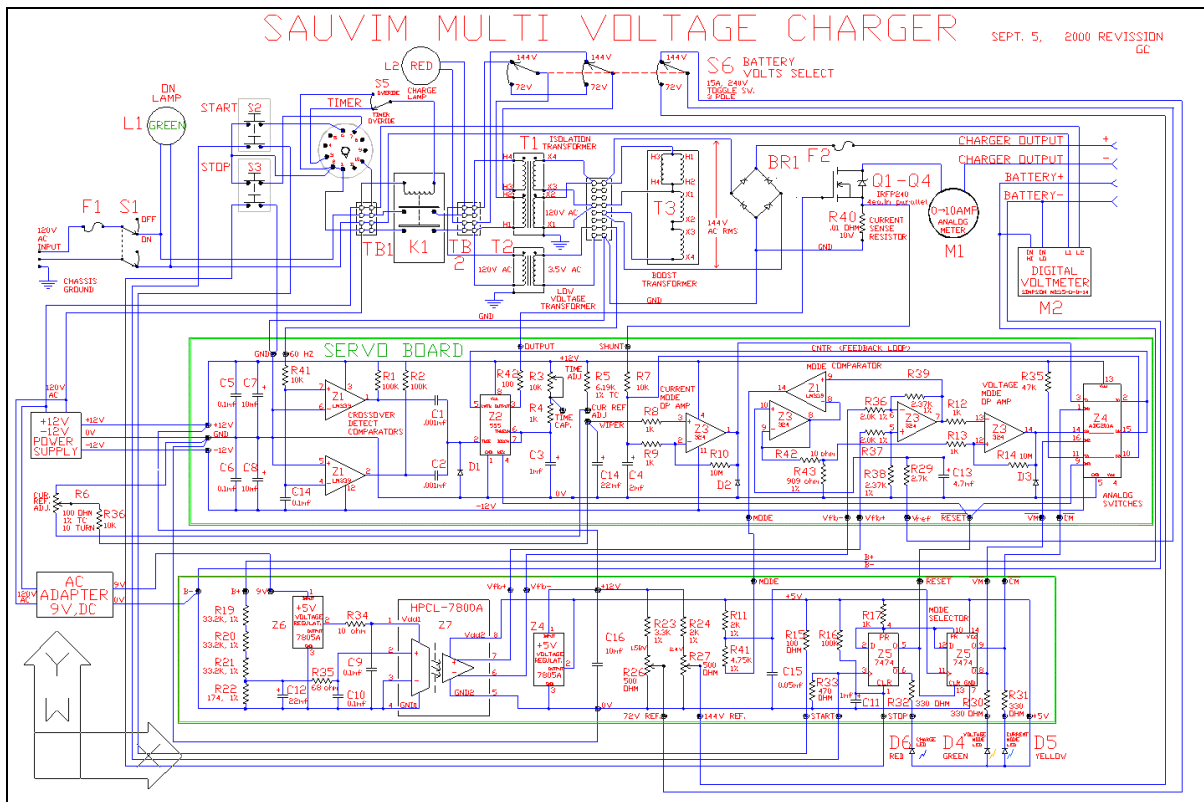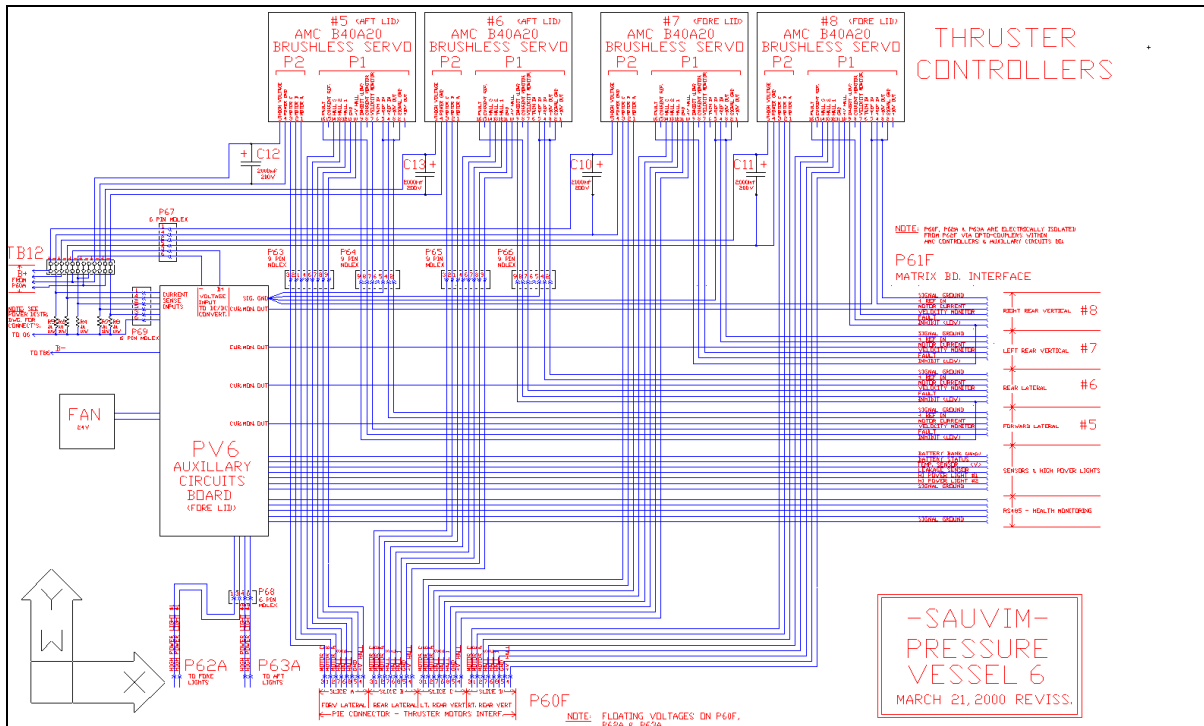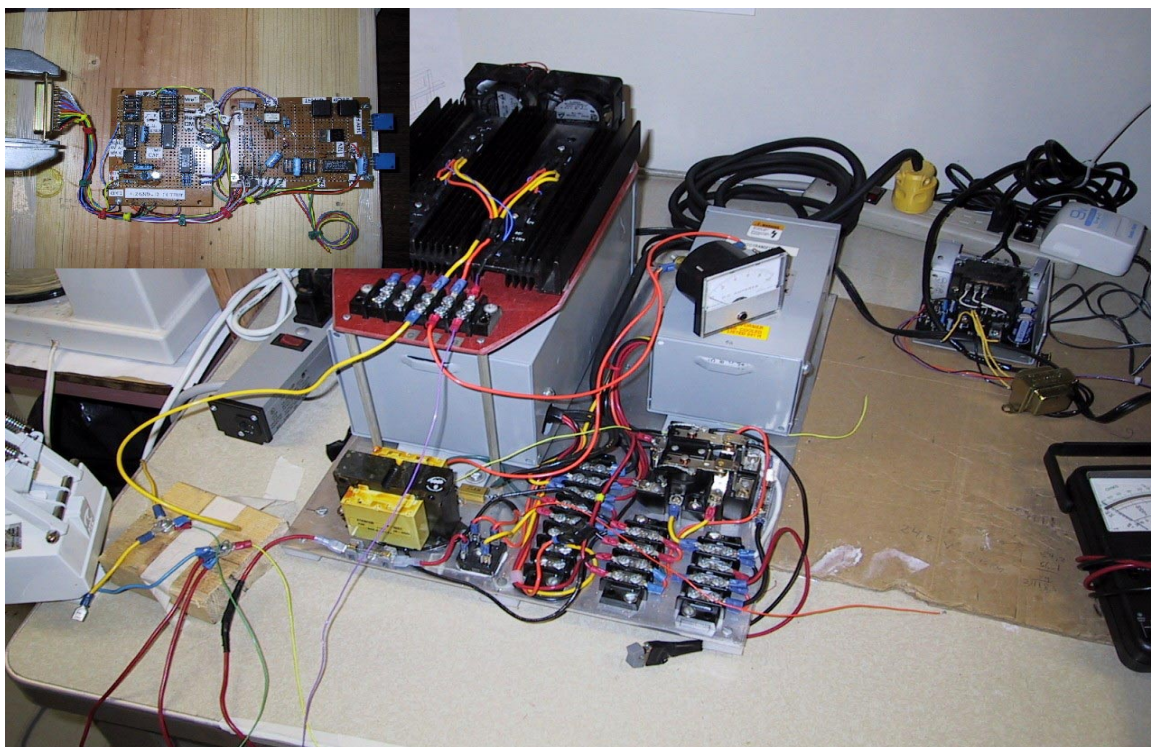Figure MED-51: Pressure Vessel #6 Contents and Wiring Concept.

Figure MED-52: Thruster Controller Bottle Wiring Schematic for Pressure Vessel#6.

Figure MED-53: Multi-Voltage Charger Schematic.

Photograph MED-33: In-House Multiple Voltage Battery Charger in Assembly.

References

[Aerotech92]   Aerotech, "Operation & Technical Manual", 1992.

[Akiba00]   Akiba T and Kakui Yoshimi, "Design and Testing of an Underwater Microscope and Image Processing System for the Study of Zooplankton Distribution", IEEE Journal of Oceanic Engineering, vol. 25, no 1, page 97-104 (2000)

[Aloimonos97]   Aloimonos, Y., Visual Navigation: From Biological Systems to Unmanned Ground Vehicles, Mahwah, NJ, Lawrence Erlbaum Associates, 1997.

[ANSYS94]   ANSYS User's Manual (Version 5.2), Ansys, Inc., Houston, TX, USA, 1994.

[ANSYS99]   ANSYS User's Manual, ANSYS, Inc., Canonsburg, PA, 1999.

[Antonelli98]   Antonelli, G., and S. Chiaverini, "Task-Priority Redundancy Resolution for Underwater Vehicle-Manipulator Systems", in Proceedings of the 1998 IEEE International Conference on Robotics & Automation, pp.756-761, Leuven, Belgium, 1998.

[Archibald93]   Archibald C and Petriu E, "Robot Skills Development Using a Laser Ranger Finder", IEEE 0-7803-1229-5, page 448-452 (1993)

[Ashby80]   Ashby, M. F., and D. R. H., Jones, "Engineering Materials 1: An Introduction to their Properties and Applications", New York: Pergamon Press, 1980.

[Askeland84]   Askeland, D. R., "The Science and Engineering of Materials" California: Wadsworth, Inc., 1984

[Atari97]   Atari A and Dodds G, "Practical Stereo Vision and Multi-Laser Scanning in Object Face Detection and Orientation Determination", IEEE 0-7803-4119-8, page 746-751 (1997)

[Atari99]   Atari A and Dodds G, "Integration of a Stereo Multiple-laser Ranger System and Force Sensor in a Virtual Robotic Environment", IEEE/RSJ Int. Conference on Intelligent Robots and Systems, page 1519-1524 (1999)

[Auran95]   Auran, P.G. and O. Silven, "Ideas for Underwater 3D Sonar Range Sensing and Environmental Modeling", Proceeding of CAMS'95, pp. 284-290, 1995.

[AUV96]   Proceedings of the 1996 Symposium on Autonomous Underwater Vehicle Technology, Monterey, California, 1996.

[Avallone87]   Avallone, E.A, and Baumeister, T., Mark's Standard Handbook for Mechanical Engineers - Ninth Edition, McGraw-Hill Book Co., 1987.

[Ayache91]   Ayache, N., Artificial Vision for Mobile Robots : Stereo Vision and Multisensory Perception, MIT Press, 1991.

[Beckwith90]   Beckwith, T.G., and Maranogoni, R.D., Mechanical Measurements, Addison-Wesley Publishing Company, 1990.

[Bollinger89]   Bollinger, J.G. and N.A. Duffie, Computer Control of Machines and Processes, Reading, MA, Addison-Wesley Publishing Company, 1989.

[Borland92]   Borland C++ User's Guide, Borland International, Inc., 1992.

[Brush75]   Brush, D.O. and B.O. Almroth, Buckling of Bars, Plates, and Shells, New York: McGraw-Hill, Inc., 1975.

[Brutzman92]   Brutzman, D.P., Y. Kanayama & M.J. Zyda, "Integrated Simulation for Rapid Development of Autonomous Underwater Vehicles," Proceedings of the IEEE Oceanic Engineering Society Autonomous Underwater Vehicle 92 Conference, Jun. 1992.

[Bushnell85]   Bushnell, D., "Computerized Buckling Analysis of Shells", Dordrecht: Martinus Nijhoff Publishers, 1985

[Caimi95]   Caimi, F, "Technical Challenges and Recent Developments in Underwater Imaging", Micro-Optics/Micromechanics and Laser Scanning and Shapining, M. Edward Motamedi, Leo Beiser, Editors, Proceedings of SPIE Vol. 2383, 408-418 (1995)

[Caimi99]   Caimi F and Kocak D and Colquitt C, "Design and performances characterization of Simultaneous Reflectance and Surface Mapping laser Scanner for Application in Underwater inspection", in Optical Scanning: Design and Application, Leo Beiser, Stephen F. Sagan, Gerald F. Marshall, Editors, SPIE Vol. 3787, 228-239 (1999).

[Callister91]   Callister, W.D., Materials Science and Engineering, John Wiley and Sons, Inc., 1991.

[Casalino00]   Casalino, G., D.Angeletti, G.Cannata, G. Marani: On the Function and Algorithmic Control Architecture of the AMADEUS Dual Arm Robotic Workcell, SURT 2000, Wailea, Hawaii, June 2000.

[Chan95]   Chan, T.F. and R.V. Dubey, "A Weighted Least-Norm Solution Based Scheme for Avoiding Joint Limits for Redundant Joint Manipulators", IEEE Transaction on Robotics and Automation, vol.11, no.2, pp.286-292, 1995.

[Chappell99]   Chappell, S.C., R.J. Komerska, L. Peng & Y. Lu, "Cooperative AUV Development Concept (CADCON) - An Environment for High-Level Multiple AUV Simulation," Proceedings of the 11th International Symposium on Unmanned Untethered Submersible Technology, Aug. 1999.

[Chiaverini93]   Chiaverini, S. and L. Sciavicco, "The Parallel Approach to Force/Position Control of Robotic Manipulators," IEEE Transaction on Robotics and Automation, vol. 9, pp. 361-373, 1993.

[Chiaverini97]   Chiaverini, S., "Singularity-Robust Task-Priority Redundancy Resolution for Real-Time Kinematic Control of Robot Manipulators," IEEE Transaction on Robotic and Automation, vol. 13, 398-410, 1997.

[Choi95a]   Choi, S.K., J. Yuh, and G.Y. Takashige, "Design of an Omni-Directional Intelligent Navigator, Underwater Robotic Vehicles: Design and Control, TSI Press, pp. 277-297, 1995.

[Choi95b]   Choi, S.K. and J. Yuh, "Development of an Omni-Directional Intelligent Navigator", IEEE Robotics and Automation Magazine, 1995.

[Choi95c]   Choi, S.K., G.Y. Takashige & J. Yuh, "Development of an Omni-Directional Intelligent Navigator," IEEE Robotics and Automation Magazine on Mobile Robots, Mar. 1995.

[Choi96]   Choi, S.K., and J. Yuh, "Experimental Study on a Learning Control System with Bound Estimation for Underwater Robots", International Journal of Autonomous Robots, 3 (2 & 3), pp. 187-194, 1996.

[Clayton82]   Clayton, B.R. and Bishop, R.E.D., Mechanics of Marine Vehicles, E. & F.N. Spon Ltd., 1982.

[Comstock67]   Comstock, J.P., Principles of Naval Architecture, Society of Naval Architects and Marine Engineers, 1967.

[Coz74]   Cox, A.W., Sonar and Underwater Sound, Lexington Books, 1974.

[Craig86]   Craig, J.J, Introduction to Robotics: Mechanics and Control, Reading, MA, Addison-Wesley, 1986.

[Crawford98]   Crawford A and Hay A, "A Simple System for Laser-Illuminated Video Imaging of Sediment Suspension and Bed Topography", IEEE Journal of Oceanic Engineering, vol. 23, no 1, page 12-19 (1998)

[Cristi96]   Cristi, R., M. Caccia, G. Veruggio and A.J. Healey, "A Sonar Based Approach to AUV Localization", Proceeding of CAMS'95, pp. 291-298, 1996.

[Cunha95]   Cunha, J.P., R.R. Costa, and L. Hsu, "Design of a High Performance Variable Structure Position Control of ROV's," IEEE Journal of Oceanic Engineering, vol. 20, no. 1, pp.42-55, 1995.

[D'egoulange94] D'egoulange, E. and P. Dauchez, P., "External Force Control of an Industrial PUMA 560 Robot," journal of Robotic Systems, vol. 11, pp. 523-540, 1994.

[de Wit96]   Candus de Wit, C., B. Siciliano, and G. Bastin (Editors), Theory of Robot Control, Springer-Verlag, Berlin, Germany, 1996.

[DeBitetto94] DeBitetto, P.A., "Fuzzy Logic for Depth Control of Unmanned Undersea Vehicles," Proceedings of the Symposium of Autonomous Underwater Vehicle Technology, pp. 233-241, 1994.

[Deepsea90]   UnderPressure Software Manual, DeepSea Power and Light Co., 1990.

[Doebelin75] Doebelin, E.O., Measurement Systems: Application and Design, New York, McGraw-Hill Book Company, 1975.

[Dote90]   Dote, Y., Servo Motor and Motion Control Using Digital Signal Processors, Englewood Cliffs, NJ, Prentice-Hall Publishing, 1990.

[Dougherty90] Dougherty, F. and G. Woolweaver, "At-Sea Testing of an Unmanned Underwater Vehicle Flight Control System," Proceedings of the Symposium of Autonomous Underwater Vehicle Technology, pp. 65-73, 1990.

[Dunningan96] Dunningan, M.W., D.M. Lane, A.C. Clegg, and I. Edwards, "Hybrid Position/Force Control of a Hydraulic Underwater Manipulator," IEEE Proceedings Control Theory and Application, vol. 143, no. 2, pp. 145-151, March 1996.

[Englemann95]   Engelmann, W.H., Handbook of Electric Motors, M. Dekker, 1995.

[Evans96]   Evans, A.J., Basic Digital Electronics - Digital System Circuits and Their Functions, Master Publishing Inc., 1996.

[Ferrerri97] Ferrerri, G., G. magnani, and P. Rocco, "Toward the Implementation of Hybrid Position/Force Control in Industrial Robots," IEEE Transaction on Robotics and Automation, vol. 16, pp. 838-845, 1997.

[Fox88]   Fox J, "Structured light imaging in turbid water", Underwater Imaging, Douglas J. Holloway, Editor, SPIE vol. 980, page 66-71 (1988).

[Fox92]   Fox, R.W. and McDonald, A.T., Introduction to Fluid Mechanics, John Wiley amd Sons, Inc., 1992.

[Gere90]   Gere, J.M. and Timoshenko, S.P., Mechanics of Materials, PWS-Kent Publishing Co., 1990.

[Geyer77]   Geyer, R. A., Submersibles and Their Use in Oceanography and Ocean Engineering, Amsterdam, Elsevier Scientific Pub. Co., 1977.

[Gill85]   Gill, R., Electrical Engineering Handbook, Siemens Co., 1985.

[Goheen98]   Goheen, K.R., and R.E. Jeffery, "Multivariable Self-Tuning Autopilots for Autonomous and Remotely Operated underwater Vehicles", IEEE Journal of Oceanic Engineering, vol. 15, pp.144-151, 1990.

[Goldberg89] Goldberg, D. E., Genetic Algorithms in Search, Optimization, and Machine Learning, Addison-Wesley, 1989.

[Harding97]   Harding, K.G. and D.J. Svetkoff (chairs/editors), Three-dimensional Imaging and Laser-based Systems for Metrology and Inspection III (Pittsburgh, PA), International Society for Optical Engineering, Bellingham, Washington, 1997.

[Healy92]   Healy, A.J. and D.B. Macro, "Slow Speed Flight Control of Autonomous Underwater Vehicles: Experimental Results with NPS AUV II", Proc. of ISOPE, pp. 523-532, 1992.

[Healy93]   Healy, A.J. and D. Lienard, "Multi-variable Sliding Mode Control for Autonomous Diving and Steering of Unmanned Underwater Vehicles," IEEE Journal of Oceanic Engineering, vol. 18, no. 3, pp. 327-339, 1993.

[Hibbeler92]   Hibbeler, R.C., Engineering Mechanics, Macmillian Publishing Co., 1992.

[Hill70]   Hill, P.G. and Peterson, C.R., Mechanics and Thermodynamics of Propulsion, Addison Wesley Publishing Co., 1970.

[Hoerner65]   Hoerner, S.F., Fluid Dynamic Drag: Practical Information on Aerodynamic and Hydrodynamic Resistance, American Institute of Aeronautics and Astronautics, 1965.

[Hollerback87] Hollerbach, J.M. and K.C. Suh, "Redundancy Resolution of Manipulator Through Torque Optimization", IEEE Journal of Robotics and Automation, vol RA-3, No.4, pp. 308-316, 1987.

[Holman89]   Holman, J.P. and W.J. Gajda, Jr., Experimental Methods for Engineers, New York, McGraw-Hill Book Company, 1989.

[Howard86]   Howard, G.. Automobile Aerodynamics: Theory and Practice for Road and Track, Motorbooks International, 1986.

[Hsu94]   Hsu, L., R. Costa, and F. Lizarralde, "Underwater Vehicle Dynamic Positioning Based on a Passive Arm Measurement System", International Advanced Robotics Programme, pp. 23-32, 1994.

[Hudson99]   Hudson, J. and Luecke J., Basic Commincations Electronics, Master Publsihing, Inc., 1999.

[Hueber95]   Huebner, K. H., E. A., Thornton, and T. G., Byrom, "The Finite Element Method for Engineers," New York: John Wiley & Sons, Inc., 1995.

[Hughes94]   Hughes, A., Electric Motors and Drives - Fundamentals, Types and Applications, BH Newnes, 1994.

[Hull83]   Hull, D., "Axial Crusing of Fibre Reinforced Composite Tubes," Structural Crashworthiness, Eds. N. Jones and T. Wierzbicki, Butterworth., pp. 118-135, 1983.

[Hyer88]   Hyer, M. W., "Respond of Thick Laminate Cylinders to External Hydrostatic Pressure," Journal of Reinforced Plastics and Composites, vol. 7, pp. 321-340, 1988.

[ICI Thermoplastic Composite92] ICI Thermoplastic Composite, "Thermoplastic Composite Handbook," 1992.

[Incropera85] Incropera, F.P. and DeWitt, D.P., Introduction to Heat Transfer, John Wiley and Sons, 1985.

[Ishii94]   Ishii, K., T. Fujii, and T. Ura, "A Quick Adaptation Method in Neural Network Based Control System for AUVs," Proceedings of the Symposium of Autonomous Underwater Vehicle Technology, pp.269-274, 1994.

[Jones92]   Jones, D. A., "Principle and Prevention of Corrosion," New York: Macmillian Publishing Company, 1992.

[Kajita97]   Kajita, H. and K. Kosuge, "Force Control of Robot Floating on the Water Utilizing Vehicle Restoring Force," Proceedings of the 1997 IEEE/RSJ International Conference on Intelligent Robot and Systems, vol.1, pp. 162-167, 1997.

[Kato93]   Kato, N., Y. Ito, K. Asakawa, and Y. Shirasaki, "Guidance and Control of Autonomous Underwater Vehicle AQUA Explorer 1000 for Inspection of Underwater Cables", Proc. 8th Int. Symposium on Unmanned, Untethered Submersible Technology, Sept. 1993.

[Kawaguchi96] Kawaguchi, K., C. Ikehara, S.K. Choi, M. Fujita, and J. Yuh, "Design of an Autonomous Underwater Robot: ODIN II," World Automation Congress, Montpellier, France, May 1996.

[Kernighan78] Kernighan, B.W. and D.M. Ritchie, The C Programming Language, Englewood Cliffs, NJ, Prentice-Hall, Inc., 1978.

[Klafter83] Klafter, R. D., Robotic Engineering: an Integrated Approach, Prentice Hall, 1989.

[Klein83] Klein, C.A. and C.S. Huang, "Review of Pseudoinverse Control for Use with Kinematically Redundant Manipulators," IEEE Trans. on System, Man, and Cybernetics, vol. SMC-13, pp. 245-250, 1983.

[Kocak99] Kocak D and Lobo N and Widder E, "Computer Vision Techniques for Quantifying, Tracking, and Identifying Bioluminescent Plankton", IEEE Journal of Oceanic Engineering, vol. 24, no 1, page 81-95 (1999)

[Kochin65] Kochin, N.E., I.A. Kibel, and N.V. Rose, Theoretical Hydrodynamics, John Wiley & Sons, 1965.

[Krar67] Krar, S.F., and Amand, J.E., Machine Shop Training, McGraw-Hill Co., 1967.

[Kuroda95] Kuroda, Y., K. Aramaki, T. Fujii & T. Ura, "A Hybrid Environment for the Development of Underwater Mechatronic Systems," Proceedings of the 1995 IEEE 21st International Conference on Industrial Electronics, Control, and Instrumentation, Nov. 1995.

[Lamb45] Lamb, H., Hydrodynamics, Dover, 1945.

[Lander87] Lander, C.W., Power Electronics, McGraw-Hill, 1987.

[Lane99] Lane D and Davies B and Robinson G and O'Brien D and Sneddon J and Seaton E and Elfstrom Anders, "The AMADEUS Dextrous Subsea Hand: Design, Modeling, and Sensor Processing", IEEE Journal of Oceanic Engineering, vol. 24, no 1, page 96-111 (1999)

[Lawry90] Lawry, M.H., I-DEAS Student Guide, Structural Dynamics Research Corp., 1990.

[Leon95] Leon, G. F. and J. C. Hall, "Case Study-Design and Testing of the Brunswick Graphite Epoxy Composite Ring-Stiffened Thermo set Cylinder," Journal of Thermoplastic Composite Materials, vol. 8., 1995.

[Lewis84] Lewis, D.J., J.M. Lipscomb, and P.G. Thompson, "The simulation of Remotely Operated Underwater Vehicle", Proceeding of ROV 1984, pp. 245-252, 1984.

[Lewis89] Lewis, E.V., Principles of Naval Architecture, Jersey City, NJ, Society of Naval Architects and Marine Engineers, 1988-1989.

[Liegeois77] Liegeois, A.,   "Automatic Supervisory Control of the Configuration and Behavior of Multibody Mechanisms," IEEE Trans. on Systems, Man, and Cybernetics, vol. SMC-7, No.2, pp.868-871, 1977.

[Lines97] Lines, D., Building Power Supplies - Useful Designs for Hobbyists and Technicians, Jerry Leucke Master Publishing Inc., 1997.

[LS-DYNA99] LS-DYNA User's Manual, Livermore Software Technology Corporation, Livermore, CA, 1999.

[Luanglat97] Luanglat, C. S., and M. N Ghasemi Nejhad., "A Crash Simulation Study of Composite Materials and Structures for Electric and Hybrid Vehicles," 14th International Electric Vehicle Symposium, Proceedings, pp. 14-17, 1997.

[Lundgren99} Lundgren, J., and P. Gudmundson, " Moisture Absorption in Glass-Fiber/Epoxy Laminates with Transverse Matrix Cracks," Composites Science and Technology, vol. 59, no. 13, pp. 1983-1991, 1999.

[Mahesh91]   Mahesh, H., J. Yuh, and R. Lakshmi, "A Coordinated Control of an Underwater Vehicle and Robot Manipulator", Journal of Robotic Systems, Vol.8, No.3, pp.339-370, 1991.

[Mallick93]   Mallick, P. K., "Fiber-reinforced Composites: Materials, Manufacturing, and Design," New York: Marcel Dekker, Inc., 1993.

[Marco96]   Marco, D.B., Autonomous Control of Underwater Vehicles and Local Area Maneuvering, Ph.D. Dissertation, Naval Postgraduate School, 1996.

[Martini84]   Martini, L.J., Practical Seal Design, Marcel Dekker, Inc., 1984.

[Mattsson89] Mattsson, E., Basic Corrosion Technology for Scientists and Engineers, Ellis Horwood Ltd., 1989.

[McLain96]   McLain, T.W., S.M. Rock, and M.J. Lee, "Experiments in the Coordinated Control of an Underwater Arm/Vehicle System", Autonomous Robots 3, pp. 213-232, Kluwer Academic Publisher, Netherlands, 1996.

[McMillan95] McMillan, D.O., and R. McGhee, "Efficient Dynamic Simulation of an Underwater Vehicle with a Robotic Manipulator," IEEE Trans. on Systems, Man, and Cybernetics, Vol.25, No.8, pp.1194-1206, August, 1995.

[Microsoft88a] Microsoft QuickBASIC - Learning to Use Microsoft QuickBASIC, Microsoft Corp., 1988.

[Microsoft88b] Microsoft QuickC - Learning to Use Microsoft QuickC, Microsoft Corp., 1988.

[Milne-Thomson68] Milne-Thomson, L., Theoretical Hydrodynamics, Macmillan, 1968.

[Mims98]   Mims, F., Getting Started in Electronics, Radioshack Co., 1998.

[Mullen99]   Mullen L and Contarino M and Laux A and Concannon B and Davis J and Strand M and Coles B, "Moduladet Laser Line Scanner for Enhanced Underwater Imaging", Airborne and In-water Underwater Imaging, Gary D. Gilbert, Editor, SPIE vol. 3761, page 2-9 (1999).

[Nakamura85] Nakamura, Y., and H. Hanafusa, "Task Priority based Redundancy Control of Robot Manipulators", Robotics Research: The Second International Symposium, Cambridge, MA: MIT Press, pp.155-162, 1985.

[Needler85]   Needler, M.A. and Baker Don E., Digital and Analog Controls, Reston Pub. Co., 1985.

[Negahdaripour90] Negahdaripour S and Yu C. H. and Shokrollahi A, "Recovering Shape and Motion From Undersea Images", IEEE Journal of Oceanic Engineering, vol 15, no 3, page 189-198 (1990)

[Nejhad91a]   Ghasemi Nejhad, M. N., R. D. Cope, and S. I. Guceri, "Thermal Analysis of In-Situ Thermoplastic-Matrix Composite Filament Winding," ASME Journal of Heat Transfer, vol. 113, no. 2, pp. 304-313, 1991.

[Nejhad91b]   Ghasemi Nejhad, M. N., R. D. Cope, and S. I. Guceri, "Thermal Analysis of In-Situ Thermoplastic-Matrix Composite Tape Laying," Journal of Thermoplastic Composite Materials, vol. 4, no. 1, pp. 29-45, 1991.

[Nejhad92a]   Ghasemi Nejhad, M. N., J. W., Jr., Gillespie, and R. D., Cope, "Prediction of Process-Induced Stresses for In-situ Thermoplastic Filament Winding of Cylinder," Proceedings of Third International Conference CADCOMP, Computer Aided Design in Composite Material Technology, pp. 225-253, 1992.

[Nejhad92b]   Ghasemi Nejhad, M. N., J. W., Jr., Gillespie, and R. D., Cope, "Processing Stresses for In-situ Thermoplastic Filament Winding Using the Divergence Method," Proceedings of ASME Winter Annual Meeting 1992, Heat Transfer Effects in Materials Processing, Guceri, S. I., and Alam M. K., Eds., HTD-vol. 233, pp. 33-43, 1992.

[Nejhad93]   Ghasemi Nejhad, M. N., "Issues Related to Processability during the Manufacture of Thermoplastic Composite Using On-line Consolidation Technique," Journal of Thermoplastic Composite Materials, vol. 6, pp. 130-145, 1993.

[Nejhad94]   Ghasemi Nejhad, M. N., J. W., Jr., Gillespie, and R. D., Cope, "Effects of Processing Parameter on Material Responses during In-situ Filament Winding of Thermoplastic Composites," International Journal of Materials and Product Technology, Concurrent Engineering of Advanced Materials-Integration of Mechanics and Manufacturing, vol. 9, no. 1/2/3, pp. 183-214, 1994.

[Nejhad97]   Ghasemi Nejhad, M. N., "Thermal Analysis for Thermoplastic Composite Tow/Tape Preheating and Pultrusion," Journal of Thermoplastic Composite Materials, vol. 10, no. 4, pp. 504-523, 1997.

[Ng00a]   Ng, R., A., Yousefpour, M., Uyema, and M. N., Ghasemi Nejhad, "Design, Analysis, Manufacture, and Test of Shallow Water Pressure Vessels using E-Glass/Epoxy Woven Composite Material for a Semi-Autonomous Underwater Vehicle, submitted to the Journal of Composite Materials, in review, 2000.

[Ng00b]   Ng, R., M., Uyema, A., Yousefpour, M. N., Ghasemi Nejhad, B., Flegal, and E., Sung, "Manufacturing and Testing of Shallow Water Composite Pressure Vessels for Semi-Autonomous Underwater Vehicle," World Automation Congress 2000 (WAC 2000), in press, June 2000.

[Nie98]   Nie, J., J. Yuh, E. Kardash, and T.I. Fossen, "On-Board Sensor-Based Adaptive Control of Small UUVs in Very Shallow Water", IFAC Symposium on Control Applications for Marine Systems, 1998.

[Nie99]   Nie, J., J. Yuh, E. Kardash, and T.I. Fossen, "On-Board Sensor-Based Adaptive Control of Small UUVs in Very Shallow Water", International Journal of Adaptive Control and Signal Processing, vol. 13, 1999.

[Nygards98]   Nygards J and Wernersson A, "On Covariances for fusing Laser Ranger and Vison with Sensors Onboard a Moving Robot", IEEE/RSJ Int. Conference on Intelligent Robots and Systems, page 1053-1059 (1998)

[Ogata87]   Ogata, K., Discrete-time Control Systems, Prentice-Hall, New Jersey, 1987.

[Omura95]   Omura, G., Mastering AutoCAD 13 for Windows95, Windows3.1, and WindowsNT, Sybex, 1995.

[Parrish73]   Parrish, A., Mechanical Engineer's Reference Book, Butterworths, 1973.

[Pascol93]   Pascoal, A., M. J. Rendas, V. Barroso, C. Silvestre, P. Oliveria and I. Lourtie, "Simulation Study of an Integrated Guidance System for an Autonomous Underwater Vehicle", Acoustic Signal Processing for Ocean Exploration (Eds. J.M.F. Moura and I.M.G. Lourtie), pp. 587-592, 1993.

[Pickering97] Pickering, E. R., "Welding Aluminum," Journal of Advance Materials & Processing, pp. 29-30, 1997.

[Porter67]   Porter, H.W., Machine Shop Operations and Setups, American Technical Society, 1967.

[Pugh70]   Pugh, H., Mechanical Behavior of Materials Under Pressure, Elsevier Publishing Co., 1970.

[Raibert81]   Raibert, M.H. and J.J. Craig, "Hybrid Position/Force Control of Manipulators," Transactions of the ASME Journal of Dynamic Systems, Measurement, and Control, vol. 12, pp. 126-133, 1981.

[Reynolds89]   Product and Data Catalog - Reynolds Aluminum Supply Company, Reynolds Aluminum Supply Company, 1989.

[ROV91]   Intervention/ROV'91 Conference & Exposition, Hollywood, Florida, Sponsored by the ROV Committee and the South Florida Section of the Marine Technology Society, 1991.

[Sagatun92]   Sagatun, S.I. Modeling and Control of Underwater Vehicles: Lagrangian Approach, Dr. Ing Thesis, Norwegian Institute of Technology, 1992.

[Sayers99]   Sayers, C., Remote Control Robotics, Springer, 1999.

[Scheck84]   Scheck, L.A.. and Edmondson, G.C., Practical Welding, Glencoe Publishing Co., 1984.

[Schlichting79] Schlichting, H., Boundry-Layer Theory, McGraw-Hill, Inc., 1979.

[Schwartz84]   Schwartz, M.M., Composite Materials Handbook, McGraw-Hill, 1984.

[Schweitzer83] Schweitzer, P.A., Corrosion and Corrosion Protection Handbook, M. Dekker, 1983.

[Serway89]   Serway, R.A. and Faughn, J.S., College Physics, Saunders College Publishing, 1989.

[Shahinpour87] Shahinpoor, M., A Robot Engineering Textbook, New York, Harper & Row Publishers, 1987.

[Shames89]   Shames, I.H, Introduction to Solid Mechanics, Prentice-Hall, Inc., 1989.

[Shen81]   Shen, C., and G. S. Springer, "Environmental Effects in the Elastic Moduli of Composite Materials," Environmental Effects on Composite Material, Ed. G. S. Springer, Westport: Technomic Publishing Company, Inc., 1981.

[Shigley89]   Shigley, J.E. and Mischke, C.R., Mechanical Engineering Design, McGraw-Hill, Inc., 1989.

[Smith90]   Smith, C.S., Design of Marine Structures In Composite Materials, Elsevier Applied Science, 1990.

[Smith96]   Smith, J. and K. Sugihara, "GA toolkit on the Web", Proc. of the First Online Workshop on Soft Computing (WSC1), pp.93-98, 1996.

[Sonmez97]   Sonmez, F.O. and H.T. Hahn, "Analysis of the On-line Consolidation Process in the Thermoplastic Composite Tape Placement", Journal of Thermoplastic Composite Materials, v. 10, pp. 543-572, 1997.

[Sprong89]   Sprong, M.W. and M. Vidyasagar, Robot Dynamics and Control, New York, John Wiley & Sons, 1989.

[SubTech85]   Submersible Technology: Proceedings of an International Conference (Subtech '85), Aberdeen, UK, pp. 29-31, 1985.

[Sugihara97]   Sugihara, K. and Yuh, J., "GA-based motion planning for underwater robotic vehicle," Proc. 10th Int'l Symp. on Unmanned Untethered Submersible Technology (UUST-10), Durham, NH, 1997, pp.406-415.

[Sugihara98a]   Sugihara, K., "GA-based on-line path planning for SAUVIM," Proc. 11th Int'l Conf. on Industrial and Engineering Applications of Artificial Intelligence and Expert Systems (IEA-98-AIE), Castellon, Spain, 1998, pp.329-338.

[Sugihara98b]   Sugihara, K. and J. Smith, Genetic Algorithms for Adaptive Planning of Path and Trajectory of a Mobile Robot in 2D Terrain, IEICE Trans. on Information and Systems, to appear 1998   .

[Sugihara98c]   Sugihara, K. and J. Yuh, "GA-based Motion Planning for Underwater Robotic Vehicles", Proc. 10th Int'l Symp. On Unmanned Untethered Submersible Technology (UUST-10), pp.406-415, 1998.

[Sugihara99]   Sugihara, K. and Smith, J., "Genetic algorithms for adaptive planning of path and trajectory of a mobile robot in 2D terrain," IEICE Trans. Information and Systems, Vol. E82-D, No. 1, pp.309-317, January 1999.

[Svensoon99]   Svensson S. and Lexander J. and Ericson B, "OBSERVATION AND INSPECTION IN SWEDISH WATERS", Underwater Imaging, Douglas J. Holloway, Editor, SPIE vol. 980, page 75-81 (1988).

[Swartz91]   Swartz B and Cummings J, "Laser range-gated underwater imaging including polarization discrimination", Underwater Imaging, Photography, and Visibility, Richard W. Spinard, SPIE vol. 1537, page 42-56 (1991).

[Tai99]   Tsai, L.W., Robot Analysis: The Mechanics of Parallel and Serial Manipulators, John Wiley and Sons, 1999.

[Takashi91]   Takashi, K., Electric Motors and their Controls: An Introduction, Oxford University Press, 1991.

[Tarn96]   Tarn, T.J., G.A., Shoultsand, and S.P. Yang, "A Dynamic Model of an Underwater Vehicle with a Robotic Manipulator using Kane's Method", Autonomous Robots 3, pp. 269-283, Kluwer Academic Publisher, Netherlands, 1996.

[TI92]   Linear Circuits Operational Amplifiers Data Book, Texas Instruments, 1992.

[Tsai99]   Tsai, L.W., Robot Analysis - The Mechanics of Parallel and Serial Manipulators, John Wiley and Sons, Inc. 1999.

[Tupper96]   Tupper, E.C., Introduction to Naval Architecture, Oxford, Butterworth-Heinemann Publishing, 1996.

[Ullman92]   Ullman, D.G., The Mechanical Design Process, McGraw-Hill Inc., 1992.

[Unimate81]   Unimate PUMA Robot: Volume 1 – Technical Manual 398H1, Unimation Inc., Condec Company, Danbury CT, 1981.

[Unimate84]   Unimate PUMA Mark II Robot: 500 Series, Volume 1 – Equipment Manual, Unimation, Westinghouse Corporation, Danbury CT, 1984.

[Unimate86]   Unimate Industrial Robot: Programming Manual, User's Guide to VAL II Version 2.0 (398AG1), Unimation, Westinghouse Corporation, Danbury CT, 1986.

[Unimate97]   Unimate – Supplement to the User's Guide to VAL II: VAL II-IVM PC Supervisor Interface (397W1), Unimation, Westinghouse Corporation, Danbury CT, 1987.

[Valentine98]   Valentine, R., Motor Control Electronics Handbook, McGraw-Hill, 1998.

[Vieville97]   Vieville, T., A Few Steps Towards Active 3D Vision, Springer-Verlag, 1997.

[Vinson87]   Vinson, J.R., and R.L. Sierakowski, The Behavior of Structures Composed of Composite Materials, Netherlands, Kluwer Academic Publishers, 1987.

[Weast81]   Weast, R.C. and Astle, M.J., CRC Handbook of Chemistry and Physics - 61st Edition, CRC Press, Inc. 1981.

[Wedermann89]   Werdermann, C., K. Friedrich, M. Cirino, and R. B. Pipes, "Design and Fabrication an On-Line Consolidation Facility for Thermoplastic Composites," Journal of Thermoplastic Composite Materials, vol. 2, pp. 293-306, 1989.

[Wells91]   Wells W, "Indirect illumination to reduce veiling luminance in seawater", Underwater Imaging, Photography, and Visibility, Richard W. Spinard, SPIE vol. 1537, page 2 (1991).

[Werdermann89]   Werdermann, C., K. Friedrich, M. Cirino, and R.B. Pipes, "Design and Fabrication an On-line Consolidation Facility for Thermoplastic Composites", Journal of Thermoplastic Composite Materials, vol. 2, pp. 293-306, 1989.

[Whitney87]   Whitney, D.E., "Historical Perspective and State of the Art in Robot Force Control," International Journal of Robotic Research, vol. 6, no.1, pp. 3-14, 1987.

[Wilson92]   Wilson, P.A., International Conference on Manoeuvring and Control of Marine Craft, Proceedings of the Second International Conference, 1992.

[Wit98]   Wit, C.C.D., E.O. Diaz, and M. Perrier, "Robust Nonlinear Control of an Underwater Vehicle/ Manipulator System with Composite Dynamics", Proc. IEEE Conf. on Robotics and Automation, pp.452-457, 1998.

[Yang98a]   Yang, K.C., J. Yuh, and S.K. Choi, "Experimental Study of Fault-tolerant System Design for Underwater Robots", Proc. IEEE Conf. on Robotics and Automation, pp. 1051-1056, 1998a.

[Yang98b]   Yang, K.C., J. Yuh, and S.K. Choi, "Experimental Study of Fault-tolerant System Design for Underwater Robots", Journal of System Sciences, 1998b.

[Yousefpour00a] Yousefpour, A., and M. N. Ghasemi Nejhad, "Effects of Geometric Optimization of Tapered End-caps on Thick Thermoplastic Composite Pressure Vessels for Deep Ocean Applications," Journal of Thermoplastic Composite Materials, submitted for publication, 2000.

[Yousefpour00b] Yousefpour, A., and M. N. Ghasemi Nejhad, "Experimental and Computational Study of APC-2/AS4 Thermoplastic Composite C-Rings," Journal of Thermoplastic Composite Materials, in press, 2000b.

[Yousefpour00c] Yousefpour, A., R., Ng, M., Uyema, M. N., and Ghasemi Nejhad, "Design and Finite Element Analysis of Shallow Water Composite Pressure Vessels for Semi-Autonomous Underwater Vehicle," World Automation Congress 2000 (WAC 2000), in press, June 2000c.

[Yousefpour99] Yousefpour, A., and M. N. Ghasemi Nejhad, "Testing and Finite Element Modeling of APC-2/AS4 Thermoplastic Composite C-rings," 31st International SAMPE Technical Conference: Advanced Materials & Processes Preparing for the New Millennium, vol. 31, pp. 643-654, Chicago, IL, 1999.

[Yuh92]   Yuh, J., V. Adivi & S.K. Choi, "Development of a 3D Graphic Test Platform for Underwater Robotic Vehicles," Proceedings of the 2nd International Offshore and Polar Engineering Conference, Jun. 1992.

[Yuh94a]   Yuh, J., "Learning Control for Underwater Robotic Vehicles", IEEE Control System Magazine, vol.15, No.2, pp.39-46, 1994.

[Yuh94b]   Yuh, J., Underwater Robotic Vehicles: Design and Control, Workshop on Future Research Directions in Underwater Robotics, TSI Press, p. 361, 1994.

[Yuh95]   Yuh, J., Underwater Robotic Vehicles: Design and Control, TSI Press, 1995.

[Yuh96]   Yuh, J., "An Adaptive and Learning Control System for Underwater Robots", 13th World Congress International Federation of Automatic Control, A, pp. 145-150, 1996.

[Yuh98a]   Yuh, J., S.K. Choi, C. Ikehara, G.H. Kim, G. McMurtry, M. Ghasemi Nejhad, N. Sarkar, and K. Sugihara, "Design of a Semi-Autonomous Underwater Vehicle for Intervention Missions (SAUVIM)," Proceeding of the Underwater Technology '98, 1998.

[Yuh98b]   Yuh, J., J. Nie, and W.C. Lee, "Adaptive Control of Robot Manipulators Using Bound Estimation", IEEE International Conference on Intelligent Robots and Systems, 1998.

[Yuh99]   Yuh, J. and J. Nie, "Experimental Study on Adaptive Control of Underwater Robots," Proceedings of the IEEE International Conference of Robotics and Automation, Detroit, MI, May 1999.

[Zege91]   Zege E and Ivanov A and Katsev I, "Image Transfer Through a Scattering Medium" Springer-Verlag, Berlin, page 277-305 (1991)

[Zuech88]   Zuech, N., Applying Machine Vision, John Wiley and Sons, Inc., 1988.

Phase I: Final Report Appendix

Appendix 1: SAUVIM Velocity Analysis

Appendix 2: SAUVIM Test Plan (Phase I – Shallow Water)

Appendix 1: SAUVIM Velocity Analysis

Motivation:

To get an initial, estimation analysis of the vehicle's performance, these series of simplified calculations were performed. These are **not** intended to be a full-featured dynamic analysis; they are merely reasonable and precise estimates of the following: 1) the acceleration responsiveness of the SAUVIM to the planned thruster units - a set of eight Technodyne Model 1020 brushless motor thrusters; 2) the ultimate cruising speed of the vehicle under neutrally buoyant thrust conditions as well as weighted descent; and 3) an estimate of the rotational (yaw-) responsiveness of the vehicle.

Introduction:

In all cases, we use SAUVIM's response in terms of lineal and angular distance covered versus time elapsed since application of thrust at 100% of the rating supplied on the manufacturer's data sheet for the given thruster set. The other information is detailed in the velocity (or angular speed) versus the time elapsed since the application of the full rated thrust. The initial state of the vehicle in all cases is a full stop position. The SAUVIM vehicle faired is of the following shape:
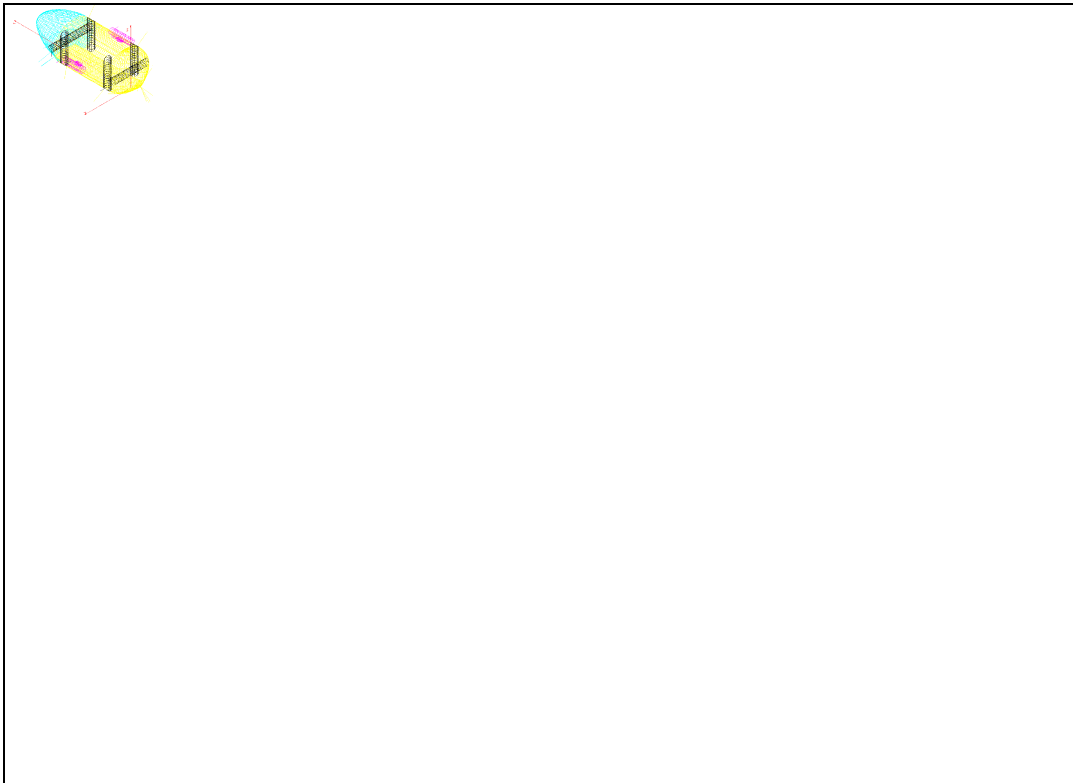

Figure 1: Isometric View of the SAUVIM Fairing with Thruster Tubes

For purposes of this analysis, the longitudinal direction is along the x-axis, the lateral direction is along the y-, and vertical direction in the z-. Four thrusters (the black tubes parallel to the z-axis) point vertical with the more powerful thrust vector pointed down, two point fore and aft (the pink tubes on pylons), the aft direction is the more powerful thrust vector. The two lateral thrusters (black

tubes parallel to the y-axis) face with the more powerful vector pointing along +y, this choice is arbitrary and is made to ensure a balanced pair of thrust in either lateral direction.

Method:

For velocity, a force balance equation was employed: Force$_{thrusters}$ = Drag$_{vehicle}$ + (Mass$_{vehicle}$)

$$T_{thrusters-set} = \frac{1}{2}\rho C_R A \dot{\theta}^2 + I \ddot{\theta}$$

where the terms, are F is the maximum thruster output force in Newton (kg$_f$ which is equivalent to 10N), each Technodyne model 1020 outputs 21.4 kg$_f$ (214N or 47 lb$_f$) in the forward direction and 14.5 kg$_f$ each (145N or 32 lb$_f$) in the reverse direction. These values were obtained right off of the Technodyne data sheets. Value should be within ±10% of actual value.

ρ, is density of seawater in kg/m^3 (=1024 kg/m^3). This was obtained from an introductory Oceanography text. Value should be within ±2-3% of actual value.

C$_D$, is Drag coefficient for SAUVIM in dimensionless form. For the drag in the forward longitudinal direction, 0.35 was used for the faired vehicle and 0.85 was used for the unfaired vehicle. The former number is a composite of the CFD results from CHAM (0.40), HSI (0.25), and the figure cited for a Ford Taurus (0.32). Value may be within ±30% of actual value, these estimates are very preliminary until a combination of thorough CFD study and/or model testing is carried out.

A, is Cross-sectional area from frontal/rearward vantage point in m^2 (= 3.74 m^2 frontal, = 10.19 m^2 lateral, =13.15 m^2 vertical) These values are derived directly from the ACADr13 model of the SAUVIM fairing. Value should be within ±2% of actual value.

m, is mass of the SAUVIM vehicle includes dry mass as well as entrained water mass within the fairing and the vehicle components, in kg (= 17,800 kg/39,000 lbs for faired SAUVIM, 8,160 kg/18,000 lbs for unfaired SAUVIM). The faired vehicle mass estimate is taken directly from the

v, is velocity of vehicle in m/sec (reported as knots though, initially set to 0 m/sec).

$\ddot{x}$, is acceleration at a given time in m/sec^2 (initially set to 0 m/sec^2).

Solution for of the differential equation (x-dot (v) and x-dot-dot) proceeds by integration along the time steps using Euler's method: the initial acceleration and velocity were '0', subsequent steps reference the previous time steps which are spaced at one second intervals. The rest of the terms were treated as constants.

For yaw response the form of the equation is Couple$_{thruster}$= Drag$_{vehicle-rot.}$ + (I$_{vehicle}$)

$$F_{thrusters} = \frac{1}{2}\rho C_D A v^2 + m\ddot{x}$$

The variables in here are the rotational equivalents of the variables in equation (1), detailed notes on their values will be discussed on the case analysis.

Cases: The following cases have been explored:

   Case I - Forward/Rearward (longitudinal translation) with fairing
   Case II - Forward/Rearward (longitudinal translation) without fairing
   Case III - Lateral Starboard/Port (lateral translation) with fairing.
   Case IV - Lateral Starboard/Port (lateral translation) without fairing.
   Case V - Vertical up/Vertical down (vertical translation) with fairing
   Case VI - Vertical up/Vertical down (lateral translation) without fairing
   Case VII - Yaw response with fairing
   Case VIII - Yaw response without fairing

Assumptions and results pertinent to each will be detailed case-by-case bases. Many items that are in a complete rigorous analysis have been discounted among these are: duct water-mass inertia, vehicle damping coefficient, duct drag losses, C_D variations with velocity change, off-centric application of forces from the center of inertial and drag resistances and resultant thrust reductions off of the maximum to accommodate balancing, reduction in thrust from the Model 1020 as SAUVIM vehicle gains speed and propulsive effective thrust drops off (propeller advance ratio effects).

The following table 1 summarizes the variables used for each case.

Table 1: Different Case Studies for Thruster Tests

Case	Thruster Force	C_D (or C_R)	A	m (or I_{zz})
Units	N		m^2	kg (kg m^2)
I - Forward with fairing	419.8	0.35	3.74	17800
I - Astern with fairing	284.5	0.35	3.74	17800
II - Forward without fairing	419.8	0.85	3.74	8160
II - Astern without fairing	284.5	0.85	3.74	8160
III - Lateral Starboard with fairing	419.8	0.75	10.19	17800
III - Lateral Port with fairing	284.5	0.75	10.19	17800
IV - Lateral Starboard without fairing	419.8	0.80	10.19	8160
IV - Lateral Port without fairing	284.5	0.80	10.19	8160
V - Vertical up with fairing	839.6	1.2	13.15	17800
V - Vertical down with fairing	569.0	1.2	13.15	17800
V - Vertical up without fairing	839.6	1.4	10.00	8160
V - Vertical down without fairing	569.0	1.4	10.00	8160
VII - Yaw with fairing	?	?	10.19	17800
VIII - Yaw without fairing	?	?	10.19	8160
IX - Unpowered 30° descent cruise	N/A	N/A	N/A	N/A

Assumptions/Results: Case-by-case breakdown will proceed.

Case I & II - This is the baseline SAUVIM case where the neutrally buoyant vehicle is accelerated straight forward. It is assumed here, as for all the subsequent cases in this analysis, that the line of action of the thruster vectors is lined up sufficiently close to the center of inertial mass as well as the singular center of drag force action to preclude having to reduce thrust in any of the set to counter the resulting rotational drifts that would occur (e.g. all forces are centric in nature). The two longitudinal thrusters are rated at 47 lb$_f$/each (214 N) in the forward direction and 32 lb$_f$/each (145 N) in the reverse direction.

The area, 3.74m^2, was obtained from the ACADR13 solid model. This is the profile cross-sectional area seen from along the vehicle's X-axis as is standard practice in drag calculations using dimensionless drag data.

For estimating the vehicle mass two methods were used; for the unfaired vehicle the mass was estimated from the itemized tally spreadsheet (Sensit4.wb3) of all the major components with some adjustment made for water that would be entrained within the major cavities of the vehicle (the wiring space above the batteries, around the pressure vessels within the main component box - for details see Figure MED-10). The table below summarizes the approximate void space within each of the major cavity spaces of the vehicle. The foam space cavity is not included as it is assumed to completely occupy SAUVIM's dry mass. The venting value is an estimated guess at the amount of water in a given cavity. It also estimates the water spillage throughout the vehicle components, and therefore, will not contribute to the inertial mass of the vehicle. The approximately 1640 kg figure of entrained water is added to the unfaired SAUVIM mass for the startup run calculations in table 2.

Table 2: Unfaired SAUVIM Entrained Water Mass Estimates

Volume Name	Cavity Height	Cavity Length	Cavity Breadth	Volume	% Volume Occupied	Adjusted Volume	Water in Voids (lbs)	Venting Estimate	Adjusted Mass (lbs)
	(in)	(in)	(in)	(ft^3)					
Battery	21.5	75.0	45.0	42.0	34%	27.52	1717.25	0.50	858.62
Ballast	21.5	32.0	45.0	17.9	11%	15.87	989.99	0.50	494.99
Arm	21.5	32.0	45.0	17.9	8%	16.50	1029.82	0.70	720.87
PV	23.0	165.0	45.0	98.8	17%	82.07	5121.35	0.30	1536.41
Approximate Mass of Water entrained inside Vehicle (lbs)									3610.89
Approximate Mass of Water entrained inside Vehicle (kg)									1639.34

The resulting unfaired SAUVIM effective inertial mass is around 6,900 kg. To give and idea of the relative volume ration between free space that floods and solid SAUVIM components the approximate volumes of some of the major components is given in table 3.

Table 3: Approximate Volumes of Components

Approximate Volumes of:	ft^3	m^3
12 Batteries	14.47	0.41
6 Pressure Vessels	16.76	0.47
Arms and Tray	1.41	0.042

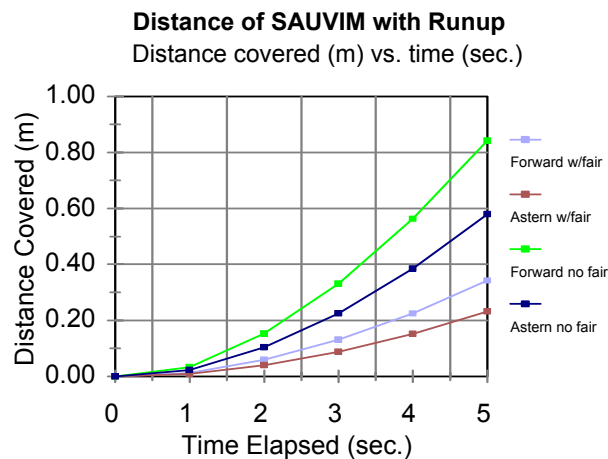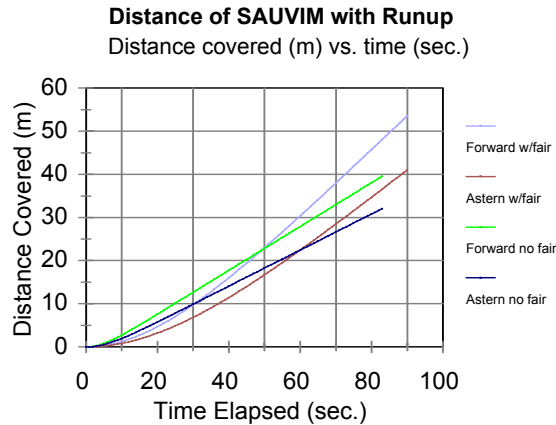|		
Ballast Tray and Ballast	2.05	0.058

For the faired vehicle the wet mass figure of 17,800 kg was arrived at simply be assuming that the SAUVIM is neutrally buoyant and determining the enclosed volume of water within the fairing shell (done in the ACADR13 model). This assumes a completely stagnant pocket of water within the fairing, which clearly not the case with the actual vehicle as the will be ports, ducts and open areas in the fairing for water to spill through. Since the worst case is to assume a completely sealed fairing, this assumption was made.

Meanwhile, a fairly conservative coefficient of drag was adopted (in the dimensionless form) as well. For forward motion a C_D of 0.35 was used. This was arrived at based on preliminary results from the Phoenics CFD code ($C_D = 0.40$), work done at Pacific Marine with CFD code ($C_D = 0.25$), and some book sources. Chosen from these book sources was the C_D of some concept cars having a very similar form to the SAUVIM fairing ($C_D = 0..35$, 0.23, pg.12-3, $C_D = 0.25$, pg. 12-9 <u>Fluid-Dynamic Drag, Practical Information on Aerodynamic Drag and Hydrodynamic Resistance</u>, Hoerner, S.F., AIAA press - 1965). These values were cited for shapes that are operating in ground effect and therefore only approximate the SAUVIM fairing in a free stream environment, hence the selection of a more conservative value for C_D. The same C_D was used for both forward and rearward motion.

The results of the analysis are summarized in these graphs, the first of which shows the SAUVIM velocity as a function of time elapsed since thruster startup, SAUVIM displacement since thruster startup and the same in a shortened time span. It can be seen with the fairing on that the ultimate forward velocity possible with the twin Technodyne 1020's will be 1.5 knots (0.79 m/sec) forward and a little over 1.2 knots at full reverse (0.65 m/sec). Full speed will be reached after 90 seconds of run up. Without the fairing, acceleration will be much better and the full speed will be reached within 20 seconds, however, high speed will drop to 1.0 knots (0.50 m/sec) and 0.8 knots (0.41 m/sec) for forward and reverse directions, respectively.

It can be seen from the third graph that pulsing the thrusters in the forward direction for the faired vehicle for 3 seconds will result in 15cm of translation, the unfaired SAUVIM will have moved 35cm.

Velocity after initialization of run
Velocity (knots) vs. time (sec.)

252

Distance of SAUVIM with Runup

Distance covered (m) vs. time (sec.)

Distance of SAUVIM with Runup

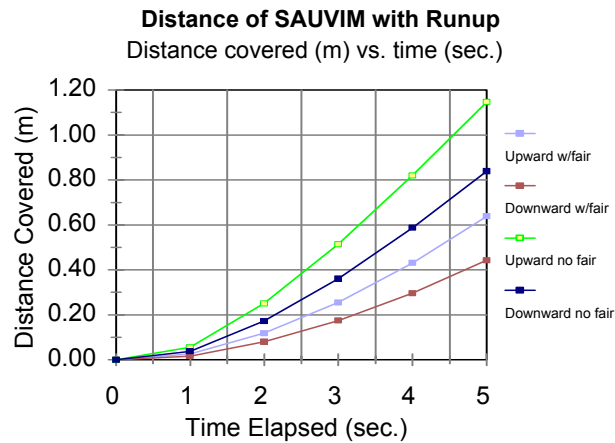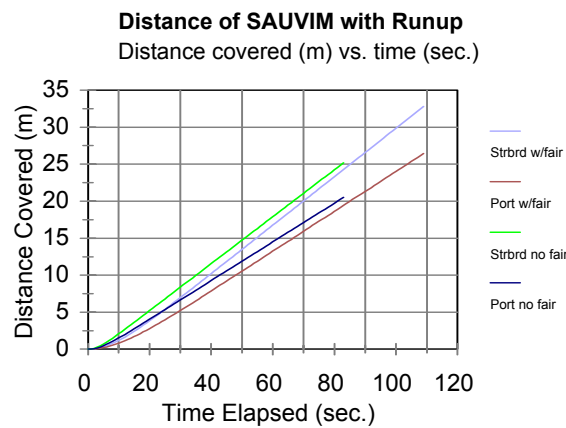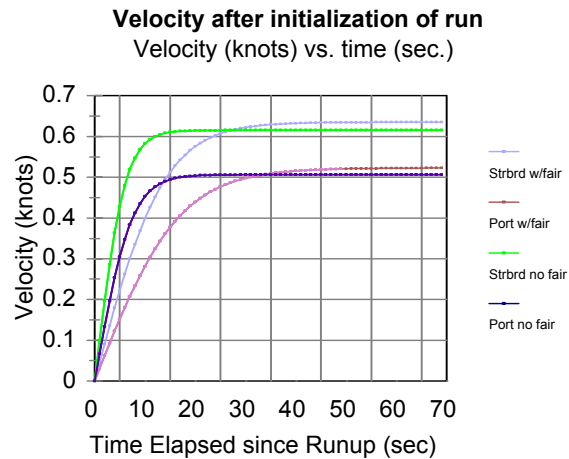Distance covered (m) vs. time (sec.)
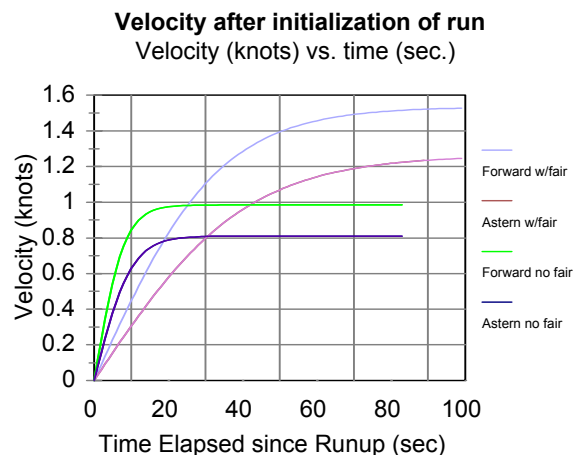
Case III & IV - The mass assumptions are the same as in cases I & II, here lateral motion is concerned. The major changes here concern, profile area, the direction of the Technodyne 1020's favored thrust direction, and C_D changes. For the C_D of both the faired and unfaired vehicle there are no variances with direction to either side as the SAUVIM is symmetric across the XZ-plane. The C_D for the faired vehicle a value of 0.75 was estimated (the data of a circular cylinder of similar aspect ratio in cross-flow with $C_D = 0.70$ was used a basis for this value, from Hoerner, S.F., AIAA press - 1965, pg. 3-16). This value was degraded to 0.80 for the unfaired vehicle to account for sharper edges on the ends of the unfaired vehicle, though the bulk cross-section remains largely unchanged. Though not accounted for in this analysis, due to the relatively complete coverage of floatation foam over the vehicles flooded spaces from this direction the entrained water mass value for the unfaired SAUVIM should probably be adjusted upward.

The more powerful thruster direction of the 1020's was chosen to be applicable for starboard motion, this was chosen arbitrarily; avoidance of any yawing during paired lateral thrusting will probably necessitate orienting the thrusters in this fashion until the symmetrical propellers are retrofitted. The profile area as seen from along the y-axis is 10.19 m². This was obtained from the ACAD R13 fairing model. The results are shown here, it can be seen that the maximum lateral speeds are around 0.63 knots (0.32 m/s) and 0.52 knots (0.26 m/s) for starboard and port directions with the fairing. Without the fairing these values become 0.61 knots (0.31 m/s) and 0.50 knots (0.26 m/s). Note from the first

253

graph that the maximum speeds are reached within 10 and 30 seconds for the unfaired and faired conditions, respectively.
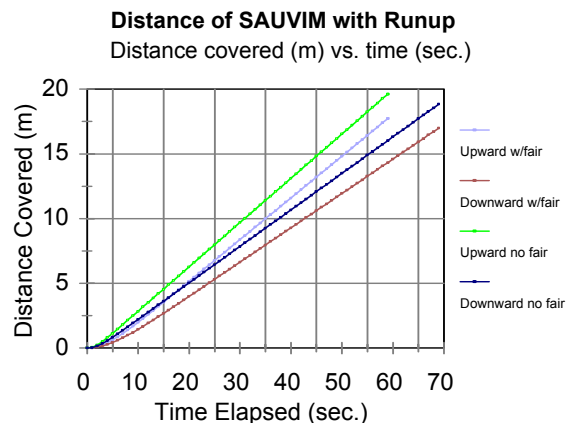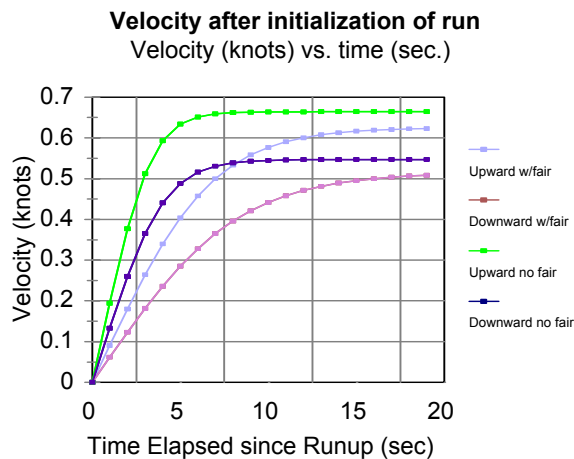
A three second pulse of full thrust will move the vehicle from about 9-28 cm depending on the fairing and favored direction of thrust.

Velocity after initialization of run

Velocity (knots) vs. time (sec.)

Distance of SAUVIM with Runup

Distance covered (m) vs. time (sec.)

Distance of SAUVIM with Runup
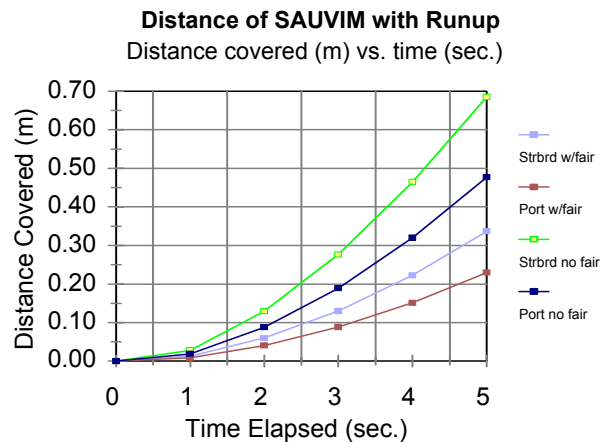
Distance covered (m) vs. time (sec.)

Case V & VI - These cases account for vertical motion. The greater power of the thrusters is due to a set of four Technodyne 1020's being selected for this direction. The favored direction of thrust in this analysis was chosen for the downward direction. This is a design issues but was chosen to fight the gravitational field should the SAUVIM be slightly heavy which due to foam compressibility is a more likely state to be in upon cruise to the bottom. So around 840 N can be applied to move vertically up and about 570 N can be applied in the downward direction. The C_D for this direction was chosen to be 1.2; this was cited for cylinders at moderate Reynolds number flows. At Reynolds flow values typical for our vehicle the C_D for cylinders actually drops to around 0.7, but this is due the migration of regions of separation back on the smooth surface of a cylinder. Since the roughly circular SAUVIM fairing form has edges that trip off flow separation in fixed locations, unlike a smooth cylinder in moderate Reynolds number flow, the higher value for C_D is chosen.

The cross-sectional area is now 13.15 m^2 , this is the profile area of the fairing as seen from the top. It is somewhat less for the unfaired vehicle as the nosecone and tail cone do add about 30% more area to the silhouetted area as opposed to the unfaired vehicle.

The results here indicate the faired vehicle can expect vertical maximum speeds on the order of 0.65 knots and 0.54 knots downward when faired and 0.62 knots and 0.51 knots when unfaired. It can be seen that a three second pulse of the thrusters at full rated load will move the vehicle from about 18-55 cm depending on the thrust direction and the presence of the fairing.

Velocity after initialization of run
Velocity (knots) vs. time (sec.)

Distance of SAUVIM with Runup
Distance covered (m) vs. time (sec.)

Distance of SAUVIM with Runup
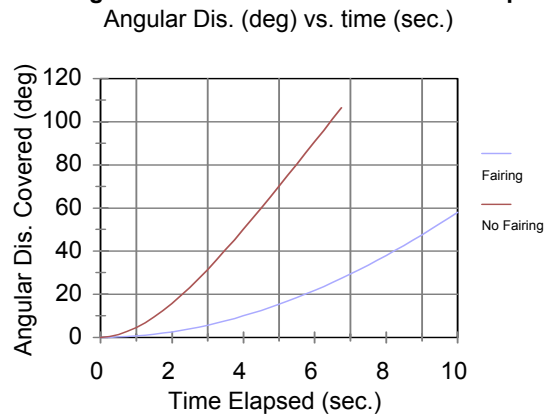Distance covered (m) vs. time (sec.)

Case VII & VIII - These cases concern yaw rotation. In this case the SAUVIM vehicle pivots about an axis parallel to the z-axis with application of thrust in opposite directions of both the longitudinal and lateral pairs of the thrusters. This has been calculated for both the faired and unfaired vehicle variants. The following assumptions run throughout the models:

- The principle rotational moment for the faired vehicle will assume the fairing volume is a uniform mass with the density of seawater. Treating the volume within the fairing model as a uniform mass and using a solid function to recover the inertial moment derived the moment value.

- $C_{D\text{-rot}}$ for the SAUVIM will be that of a rectangular parallelepiped of similar aspect ratio. The value was degraded somewhat for the unfaired vehicle owing to separation around the edges on the aft and forward ends.

- Two sets of thrusters will contribute to the couple moment, the lateral and longitudinal pairs, furthermore no wake coupling effects will be accounted for.

- The principle moment for the unfaired vehicle was found by applying the mass moment formula to the major components that are tracked on the datasheet.

- The couples coming off of the thrusters we using the minimum thrust rating at the shortest moment arm from the inertial axis. For the lateral pair of thrusters this was 14.5 kg of thrust at 60 inches from the inertial axis, for the longitudinal pair it was again 14.5 kg at 60 inches from the inertial axis.

- The inertial axis (I_{zz}) was calculated to be at vehicle coordinates for the X=85in and Y=0 in for the unfaired vehicle, the location of I_{zz} on the faired vehicle was at X=85in and Y=0in again.

- The magnitude of I_{zz} is 41,850 kg-m^2 for the faired vehicle and reduces to 6,615 kg-m^2 when the fairing is removed.

The graphs below summarize the results. As expected the faired vehicle has a slower initial response than the unfaired variant; however, the ultimate high rotational speed is not critical as the likely

maneuvers will be completed before obtaining the maximum speed. All of the angular distances are given in degrees.

Angular Distance of SAUVIM with Runup
Angular Dis. (deg) vs. time (sec.)

Velocity after initialization of run
Ang. Velocity (deg/s) vs. time (sec.)
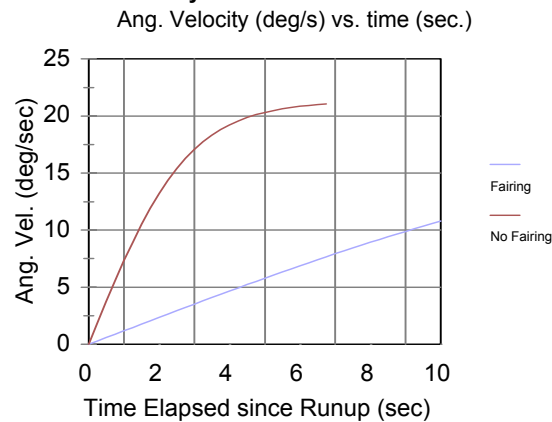
Unpowered Cruise - This case is still under investigation.

General Observations:

A free-flooded fairing incurs both advantages and disadvantages to a vehicle equipped with it, though it may be very useful for open ocean operations, it does result in a real hit on inertial response of the vehicle upon thruster startup and short term pulsing for active station-keeping. The vehicle will not be nearly as responsive to thruster inputs with it installed although cruising range and inertial damping to disturbances will be increased. For a vehicle cruising at near constant speeds or involved in station keeping for extended periods in a steady current using passive inertial damping, the fairing may yield a distinct advantage even though it effectively doubles the vehicle inertial mass from 8,200 kg to 17,800 kg.

Cruising range under full power is affected by the fairing. Consider the longitudinal thrusters only. These thrusters are powered by three lead-acid DeepSea SB-48/18 batteries, arranged in a serial bank to provide 144VDC at 18 Amp-Hours of continuous draw (2.60 kW·hr). This gives the vehicle with

two Technodyne thrusters drawing 1550 Watts continuously the following ranges: 2.70 nautical miles (5.0 km) with the fairing and 1.73 nautical miles (3.2 km) without the fairing.

Recommendations:

The Theoretical Modeling (TM) dynamics group may want to explore the following parametric changes to the SAUVIM vehicle:

Fairing size changes - Fairing size changes in the lineal distances will have a square-law change influence on the profile areas and therefore the magnitude of the drag forces. A 10% reduction in fairing size may reduce hydrodynamic drag to about 81% of the baseline case; meanwhile the inertial mass will drop to about 75% of the baseline case. Maximum cruise speed will climb about 10-12% and initial responsiveness will climb modestly, however, loss of the vehicle expansion/design flexibility that the prototype has will be suffered. The most feasible fairing size change is to redistribute some of the foam up on the top of the vehicle to down within the battery tray area and into some of the larger pockets formed between the pressure vessels. A side effect of doing this relocation would be a shorter separating distance between the centroid of the volume of all the SAUVIM components and the center of mass; this would result in a more tightly responsive vehicle to ballast trim, thruster and fin trim inputs, conversely also to arm inputs and being buffeted by currents, external influences.

Thruster Power Changes: Migrating from the Technodyne 1020 to the 2010 model would nearly quadruple the thrust from each unit (Technodyne 2010 data sheets rating 143 lb_f (650 N) forward and 80 lb_f (364 N) reverse). The Technodyne manufacturing representative has stated that these values are only about 75% of the thrust that the 2010 can actually sustain under continuous load. Raising thruster power by a factor of four will double the maximum speed as drag is a square law dependency on velocity. Note though that the cruising range under maximum cruise speed possible with 2010 units is only about 50% of that with the smaller thruster units running at their maximum rated thrust. Of course economic concerns enter here as the Model 2010 units cost around $9,500 apiece as opposed to the $5,800 that the 1020 units run.

Decent Cruise: This is not critical for shallow water variant of the SAUVIM but will become a critical portion of the mission phases as the SAUVIM proceeds into deep-water missions. The ability to glide in a controlled fashion and make course corrections to ensure arrival close to the task site with minimal, if any, thruster application will be critical from the standpoint of the small cruising range imposed by the battery bank energy limits and the minimization of time during which fixed electrical loads (e.g. computers, long-baseline sensors, etc) draw power. Hence further exploration of this mode of vehicle motion warrants conceptual consideration, if not detailed analysis, even prior to commencement of shallow water operations.

Recommended Tasks: These steps will be needed for a more accurate dynamic model the TM-dynamics group should consider the following tasks: 1) locate the center of drag action for the three principle directions, 2) locate the inertial center for both the faired and unfaired vehicles using the AutoCAD fairing model and the Quattro spreadsheet tally of the major SAUVIM component masses, 3) from the former two steps and knowing where the thrusters are located determine the thrust tuning adjustments needed to cancel non-centric effects and 4) determine and map the combined drag/inertial resistance centroid location with velocity location.

Also it will be worth determining the effects of the three planned fins on the vehicle dynamics for both powered and decent cruise. This will be of great value in sizing of the foils for the fin units to ensure the right balance between vehicle-response and vehicle-handling concerns.

Appendix 2: SAUVIM Test Plan (Phase I – Shallow Water)

Objective

- To test essential hardware and software functions and to check the integrity of the system.

In this write-up, it is assumed that the vehicle is completed for experiments. The joystick-based controller will be used in most cases. After the completion of these basic tests, a simple "dead-reckoning" control algorithm and a simple object-following control algorithm will be tested for initial closed-loop control and navigation purposes. The basic tests plans are:

Test Plan 1

Goal - Test the basic emergency handling functions.

The weight dropping functions will be tested. This test is made of two parts. In the first part, weight will be dropped as the vehicle reaches desired depth by monitoring depth sensor. (The desired depth is not determined yet, but it should be limited within 60 ft so that divers can reach to the vehicle for recovery.) The second part will simulate leakage in the pressure vessels. Timer switch can be connected to one of the leakage sensors to simulate the leakage. During the test, battery level will be monitored and logged.

Sensors: depth sensor, leakage sensor, battery gauges
Actuator: weight drop

Test Plan 2

Goal - Test if all the sensors and other hardware devices are working properly and to log acquired data for future analysis.

The sensors, which provide information of vehicle movement, will be checked to see if they provide correct values. These values will be stored in a local storage device and transmitted to the other computer for backup. Thrusters will be turned on in short intervals (for example, 30 seconds for each thruster). As the vehicle moves, the INS and electric compass data will be monitored. Thruster will be operated with open loop controller for the simplicity in early phase of development. The fins will be tested while the vehicle stops and moves.

Sensors: INS, electric Compass
Actuator: thrusters, fins

Test Plan 3

Goal - Test the sonar-based sensors.

The sonar-based sensors such as altimeters and scan sonar will be tested. The vehicle will be fixed at an arbitrary point to minimize disturbance to sensor signals. Operator can place objects in front of each altimeter and check the readings from the sensors. The distance of the objects from the vehicle and the size of the objects are not determined. The readings will be stored in a local storage and transmitted to the remote operator. Because scan sonar will not be used by the first phase, all the data

will be stored in a local storage for future analysis. The data can be analyzed with experimental algorithm or program, but the specific plan is not yet determined.

Sensors: altimeters, scan sonar
Actuator: none

Test Plan 4

<u>Goal</u> - Test the basic vehicle maneuvering function and miscellaneous functions.

The basic maneuvering function will be tested. The vehicle will move using thruster and fins based on the data from sensors. Sonar data will be monitored but will not be used in navigation until next phase starts. Only open loop control will be used. Lights will be turned on and off during navigation. The other sensors, which are not mentioned here, will be monitored and logged for future reference.

Sensors: INS, compass, depth sonar, altimeter, scan sonar, battery level.
Actuator: thrusters, fins, light switch

Publications

Sugihara, K. and Yuh, J., "GA-based motion planning for underwater robotic vehicle," Proc. 10th Int'l Symp. on Unmanned Untethered Submersible Technology (UUST-10), Durham, NH, 1997, pp.406-415.

Yuh, J, Choi, S.K., Ikehara, C., Kim, G.H., McMurtry, G., Nejhad, M., Sarkar, N., & Sugihara, K., "Design of a Semi-Autonomous Underwater Vehicle for Intervention Missions (SAUVIM)," The Proceedings of the IEEE Oceanic Engineering Society Underwater Technology '98, Tokyo, JAPAN, Apr. 1998.

Sugihara, K., "GA-based on-line path planning for SAUVIM," Proc. 11th Int'l Conf. on Industrial and Engineering Applications of Artificial Intelligence and Expert Systems (IEA-98-AIE), Castellon, Spain, 1998, pp.329-338.

Sugihara, K. and Smith, J., "Genetic algorithms for adaptive planning of path and trajectory of a mobile robot in 2D terrain," IEICE Trans. Information and Systems, Vol. E82-D, No. 1, pp.309-317, January 1999.

Yousefpour, A., and Ghasemi Nejhad, M. N., "Testing and Finite Element Modeling of APC-2/AS4 Thermoplastic Composite C-rings," 31st International SAMPE (Society for the Advancement of Material and Process Engineering) Technical Conference: Advanced Materials & Processes Preparing for the New Millennium, vol. 31, pp. 643-654, Chicago, IL, October 1999.

Yuh, J. and Choi, S.K., "Semi-Autonomous Underwater Vehicle for Intervention Missions (SAUVIM)," Sea Technology, Oct. 1999.

Choi, S.K., Easterday, O., Ikehara, C., Coutsourakis, C., & Yuh, J., "Development of SAUVIM," The Proceedings of the Symposium of Underwater Robotic Technologies (SURT) 2000, Maui, HI, Jun. 2000.

Choi, S.K., Sugihara, K., Menor, S., Nip, A., & Yang, Z., "A Predictive Virtual Environment Monitor for SAUVIM," The Proceedings of the Symposium of Underwater Robotic Technologies (SURT) 2000, Maui, HI, Jun. 2000.

Kim, T.W., Choi, S.K., Lee, J.W., West, M.E., & Yuh, J., "A Real-Time Distributed Control Architecture for AUVs," The Proceedings of the Symposium of Underwater Robotic Technologies (SURT) 2000, Maui, HI, Jun. 2000.

Marani, G., Bozzo, T., & Choi, S.K., "A Fast Prototyping Approach for Designing the Maris Manipulator Control," The Proceedings of the Symposium of Underwater Robotic Technologies (SURT) 2000, Maui, HI, Jun. 2000.

Ng, R., Uyema, M., Yousefpour, A., Ghasemi Nejhad, M.N., Flegal, B., and Sung, E., "Manufacturing and Testing of Shallow Water Composite Pressure Vessels for Semi-Autonomous Underwater Vehicle," World Automation Congress 2000 (WAC 2000), in press, June 2000.

Sugihara, K. and Yuh, J., "Adaptive, intelligent motion planning system for AUV's," Proc. SURT2000, Maui, Hawaii, 2000.

Yousefpour, A., Ng, R., Uyema, M., and Ghasemi Nejhad, M.N., "Design and Finite Element Analysis of Shallow Water Composite Pressure Vessels for Semi-Autonomous Underwater Vehicle," World Automation Congress 2000 (WAC 2000), in press, June 2000.

Choi, S.K., Menor, S. & Yuh, J., "Distributed Virtual Environment Collaborative Simulator for Underwater Robots" The Proceedings of the International Conference on Intelligent Robots and Systems (IROS) 2000, Takamatsu, JAPAN, Nov. 2000

Choi, S.K. & Easterday, O.T., "The Development of an Underwater Vehicle Monitoring System and Its Sensor Systems," The Proceedings of the International Symposium on Experimental Robotics (ISER), Honolulu, HI, Dec. 2000.

Ng, R., A., Yousefpour, M., Uyema, and M. N., Ghasemi Nejhad, "Design, Analysis, Manufacture, and Test of Shallow Water Pressure Vessels using E-Glass/Epoxy Woven Composite Material for a Semi-Autonomous Underwater Vehicle, submitted to the Journal of Composite Materials, in review, 2000.

Yousefpour, A. and M. N., Ghasemi Nejhad "Experimental and Computational Study of APC-2/AS4 Thermoplastic Composite C-Rings," Journal of Thermoplastic Composite Materials, in press, 2000.

Yousefpour, A., and M. N. Ghasemi Nejhad, "Effects of Geometric Optimization of Tapered End-caps on Thick Thermoplastic Composite Pressure Vessels for Deep Ocean Applications," Journal of Thermoplastic Composite Materials, submitted for publication, 2000.

Choi, S.K. and Yuh, J., "A Virtual Collaborative World Simulator for Underwater Robots using Multi-Dimensional, Synthetic Environment, "Submitted to the IEEE International Conference on Robotics and Automation (ICRA) 2001, Seoul, KOREA, May 2001.

Choi, S.K. and Yuh, J. (Editors), Underwater Robotic Vehicle Technologies, TSI Press, Albuquerque, NM, expected to be published 2001.